Development and application of computational quantum many-body methods for strongly correlated models and materials

A Thesis
Submitted For the Degree of
DOCTOR OF PHILOSOPHY
in the Faculty of Science

by

Nagamalleswara Rao Dasari

THEORETICAL SCIENCES UNIT
JAWAHARLAL NEHRU CENTRE FOR ADVANCED SCIENTIFIC RESEARCH
Bangalore – 560 064, India

NOVEMBER 2015

This thesis is dedicated to my family

For their endless love, support and encouragement

DECLARATION

I hereby declare that the matter embodied in the thesis entitled "**Development and application of computational quantum many-body methods for strongly correlated models and materials**" is the result of investigations carried out by me at the Theoretical Sciences Unit, Jawaharlal Nehru Centre for Advanced Scientific Research, Bangalore, India under the supervision of Prof. N. S. Vidhyadhiraja and that it has not been submitted elsewhere for the award of any degree or diploma.

In keeping with the general practice in reporting scientific observations, due acknowledgement has been made whenever the work described is based on the findings of other investigators. Any omission that might have occurred by oversight or error of judgement is regretted.

Nagamalleswara Rao Dasari

CERTIFICATE

I hereby certify that the matter embodied in this thesis entitled "**Development and application of computational quantum many-body methods for strongly correlated models and materials**" has been carried out by Mr. Nagamalleswara Rao Dasari at the Theoretical Sciences Unit, Jawaharlal Nehru Centre for Advanced Scientific Research, Bangalore, India under my supervision and that it has not been submitted elsewhere for the award of any degree or diploma.

Prof. N. S. Vidhyadhiraja
(Research Supervisor)

Contents

Preface ix

Acknowledgements xv

Publications xix

List of Figures xxi

List of Tables xxxi

1 Introduction 1

1.1 Strongly correlated electronic systems 3

1.2 Microscopic model Hamiltonian's: 4

1.3 Dynamical mean field theory 6

1.4 Maximum Entropy Method 12

1.5 DFT+DMFT 14

Bibliography 15

2 A multi-orbital iterated perturbation theory for model Hamiltonians and real material-specific calculations of correlated systems 21

2.1 Introduction 21

2.2 Model and Formalism 27

2.3 Results and Discussion 30

2.3.1 Single band Hubbard model: Half-filled case 31

2.3.2 Single band Hubbard model: Doped Mott insulator case . . . 33
2.3.3 Covalent Insulator 35
2.3.4 Two orbital Hubbard model 37
2.3.5 Two orbital Hubbard model: Crystal field splitting and Hund's coupling 45
2.3.6 Application to real materials: $SrVO_3$ 47
2.4 Conclusions 55
Bibliography 56

3 Analytic continuation of hybridization expansion continuous-time quantum Monte-Carlo data using maximum entropy method 65

3.1 Introduction 65
3.2 A brief review of the maximum entropy method (MEM) 68
3.2.1 Prior probability 68
3.2.2 Likelihood function 70
3.2.3 Preparing uncorrelated data 70
3.2.4 Selection of α 72
3.2.5 Default model selection 73
3.2.6 Annealing method 74
3.3 Model and formalism 74
3.3.1 Single particle quantities 75
3.3.2 Two particle quantities 77
3.4 Results and discussion 79
3.4.1 Binning in CTQMC 79
3.4.2 Half-filling case 82
3.4.3 Doped case 85
3.5 Thermodynamic observables: NMR, Knight shift and Korringa ratio . 86
3.6 MEM for real materials: $SrVO_3$ 88
3.7 Conclusions 89

Bibliography 90

4 Quantum critical dynamics of a magnetic impurity in a semiconducting host 95

4.1 Introduction 95

4.2 Model and Formalism 97

4.3 Results and Discussion 98

4.4 Conclusions 107

Bibliography 107

5 A continuous time quantum Monte-Carlo study of local quantum critical dynamics in the asymmetric gapped Anderson impurity model 111

5.1 Introduction 111

5.2 Model and Formalism 113

5.3 Results and Discussion 114

5.4 Conclusions 122

Bibliography 122

6 Interplay of strong correlations and covalency in ionic band insulators 127

6.1 Introduction 127

6.2 Models and Methods 129

6.3 Results and Discussion: 132

    6.3.1 Analytical results: T=0 132

    6.3.2 Analytical results: T>0 137

    6.3.3 Numerical results 137

6.4 Conclusions 149

Bibliography 150

7 A first principles investigation of cubic BaRuO$_3$: A Hund's metal 155

7.1 Introduction 155

7.2 Details of the density functional theory calculations and results . . . 158

7.3 GGA+DMFT: Results and Discussion 161

7.3.1 Single Particle Dynamics 162

7.3.2 Two Particle Dynamics 166

7.3.3 Cubic(3C)-BaRuO$_3$ 169

7.4 Conclusions 171

Bibliography 172

8 Weak ferromagnetism and magnetization reversal in YFe$_{1-x}$Cr$_x$O$_3$ 177

8.1 Introduction 177

8.2 Model and Results 181

8.3 Conclusions 189

Bibliography 191

A Derivations for A$_\alpha$, B$_\alpha$ in the MO-IPT ansatz 195

Bibliography 199

Preface

The theme underlying this thesis is the investigation of strongly correlated model Hamiltonians and materials. In this context, the first chapter provides a general introduction to the strongly correlated electronic systems next two chapters 2 & 3 describe the development and implementation of two methods, namely multi-orbital iterated perturbation theory and maximum entropy method, while the chapters 4-7 investigate the physics arising from the application of these methods along with a numerically exact method namely continuous time quantum Monte-Carlo (CTQMC) to the gapped Anderson impurity model (chapters 4 and 5), correlated band insulator models (chapter 6) and to the cubic perovskite material 3C-$BaRuO_3$ in chapter 7. The final chapter examines a system in the extreme strong correlation limit, where the charge degree of freedom is completely frozen, and hence the Heisenberg model along with the Dzyaloshinskii-Moriya interactions yields an excellent description. The system is an orthoferrite alloy, namely $YFe_{1-x}Cr_xO_3$, which displays weak ferromagnetism and magnetization reversal in certain parameter regimes. We now describe the work contained in these chapters in some detail.

Theoretical investigations of quantum correlated systems represent a great challenge in modern condensed matter physics. The greatest difficulty lies in the absence of methods that can deal satisfactorily with all aspects of the problem, namely the multiple degrees of freedom such as spin, charge, orbital and lattice, in the presence of strong Coulomb interactions. Although a single method possessing the above mentioned capability remains a holy grail, a less ambitious goal would be to find an approximate method that is computationally inexpensive, yields data directly on real frequencies, can handle all interactions strengths and temperatures, and most importantly, is extensively benchmarked with exact methods to ascertain its range of validity. This thesis describes the development of such a method in its second chapter. The method is named multi-orbital iterated perturbation theory (MO-IPT), which as the name suggests is a diagrammatic perturbation theory based method. We used MO-IPT to study N-fold degenerate and non degenerate Anderson impurity models. As applications of the solver, we have combined the method with dynamical mean field theory to explore lattice models like the single orbital Hubbard model, covalent band insulator and the multi-orbital Hubbard model for density-density type interactions in different parameter regimes. The Hunds coupling effects in case of multiple orbitals is also studied. The limitations and quality of results are gauged through extensive comparison with data from the numerically exact continuous time quantum Monte Carlo method (hybridization expansion CTQMC). In the case of single orbital Hubbard model, covalent band insulators and non degenerate multi-orbital Hubbard models, we obtained an excellent agreement between the Matsubara selfenergies of MO-IPT and hybridization expansion CTQMC. But, for the degenerate multi-orbital Hubbard model, we observe that the agreement with CTQMC results gets better as we move away from particle-hole symmetry. We have integrated MO-IPT with density functional theory based electronic structure methods to study real material systems. As a test case, we have studied the classic, strongly correlated electronic material, $SrVO_3$. A comparison of density of states and photo emission spectrum (PES) with results obtained from different impurity solvers and experiments yields good agreement. We find that the method performs excellently in all regimes except close to half-filling or in the proximity of quantum phase transitions.

It is very well known that quantum Monte-Carlo (QMC) algorithms are numerically exact and produce data on the imaginary frequency/time (Matsubara) axis. But the usefulness of these algorithms is restricted because of the ill-posed problem of Wick's rotation or analytic continuation involved in extracting real frequency data from imaginary axis. This in turn requires bins of data along with the covariance matrix. For traditional Monte-Carlo methods such as Hirsch-Fye QMC, the maximum entropy method (MEM) based on binned data performs very well. However, unlike Hirsch-Fye QMC methods, binning cannot be implemented in the present implementations of CTQMC due to prohibitive computational cost. Hence, in chapter 3, we propose an alternative way to create bins by mapping each bin to a different random seed used in the Markovian chain of the CTQMC algorithm. The bins obtained by each random seed, if used to generate a covariance matrix, is amenable to analytic continuation by MEM. We benchmark this procedure by carrying out MEM calculations for single and two particle quantities of single-impurity Anderson model and lattice model as well. Using the analytically continued dynamical susceptibility, we calculate thermodynamic quantities like nuclear magnetic relaxation rate ($\frac{1}{T_1 T}$), Knight shift(K_s) and Korringa ratio(κ) for single-impurity Anderson model in the particle-hole symmetric and asymmetric cases.

In chapters 4 and 5, we applied the CTQMC method followed by MEM to investigate the physics of a magnetic impurity in a semi-conducting host. The screening of a magnetic impurity by conduction electrons in a metal generates a new energy scale called Kondo temperature (T_K) and the associated many-body screening resulting in a singlet ground state is called the Kondo effect. This is a very well understood phenomenon. The fate of a magnetic impurity in a semiconducting host is, however, debated. The question is - To what extent is the Kondo screening active if there are no conduction electrons at the Fermi level? We find, in a symmetric impurity case (Chapter-4), that for any finite gap (δ) in the conduction band, the Kondo effect is suppressed and the ground state is a doublet. The imaginary part of Matsubara self-energy (-Im $\Sigma(i\omega_n)$) exhibits universal scaling in terms of ω_n/T_K for a fixed gap of δ/T_K , which is in parallel to the single-particle spectral function on real frequency axis. Using the self-energy and the longitudinal static susceptibility, we obtain a phase diagram in the temperature-gap plane. The separatrix between the low temperature local moment phase and the high temperature generalized Fermi liquid phase of this phase diagram is shown to be the lower bound of the critical scaling region of the zero gap quantum critical point. Based on dynamical spin susceptibility scaling as a function of ω/T, we classified the zero gap quantum critical point as an interacting type. We have computed the nuclear magnetic spin-lattice relaxation rate, the Knight shift and the Korringa ratio, which show strong deviations for any non-zero gap from the corresponding quantities in the gapless Kondo screened impurity case. In the asymmetric case (Chapter-5), we find a critical Kondo destruction of the Fermi surface in the quantum relaxation regime for a finite value of gap δ in the bath density of states. The critical gap δ_c increases with increasing particle-hole asymmetry.

The unusual effects of local Coulomb repulsion (U) in band insulators is the theme of chapter 6. The localizing effect of U is intuitive and well-known from extensive studies of the Mott metal-insulator transition. However, a recent study by Garg et al opened up the possibility of finding an interaction driven metal in an otherwise non-interacting ionic band insulator. We examine the role of U in models that incorporate covalency into the ionic Hubbard model, and ask if metallicity is further enhanced or suppressed. The CTQMC as well as IPT methods have been used in this work within the framework of dynamical mean field theory (DMFT). A rich phase diagram in the temperature-covalency (ionicity) plane was found. The interaction driven metallic region found by Garg et al, here is shown analytically to be just a line of measure zero in the U-V(ionic potential) plane for the ionic Hubbard model. Especially, the point where the covalency is equal to the ionicity was found to have two metallic regimes, one at the non-interacting level, and the other at large interactions. Even more surprising is the finding that these two metallic regions are separated by a correlated band-insulator phase. Hence correlations can not only delocalize but also force a metal into a band-insulator.

A highly successful framework to study electronic correlations in real materials is the integration of density functional theory with DMFT. In chapter 7, a first-principles investigation of cubic-BaRuO$_3$, by combining density functional theory with dynamical mean-field theory along with MEM, has been carried out. The Ruthenates have strong hybridization with Oxygen due to the extended nature of 4d orbitals in space. The screened Coulomb interaction in these materials is of the order of 4d bandwidth, so we should expect weak to intermediate electronic correlations in these materials. But experimentally, these oxides exhibit characteristic signatures of strong electronic correlations such as high effective mass and non-Fermi liquid behaviour. There are theoretical predictions that strong correlations and non-Fermi liquid signatures in these materials are due to the Hund's coupling. The name coined for them in the literature is Hund's metals. In BaRuO$_3$ the local, on-site Coulomb repulsion, U , was chosen to be the same as that found through constrained random phase approximation calculations for the closely related Strontium ruthenates. We determine the Hunds exchange, J, appropriate for 3C-BaRuO3 such that the computed high temperature paramagnetic moment matches the experimentally found value. Non-magnetic calculations with these parameters for single-particle dynamics and static susceptibility show that cubic-BaRuO3 is in a spin-frozen state at temperatures above the ferromagnetic transition point. A strong red shift with increasing J of the peak in the dynamical susceptibility indicates a dramatic suppression of the Fermi liquid coherence scale in cubic-BaRuO3. Such a clean separation of energy scales in this system provides scope for an incoherent spin-frozen phase, that extends over a wide temperature range, to manifest in non-Fermi liquid behaviour at high temperatures and to be the precursor for the magnetically ordered ground state.

In the final chapter, we build a semi-classical model to explain weak ferromagnetism and magnetization reversal observed experimentally in YFe$_{1-x}$Cr$_x$O$_3$. These

orthoferrite alloys are in fact canted antiferromagnets wherein the Dzyaloshinskii-Moriya (DM) interaction plays a prominent role in the canting of spins. We successfully explain the weak ferromagnetism and magnetization reversal in $YFe_{1-x}Cr_xO_3$ at all values of x. The reason for magnetization reversal for the doping of x=0.4 and 0.5 is that Dzyaloshinskii-Moriya interaction between Fe-Fe and Cr-Cr is in opposite direction to that between the Iron and Chromium atoms.

Acknowledgements

This thesis has been kept on track and been seen through to completion with the support and encouragement of numerous people which includes my well wishers, my friends, my colleagues and collaborators. I take this opportunity to thank all the people who have inspired, encouraged and supported me in my academic as well as personal life.

First and foremost, I would like to thank my research supervisor, Prof. N. S. Vidhyadhiraja for giving me the opportunity to explore the field of strongly correlated electronic systems and the academic freedom which I have received in his group. The ideas suggested by him was helpful in overcoming many numerical problems which I had encountered. I sincerely acknowledge him for providing an opportunity to interact with the leading scientists, Prof. Mark Jarrell and Prof. Juana Moreno. I am extremely thankful to him for giving me an opportunity to visit Louisiana state University, USA, for six months which helped me to interact and exchange ideas with experts in my field. He has been very supportive in my professional life, and I convey my deepest sense of gratitude for providing excellent guidance through scientific inputs throughout my Ph.D. tenure and even during his sabbatical leave. His encouragement and scientific inputs have played a pivotal role in shaping my thesis. His unflinching courage, dedication and honesty in the work has inspired me and has played a significant role in making me a better scientist.

I would like to thank Prof. Mark Jarrell and Prof. Juana Moreno, for providing me an opportunity joining their group as a visiting scholar. I sincerely thank Prof. Mark Jarrell for teaching me maximum entropy method which I have used in my works. I am also thankful to Prof. Mark and Prof. Juana for the discussion every week. I also sincerely acknowledge Prof. Mark and Prof. Juana for giving access to their computational facilities which I have used for most of the work in this thesis.

I acknowledge the computational facilities provided by Center for Computation & Technology, Louisiana State University, USA. I specially thank Dr. Sandeep Kumar Reddy, who has helped me in using these computational facilities. I am also thankful to the Jawaharlal Nehru Centre for providing excellent research and computational facilities.

I am thankful to the faculty members of theoretical sciences unit, Prof. Umesh V. Waghmare, Prof. Shobhana Narasimhan, Prof. Swapan K Pati, Prof. N. S. Vidhyadhiraja, Prof. Subir K. Das and Prof. Kavita Jain for the various courses they offered. I also thank Prof. Vijay B. Shenoy (IISC - Bangalore) for the advanced many-body course and Prof. S. Ramasesha (IISC - Bangalore) for the help in multi-spin coding. I sincerely acknowledge Prof. H. R. Krishnamurthy (IISC - Bangalore) for fruitful discussions.

I express my sincere thanks to all my collaborators, Prof. Mark Jarrell (LSU - USA), Prof. Juana Moreno (LSU - USA), Prof. Dr. Thomas Pruschke (University of Göttingen - Germany), Prof. Ross H. McKenzie (University of Queensland - Australia), Prof. Dr. Alessandro Toschi (TU Wien - Wien), Prof. Dr. Giorgio Sangiovanni (Würzburg - Germany), Prof. Arghya Taraphder (IITKGP - Kharagpur), Dr. Manish Jain (IISC - Bangalore), Prof. Sundaresan (JNCASR - Bangalore), Prof. Swapan K Pati (JNCASR - Bangalore), Prof. Tanusri Saha-Dasgupta (SNBOSE - Kolkata), Dr. P. Mondal, Dr. Peng Zhang, Swagata Acharya, SRKC Sharma Yamijala and Andi for various discussions.

I am thankful to the open source community for providing useful software's and operating systems. I particularly acknowledge the developers of ALPS, TRIQS, MEM, QUANTUM ESPRESSO, WIEN2K, WANNIER-90, PYTHON, LATEX, and INTEL LIBRARIES.

I thank CICS (India), ICAM-I2CAM (USA), JNCASR (India) for international travel fellowships and UGC-CSIR (India) for junior and senior research fellowships.

I express thanks to the teaching and non-teaching staffs of JNCASR for their prompt assistance and cooperative attitude.

I am thankful to all past and present lab mates: Dr. Himadri Barman, Dr. Pramod Kumar, Sudeshna, Rukhsan-Ul-Haq and Wasim Raja Mondal for their help.

I thank all my friends at JNCASR, especially Sandeep, Srinu, Narendra, Sharma, Pandu (JNC Arnold Schwarzenegger), Satya, Malli Tangi, Malli Karjun, Gangayya, Pralok, L. N. Reddy and Sarayya (Srimanthudu) for being always helpful and for making my six and a half years of stay in JNC joyful and memorable.

I am also thankful to Telugu community of JNCASR for the fun we had during lunch and dinner time in the mess.

I express my special acknowledgement to Sharma, Swagata, Dhanya, Rukhsan-Ul-Haq, Amit, Anirudha Mirmira, Satya, Rajaji and Divya Bharati for correcting thesis chapters.

Last but not least, my father, mother, sister Geetha and my brother in law Rama Krishna deserve special mention for their inseparable support, encouragement and prayers.

I also thank all those who have helped me directly or indirectly.

Nagamalleswara Rao Dasari

Publications

1. **Nagamalleswara rao Dasari**, P. Mandal, A. Sundaresan and N. S. Vidhyadhiraja , “Weak ferromagnetism and magnetization reversal in $\mathrm{YFe}_{(1-x)}\mathrm{Cr}_x\mathrm{O}_3$”, **Europhysics Letters**, 99, 17008 (2012).

2. **Nagamalleswara rao Dasari**, Wasim Raja Mondal, Peng Zhang, Juana Moreno, Mark Jarrell and N. S. Vidhyadhiraja, “A multi-orbital iterated perturbation theory for model Hamiltonians and real material-specific calculations of correlated systems”, **Manuscript under review in PRB, arXiv:1504.04097.**

3. **Nagamalleswara rao Dasari**, Swagata Acharya, A. Taraphder, Juana Moreno, Mark Jarrell and N. S. Vidhyadhiraja, “Quantum critical dynamics of a magnetic impurity in a semiconducting host”, **to be submitted, arXiv:1509.09163.**

4. **Nagamalleswara rao Dasari**, SRKC Sharma Yamijala, Swapan K. Pati, Manish Jain, Tanusri Saha-Dasgupta, Juana Moreno, Mark Jarrell, N. S. Vidhyadhiraja, “A first principles investigation of cubic BaRuO_3: A Hund’s metal”, **to be submitted, arXiv:1511.01371.**

5. **Nagamalleswara rao Dasari**, Juana Moreno, N. S. Vidhyadhiraja and Mark Jarrell, “Analytic continuation of hybridization-expansion continuous-time quantum Monte-Carlo data by using maximum entropy method (MEM)”, **Draft under revision.**

6. **Nagamalleswara rao Dasari**, Juana Moreno, Mark Jarrell and N. S. Vidhyadhiraja, “Interplay of covalency and ionicity in correlated band insulators”,

Draft under revision.

7. **Nagamalleswara rao Dasari**, Juana Moreno, Mark Jarrell and N. S. Vidhyadhiraja, "A continuous time quantum Monte Carlo study of local quantum critical dynamics in the asymmetric gapped Anderson impurity model", **Manuscript in preparation.**

8. **Nagamalleswara rao Dasari**, Juana Moreno, Mark Jarrell, N. S. Vidhyadhiraja and Ross. H. Mckenzie, "Dynamical spin susceptibility of bad metals", **Manuscript in preparation.**

9. Wasim Raja Mondal, **Nagamalleswara rao Dasari**, Manish Jain, Juana Moreno, Mark Jarrell and N. S. Vidhyadhiraja, "An LDA+DMFT study of new perovskite $BaVO_3$", **Draft under revision.**

10. Swagata Acharya, **Nagamalleswara rao Dasari**, N. S. Vidhyadhiraja and A. Taraphder "Metamagnetic quantum criticality in multi-orbital systems", **Manuscript in preparation.**

11. Swagata Acharya, **Nagamalleswara rao Dasari**, N. S. Vidhyadhiraja and A. Taraphder "Signatures of pseudo gap across orbital selective Mott-transition.", **Manuscript in preparation**.

12. Rukhsan-ul-haq, **Nagamalleswara rao Dasari** and N. S. Vidhyadhiraja, "Role of valence fluctuations in heavy fermion systems", **Manuscript in preparation.**

New Developments :

A quantum impurity solver called multi-orbital iterated perturbation theory(MO-IPT) implementation in Fortran-90; Available as an open source package at

www.institute.loni.org/lasigma/package/mo-ipt/ .

List of Figures

1.1 (color online) Schematic representation of diagramatic, perturbation series expansion of CT-INT at the second order level in terms of Feynman, diagrams. 11

1.2 (color online) Schematic representation of insertion and removal updates in CT-INT method. 12

1.3 (color online) Schematic of Wick's rotation for single particle and two particle quantity 13

1.4 (color online) Schematic of MEM procedure 13

2.1 (Color online) (a) Quasi-particle weight Z of the single band half-filled Hubbard model obtained with different impurity solvers (see text for more details) (b) Double occupancy D obtained from MO-IPT and S-CTQMC. 32

2.2 (color online) Comparison of the imaginary part of Matsubara Green's function (left panels) and self energy (right panels) obtained from MO-IPT, S-CTQMC and W-CTQMC[44] for $U/W = 1.0$ (top panels) and $U/W = 1.5$ (bottom panels) at $\beta = 64$. 33

2.3 (color online) Quasi-particle weight obtained from MO-IPT (or IPT-L) is compared to the same obtained from CTQMC for the paramagnetic doped Mott-insulator as a function of filling with $U/W = 1.5$ and $\beta = 64$. 34

2.4 (color online) Doped Mott insulator: Comparison of imaginary part of Matsubara Green's function and self energy obtained from MO-IPT, W-CTQMC and S-CTQMC for U/W = 1.5 at different fillings and $\beta = 64$. 35

2.5 (color online) Covalent insulator: (a) Quasi-particle weight Z as a function of U/W obtained from MO-IPT (black circles) and CTQMC (red squares) for $\beta = 60$ and V=0.5.(b) Double occupancy as a function of U/W obtained from MO-IPT and S-CTQMC. (c) Charge gap as a function of U/W obtained from MO-IPT at T=0. 37

2.6 Covalent insulator: Spectral functions (left panels) and imaginary part of self energy (right panels) from MO-IPT at $U/W = 5.0$ and V=0.5 for a range of $\beta = 1/T$ values (increasing T from top to bottom). . . 38

2.7 (color online) Covalent insulator: Comparison of the imaginary part of Matsubara (a) Green's function and (b) self-energy obtained from MO-IPT (black) and S-CTQMC (red) for various U/W values and β=60. 38

2.8 (color online) (a) Two-orbital SU(4) symmetric Hubbard model at half-filling: Quasi particle weight obtained from different impurity solvers as a function of U/W for $\beta = 64$. (b) Double occupancy obtained from MO-IPT (black circles) and hybridization expansion CTQMC (red squares) for β=64. 39

2.9 (color online) Two-orbital, SU(4) symmetric Hubbard model at half-filling: Imaginary part of Matsubara Green's function (left panels) and self energy (right panels) obtained from MO-IPT (red solid lines) and S-CTQMC (black solid lines) at β=64. 40

2.10 (color online) Two orbital half-filled Hubbard model, finite J: Quasi particle weight dependence on U/W obtained from (a) strong coupling CTQMC, (b)ED and (c) MO-IPT for various J values. Insets in the panels (a) and (b) show the effect of J on Z in the weak coupling regime. 41

2.11 (color online) Two orbital half-filled Hubbard model, finite J: Imaginary part of Matsubara Green's functions (left panels) and self-energy (right panels) obtained from S-CTQMC (black) and MO-IPT (red) for different values of J and U/W at β=64. 42

2.12 (color online) Two-orbital Hubbard model: Effect of J away from half-filling ($n_{tot} = 1.1$) The imaginary part of the Matsubara self-energy for various J-values, and fixed $U/W = 1$ as computed within (a) S-CTQMC and (b) MO-IPT. Comparison of quasi particle weight obtained from MO-IPT (black circles) and CTQMC (red squares) as a function of U/t for (c) $J = 0.0$, (d) $J = U/4$ and (e) $J = U/3.5$ for $\beta = 64$; and (f) as a function of J for a fixed $U/W = 1.0$. 43

2.13 (color online) Two-orbital Hubbard model, away from half-filling: Real frequency spectral functions (left panels) and minus imaginary part of self energy (right panels) for various U/W and J values. 44

2.14 (color online) Two-orbital degenerate Hubbard model, away from half-filling: Comparison of Imaginary part of Matsubara Green's function (left panels) and self energy (right panels) obtained from MO-IPT and S-CTQMC for various values of J at $U/W = 1.25$. 45

2.15 (color online) Crystal field effects: Quasi particle weights for (a) orbital-1 and (b) orbital-2, obtained from MO-IPT and CTQMC for various U/W values with $J = U/4$ at β=64. The insets show the corresponding occupancies. 46

2.16 (color online) Crystal field effects: Comparison of imaginary part of self energy for orbital-1(left) and orbital-2(right) obtained from MO-IPT and S-CTQMC for various values of U/W and $J = U/3.5$. . 47

2.17 (color online) Band structure of $SrVO_3$ obtained from DFT. 50

2.18 (color online) The projected density of states (DOS) of $SrVO_3$ as calculated by GGA (LAPW). 51

2.19 (color online) Comparison of spectral function of $SrVO_3$ obtained from different methods for U = 3.44 eV and J = 0.46 eV (see text for details). 51

2.20 (color online) Comparison of photo emission spectra obtained from different methods GW+DMFT [74], GGA+DMFT (MO-IPT), LDA+DMFT (CTQMC)[74] and experiment [75]. 55

3.1 (color online) Schematic of the binning procedure for impurity problem. 79

3.2 Square root of eigen values of the covariance matrix obtained from (a) Matsubara time Green's function and (b) Matsubara frequency self-energy for $U/W = 1$ and $\beta = 4$. 81

3.3 Square root of eigen values of the covariance matrix obtained from (a) Matsubara time two particle correlation function and (b) Matsubara frequency two particle correlation function. 82

3.4 (color online) (a) Imaginary part of the analytically continued self energy on real frequency axis for different β and $U/W = 1$ (b) Real part of self energy on real frequency axis and (c) the impurity spectral function for same parameters as (a). ($\Delta_0 = \frac{\pi V^2}{W} = 0.7853$) 83

3.5 (color online) Imaginary part of dynamical spin susceptibility on real frequency axis for different β and $U/W = 1$. 84

3.6 (color online) (a) Imaginary part of self energy on real frequency axis for different β and $U/W = 1.0$ (b) Real part of self energy and (c) impurity spectral functions for same parameters as (a). ($\Delta_0 = \frac{\pi V^2}{W} = 0.7853$) 85

3.7 (color online) Imaginary part of dynamical spin susceptibility on real frequency axis for different β and $U/W = 1$. 86

3.8 (color online) (a) Nuclear magnetic relaxation rate (b) Knight shift and (c) Korringa ratio at $U/W = 1$ and for $n = 1, 0.83$. 87

3.9 (color online) Schematic of the binning procedure for lattice problem. 89

3.10 (color online) MEM spectrum obtained from DFT+DMFT(HY-CTQMC) data (using MO-IPT as a default model) for $SrVO_3$ at $U = 3.4$ eV, $J = 0.44$ eV and $\beta = 40$ eV^{-1}. 90

4.1 (color online)Imaginary part of Matsubara frequency self energy for a range of values of gap in the conduction bath density of states at (a) $\beta = 10$, (b)$\beta = 45$ and (c) $\beta = 400$ with $U = 4.0$ and $V = 1.0$. The dashed line is a power law fit to the low frequency part of the gapless case.(d) For a fixed δ/T_K=0.1 and $\beta = 500$, the low frequency imaginary part of the self-energy for various U-values collapses onto a universal scaling power law when plotted *vs* ω_n/T_K and scaled by a multiplicative factor, $Y_f \sim \mathcal{O}(1)$. 99

4.2 (color online) A phase diagram in the $\frac{T}{T_K}$-$\frac{\delta}{T_K}$ plane for varying U values. The shaded region is the generalized Fermi liquid while the unshaded is the local moment regime. The dashed line is the extrapolated, asymptotic strong coupling separatrix between the GFL and LM phases. 100

4.3 (color online) (a) The product of temperature and the local static spin susceptibility (4T$\chi_{loc}(T)$) as a function of T/T_K for a range of gap values (indicated in legends) for a $U = 6.0$. The dashed line is a linear fit in the gapless case. (b)The $T \rightarrow 0$ residual moment on the impurity for different U values as a function of gap. The brown dashed line is a power law fit to the low gap part of the $U = 8.0$ data. 101

4.4 (color online) Spectral function f(ω,T)= $\frac{\pi\chi^{''}(\omega)T_K}{2\omega\chi_{loc}(T)}$ for different gap values and $\beta = 100$, which corresponds to a $T/T_K = 0.06$ for $U = 4.0$. 102

4.5 (color online) Dynamical susceptibility scaling collapse: (a) $\chi(\tau)$ *vs* $\pi T/\sin(\pi\tau T)$, (b) $\frac{\mathrm{Im}\chi(\omega)}{\chi_{loc}(T)}$ *vs.* ω/T for various temperature fractions with $U = 6.0$ and $\delta/T_K = 0.5$. The dashed lines in both the panels are power law fits. 103

4.6 (color online) Single particle, two particle Green's functions and Dynamical susceptibility scaling collapse: (a) $G(\tau)$ *vs* $\pi T/\sin(\pi\tau T)$, (b) $\chi(\tau)$ *vs* $\pi T/\sin(\pi\tau T)$, (c) $\frac{\mathrm{Im}\chi(\omega)}{\chi_{loc}(T)}$ *vs.* ω/T for various temperature fractions with $U = 6.0$ and $\delta/T_K = 0.25$. The dashed lines in all panels are power law fits. 104

4.7 (color online) Single particle, two particle Green's functions and Dynamical susceptibility scaling collapse: (a) $G(\tau)$ *vs* $\pi T/\sin(\pi\tau T)$, (b) $\chi(\tau)$ *vs* $\pi T/\sin(\pi\tau T)$, (c) $\frac{\mathrm{Im}\chi(\omega)}{\chi_{loc}(T)}$ *vs.* ω/T for various temperature fractions with $U = 6.0$ and $\delta/T_K = 1.0$. The dashed lines in all panels are power law fits. 104

4.8 (color online) (a) Nuclear spin-lattice relaxation rate, (b) Knight shift and (c) Korringa ratio as a function of temperature for various gap values and $U = 4.0$. Inset: Knight shift at low temperature. 105

5.1 (color online) Imaginary part of Matsubara self energy for different gap values in the bath density of states for a $U = 6.0$ corresponding to which a gapless Kondo scale is obtained as $T_K = 0.12$. The temperature is $\beta = 1/T = 800$ and the particle-hole asymmetry, $\eta = 0.4$. 116

5.2 (color online) Local static spin susceptibility as a function of temperature for different gap values at $U = 6$ and and $\eta = 0.4$, for which $T_K = 0.12$. 117

5.3 (color online) Self energy in the main panel and moment in the inset.U=6, $\eta = 0.4, \beta = 700$. 118

5.4 (color online) Critical δ *vs.* η phase diagram (a) for T$_K$ = 0.172 and β = 700. (b) for T$_K$ = 0.12 and β = 800. 119

5.5 (color online) Quasi particle weight (Z(T)) as a function of temperature for different gap values at T$_K$ = 0.172. The interaction strength, $U = 5.0$ and asymmetry, η is 0.4. 120

5.6 (color online) Matsubara time spin-spin correlation function for different gap values at $T_K = 0.12$, $\beta = 800$ and for $\eta = 0.4$. 121

6.1 (color online) (a) Re$\zeta_{1\sigma}(0)$ as a function of U for δn = 0.0025,0.0050 obtained from HF-theory (b) Re$\zeta_{1\sigma}(0)$ as a function of U for δn = 0.0025 obtained from DMFT (IPT). In the inset we have zoomed on the zero crossing to show that we have a single zero crossing as a function of U (We have used η=10^{-9} and energy unit D = $\frac{W}{2}$ = 2). . 138

6.2 (color online) Fermi-level spectral weight $\tilde{A}_{1\sigma}$ as a function of U for different β values obtained from HY-CTQMC for x=1.(Downarrow corresponds to increase in U, Uparrow corresponds to decrease in U, Energy unit D = $\frac{W}{2}$ = 1) 139

6.3 (color online) Finite temperature phase diagram of Ionic band Insulator (x=1.0) obtained from HY-CTQMC (BI: Band Insulator, M: Metal and MI: Mott Insulator), Inset: Linear fit to $\tilde{A}_{1\sigma}$ in the metallic region at β=128. 140

6.4 (color online) (a) Quasi particle weight(Z) as a function of $\frac{U}{W}$ obtained from IPT. (b) Charge gap as a function of $\frac{U}{W}$ obtained from IPT.(We have used η= 10^{-2} and energy unit is D=$\frac{W}{2}$=2) 141

6.5 (color online) Fermi-level spectral weight as a function of $\frac{U}{W}$ for different β values obtained from HY-CTQMC for x=0.0 (Energy unit D=W/2=1.0) 142

6.6 (color online) Finite temperature phase diagram of Covalent band Insulator (x=0.0) on T Vs U plane (Energy unit D=W/2=1.0). . . . 143

6.7 (color online) Non-interacting spectral function for x=0.5 (We have used η=10^{-2} and energy unit = D = $\frac{W}{2}$ = 1) 143

6.8 (color online) Fermi-level spectral weight as a function of $\frac{U}{W}$ obtained from HY-CTQMC for different β values and x=0.5 (Energy unit D = $\frac{W}{2}$ = 1). 144

6.9 (color online)(a) Fermi-level spectral weight as a function of $\frac{U}{W}$ obtained from HY-CTQMC for x=0.5 and β = 300 (c) Fermi-level spectral weight as a function $\frac{U}{W}$ obtained from IPT for x=0.5 and β = 300 (Energy unit D=$\frac{W}{2}$ = 1). 145

6.10 (color online) Finite temperature phase diagram (T Vs U) for x=0.5 covalency (Energy unit D=W/2=1). 146

6.11 (color online) Non-interacting occupancy (a) for orbital 1 (b) for orbital 2 and (c) gap in the spectral function as function of x (V = 0.5 and Energy unit=D=$\frac{W}{2}$=1) 147

6.12 (color online) T Vs U phase diagram for 0.5> x <1.0 (Energy unit = D = $\frac{W}{2}$=1). 147

6.13 (color online) T Vs U phase diagram for 0.0> x <0.5 (Energy unit = D = $\frac{W}{2}$=1) 148

6.14 (color online) Critical U values Vs x Phase diagram for V = 0.5 and β=128 (Energy unit D=W/2=1) 149

7.1 (color online) Band-structure of cubic $BaRuO_3$ in its nonmagnetic phase. Energies are scaled to the Fermi-level (dotted line). 159

7.2 (color online) Projected density of states (PDOS) of $BaRuO_3$. Green (shaded light gray), violet (shaded dark gray), black (thick line), gray (dotted and dashed line) and orange (dashed line) colors represents the density of states (DOS) of whole system, Ru-atom, O-atom, Ru-t_{2g} and Ru-e_g, respectively. 159

7.3 (color online) Orbital plots of maximally localized Wannier functions used to reproduce the low energy subspace Hamiltonian. 160

7.4 (color online) Low energy subspace band-structure obtained from (a) Plane-wave basis and (b) Wannier basis. 160

7.5 (color online) Imaginary part of Matsubara self energy ($-\mathrm{Im}\Sigma(i\omega_n)$) for $U = 2.3$ eV and different J values for (a) T=60 K, and (b) T=116 K. 162

7.6 (color online) Imaginary part of Matsubara Self energy for T=60 K and different J values (mentioned in legends) with (a) $U = 3$ eV, and (b) $U = 4$ eV. 163

7.7 (color online) Exponent α (left) and intercept C (right) obtained by fitting the data to -Im $\Sigma(i\omega_n) = C + A\ |\omega_n|^\alpha$ at different J values, U = 2.3 eV and T = 60 K, 116K and 232K. 164

7.8 (color online) Imaginary part of self energy (-Im $\Sigma(\mathrm{i}\omega_n)$) fitted to 4th order polynomial: (a) zeroth order coefficient, C_0 (b) $Z = 1/(1 + C_1)$, where C_1 is the linear coefficient, for different J values, U=2.3 and 3.0 eV and T = 60 K. 166

7.9 (color online) Matsubara time spin-spin correlation function for different J values and U = 2.3 eV, T = 60 K. 167

7.10 (online) Local static spin susceptibility; Dashed curves represent a power law fit at low temperatures. Inset: screened magnetic moment as a function of temperature for different J values and U = 2.30 eV. . 168

7.11 (color online) Imaginary part of dynamical spin susceptibility on real frequency axis obtained from maximum entropy method for various J values, U = 2.3 eV and T = 60 K. 169

8.1 (color online) Variation of lattice parameters and volume as a function of x in $\mathrm{YFe}_{1-x}\mathrm{Cr}_x\mathrm{O}_3$. 179

8.2 (color online) Variation of Néel temperature (experiment:triangles and theory:circles) with increasing Cr content. The theoretical curve has been computed with $J_{FeCr} = 24$ K. 183

8.3 Schematic spin structure for the $YFe_{1-x}Cr_xO_3$ system. 185

8.4 (color online) Magnetization (experiment and theory, see legends) as a function of temperature for the parent compounds $YFeO_3$ and $YCrO_3$. The inset shows that a common mechanism underlies the WFM of both the parent compounds, since the $M/M_{\max}$ *vs.* T/T_N is almost identical for both. 186

8.5 (color online) Magnetization (experiment:black and theory:red) as a function of temperature for three compositions, $x = 0.1$ (left), 0.2(middle) and 0.3 (right). 187

8.6 (color online) Magnetization (experiment:black and theory:red) as a function of temperature for $x = 0.4$ (left) and 0.5 (right). Magnetization reversal is seen in this composition range. 189

8.7 (color online) Temperature dependent magnetization (experiment: black and theory:red) for $x = 0.6$ (left), 0.7 (middle) and 0.9(right). . 190

8.8 (color online) The DM interaction D_{FeCr} between the Fe and Cr atoms, as obtained from the comparison of theory and experiment is shown as a function of composition x. It is intriguing to note that it is maximum in magnitude close to $YFeO_3$ and decreases almost monotonically with increasing x. 191

List of Tables

1.1 Pros and Cons of impurity solvers within DMFT: (QMC: quantum Monte-Carlo, NRG: numerical renormalization group, ED: exact diagonalization, DMRG: density matrix renormalization group, IPT: iterative perturbation theory, LMA: local moment approach, NCA: non-crossing approximation and FLEX: fluctuation exchange approximation) 9

7.1 Magnetic ground state and the ratio of γ to γ_{LDA} for 4d Ru-based compounds 156

Chapter 1

Introduction

“Correlation” is the behavioral dependence among two or many entities. In this thesis, we are interested in quantum dynamical correlations between electrons in solids. Consider a typical material containing electrons, and positive ions (have mass $\sim$ 1000 times the electron mass). Since our primary focus is on dynamics of electrons at relatively low energy scales($\sim$ 1-2 eV), relativistic effects need not be considered. Employing the Born-Oppenheimer approximation[1] we can write a general Hamiltonian that describes the electron dynamics in solids as,

$$H = \sum_{i=1}^{N} \left(\frac{-\hbar^2}{2m} \nabla_i^2 + V(r_i) \right) + e^2 \sum_{i<j} \frac{1}{r_i - r_j} \,, \tag{1.1}$$

where $V(r_i)$ is the potential felt by an electron at position r_i due to the periodic array of positive ions. The last term in the above equation represents the Coulomb interaction between electrons. The long range nature of Coulomb interactions, $(\frac{1}{r_{ij}})$, should, intuitively, lead to strong correlations. However, this is not the case, especially when the systems have valence electrons in s and p shells. Due to the extended nature of s and p orbitals in real space, the Coulomb repulsion between electrons in these orbitals is highly screened. In such situations, a static mean field theory works quite well in general. The basic idea of a mean-field theory is that the Coulomb interaction between electrons can be replaced by an interaction between a single electron with an effective field generated by all other electrons. With this simple approach, the systems that have valence in s and p orbitals can be understood in a straightforward manner.

A highly successful approach towards solving eq. 1.1 is provided by the density functional theory(DFT)[2], which is based on two theorems by Hohenberg and Kohn[2, 3]. These state that (a) the ground state density ρ_{GS}(r) of a bound system of interacting electrons in some external potential $V(r)$ determines this potential uniquely; (b) the density that minimizes the total energy is the exact groundstate density[4]. These statements basically reduce the problem of finding a many-body wavefunction dependent on 3N variables on a problem of finding a function, namely the density $\rho(r)$ of only 3 variables. The catch is that the functional dependence of energy on density is, in general, unknown. But, if we approximate the energy functional $E_v[\rho]$, then from the second theorem we can find an approximation to the ground-state density, simply by minimizing it with respect to density. One of the most successful early approximations among such functionals is the local density approximation(LDA)[5, 6] where $E_v[\rho]$ is represented by just a local functional of density $\rho(r)$. Subsequent improvements over the LDA functional include the local spin density approximation and generalized gradient approximation (GGA). However, there is no systematic way of deriving these functionals and different type of functionals are appropriate for different class of compounds[7–9]. DFT, in principle, yields the ground state density of the system and the ground state wave function has a single Slater determinant of single particle wave functions. However, within DFT, we can not treat real spins and any information about the excitation spectrum of eq. 1.1 can not be obtained. Despite the above mentioned draw backs, DFT with LDA/GGA functionals has been successfully used to explain the experimental band structures in a very wide range of materials

1.1 Strongly correlated electronic systems

DFT, however, fails to explain the spectral properties of solids which have partially filled d and f shells. For this class of compounds, DFT quite often predicts a metallic ground state but experiments show that they are insulators. Due to the localized nature of d and f orbitals in space, screening of Coulomb interaction between electrons in those orbitals is poor. Thus, the electrons in d and f orbitals experience a much higher Coulomb repulsion than in the s/p orbitals, leading to strong correlation effects, which in turn imply the break down of any effective one particle picture where the ground state wavefunction of the system is a combination of Slater determinants, and there are no well defined one electron excitations in the system. Because of strong correlations, these systems exhibit interesting properties and phases. The materials which come under this category are termed as strongly correlated electronic systems (SCES). Typical examples of SCES[10] include cuprates, rare-earth compounds, actinides and transition metal oxides. Some of the features of strong correlation effects include metal to Mott transition in V_2O_3[11–16], itinerant magnetism in transition metal oxides[17], giant magneto-resistance in manganites[18, 19], and high-temperature superconductivity in cuprates[20]. Theoretical studies of SCES require quantum many-body methods which are capable of handling strong correlations between electrons. Traditionally, these methods have been applied to studying model Hamiltonian's, that ignore material specific information. With the advent of dynamical mean-field theory (DMFT), it has become possible to combine methods that capture material specific information based on DFT with many body methods that are capable of handling strong correlation effects. Before we delve into the DFT+DMFT framework, we briefly review some of the model Hamiltonian's below.

1.2 Microscopic model Hamiltonian's:

The multi-orbital Hubbard model(MO-HM)[17, 21–24]is a paradigm for study of electronic correlations in SCES. In the standard second quantization notation, the MO-HM can be written as,

$$\begin{aligned}\mathcal{H} =& \sum_{i\alpha\sigma} \epsilon_{i\alpha} n_{i\alpha\sigma} + \sum_{ij\alpha\beta\sigma} T_{ij}^{\alpha\beta} (c^{\dagger}_{i\alpha\sigma} c_{j\beta\sigma} + H.c.) + \sum_{i\alpha} U n_{i\alpha\uparrow} n_{i\alpha\downarrow} + \sum_{i\alpha\neq\beta} U' n_{i\alpha\uparrow} n_{i\beta\downarrow} \\ &+ \sum_{i\sigma\alpha<\beta} (U' - J) n_{i\alpha\sigma} n_{i\beta\sigma} - \sum_{i\alpha\neq\beta} J (c^{\dagger}_{i\alpha\uparrow} c^{\dagger}_{i\beta\downarrow} c_{i\beta\downarrow} c_{i\alpha\uparrow} + c^{\dagger}_{i\beta\uparrow} c^{\dagger}_{i\beta\downarrow} c_{i\alpha\uparrow} c_{i\alpha\downarrow} + H.c.) \,,\end{aligned} \tag{1.2}$$

where $c^{\dagger}_{i\alpha\sigma}$ creates an electron at lattice site i, in orbital α, with spin σ and $c_{j,\beta,\sigma}$ annihilates an electron at site j, in orbital β, with spin σ. The first term represents the onsite energy of each orbital; the second term represents nearest neighbour hopping between electrons in the orbitals. $U(U')$ represents the intra(inter) orbital local Coulomb interaction. The last three terms represents the Ising, spin flip and pair-hopping Hund's coupling terms, respectively. This is a model of great interest to the many-body community because the interplay between orbital and spin degrees of freedom leads to a rich variety of quantum phases. This model has, unfortunately, not been amenable to exact solutions except in limiting cases such as in one dimension for a single orbital. So, approximate analytical schemes and numerical methods to find the solution are necessary. As a brute force method, one can diagonalize[25] the Hamiltonian in eq. 1.2 for finite number of lattice sites to get eigen vectors and eigen values. However as we increase the number of lattice sites, the dimension of Hilbert space grows exponentially and hence the problem is no more tractable. We can solve the above models exactly by using dynamical matrix renormalization group theory[26–28] (DMRG) in one dimension but the application of the method to higher dimensions[29] is not well established. There are other approaches as well, but they are in the process of development. It is necessary to develop approximate methods, that capture the essential physics of the model and are tractable computationally. In this respect dynamical mean field theory has emerged as the method of choice, wherein a lattice problem is mapped onto a quantum impurity problem with a self-consistently determined hybridization, that can be solved analytically (in an approximate way) or numerically. Most of this thesis is devoted to the study of MO-HM, so we will revisit this model again in the later chapters of this thesis.

Before we begin discussing DMFT, we must mention another fundamental model, namely the multi-orbital single-impurity Anderson model (MO-SIAM)[17] which is required to understand the effect of magnetic impurities in metals and semiconductors. The MO-SIAM embodies a single magnetic impurity with discrete quantum states (orbitals) coupled to a continuum of non-interacting degrees of freedom called the bath, which could also have a multi-band structure. In second quantization notation, we can write MO-SIAM as,

$$\begin{aligned}\mathcal{H} = \sum_{i\alpha\sigma} \epsilon_{i\alpha} n_{i\alpha\sigma} + \sum_{ij\alpha\beta\sigma} T_{ij}^{\alpha\beta}(c^\dagger_{i\alpha\sigma} c_{j\beta\sigma} + H.c.) + \sum_{m\sigma} \epsilon_m n_{m\sigma} + \sum_{i\alpha m\sigma} V_i^{\alpha m}(c^\dagger_{i\alpha\sigma} d_{m\sigma} + H.c.) \\ + \sum_m U n_{m\uparrow} n_{m\downarrow} + \sum_{m<m'} U' n_{m\uparrow} n_{m'\downarrow} + \sum_{\sigma, m<m'} (U' - J) n_{m\sigma} n_{m'\sigma} \\ - \sum_{m \neq m'} J(d^\dagger_{m\uparrow} d^\dagger_{m'\downarrow} d_{m'\downarrow} d_{m\uparrow} + d^\dagger_{m'\uparrow} d^\dagger_{m\downarrow} d_{m\uparrow} d_{m\downarrow} + H.c.)\,, \end{aligned} \tag{1.3}$$

where $c^\dagger_{i\alpha\sigma}(c_{i\alpha\sigma})$ creates(annihilates) the electron at lattice site i, in orbital α with spin σ and $d^\dagger_{m\sigma}(d_{m\sigma})$ creates(annihilates) the electron in orbital m with spin σ on impurity. $V_i^{\alpha m}$ is the hybridization between bath and impurity, which allows the electrons to hop from impurity to conduction band and vice-versa. The last four terms in MO-SIAM represent interactions between impurity electrons in different orbitals. We can also describe MO-SIAM in the effective action formalism, which is given by,

$$\begin{aligned} S_{eff} = &- \int_0^\beta d\tau \int_0^\beta d\tau' \sum_{ij\sigma} c^\dagger_{i\sigma}(\tau) \mathcal{G}^0_{ij}(\tau-\tau') c_{j\sigma}(\tau') \\ &+ \sum_{ijkl\sigma\sigma'} \frac{U_{ijkl}}{2} \int_0^\beta d\tau c^\dagger_{i\sigma}(\tau) c^\dagger_{k\sigma'}(\tau) c_{l\sigma'}(\tau) c_{j\sigma}(\tau)\,, \end{aligned} \tag{1.4}$$

where indices, i, j, k, l denote orbitals on the impurity, and the matrix U_{ijkl} represents the interactions between orbitals on impurity. $\mathcal{G}^{\mathbf{0}}(i\omega_n)$ is the time dependent bare electron Green's function, which is given by

$$\mathcal{G}^{\mathbf{0}}(i\omega_n) = \frac{1}{(i\omega_n + \epsilon_m)\mathbf{I} - \mathbf{\Delta}(i\omega_n)}\,, \tag{1.5}$$

where $\mathbf{I}$ represents the identity matrix of size $m \times m$ (and m is the number of orbitals on impurity). $\mathbf{\Delta}(i\omega_n)$ is the hybridization function, which has information about the structure of the bath. The above action represents a general impurity model that can be used to study Kondo effect in the multi-orbital case. The method which solves the above impurity problem is called impurity solver and it is a numerical program or analytical scheme which is able to calculate observables like the local Green's function $\mathbf{G}(\tau - \tau') = -\langle T_\tau c\ (\tau) c^\dagger(\tau')\rangle_{S_{eff}}$ and self energy $\mathbf{\Sigma}_{imp}(i\omega_n)$.

1.3 Dynamical mean field theory

Finding a non-perturbative solution for correlated models such as eq. 1.2 used to be an impossible task before 1989, when Metzner and Vollhardt found a new limit of the correlated models called infinite coordination number[30] or equivalently the infinite dimensional limit. This limit took inspiration from classical mean field theories, many of which become exact in the limit of high dimensions. The advantage of this new limit is that the contribution of non-local diagrams to the self-energy is zero and it turns out to be a purely local quantity i.e., $\Sigma_{ij}(i\omega_n) = \delta_{ij}\Sigma_{ii}(i\omega_n)$. In the infinite-dimensional limit, by appropriate scaling of hopping elements, the competition between the kinetic energy and Coulomb energy is retained in a non-trivial way. Subsequently, E. Müller-Hartmann et. al.[31] justified the neglect of k dependence of self-energy in the infinite-dimensional limit. Later, it was shown by Antoine Georges et.al.[32] that in the infinite-dimensional limit one can map the correlated lattice problem on to a self-consistent quantum impurity model such as eq. 1.4.

The DMFT equations may be derived in many ways; one of them being the cavity method. The basic idea of cavity method is the following; Suppose we have a periodic lattice of N lattice sites. We can pick one lattice site and call it as a site-0 or an impurity site. Treat it as isolated from the remaining lattice sites i.e., an artificial cavity surrounding the site-0 or impurity site has been created. We can define an effective dynamics for the impurity site by explicitly integrating out all the electronic degrees of freedom on the cavity except those of site-0. This yields an effective action such as the one given by eq. 1.4 in case of MO-HM. In this effective action, $\mathcal{G}^0_{ij}(\tau - \tau')$ represents the Weiss mean field or the host Green's function. In Matsubara space, the host Green's function is represented as,

$$\mathcal{G}^0(i\omega_n) = \frac{1}{(i\omega_n + \epsilon_m)\mathbf{I} - \mathbf{\Delta}(i\omega_n)}\,, \tag{1.6}$$

where $\mathbf{\Delta}(i\omega_n)$ is the hybridization function, and it represents retardation effects from cavity states that we have integrated already. In comparison with classical mean field theory, the Weiss effective field in DMFT is a function of energy or time rather than being just a scalar. The dynamical dependence of Weiss effective field is essential for incorporating local temporal quantum fluctuations, which is the main objective of DMFT. Thus, DMFT is the quantum analog of a classical mean field theory. One of the quantities of interest in DMFT is the local interacting Green's function given by,

$$\mathbf{G}_{loc}(\tau - \tau') = -\langle T_\tau c\ (\tau) c^\dagger(\tau')\rangle_{S_{eff}} \tag{1.7}$$

Now, we need to find a self-consistency condition which relates the local Green's function ($\mathbf{G}_{loc}(i\omega_n)$) with the Weiss dynamical field $\mathcal{G}^0(i\omega_n)$. By using effective action defined in eq. 1.4, one can calculate impurity self-energy, $\mathbf{\Sigma}_{imp}(i\omega_n)$ from the interacting Green's function and Weiss effective field,

$$\mathbf{\Sigma}_{imp}(i\omega_n) = \mathcal{G}^0(i\omega_n)^{-1} - \mathbf{G}^{-1}_{loc}(i\omega_n) = (i\omega_n + \epsilon_m)\mathbf{I} - \mathbf{\Delta}(i\omega_n) - \mathbf{G}^{-1}_{loc}(i\omega_n)\,. \tag{1.8}$$

In the infinite-dimensional limit, one can neglect the momentum dependence of lattice self-energy ($\mathbf{\Sigma}_{lattice}(i\omega_n) = \mathbf{\Sigma}_{lattice}(k, i\omega_n)\,\forall\, k$). Then, the local Green's function can be written as,

$$\sum_{\mathbf{k}} \frac{1}{(i\omega_n + \epsilon_\alpha)\mathbf{I} - \mathbf{H}(\mathbf{k}) - \mathbf{\Sigma}_{lattice}(i\omega_n)} = \mathbf{G}_{loc}(i\omega_n)\,. \tag{1.9}$$

The approximation made to get the self-consistency condition is that the lattice self-energy must be equal to the impurity self-energy[32, 33] i.e., $\mathbf{\Sigma}_{imp}(i\omega_n) = \mathbf{\Sigma}_{lattice}(i\omega_n)$. With this approximation, we can immediately find a self-consistency condition for the local Greens' function $\mathbf{G}_{loc}$, which is nothing but an impurity Greens' function and the condition is,

$$\sum_{\mathbf{k}} \frac{1}{\mathbf{\Delta}(i\omega_n) + \mathbf{G}^{-1}_{loc}(i\omega_n) + \mathbf{I}(\epsilon_\alpha - \epsilon_m) - \mathbf{H}(\mathbf{k})} = \mathbf{G}_{loc}(i\omega_n)\,. \tag{1.10}$$

Now we can find $\mathcal{G}^0(i\omega_n)$ and $\mathbf{G}_{loc}(i\omega_n)$ by using an iterative procedure. An example of a self-consistency procedure for implementing DMFT could be as follows; Start with an initial guess of Weiss effective field $\mathcal{G}^0(i\omega_n)$. Then by employing an impurity solver, calculate the self-energy. By using DMFT mapping, ($\mathbf{\Sigma}_{imp}(i\omega_n) = \mathbf{\Sigma}_{lattice}(i\omega_n)$) and eq. 1.10, we will calculate lattice Green's function($\mathbf{G}_{loc}(i\omega_n)$). With this lattice Green's function and impurity self-energy, find a new Weiss effective field $\mathcal{G}^0((i\omega_n)$ by using lattice Dyson equation, eq. 1.8. Then again solve the impurity problem using new Weiss effective field. Iterate the procedure until convergence in the Weiss effective field or the self-energy reaches the desired accuracy. While DMFT is exact in the infinite-dimensional limit, it may be used as an approximation in finite dimensions. The most challenging step in the DMFT loop is solving the impurity problem, which is done by using impurity solver as discussed earlier. There are semi-analytical and numerically exact methods available as impurity solvers within DMFT. However, each method has pros and cons, and we present a brief comparison in Table 1.1.

Table 1.1: Pros and Cons of impurity solvers within DMFT: (QMC: quantum Monte-Carlo, NRG: numerical renormalization group, ED: exact diagonalization, DMRG: density matrix renormalization group, IPT: iterative perturbation theory, LMA: local moment approach, NCA: non-crossing approximation and FLEX: fluctuation exchange approximation)

Impurity Solvers in **DMFT**	Category	Issues
QMC	Exact	Computationally expensive, Very hard to reach low temperature and need Wick's rotation for real frequency data.
NRG	Exact	Low frequency problems; lacking for multi-orbitals.
ED	Exact	Discrete single particle spectrum.
DMRG	Exact	Stability issues and numerical artifacts.
IPT	Approximate	Well benchmarked for single orbital models.
LMA	Approximate	Well benchmarked for single orbital models; non-perturbative
NCA	Approximate	Restricted to high temperature.
FLEX	Approximate	Lacking strong coupling physics.

In this thesis, we extended an iterative perturbation theory to multi orbital problems, which is called a multi orbital iterative perturbation theory (MO-IPT)[34]. It is an interpolative approach and more details about MO-IPT can be found in the one of the chapters of this thesis. In most of the chapters of this thesis, we have used a numerically exact method called hybridization expansion continuous time quantum Monte-Carlo (HY-CTQMC) as a solver and details about HY-CTQMC can be found in the beautiful review by Emanuel Gull et. al[35]. Here we are going to compare CTQMC method with classical Ising Monte-Carlo (IMC) method in the following steps.

Step:1

In IMC, we deal with a Hamiltonian of the form $H_I = \sum_{ij} J\sigma_i \cdot \sigma_j$. In case of CTQMC methods, we work with quantum impurity Hamiltonian's which can be written as the sum of two parts $H_{imp} = H_a + H_b$. Then we will treat H_b as a perturbation term. There are three flavors of CTQMC based on H_b. They are continuous time interaction expansion (CT-INT) algorithm, continuous time auxiliary field (CT-AUX) algorithm and continuous time hybridization expansion (HY-CTQMC) algorithm. In case of CT-INT and CT-AUX algorithms, the interaction term is the perturbation term, i.e $H_b = H_{int}$ while in HY-CTQMC the hybridization between impurity and bath is the perturbation term, i.e $H_b = H_{hyb}$.

Step:2

The partition function in the classical case (IMC) is given by $Z = \mathrm{Tr}[\exp(-\beta H_I)]$. In case of CTQMC methods, the partition function in the diagrammatic perturbation theory representation is given by $\mathrm{Tr}[e^{-\beta H_a} T_\tau e^{(-\int_0^\beta d\tau H_b(\tau))}]$.

Step:3

We can represent partition function in the IMC as a sum of all Ising configurations of configuration space ($\mathcal{C}$) i.e., $Z = \sum_{\mathrm{x}\in\mathcal{C}}[\exp(-\beta H_I(x))] = \sum_{\mathrm{x}\in\mathcal{C}} \mathcal{W}(x)$. In case of CTQMC methods, we expand the partition function in powers of H_b then we can write $Z = \sum_{k=0}^{\infty} \int\int\int_0^\beta d\tau_1 ... d\tau_k p(\tau_1, ..., \tau_k) = \sum_{\mathrm{x}\in\mathcal{C}} \mathcal{W}(x)$. Each term in the expansion series represents a set of Feynman diagrams and the weight of the diagrams (configuration) at k-th order is $\mathcal{W}(x) = p(\tau_1, ..., \tau_k) d\tau_1 ... d\tau_k$.

Step:4

The elements of configuration space ($\mathcal{C}$) in the Ising case contains a set of N "Ising spins" each assuming either an up or down state, i.e, $\mathcal{C} = \{\{\uparrow,\uparrow,\downarrow,\uparrow,..\},\{\uparrow,\downarrow,\downarrow,\downarrow,..\},...,\{\uparrow,\downarrow,\downarrow,\uparrow,..\}\}$. The elements of configuration space ($\mathcal{C}$) in CTQMC methods depend upon perturbation term H_b. In case of CT-INT methods, for single orbital case, the elements of configuration space ($\mathcal{C}$) contains perturbation order and interaction vertex at different Matsubara times, $\mathcal{C} = \{\{\},\{1,\tau_1\},\{2,\tau_1,\tau_2\},..,\{k,\tau_1,..\tau_k\}\}$.

Step:5

In Monte-Carlo methods, we stochastically sample the elements of configuration space ($\mathcal{C}$). For IMC, these correspond to configurations of binary spins; while in CTQMC they correspond to terms of the diagrammatic expansion series. By connecting the vertex at different Matsubara times (in case of CT-INT) by non-interacting propagators G^0, we can show that the terms of expansion series are nothing but a set of Feynman diagrams. In figure 1.1, we show the schematic of one such diagram at the second order in the expansion series for CT-INT.

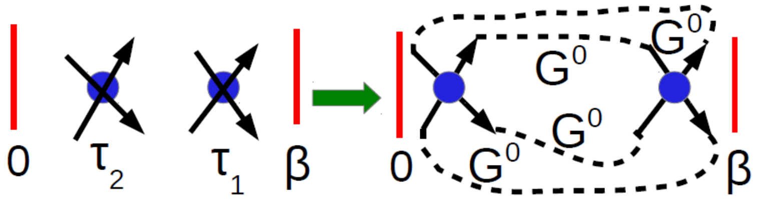

Figure 1.1: (color online) Schematic representation of diagramatic, perturbation series expansion of CT-INT at the second order level in terms of Feynman, diagrams.

Step:6

By using a Markov chain, elements of configuration space ($\mathcal{C}$) may be generated in both the methods, i.e., IMC and CTQMC methods.

Step:7

In case of IMC, we begin with a particular Ising configuration and then randomly pick a site and flip the Ising spin at that site. This kind of update leads to a new Ising configuration ($\{\uparrow,\uparrow,\downarrow,\uparrow,..\} \rightarrow \{\uparrow,\downarrow,\downarrow,\uparrow,..\}$). In case of CTQMC, we start with a particular order of perturbation series say kth order. Then either we insert a vertex randomly in the interval [0,β] or pick a particular vertex randomly from the present order and then remove it. When we insert a vertex, then the order of perturbation series increases from k to k+1 and in case of the removal of vertex, the order of perturbation series decreases from k to k-1. These are the most common updates that have been used in case of CTQMC methods. We have showed this kind of updates for CT-INT at the second order of perturbation series in figure 1.2.

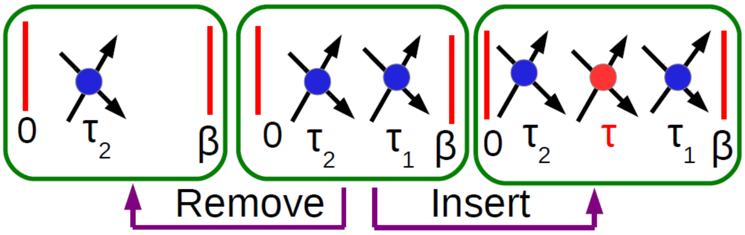

Figure 1.2: (color online) Schematic representation of insertion and removal updates in CT-INT method.

Step:8

Once the new configuration in the Markov chain is generated, one can accept or reject those configurations by using Metropolis acceptance probability. For the case of Ising Monte-Carlo, it is $\mathrm{W}_{acc} = \min(1,\, e^{-\beta\Delta E})$ and for CTQMC methods, it is $\mathrm{W}_{acc} = \min\,[1,\, \frac{\beta p(\tau_1,.\tau,.\tau_k)}{k+1 d\tau p(\tau_1,..\tau_k)}]$.

Step:9

If the new configuration is accepted by the Metropolis algorithm, then we can calculate the quantities of interest such as single and two particle Green's function for that configuration.

1.4 Maximum Entropy Method

The CTQMC solvers are numerically exact methods, but the usefulness of the methods is limited because the data obtained from these methods is only on the imaginary axis, whereas, most of the experiments measure correlation functions on the real frequency axis. To get real frequency data from quantum Monte-Carlo (QMC) methods, we need an analytic continuation of QMC data from Matsubara axis to the real frequency axis. In figure 1.3 we have plotted the schematic pictures of analytic continuation or Wick's rotation for single and two particle quantities.

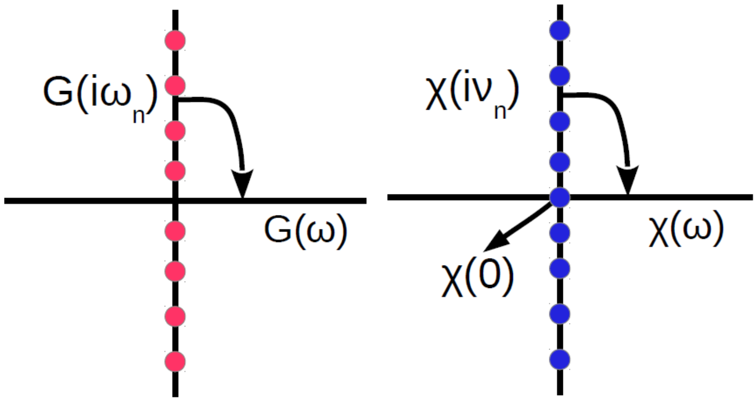

Figure 1.3: (color online) Schematic of Wick's rotation for single particle and two particle quantity

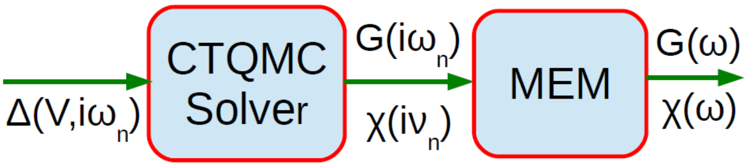

Figure 1.4: (color online) Schematic of MEM procedure

The relation between fermionic single particle Green's function and real frequency spectrum ($A(\omega)$) in Matsubara time and frequency [36, 37] are given by,

$$G(\tau) = \int d\omega A(\omega) K(\tau, \omega) \tag{1.11}$$

$$G(i\omega_n) = \int d\omega A(\omega) K(i\omega_n, \omega)\,, \tag{1.12}$$

where the expression for kernels are[37–39]

$$K(\tau, \omega) = \frac{e^{-\tau\omega}}{1 + e^{-\beta\omega}} \tag{1.13}$$

$$\text{and} \quad K(i\omega_n, \omega) = \frac{1}{i\omega_n - \omega} \tag{1.14}$$

. Inverting the equations 1.11 and 1.12 is an ill-posed problem because of the exponential nature of kernels $K(i\omega_n, \omega)$ and $K(\tau, \omega)$. At finite τ, and for large frequency ω, kernel $K(\tau, \omega)$ in eq 1.11 is exponentially small, so the $G(\tau)$ is insensitive to the high-frequency features of $A(\omega)$. This means that there exist an infinite number of $A(\omega)$'s for a given $G(\tau)$ (within numerical accuracy), and hence the uniqueness of $A(\omega)$ is lost. Another way to see this is that, if we approximate the G and A in the above equations by equal length vectors and K by a square matrix, then should find that the determinant of K, is exponentially small (i.e., K^{-1} is ill-defined). In this thesis, we have developed and used a powerful method, namely, the maximum entropy method (MEM) for Wick's rotation of CTQMC data. The basic idea of MEM is, for a given G(τ), instead of asking - what is $A(\omega)$, we should ask - what is the most probable $A(\omega)$. This can be obtained by maximizing the conditional probability of $A(\omega)$ for a given data G i.e., $P(A|G)$. The output of CTQMC solver is the local Green's function($G(i\omega_n)$) and the two particle susceptibility($\chi(i\nu_n)$) on Mastubara axis. We will pass these outputs as input to the MEM code. The output of the MEM code is the real frequency Green's function($G(\omega)$) and two particle susceptibility ($\chi(\omega)$) on real frequency axis. A schematic of this procedure is shown in figure 1.4.

1.5 DFT+DMFT

As mentioned earlier, the current framework of choice for studying strongly correlated materials is the combination of DMFT with *abinitio* methods such as DFT[40], with an LDA/GGA functional. The basic idea of DFT+DMFT[41] is to build a low energy effective model for the real material by projecting the band structure obtained from DFT on to a low-energy subspace of interest. In this thesis, we have used Wannier 90[42] technique, using which we can construct the maximally localized Wannier orbitals, and then project the DFT band structure on to them for the chosen energy window. Once we obtain the low energy effective model ($\mathbf{H}_{GGA}(\mathbf{k})$) for a given real material, then we can introduce local electronic correlations by using DMFT. The main object of interest in DFT+DMFT is the local electronic Green's function, which is given by,

$$\mathbf{G}_{loc}(i\omega_n) = \sum_{\mathbf{k}} \frac{1}{(i\omega_n + \mu)\mathbf{I} - \mathbf{H}_{GGA}(\mathbf{k}) - \mathbf{\Sigma}_{lattice}(i\omega_n)} . \tag{1.15}$$

We obtain it by using various impurity solvers, some of which have been mentioned above in the section 1.3 on DMFT. With this short introduction on strongly correlated electronic systems and numerical techniques which have been used to study SCES, we are going to discuss the work contained in this thesis briefly.

Bibliography

[1] M. Born and R. Oppenheimer, Annalen der Physik **389**, 457 (1927), ISSN 1521-3889, URL `http://dx.doi.org/10.1002/andp.19273892002`.

[2] P. Hohenberg and W. Kohn, Phys. Rev. **136**, B864 (1964), URL `http://link.aps.org/doi/10.1103/PhysRev.136.B864`.

[3] W. Kohn and L. J. Sham, Phys. Rev. **140**, A1133 (1965), URL `http://link.aps.org/doi/10.1103/PhysRev.140.A1133`.

[4] J. Chayes, L. Chayes, and M. Ruskai, Journal of Statistical Physics **38**, 497 (1985), ISSN 0022-4715, URL `http://dx.doi.org/10.1007/BF01010474`.

[5] R. O. Jones and O. Gunnarsson, Rev. Mod. Phys. **61**, 689 (1989), URL `http://link.aps.org/doi/10.1103/RevModPhys.61.689`.

[6] R. M. Dreizler and E. K. Gross, *Density functional theory: an approach to the quantum many-body problem* (Springer Science & Business Media, 2012).

[7] D. C. Langreth and M. J. Mehl, Phys. Rev. B **28**, 1809 (1983), URL `http://link.aps.org/doi/10.1103/PhysRevB.28.1809`.

[8] A. D. Becke, Physical review A **38**, 3098 (1988).

[9] A. D. Becke, The Journal of Chemical Physics **98** (1993).

[10] M. Imada, A. Fujimori, and Y. Tokura, Rev. Mod. Phys. **70**, 1039 (1998), URL `http://link.aps.org/doi/10.1103/RevModPhys.70.1039`.

[11] D. B. McWhan and J. P. Remeika, Phys. Rev. B **2**, 3734 (1970), URL `http://link.aps.org/doi/10.1103/PhysRevB.2.3734`.

[12] D. B. McWhan, T. M. Rice, and J. P. Remeika, Phys. Rev. Lett. **23**, 1384 (1969), URL `http://link.aps.org/doi/10.1103/PhysRevLett.23.1384`.

[13] L. Baldassarre, A. Perucchi, D. Nicoletti, A. Toschi, G. Sangiovanni, K. Held, M. Capone, M. Ortolani, L. Malavasi, M. Marsi, et al., Phys. Rev. B **77**, 113107 (2008), URL `http://link.aps.org/doi/10.1103/PhysRevB.77.113107`.

[14] F. Rodolakis, P. Hansmann, J.-P. Rueff, A. Toschi, M. W. Haverkort, G. Sangiovanni, A. Tanaka, T. Saha-Dasgupta, O. K. Andersen, K. Held, et al., Phys. Rev. Lett. **104**, 047401 (2010), URL `http://link.aps.org/doi/10.1103/PhysRevLett.104.047401`.

[15] A. Toschi, P. Hansmann, G. Sangiovanni, T. Saha-Dasgupta, O. K. Andersen, and K. Held, Journal of Physics: Conference Series **200**, 012208 (2010), URL `http://stacks.iop.org/1742-6596/200/i=1/a=012208`.

[16] P. Hansmann, A. Toschi, G. Sangiovanni, T. Saha-Dasgupta, S. Lupi, M. Marsi, and K. Held, physica status solidi (b) **250**, 1251 (2013), ISSN 1521-3951, URL `http://dx.doi.org/10.1002/pssb.201248476`.

[17] A. Georges, L. de' Medici, and J. Mravlje, Annual Review of Condensed Matter Physics **4**, 137 (2013), `http://dx.doi.org/10.1146/annurev-conmatphys-020911-125045`, URL `http://dx.doi.org/10.1146/annurev-conmatphys-020911-125045`.

[18] S. Jin, T. H. Tiefel, M. McCormack, R. A. Fastnacht, R. Ramesh, and L. H. Chen, Science **264**, 413 (1994), `http://www.sciencemag.org/content/264/5157/413.full.pdf`, URL `http://www.sciencemag.org/content/264/5157/413.abstract`.

[19] R. von Helmolt, J. Wecker, B. Holzapfel, L. Schultz, and K. Samwer, Phys. Rev. Lett. **71**, 2331 (1993), URL `http://link.aps.org/doi/10.1103/PhysRevLett.71.2331`.

[20] J. Bednorz and K. Mller, Zeitschrift fr Physik B Condensed Matter **64**, 189 (1986), ISSN 0722-3277, URL `http://dx.doi.org/10.1007/BF01303701`.

[21] J. Hubbard, Proceedings of the Royal Society of London A: Mathematical, Physical and Engineering Sciences **276**, 238 (1963), ISSN 0080-4630.

[22] J. E. Han, M. Jarrell, and D. L. Cox, Phys. Rev. B **58**, R4199 (1998), URL `http://link.aps.org/doi/10.1103/PhysRevB.58.R4199`.

[23] S. Sakai, R. Arita, and H. Aoki, Phys. Rev. B **70**, 172504 (2004), URL `http://link.aps.org/doi/10.1103/PhysRevB.70.172504`.

[24] L. de'Medici, A. Georges, and S. Biermann, Phys. Rev. B **72**, 205124 (2005), URL `http://link.aps.org/doi/10.1103/PhysRevB.72.205124`.

[25] H. Lin, J. Gubernatis, H. Gould, and J. Tobochnik, Computers in Physics **7** (1993).

[26] S. R. White, Phys. Rev. Lett. **69**, 2863 (1992), URL `http://link.aps.org/doi/10.1103/PhysRevLett.69.2863`.

[27] S. R. White, Phys. Rev. B **48**, 10345 (1993), URL `http://link.aps.org/doi/10.1103/PhysRevB.48.10345`.

[28] K. A. Hallberg, Advances in Physics **55**, 477 (2006), `http://dx.doi.org/10.1080/00018730600766432`, URL `http://dx.doi.org/10.1080/00018730600766432`.

[29] S. Liang and H. Pang, Phys. Rev. B **49**, 9214 (1994), URL `http://link.aps.org/doi/10.1103/PhysRevB.49.9214`.

[30] W. Metzner and D. Vollhardt, Phys. Rev. Lett. **62**, 324 (1989), URL `http://link.aps.org/doi/10.1103/PhysRevLett.62.324`.

[31] E. Mller-Hartmann, Zeitschrift fr Physik B Condensed Matter **76**, 211 (1989), ISSN 0722-3277, URL `http://dx.doi.org/10.1007/BF01312686`.

[32] A. Georges, G. Kotliar, W. Krauth, and M. J. Rozenberg, Rev. Mod. Phys. **68**, 13 (1996), URL `http://link.aps.org/doi/10.1103/RevModPhys.68.13`.

[33] A. Georges, AIP Conference Proceedings **715** (2004).

[34] N. Dasari, W. R. Mondal, P. Zhang, J. Moreno, M. Jarrell, and N. Vidhyadhiraja, arXiv preprint arXiv:1504.04097 (2015).

[35] E. Gull, A. J. Millis, A. I. Lichtenstein, A. N. Rubtsov, M. Troyer, and P. Werner, Rev. Mod. Phys. **83**, 349 (2011), URL `http://link.aps.org/doi/10.1103/RevModPhys.83.349`.

[36] J. E. Gubernatis, M. Jarrell, R. N. Silver, and D. S. Sivia, Phys. Rev. B **44**, 6011 (1991), URL `http://link.aps.org/doi/10.1103/PhysRevB.44.6011`.

[37] M. Jarrell and J. E. Gubernatis, Physics Reports **269**, 133 (1996).

[38] H. B. Schüttler and D. J. Scalapino, Phys. Rev. Lett. **55**, 1204 (1985), URL `http://link.aps.org/doi/10.1103/PhysRevLett.55.1204`.

[39] H. B. Schüttler and D. J. Scalapino, Phys. Rev. B **34**, 4744 (1986), URL `http://link.aps.org/doi/10.1103/PhysRevB.34.4744`.

[40] P. Giannozzi, S. Baroni, N. Bonini, M. Calandra, R. Car, C. Cavazzoni, D. Ceresoli, G. L. Chiarotti, M. Cococcioni, I. Dabo, et al., Journal of Physics: Condensed Matter **21**, 395502 (19pp) (2009), URL `http://www.quantum-espresso.org`.

[41] G. Kotliar, S. Y. Savrasov, K. Haule, V. S. Oudovenko, O. Parcollet, and C. A. Marianetti, Rev. Mod. Phys. **78**, 865 (2006), URL `http://link.aps.org/doi/10.1103/RevModPhys.78.865`.

[42] N. Marzari and D. Vanderbilt, Phys. Rev. B **56**, 12847 (1997), URL `http://link.aps.org/doi/10.1103/PhysRevB.56.12847`.

Chapter 2

A multi-orbital iterated perturbation theory for model Hamiltonians and real material-specific calculations of correlated systems [⋆]

2.1 Introduction

The development of efficient methods to solve quantum impurity problems, especially those involving multiple orbitals, has been a significant research direction in the field of theoretical condensed matter physics. Subsequent to the development of the dynamical mean field theory (DMFT)[1], which is exact in the limit of infinite dimensions and an excellent local approximation in finite dimensions, the importance of obtaining reliable solutions to general quantum impurity problems has increased further.

[⋆] Nagamalleswararao Dasari, Wasim Raja Mondal, Peng Zhang, Juana Moreno, Mark Jarrell and N. S. Vidhyadhiraja, Manuscript under review in PRB, arXiv:1504.04097117.

Within the DMFT framework, a lattice model may be mapped onto a quantum impurity embedded in a self-consistently determined host. The impurity problem may then be solved by a variety of techniques including– numerically exact methods like quantum Monte Carlo (QMC), numerical renormalization group (NRG), exact diagonalization (ED) and density matrix renormalization group (DMRG) or semi-analytical methods like iterated perturbation theory (IPT), local moment approach (LMA), non-crossing approximation (NCA) and fluctuation exchange approximation (FLEX). Each method has its own advantages as well as pitfalls. For example, QMC[2] is a numerically exact method, but is computationally expensive. It yields data on the Matsubara axis (or imaginary time) so to obtain dynamical quantities such as the density of states and transport quantities, analytic continuation of the data to real frequencies is essential[3], which is a mathematically ill-posed problem. Additionally, it is very difficult to access the low temperature region where statistical errors become important. As a real frequency method, NRG[4] can avoid the difficulties that arise from the need to carry out analytic continuation. However, the method becomes extremely cumbersome for more than one impurity or channel. NRG is better suited for low temperature studies. Recently,[5] NRG was applied to study degenerate multi-orbital lattice problems, but the non-degenerate case remains unexplored. ED[6] is also a real-frequency method, but one considers only a finite number of bath states, so the resulting energy spectrum is discrete, and the broadening procedure for obtaining continuous spectra is not free of ambiguities. Moreover, large systems or multi-orbitals are not accessible. DMRG[7] for the single site case has some numerical artifacts and its accuracy as an impurity solver is not entirely clear[2].

The semi-analytical methods are perturbation theory based solvers that attempt to capture the essential physics by constructing an ansatz for the single-particle quantities. The ansatz is based on satisfying various limits or conservation laws, and comprises diagrams up to a certain order or sums a specific class of processes to infinite order. The main advantages of these methods are that they are computationally less expensive than the numerically exact methods listed above, while also yielding real frequency data. However, semi-analytical methods are, by definition, approximate and need to be benchmarked against exact results to gauge their range of validity. For example, although NCA[8] gives qualitatively correct results for temperatures higher than the Kondo temperature, spurious non-analyticity at the Fermi energy develops at lower temperatures[9]. To recover the correct Fermi liquid behavior at low temperatures, one needs to consider a larger class of diagrams[10]. The FLEX approximation is conserving in the Baym-Kadanoff sense, but it does not have the correct strong coupling behavior. So when it is employed for the half-filled Hubbard model, strong coupling physics like the Mott transition is not captured[11, 12]. The FLEX[13] has been extended to study degenerate multi-orbital problems but the issues plaguing single-orbital problems remain. The LMA is a highly[14, 15] accurate technique, that has been benchmarked extensively [16] with NRG, but the method has not been used to study lattice problems except the periodic Anderson model[17]. Moreover, extensions to symmetry broken phases or multiple orbital problems remain to be carried out.

The IPT is a simple, second order perturbation theory based method and it has been used widely to solve impurity[18, 19] and lattice problems[20] at zero as well as at finite temperature. In the IPT, a self-energy ansatz is constructed that interpolates between known limits (i.e., weak coupling, atomic and high frequency limits) which is why it is also called an interpolative approach. It is clear that even the single-orbital IPT is not free of ambiguities so different constraints or limits to construct the ansatz yield different results. Hence, an IPT for multi-orbital problems has been ‘synthesized’ in many different ways by various groups[21], and we discuss these variations next.

The IPT ansatz for the self-energy $\Sigma(\omega)$ is based on a rational or continued fraction expansion of a specific subset of diagrams, and consists of a small number of free variables that are fixed by satisfying various limits, such as atomic and high frequency limits and conservation laws such as the Luttinger's theorem. Such an interpolative approach was first initiated by Mart´in Rodero[18, 22] for the single impurity and periodic Anderson models. The approach used the second order self-energy as a building block and the pseudo-chemical potential μ_0, was fixed by assuming that the occupation n_0 of the non-interacting part of the Anderson impurity problem is equal to the lattice occupation n. For the single impurity Anderson model (SIAM), Yosida and Yamada[19, 23] demonstrated that perturbation theory in U is quite well behaved for the symmetric case when expanding around the Hartree-Fock solution. Based on these findings, Georges and Kotliar[20, 24] introduced an impurity solver called iterative perturbation theory (IPT) to solve the single band Hubbard model within DMFT.

Subsequently, Kajueter and Kotliar[25, 26] proposed a modification to the IPT called modified iterative perturbation theory (MIPT). In addition to the usual constraints of IPT, the MIPT constrains the zero frequency behavior of the self energy by adding a pseudo chemical potential μ_0 to the Hartree corrected bath propagators. This pseudo-chemical potential, μ_0, can be obtained in different ways so there is an ambiguity in the method. Kajueter[25] fixed this free parameter by satisfying the Friedel's sum rule (equivalently Luttinger theorem), hence his method is called IPT-L. The Luttinger theorem and Friedel's sum rule are valid only at zero temperature, hence for finite temperature calculations, Kajueter[21] used the same μ_0 that was obtained at zero temperature.

To study spontaneous magnetism in the single band Hubbard model, Potthoff, Wegner and Nolting[27, 28] improved MIPT further by taking into account the spectral moments up to third order and instead of fixing μ_0 by using Luttinger theorem, they fixed it by the $n = n_0$ constraint. This method may be called IPT-n_0. They also considered the simpler option, where lattice chemical potential μ is equal to the pseudo chemical potential μ_0. This is called IPT-μ_0 and they bench-marked IPT-L and IPT-n_0 with IPT-μ_0. Recently, Arsenault, Sémon, and Tremblay[29] bench-marked IPT-n_0 with CTQMC and found the pathology in IPT-n_0 that, in the strong coupling regime, the method does not recover a Fermi-liquid for filling close to $n = 1$. They suggested a new method (IPT-D) to fix the μ_0 through a double occupancy constraint. The range of schemes originating from the inherent ambiguities at the single-orbital level give an idea of the far larger range of approximations that can be built at the multi-orbital level. These schemes will be described next.

Kajueter[21] extended his single orbital perturbative scheme to the degenerate multi-orbital case. He used the coherent potential approximation (CPA) to calculate higher order correlation functions in the self energy. He showed, by benchmarking against ED, that the scheme provides reasonable results only if the total particle density per site is less than one. For fillings greater than one, his scheme produced a false double peaked structure at the Fermi level instead of a single resonance. The reason for such a spurious structure is that the high frequency tails in the continued fraction expansion can be systematically improved by considering poles involving higher-order correlations functions in the self-energy, but this in turn seriously degrades the low frequency behavior when the Luttinger's theorem is attempted to be satisfied. To study quantum transport in mesoscopic systems such as multi-level quantum dots, Yeyati et al. [30] introduced an interpolative scheme based on IPT-n_0. Liebsch[31] applied an extension of IPT to study the orbital selective Mott-transition, using which he showed that inter-orbital Coulomb interactions gives rise to a single first-order transition rather than a sequence of orbital selective transitions. In Liebsch's extension of IPT for the multi-orbital case, he chose the self energy to be the combination of Hartree term and second order pair-bubble diagram with interaction vertices between electrons in different orbitals on the impurity. Laad et al.[32] constructed an interpolative scheme for multi-orbitals that was used extensively to study real materials through the LDA+DMFT framework. In a similar context, Fujiwara et al.[33] developed an interpolative approach for degenerate multi-orbitals. The novelty of their method was that they used ligand field theory in the atomic limit to find the higher-order correlation functions.Although there exist a large range of schemes for extending IPT to the multi-orbital case, extensive benchmarking of any single method has not been carried out. Recently Savrasov et al. [34], and Oudovenko et al.[35] developed an interpolative approach for degenerate multi-orbitals based on a simple rational form of the self-energy, where the unknown coefficients in the self-energy are determined using slave boson mean-field and Hubbard I approximations. In their Hirsch-Fye-QMC work on the SU(4) Hubbard model, they have observed a good agreement in the particle-hole asymmetric cases.

In the present work, we build upon the previous knowledge to develop an interpolative scheme for solving a general multi-orbital quantum impurity problem. Our scheme is also based on the second-order self-energy as a building block and we use the generic name for the method as simply multi-orbital iterative perturbation theory (MO-IPT). Our method has a single pseudo-chemical potential μ_0, that is found by satisfying the Luttinger's theorem. We impose the correct high frequency and atomic limits to get the unknown coefficients in the self-energy ansatz. In the single orbital case, we find that MO-IPT recovers the usual MIPT self energy expression and for the degenerate multi-orbital case, our MO-IPT self-energy expression reduces to that of Kajueter[21]. The main novelty lies in handling the high frequency poles in a systematic way. The method is general enough that it can be applied to study symmetry broken phases, Hund's coupling (density-density type) and crystal field effects.

Since, MO-IPT is a semi analytical method it needs to be bench-marked. Subsequent to the description of the method, we embark upon an extensive benchmarking of MO-IPT with numerically exact, hybridization expansion continuous time quantum Monte Carlo method (S-CTQMC)[36] as implemented in the ALPS[37] libraries and our own implementation of interaction expansion CTQMC (W-CTQMC). Our main conclusion is that the MO-IPT method works very well when used away from integer-fillings, even at reasonably strong coupling. At or close to integer-fillings, the physics is captured only qualitatively, and the asymptotic behavior close to phase transitions could even be wrong. We have also integrated the MO-IPT with material-specific, density functional theory based calculations (GGA+DMFT), and thus tested it for a prototypical example of strongly correlated electronic system, $\mathrm{SrVO_3}$. We compare the density of states (DOS) obtained from MO-IPT with hybridization expansion CTQMC. A rather good agreement is obtained when the MO-IPT photo-emission spectra (PES) is compared with experiments.

2.2 Model and Formalism

The multi-orbital Hubbard model for density-density type interactions and for cubic environment in standard second quantization notation is given by

$$\begin{aligned}\mathcal{H} = \sum_{i\alpha\sigma} \epsilon_{i\alpha} n_{i\alpha\sigma} + \sum_{ij\alpha\beta\sigma} T_{ij}^{\alpha\beta}(c^{\dagger}_{i\alpha\sigma} c_{j\beta\sigma} + h.c) + \sum_{i\alpha\sigma} \frac{U}{2} n_{i\alpha\sigma} n_{i\alpha\bar{\sigma}} \\ + \sum_{i\alpha\sigma \neq \beta\sigma'} \frac{(U-2J)}{2} n_{i\alpha\sigma} n_{i\beta\sigma'} + \sum_{i\sigma\alpha\neq\beta} \frac{(U-3J)}{2} n_{i\alpha\sigma} n_{i\beta\sigma} \, .\end{aligned} \tag{2.1}$$

where $c^{\dagger}_{i\alpha\sigma}$ creates the electron at lattice site i, in orbital α with spin σ and $c_{j\beta\sigma}$ annihilates the electron at site j, in orbital β with spin σ. We are mainly interested in the local single particle electron dynamics, which is given by the momentum sum of the lattice Green's function

$$\hat{G}_{loc}(\omega^+) = \sum_{\mathbf{k}} \frac{1}{(\omega^+ + \mu)\mathbb{I} - \hat{H}(\mathbf{k}) - \hat{\Sigma}(\mathbf{k}, \omega^+)} \, . \tag{2.2}$$

Here $\hat{H}(\mathbf{k})$ comprises intra-unit-cell hybridization and inter-unit-cell hopping, namely

$$\hat{H}(\mathbf{k}) = \hat{H}_{intra} + \hat{H}(\mathbf{k})_{inter} \tag{2.3}$$

$$\text{where} \quad \left(\hat{H}_{intra}\right)_{\alpha\beta} = \epsilon_{\alpha}\delta_{\alpha\beta} + T_{ii}^{\alpha\beta} \tag{2.4}$$

$$\text{and} \quad \left(\hat{H}(\mathbf{k})_{inter}\right)_{\alpha\beta} = \epsilon(\mathbf{k})_{\alpha\beta} \, , \tag{2.5}$$

where ϵ_α are orbital energies, $\mathrm{T}_{ii}^{\alpha\beta}$ are intra-unit cell hybridization matrix elements, and $\epsilon(\mathbf{k})_{\alpha\beta}$ is the dispersion of the lattice, that depends on its geometry. For example, in the case of a simple cubic lattice, $\epsilon(\mathbf{k})_{\alpha\beta}$ assumes the form, $-2t_{\alpha\beta}(\cos k_x + \cos k_y + \cos k_z)$.

Within DMFT, one can map the multi-orbital Hubbard model on to an auxiliary impurity problem with a self consistently determined bath. The Hamiltonian of the corresponding single impurity multi-orbital Anderson model, is expressed in standard notation as:

$$\begin{aligned} \mathcal{H}_{imp} =& \sum_{\alpha}(\epsilon_\alpha - \mu) f^\dagger_\alpha f_\alpha + \frac{1}{N}\sum_{k,\alpha} V_{k\alpha}\left(c^\dagger_{k\alpha} f_\alpha + f^\dagger_\alpha c_{k\alpha}\right) \\ &+ \sum_{k,\alpha,\beta} \epsilon_{k\alpha\beta} c^\dagger_{k\alpha} c_{k\beta} + \frac{1}{2}\sum_{\alpha\neq\beta} U_{\alpha\beta} n_\alpha n_\beta \end{aligned} \tag{2.6}$$

Here α and β are impurity orbital indices including spin. The first term in the above equation represents the orbital energy; the second term is the hybridization between the impurity and the host conduction electrons, the third term represents the host kinetic energy and the final term is the local Coulomb repulsion between electrons at the impurity. The corresponding impurity Green's function is given by,

$$\hat{G}_{imp} = \frac{1}{(\omega^+ + \mu)\mathbb{I} - \hat{\epsilon} - \hat{\Delta}(\omega^+) - \hat{\Sigma}_{imp}(\omega^+)}\,, \tag{2.7}$$

where $(\hat{\epsilon})_{\alpha\beta} = \epsilon_\alpha \delta_{\alpha\beta}$. $\hat{\Delta}(\omega^+) = \sum_{\mathbf{k}} |V_{k\alpha}|^2 (\omega^+ \mathbb{I} - \hat{H}(\mathbf{k}))^{-1}$ is the hybridization matrix or equivalently the self-consistently determined bath; $\hat{\Sigma}_{imp}(\omega^+)$ is the impurity self-energy obtained by solving the impurity problem. The set of equations is closed by noting that, within DMFT, the lattice self-energy is momentum-independent and is the same as the impurity self-energy, i.e $\hat{\Sigma}(\mathbf{k},\omega^+) = \hat{\Sigma}_{imp}(\omega^+)$. The local Green's function obtained in Eq. (6.2) is used for defining a new hybridization as

$$\hat{\Delta}(\omega^+) = (\omega^+ + \mu)\mathbb{I} - \hat{\epsilon} - \hat{\Sigma}_{imp}(\omega^+) - \hat{G}^{-1}_{loc}(\omega^+)\,. \tag{2.8}$$

Obtaining the self-energy however is the most challenging step, and we employ multi-orbital iterated perturbation theory to solve the multi-orbital Anderson model. The starting point, as usual, is an ansatz for the impurity self-energy, given by[25]

$$\left(\hat{\Sigma}_{imp}(\omega)\right)_{\alpha\beta} = \delta_{\alpha\beta}\left(\sum_{\gamma\neq\alpha} U_{\alpha\gamma}\langle n_\gamma\rangle + \frac{A_\alpha \sum_{\gamma\neq\alpha}\Sigma^{(2)}_{\alpha\gamma}(\omega)}{1 - B_\alpha \sum_{\gamma\neq\alpha}\Sigma^{(2)}_{\alpha\gamma}(\omega)}\right). \tag{2.9}$$

The self-energy is thus restricted to being diagonal in the orbital basis. In the above ansatz, the first term is simply the Hartree energy and the second term contains the second order pair-bubble diagram $\hat{\Sigma}^{(2)}$ of matrix size N×N, where N is the number of orbitals. The second order pair-bubble diagram on the real frequency axis is given by

$$\begin{aligned}\Sigma^{(2)}_{\alpha\beta}(\omega) =& U^2_{\alpha\beta}\int\int\int d\epsilon_1 d\epsilon_2 d\epsilon_3 \rho_\alpha(\epsilon_1)\rho_\beta(\epsilon_2)\rho_\beta(\epsilon_3) \\ & \frac{n_F(-\epsilon_1)n_F(\epsilon_2)n_F(-\epsilon_3) + n_F(\epsilon_1)n_F(-\epsilon_2)n_F(\epsilon_3)}{\omega^+ - \epsilon_1 + \epsilon_2 - \epsilon_3},\end{aligned} \tag{2.10}$$

where $\rho_\alpha = -\frac{1}{\pi}\mathrm{Im}\tilde{\mathcal{G}}_\alpha$ and $\tilde{\mathcal{G}}_\alpha$ is the Hartree corrected bath propagator, which is obtained from a Dyson like equation, and is given by

$$\tilde{\mathcal{G}}_\alpha^{-1} = \left(\hat{G}^{-1}_{loc} + \hat{\Sigma} + \hat{\epsilon} - (\mu - \mu_0)\,\mathbb{I}\right)_{\alpha\alpha}. \tag{2.11}$$

The pseudo chemical potential, μ_0, is found at $T = 0$ by satisfying the Luttinger's theorem,

$$-\frac{\mathrm{Im}}{\pi}\int_{-\infty}^{0} d\omega \mathrm{Tr}\left(\frac{d\hat{\Sigma}(\omega)}{d\omega}\hat{G}_{imp}(\omega)\right) = 0\,. \tag{2.12}$$

At finite temperature, an ambiguity exists in the determination of the pseudo-chemical potential. We choose to use the μ_0 determined at zero temperature for all finite temperatures. The chemical potential, μ, is found by fixing the total occupancy from the local Green's function, $\hat{G}_{loc}$, to be equal to the desired filling,

$$-\frac{1}{\pi}\mathrm{Im}\int_{-\infty}^{0} \mathrm{Tr}\hat{G}_{loc} = n_{tot}\,, \tag{2.13}$$

where the trace is over the spin and orbital indices. The unknown coefficients A_α, B_α from Eq. (2.9) are obtained in the standard way by satisfying the high frequency limit and the atomic limit respectively. The detailed procedure to derive A_α, B_α and their expressions are discussed in the Appendix A. These coefficients contain higher order correlation functions. The order of the correlation functions depends on number of poles in the self energy. For example a pole of order n involves $(\mathrm{n+1})^{\mathrm{th}}$ order correlation functions. For a two pole ansatz A_α and B_α involve two and three particle correlation functions. We calculate the two particle correlation function [38] using the equation of motion method to obtain [39]

$$\sum_{m' \neq m} U_{mm'} \langle n_m n_{m'} \rangle = -\frac{1}{\pi} \int d\omega n_F(\omega) \mathrm{Im} \left[\Sigma_m(\omega) G_m(\omega) \right] . \tag{2.14}$$

This single equation is not sufficient to find all the two-particle correlators. Hence as an approximation, we use the following:

$$\langle n_m n_{m'} \rangle = -\frac{\int d\omega n_F(\omega) \mathrm{Im}(\Sigma_m(\omega) G_m(\omega))}{\pi U_{mm'} (N_{orb} - 1)} . \tag{2.15}$$

We calculate the three particle correlation function encountered in B_α approximately by decoupling it in terms of two and single particle correlation functions. In this work, we have ignored the three particle correlation function.

2.3 Results and Discussion

The formalism developed in the previous section is applied to a wide variety of correlated systems. We begin with a discussion of the well studied paramagnetic Mott transition in the half-filled single-band Hubbard model. Then we examine the doped Mott insulator. The covalent insulator is considered next, followed by the two-orbital Hubbard model. For the latter, We investigate the effect of filling, Hund's coupling and crystal field splitting. Finally, we move to real material calculations considering specifically the case of $SrVO_3$. As mentioned earlier we bench-mark our results with those from numerically exact CTQMC[36] methods. The CTQMC formalism yields results on the Matsubara frequency axis so to get the real frequency data, analytical continuation is required. We avoid analytic continuation by transforming the real frequency data obtained from MO-IPT to imaginary frequencies using the following spectral representations:

$$G(i\omega_n) = \int \frac{A_G(\omega)d\omega}{i\omega_n - \omega}, \tag{2.16}$$

and

$$\Sigma(i\omega_n) = \int \frac{A_\Sigma(\omega)d\omega}{i\omega_n - \omega}, \tag{2.17}$$

where $A_G(\omega) = -\text{Im}G(\omega)/\pi$ and $A_\Sigma(\omega) = -\text{Im}\Sigma(\omega)/\pi$. In order to quantify the efficiency of the method, the imaginary part of the self energy needs to be bench-marked rather than the Green's function. This is because the former is far more sensitive than the latter and moreover, the low energy scale of the system depends on the imaginary part of the self energy.

2.3.1 Single band Hubbard model: Half-filled case

The Hamiltonian for the single band Hubbard model is given by

$$\mathcal{H} = \sum_{ij\sigma} T_{ij}^{\sigma}(c_{i\sigma}^{\dagger}c_{j\sigma} + h.c) + \sum_{i\sigma} \epsilon_{i\sigma}n_{i\sigma} + \sum_{i\sigma} \frac{U}{2} n_{i\sigma}n_{i\bar{\sigma}} \,. \tag{2.18}$$

We study the above model within DMFT for a semi-elliptical density of states, given by

$$\rho(\epsilon) = \frac{4}{\pi W}\sqrt{\left(\frac{W}{2}\right)^2 - \epsilon^2}\,. \tag{2.19}$$

Here W is the full-band width. In our calculations, we choose the energy unit to be $\frac{W}{2} = 1$.

The half-filled Hubbard model exhibits an interaction-driven metal-insulator Mott transition at a critical U_c. Terletska et al. [40] found that the critical exponents and

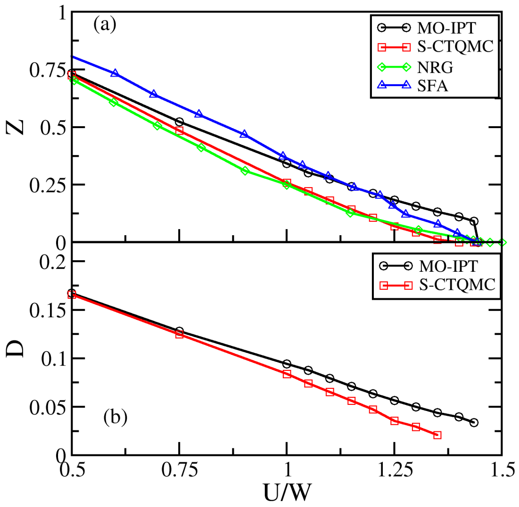

Figure 2.1: (Color online) (a) Quasi-particle weight Z of the single band half-filled Hubbard model obtained with different impurity solvers (see text for more details) (b) Double occupancy D obtained from MO-IPT and S-CTQMC.

scaling functions obtained by IPT are identical to those from CTQMC. Here, we revisit this case and benchmark the quasiparticle weight, double occupancy, spectra and imaginary part of the self-energy. The MO-IPT method reduces to the second order perturbation theory in terms of Hartree-corrected propagators. In Fig. 2.1(a) we compare the quasi-particle weight Z obtained from different impurity solvers and several values of the Coulomb interaction. The values of Z obtained from S-CTQMC match well with those from NRG[41] for all values of U/W except close to the Mott-transition. This is most likely because we have done CTQMC calculations at $\beta = 64$, while NRG is at zero temperature. The critical interaction strength, $\frac{U_c}{W} \approx 1.35$ obtained from both the methods[42] agrees very well. The Z obtained from MO-IPT at $\beta = 64$ matches quantitatively with CTQMC and NRG in the weak coupling limit and only qualitatively in the proximity of the transition. On the other hand, the results of the self energy functional approach (SFA)[43] agree with MO-IPT in the strong coupling limit rather than in the weak coupling limit. The MO-IPT yields the critical value of $\frac{U_c}{W} = 1.42$, which is in good agreement with

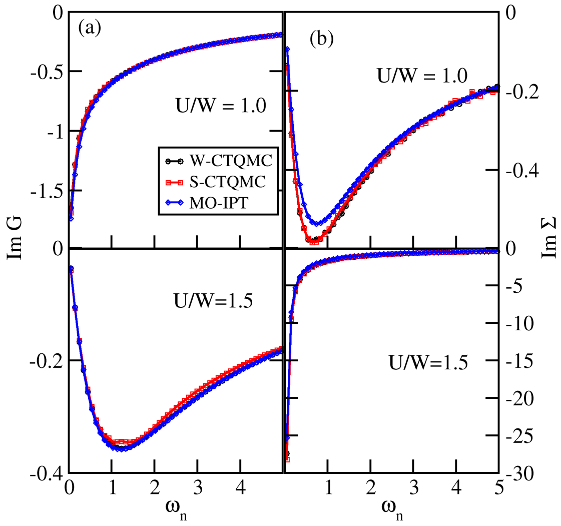

Figure 2.2: (color online) Comparison of the imaginary part of Matsubara Green's function (left panels) and self energy (right panels) obtained from MO-IPT, S-CTQMC and W-CTQMC[44] for $U/W = 1.0$ (top panels) and $U/W = 1.5$ (bottom panels) at $\beta = 64$.

the critical value $\frac{U_c}{W} = 1.45$ obtained from SFA[43] at zero temperature. The double occupancy obtained from MO-IPT and S-CTQMC (shown in panel (b) of Fig. 2.1) also match, except very close to the transition. A detailed comparison of spectra from S-CTQMC and W-CTQMC with the same from MO-IPT (transformed to imaginary frequencies) is shown in Fig. 2.2. The left panels show the imaginary part of the Green's function at $U/W = 1.0$ (top panel) and $U/W = 1.5$ (bottom panel), while the right panels show the imaginary part of the corresponding self-energies. The excellent agreement between the three methods is clearly evident.

2.3.2 Single band Hubbard model: Doped Mott insulator case

The single band Hubbard model has gained a lot of interest, because the doped Mott insulator regime is believed to capture the essential physics of high T$_c$ superconductors[45]. This regime is, in reality, highly complex, because many different factors such as proximity to the antiferromagnetic Mott insulator, disorder, d-wave superconducting fluctuations and pseudogap physics have to be treated on an equal footing. Hence, investigations of the doped Mott insulator in all its glory represents one of the toughest challenges in condensed matter. Here, we take a simplistic approach to the problem, and investigate the performance of MO-IPT in the paramagnetic doped Mott insulator in infinite dimensions. Our MO-IPT reduces basically to the IPT-L in this regime.

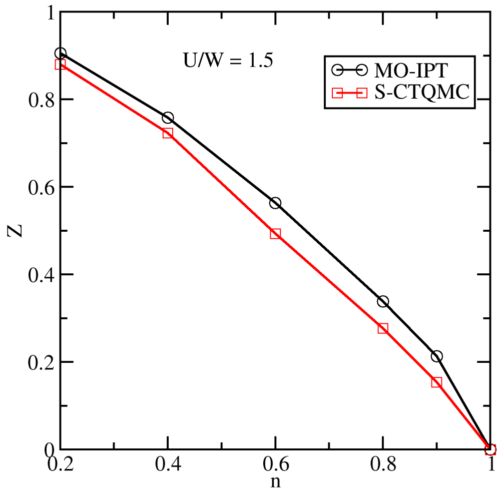

Figure 2.3: (color online) Quasi-particle weight obtained from MO-IPT (or IPT-L) is compared to the same obtained from CTQMC for the paramagnetic doped Mott-insulator as a function of filling with $U/W = 1.5$ and $\beta = 64$.

A comparison of quasi-particle weight at $U/W = 1.5$ obtained from MO-IPT and S-CTQMC as a function of filling (Fig. 2.3) yields, surprisingly, an excellent agreement. We observe that as we decrease the filling (from 1) for a given U/W, the Mott insulator turns into a strongly correlated metal and finally ends up as a simple metal. In the strong coupling limit, for filling close to $n = 1$, the IPT-n$_0$ method gives an insulating solution, while the IPT-L correctly predicts a metal in agreement with exact methods. Kajueter and Kotliar have benchmarked the real-frequency spectral functions obtained from IPT-L with exact diagonalization calculations and had found good agreement. We find that the imaginary part of the Green's function

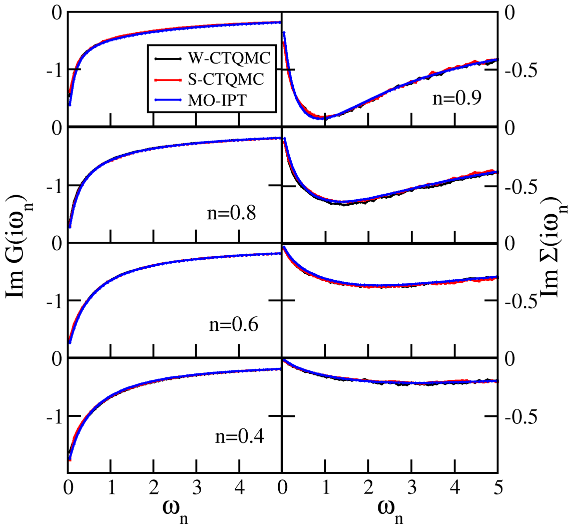

Figure 2.4: (color online) Doped Mott insulator: Comparison of imaginary part of Matsubara Green's function and self energy obtained from MO-IPT, W-CTQMC and S-CTQMC for U/W = 1.5 at different fillings and $\beta = 64$.

and self-energy obtained from IPT, when transformed to the Matsubara frequency axis using equations 2.16, 2.17 are almost identical to those obtained from the strong coupling and weak-coupling variants of CTQMC (see Fig. 2.4). The slope of the Im$\Sigma(i\omega_n)$ as $\omega_n \to 0$ is $1 - 1/Z$, and the good agreement of Z shown in Fig. 2.3 is simply a reflection of the detailed agreement for all frequencies. Such an excellent agreement is truly surprising because IPT is a perturbative method by construction and the strongly correlated, doped Mott insulator regime should not, in general, be amenable to perturbative methods.

2.3.3 Covalent Insulator

The discovery of topological insulators [46] has led to a renewed interest in the role of e-e correlations in band insulators (BI)[47]. The prime examples of such materials would be FeSi[48] and FeSb$_2$[49], since experimental measurements indicate a small optical gap and large thermopower (at low T). Increasing temperature leads to closing of the gap, and concomitantly a insulator-metal crossover in the resistivity.

Such large scale spectral weight transfers are highly indicative of strong correlations. Specific heat measurements also seem to validate this observation. The band gap in these systems is a simple consequence of the structure of the hopping matrix and not of completely filled electronic shells [50]. Hence these materials are called covalent insulators[47, 50]. A Hamiltonian that describes the covalent insulator is given by[50]

$$\mathcal{H} = \sum_{\mathbf{k}\sigma} \begin{pmatrix} a^{\dagger}_{\mathbf{k},\sigma} & b^{\dagger}_{\mathbf{k},\sigma} \end{pmatrix} \hat{H}(\mathbf{k}) \begin{pmatrix} a_{\mathbf{k},\sigma} \\ \\ b_{\mathbf{k},\sigma} \end{pmatrix} + \sum_{i\alpha} U_{\alpha\alpha} n_{i\alpha\uparrow} n_{i\alpha\downarrow}\,, \tag{2.20}$$

where α = a and b are two sub-lattices with semi-elliptic bands and having dispersion $\epsilon_{\mathbf{k}}$ and -$\epsilon_{\mathbf{k}}$ respectively. The two sub-lattices are coupled by a $\mathbf{k}-$independent hybridization V. While the unit of energy is chosen to be W = 2 throughout, for this subsection W=4 has been chosen in order to benchmark with earlier results[50]. This is the first two-band model we have studied in this work, since the previous cases pertained to the single-band Hubbard model. Hence this will be the first real test of the 'multi-orbital' part of MO-IPT. Since this is still the half-filled case, Luttinger's theorem does not have to be satisfied explicitly. The $A_\alpha = 1$ and $B_\alpha = 0$ for all orbitals. Thus, the MO-IPT used for the covalent insulator case is equivalent to that employed by Liebsch [31] for studying the Mott transition in the two-band Hubbard model.

The quasi-particle weights (Fig. 2.5(a)) and double occupancy (Fig. 2.5(b)) obtained from MO-IPT and S-CTQMC (shown as black circles and red squares respectively) are in close agreement except in the proximity of the transition of the correlated band insulator to a Mott insulator. Unlike the ionic Hubbard model case[51], we do not see any intervening metallic phase between the correlated band insulator and the Mott insulator. This is also consistent with the S-CTQMC results. At high temperatures, the correlated band insulator should be gapless, and must develop the gap with decreasing temperature. Precisely this behavior is seen in the real frequency spectra (left panels, Fig. 2.6), which arises from the spectral

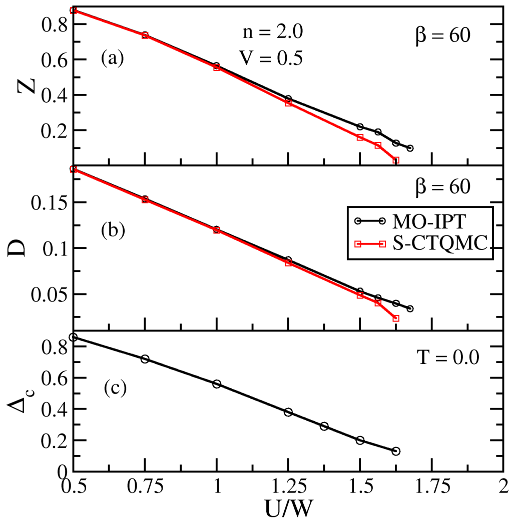

Figure 2.5: (color online) Covalent insulator: (a) Quasi-particle weight Z as a function of U/W obtained from MO-IPT (black circles) and CTQMC (red squares) for $\beta = 60$ and V=0.5.(b) Double occupancy as a function of U/W obtained from MO-IPT and S-CTQMC. (c) Charge gap as a function of U/W obtained from MO-IPT at T=0.

weight transfer in the self-energy as a function of temperature. The high reliability of these spectra and self-energies computed through MO-IPT is apparent in the excellent agreement with the same obtained through strong coupling CTQMC (on the Matsubara axis, in Fig. 2.7). The crossover of the band-insulator to Mott insulator is also visible in the increasing (negative) slope of the imaginary part of self-energy with increasing U/W.

2.3.4 Two orbital Hubbard model

Encouraged by the excellent benchmarking of MO-IPT with CTQMC for the two-band covalent insulator system, we now move on to the two-orbital Hubbard model[52, 53]. The Hamiltonian, in standard notation, for a cubic environment and for unbroken spin symmetry, is described in equation 2.1. Throughout the chapter, we have considered local interactions of density-density type which are obtained by neglecting spin flip and pair-hopping terms that must be present for a rotationally invariant Hund's coupling. The hopping is taken to be diagonal in orbital indices for simplicity.

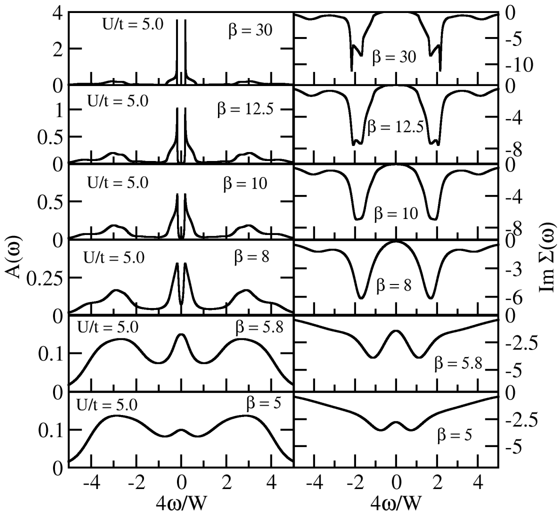

Figure 2.6: Covalent insulator: Spectral functions (left panels) and imaginary part of self energy (right panels) from MO-IPT at $U/W = 5.0$ and V=0.5 for a range of $\beta = 1/T$ values (increasing T from top to bottom).

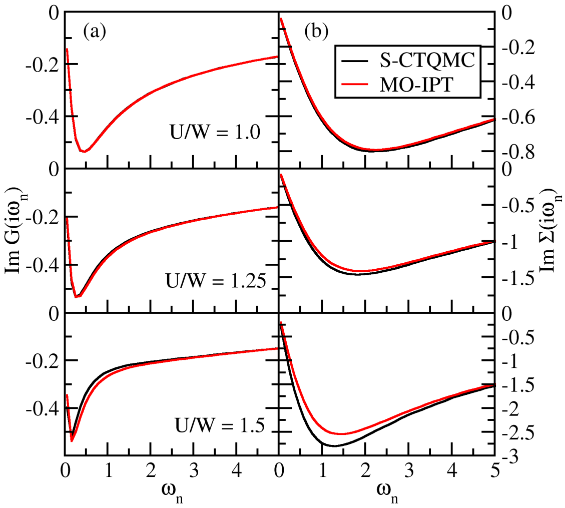

Figure 2.7: (color online) Covalent insulator: Comparison of the imaginary part of Matsubara (a) Green's function and (b) self-energy obtained from MO-IPT (black) and S-CTQMC (red) for various U/W values and β=60.

(a) Half-filling: J = 0

We begin by considering the half-filled case (total occupancy is two) with $J = 0$. The Hamiltonian (equation 2.1) has SU(4) symmetry in this situation. We have employed a semi-elliptic non-interacting density of states of full-band width W = 2 for the MO-IPT-DMFT calculations.

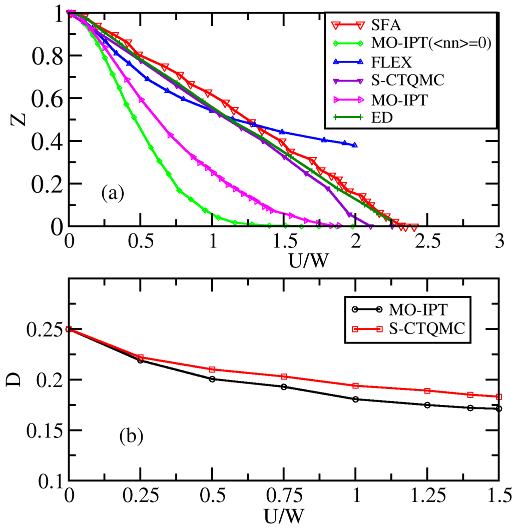

Figure 2.8: (color online) (a) Two-orbital SU(4) symmetric Hubbard model at half-filling: Quasi particle weight obtained from different impurity solvers as a function of U/W for $\beta = 64$. (b) Double occupancy obtained from MO-IPT (black circles) and hybridization expansion CTQMC (red squares) for β=64.

In Fig. 2.8(a), we plot the quasi-particle weight (Z) obtained from different impurity solvers for the particle-hole symmetric case. The results from strong coupling CTQMC, ED[54] and SFA[43], including the critical U$_c$, where the system transitions from metal to Mott-insulator, are in good agreement. The critical value U$_c$ obtained in the multi-orbital case is greater than the value obtained in the single band case. The Mott transition is absent in the FLEX result [13]. The MO-IPT is seen to underestimate the quasiparticle weight as compared to the other methods (except MO-IPT<nn>=0; see below). However, the critical U_c agrees reasonably well with that from hybridization expansion CTQMC. The green diamonds are from a variant of MO-IPT (used e.g. by Fujiwara et al. [33]) where the two-particle correlation function is simply decoupled into two single-particle terms ($\langle n_\alpha n_\beta \rangle = \langle n_\alpha \rangle \langle n_\beta \rangle$). The neglect of two particle correlations leads to a much worse comparison than MO-IPT. In contrast to the not-so-good agreement with exact methods for the quasiparticle weight, the average double occupancy obtained from MO-IPT shows excellent agreement with CTQMC (see Fig. 2.8(b)). Since the total energy of the system depends on single particle and two particle correlation functions, we expect that thermodynamic quantities like total energy or specific heat computed through MO-IPT might be reliable. One more important observation is that the double occupancy remains finite and almost constant even beyond the Mott transition, unlike the the single band case. We also compare the single-particle Green's function and self-energy on the Matsubara frequency axis (Fig. 2.9). At high frequencies, the agreement between MO-IPT and S-CTQMC is seen to be excellent, while the agreement worsens at low frequencies, especially with increasing U/W.

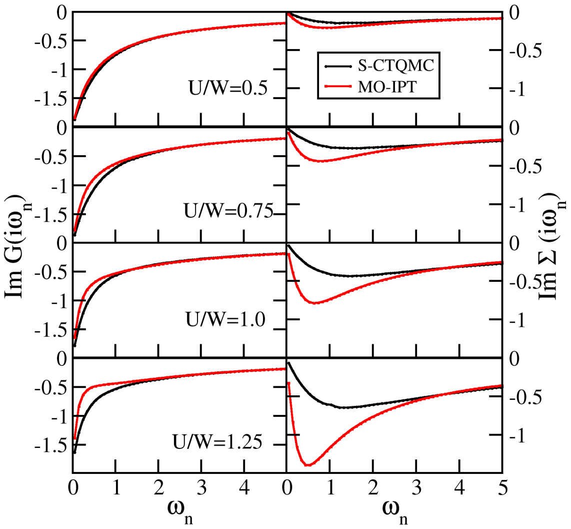

Figure 2.9: (color online) Two-orbital, SU(4) symmetric Hubbard model at half-filling: Imaginary part of Matsubara Green's function (left panels) and self energy (right panels) obtained from MO-IPT (red solid lines) and S-CTQMC (black solid lines) at β=64.

(b) Half-filling: Effect of Hund's coupling (J)

The interplay of Hund's coupling, J, and a local interaction U, has been investigated by several groups. The main consensus is that strong correlation effects can be affected significantly through J [54, 55]. For example, in the half-filled case, the U_c for Mott transition is lowered by $(N-1)J$, where N is the number of orbitals, while the critical U is enhanced by $3J$ in the non-half-filled (but integral occupancy) case [54]. It is important to know the extent to which the interplay between J and U is captured by the MO-IPT method. In Fig. 2.10(a) and (b), the quasi-particle weight Z for different values of J obtained from S-CTQMC and ED [54] are shown. Indeed, with increasing J, the U_c at which $Z \to 0$ decreases sharply, as expected from the atomic limit. Also, for each J, the quasiparticle weight decreases monotonically with increasing interaction strength. Although the latter trend is qualitatively captured by the MO-IPT result (shown in Fig. 2.10(c)) for larger J, there is a disagreement with the exact results at lower J values. The MO-IPT yields a U_c that is a non-monotonic function of J. The insets of panels a and b in Fig. 2.10

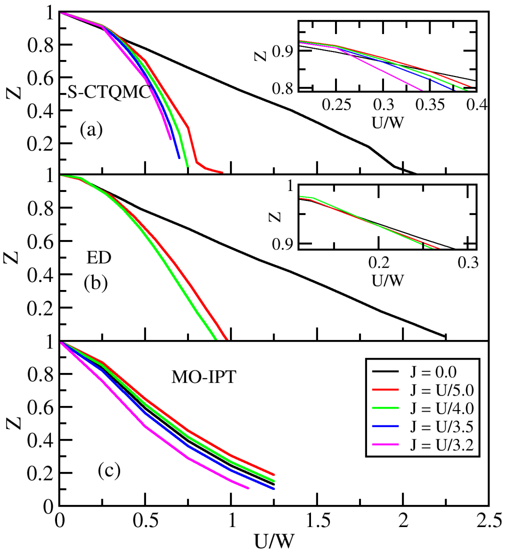

Figure 2.10: (color online) Two orbital half-filled Hubbard model, finite J: Quasi particle weight dependence on U/W obtained from (a) strong coupling CTQMC, (b)ED and (c) MO-IPT for various J values. Insets in the panels (a) and (b) show the effect of J on Z in the weak coupling regime.

zoom in on the low interaction ($U/W \lesssim 0.3$) part of the main panels. Unlike for $U/W \gtrsim 0.3$, where increasing J leads to a monotonic reduction of Z, a rise and fall of Z is observed for $U/W \lesssim 0.3$. Although such a trend is achieved by MO-IPT as well, the non-monotonicity sustains even for larger U/W. A frozen local-moment phase is seen in the S-CTQMC calculations for any given J in the strong coupling limit, while such a phase is not observed either by ED[54] or MO-IPT calculations. It must be mentioned here that the CTQMC calculations employ a density-density type Hund's coupling, while the ED employs a fully rotationally invariant J. Although the quasiparticle weight dependence on U and J is not accurately captured by MO-IPT, the single-particle dynamics on all scales is in qualitative agreement with S-CTQMC calculations (as seen in Fig. 2.11).

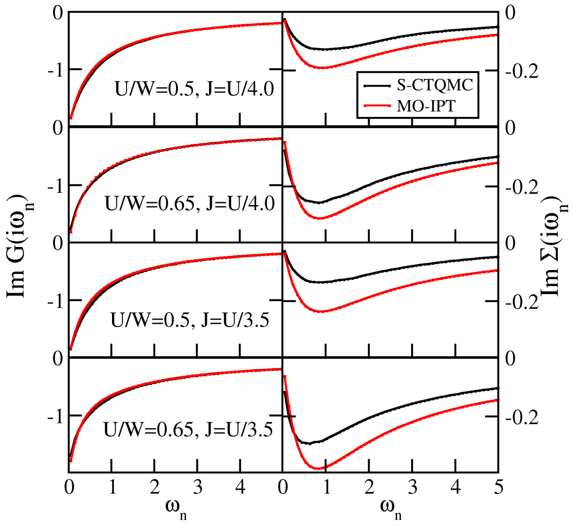

Figure 2.11: (color online) Two orbital half-filled Hubbard model, finite J: Imaginary part of Matsubara Green's functions (left panels) and self-energy (right panels) obtained from S-CTQMC (black) and MO-IPT (red) for different values of J and U/W at β=64.

(c) Away from Half-filling: Effect of J

The MO-IPT method works best away from half-filling, which is consistent with the results of comparisons carried out previously by other groups[56]. In order to illustrate this, here we study the two orbital Hubbard model for a $n_{tot} = 1.1$. The imaginary part of the Matsubara self-energy obtained from S-CTQMC matches well with that from MO-IPT (Fig. 2.12, panels (a) and (b)), hence the latter does well in this regime. This observation is reinforced by the panels (c)-(e), which show a comparison of the quasiparticle weights as a function of U/W for three values of J, namely $J = 0, U/4.0$ and $U/3.5$. The results of MO-IPT are seen to agree very well with those from CTQMC. For most real material calculations, the regime considered in this subsection is perhaps the most relevant. Hence, accurate results from MO-IPT in this regime prove its efficacy for integration into first-principles approaches. The Hund's coupling and Coulomb interaction have a synergistic effect

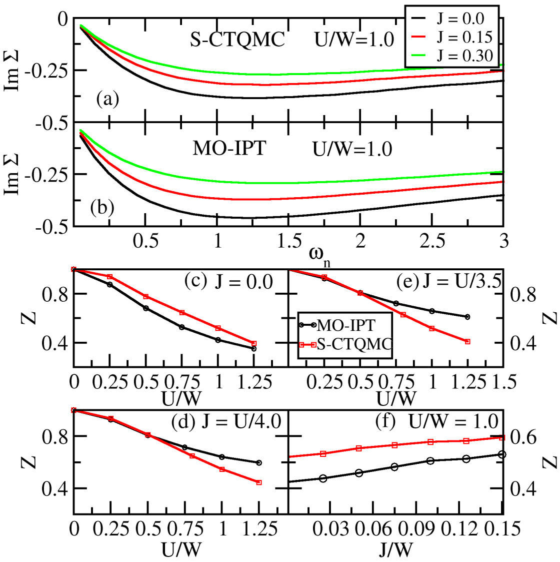

Figure 2.12: (color online) Two-orbital Hubbard model: Effect of J away from half-filling ($n_{tot} = 1.1$) The imaginary part of the Matsubara self-energy for various J-values, and fixed $U/W = 1$ as computed within (a) S-CTQMC and (b) MO-IPT. Comparison of quasi particle weight obtained from MO-IPT (black circles) and CTQMC (red squares) as a function of U/t for (c) $J = 0.0$, (d) $J = U/4$ and (e) $J = U/3.5$ for $\beta = 64$; and (f) as a function of J for a fixed $U/W = 1.0$.

at half-filling, while in the doped case, the reverse occurs[55]. This is shown in panel (f) of Fig. 2.12, where an increase of Z is seen with increasing Hund's coupling at a fixed interaction strength. It is quite instructive to study the real frequency spectral functions and self-energies as obtained from MO-IPT. These are shown in Fig. 2.13

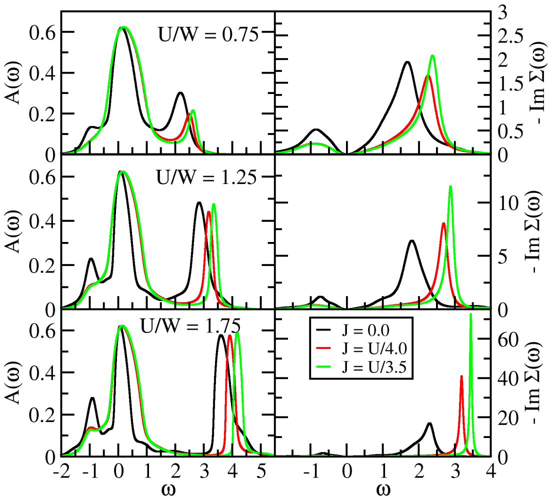

Figure 2.13: (color online) Two-orbital Hubbard model, away from half-filling: Real frequency spectral functions (left panels) and minus imaginary part of self energy (right panels) for various U/W and J values.

for various values of interaction strength and Hund's coupling, J. In the absence of Hund's coupling, the spectrum (shown in the left panels of Fig. 2.13) exhibits spectral weight transfers characteristic of increasing correlation strength: a central resonance that becomes sharper, and Hubbard bands that grow in prominence with increasing U/W. However, at a fixed U/W, increasing Hund's coupling leads to a reversal of the aforementioned trend, i.e, a broadening of the resonance and a melting of the Hubbard band (see e.g. left panel bottom figure of 2.13). In this parameter regime, a previous formulation of the multi-orbital iterated perturbation theory[56] found a double peak structure at the chemical potential. Such a feature was shown by the authors[25] to be spurious by comparison to results from exact diagonalization. The reason we do not observe such a spurious feature is that we have considered only two poles in the self-energy, in contrast to the formulation of Ref. [25], where they have retained all the eight poles (for a two-orbital model). Although our ansatz seems like an ad-hoc truncation scheme, the justification for such a scheme lies in its excellent agreement with CTQMC results (shown in Fig. 2.14) and the absence of spurious features. In Fig. 2.14, the imaginary part of Matsubara Green's functions and self energies obtained from MO-IPT are compared with those from CTQMC for three values of J at $U/W = 1.25$ and β =64. For all values of the Hund's coupling, an excellent agreement is obtained.

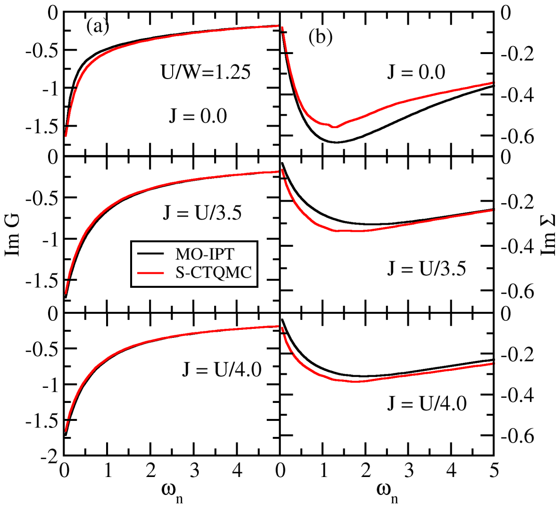

Figure 2.14: (color online) Two-orbital degenerate Hubbard model, away from half-filling: Comparison of Imaginary part of Matsubara Green's function (left panels) and self energy (right panels) obtained from MO-IPT and S-CTQMC for various values of J at $U/W = 1.25$.

2.3.5 Two orbital Hubbard model: Crystal field splitting and Hund's coupling

We now proceed to the case of a two-orbital model with non-degenerate orbitals, i.e., with crystal field splitting[57] in the presence of Hund's coupling. In most materials, the crystalline environment lifts the orbital degeneracy[58]. For example in transition metal oxides, due to crystal field effects, the five fold degenerate d-level splits into triply degenerate t_{2g} and doubly degenerate e_g levels and the corresponding energy gap is ~1-2 eV. The degeneracy of each of these levels (t_{2g}, e_g) is further lifted by distortions such as the $GdFeO_3$ type, or arising through the Jahn-Teller effect or spin-orbit coupling. The energy cost for such distortion induced splitting is ~few meV. Recently, Pavarini et al.[59] studied crystal field effects in d^1 type perovskites such as $SrVO_3$, $CaVO_3$, $LaTiO_3$ and $YTiO_3$ theoretically. It was found that crystal field effects and cation-covalency ($GdFeO_3$ -type distortion) lift the orbital degeneracy and reduce the orbital fluctuations. Thus, investigating crystal field effects in model Hamiltonians is highly relevant for understanding of real materials.

We have investigated the Hamiltonian in equation 2.1 by considering two orbitals with energies $\epsilon_1 = 0.0$ and $\epsilon_2 = -0.2W$, which corresponds to a crystal field splitting of $0.2W$. The results from MO-IPT, for a fixed total filling of $n_{tot} = 1.1$, are compared with those from strong coupling CTQMC at the corresponding orbital occupancies. In Fig. 2.15, we compare the quasi particle weights of the two orbitals obtained from MO-IPT with that of CTQMC. We observe a better agreement of Z for orbital-1 than for orbital-2. This must be expected, since orbital-1 is further away from particle-hole symmetry than orbital-2. The corresponding orbital occupancies as a function of increasing interaction (and hence J) are shown in Fig. 2.15. The deviation between results from the two methods increases with increasing U and $J(= U/4)$, which indicates that MO-IPT is almost exact for $U/W \lesssim 0.5$.

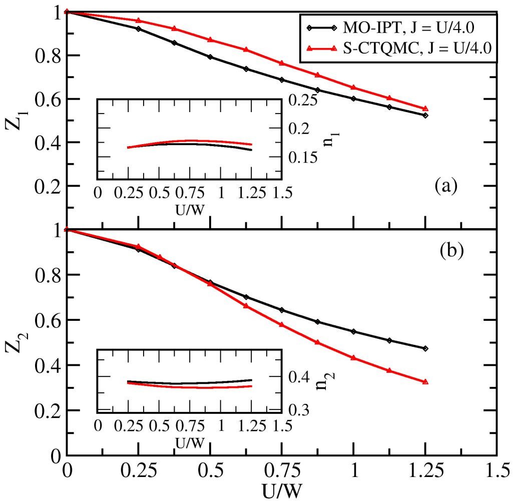

Figure 2.15: (color online) Crystal field effects: Quasi particle weights for (a) orbital-1 and (b) orbital-2, obtained from MO-IPT and CTQMC for various U/W values with $J = U/4$ at β=64. The insets show the corresponding occupancies.

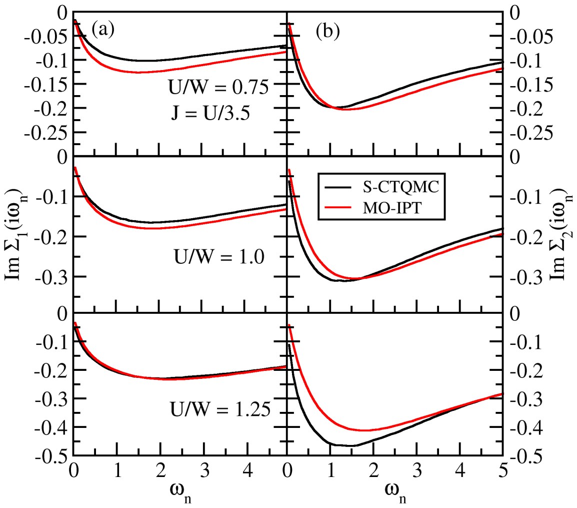

Figure 2.16: (color online) Crystal field effects: Comparison of imaginary part of self energy for orbital-1(left) and orbital-2(right) obtained from MO-IPT and S-CTQMC for various values of U/W and $J = U/3.5$.

Next, we benchmark the single-particle dynamics in the presence of crystal field splitting. In Fig. 2.16, we show the imaginary part of the Matsubara frequency self energies obtained from MO-IPT and CTQMC for orbitals-1 and 2 (left and right panels respectively). The agreement between the results is quite evident, this suggesting that the MO-IPT should serve as a good method to study interacting, real material systems with finite crystal field effects and Hund's couplings. This is especially true if the material in question has a large number of bands, which would make it prohibitively expensive to treat with CTQMC, while MO-IPT would be able to handle it with ease. We now demonstrate the efficacy of MO-IPT when applied to a well studied, real material system, namely $SrVO_3$.

2.3.6 Application to real materials: $SrVO_3$

Over the past decade or so, the combination of density functional theory (DFT) with dynamical mean field theory, such as LDA+DMFT[60], has emerged as one of the most powerful methods for electronic structure calculations of strongly correlated electronic systems. Although the DFT results contain rich, material specific information, being a single particle theory, it works well only for weakly correlated systems where the ratio of Coulomb interaction (U) to bandwidth (W) is small i.e., $U/W \ll 1$. If we consider the opposite limit of $U/W \gg 1$, we have successful methods like the Hubbard-I and Hubbard-III approximations or the LDA+U method for predicting the ground state of the system. But these also have limitations, such as the neglect of dynamical fluctuations in the LDA+U method. In nature, there are many materials, for example, transition metal oxides which lie in between these two limits. It has been established in the context of model Hamiltonians that the DMFT can handle both the limits quite efficiently. Hence a natural combination of LDA with DMFT is expected to bring predictive capabilities in the theory of strongly correlated electronic systems. Nevertheless, LDA+DMFT is not without its own bottlenecks.

One of the central issues of LDA+DMFT method is the correct definition of a correlated subspace. The basic idea of a correlated subspace is to make an appropriate choice of energy window around the Fermi level and fit the band structure to a few-orbital tight-binding model. Many techniques have been proposed to construct such a material specific ‘non-interacting’ Hamiltonian. The two major techniques for this purpose are down-folding [61] and projection based Wannier function technique [62]. In general, for example in transition metal compounds, bands which are crossing the Fermi level like those having d-orbital character are considered in the desired energy window for Hamiltonian construction. This process becomes simple if there is no hybridization in the system in the sense that these bands with d-orbital character are well separated from other bands like bands with p-orbital character. As Dang et al.[63] pointed out, a mixing of these d orbital bands with p orbital bands can create several complications. However, after getting the ’non-interacting’ Hamiltonian , one can add various types of interactions terms to this Hamiltonian to obtain a full material-specific multi-orbital Hamiltonian. The solution of such a Hamiltonian is however a major challenge and this is where the MO-IPT can be most useful, since it scales only algebraically with increasing number of bands, while yielding real frequency quantities directly. In contrast, impurity solvers like CTQMC and ED scale exponentially with increasing number of orbitals and are naturally very expensive, especially for investigations of real materials. As a test case, we study $SrVO_3$ which is considered a prototypical example of a strongly correlated electronic system.

(a) Computational Details

We perform our density functional theory (DFT) calculations with linearized augmented plane wave (LAPW) based method as implemented in the all-electron package WIEN2K[64]. The experimentally determined structure[65] of cubic $SrVO_3$ in a non-magnetic phase was used for the calculations (neglecting spin-orbit coupling). The product of plane-wave cut off (K_{max}) and smallest atomic sphere radius (R_{MT}) was chosen as $R_{MT} \times K_{max} = 7.0$ for controlling the basis set. The radii of the muffin-tin spheres were chosen to be $10-15\%$ larger than the corresponding atomic radii. Thus, the values used for R_{MT} were 2.50 for Sr, 1.89 for V and 1.71 for O. With these parameters, charge leakage was absent and our DFT results agree well with results from DFT calculation with other basis sets [66]. We utilize the generalized gradient approximation (GGA) of Perdew, Burke and Ernzerhof[67] for the exchange and correlation functional. In this calculation, we consider 512 **k**-points in the irreducible part of the Brillouin zone. After getting the Bloch-eigen states, all the necessary inputs for constructing the maximally localized Wannier functions (MLWFs) are prepared by the WIEN2WANNIER code[68]. Finally, the Hamiltonian $\mathcal{H}_{\mathcal{DFT}}$ is constructed in the maximally localized Wannier basis by taking a projection of three $V - t_{2g}$ orbitals within the energy window of -1.0 eV to 1.8 eV with respect to the Fermi level with a standard procedure as implemented in Wannier90[69]. We begin by discussing the DFT results.

(b) GGA+DMFT: Results and discussion

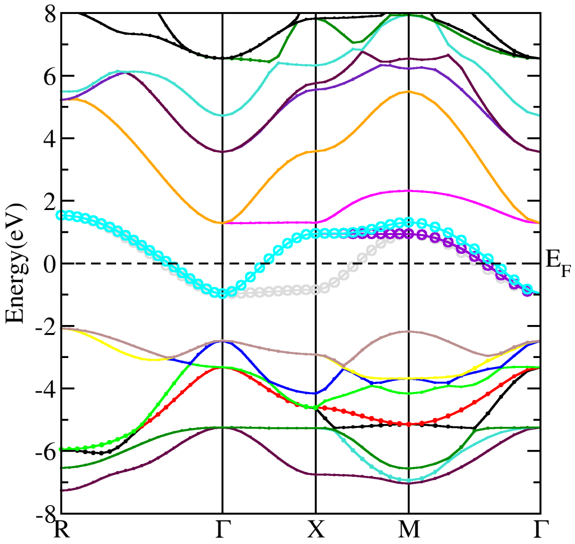

Figure 2.17: (color online) Band structure of SrVO$_3$ obtained from DFT.

Our computed band structure and density of states (DOS) are presented in Fig. 2.17 and Fig. 2.18. The three bands, crossing the Fermi level, are highlighted in cyan, violet and grey colors. These bands originate from the $V - t_{2g}$ states, and are located between -1.1eV and 1.5eV. The $V - e_g$ states lie at higher energies, between 1.1eV to 5.8eV (see the projected density of states in Fig. 2.18). The band structure agrees well with previous results by Ishida et. al.[70] obtained in the LAPW basis. When compared with results from the linear muffin-tin orbital (LMTO) calculations of Nekrasov et al. [71], the position of $V - t_{2g}$ bands agrees well but the position of $V - e_g$ states differs by about 0.3 eV. This discrepancy is, most likely, due to the difference in basis sets used in the two calculations. A significant computational simplification results from ignoring the hybridization between $V - t_{2g}$ and $V - e_g$ orbitals, since the low energy correlated subspace comprises just three $V - t_{2g}$ orbitals.

Thus, the DFT results yield a 'non-interacting' Hamiltonian $\hat{H}_{DFT}(\mathbf{k})$, which in this case is a 3×3 matrix for each $\mathbf{k}$. Thus, the full $DFT + DMFT$ Hamiltonian is

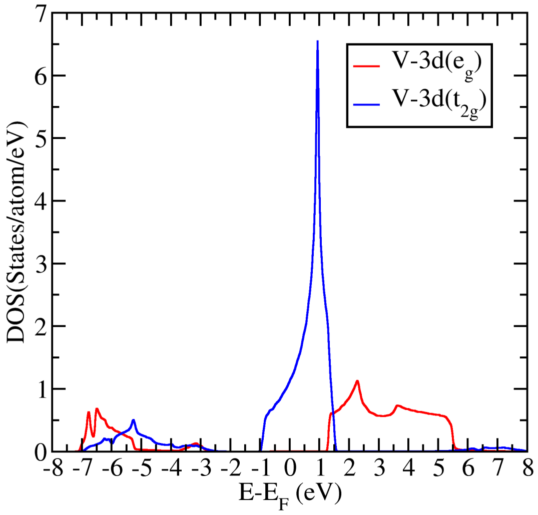

Figure 2.18: (color online) The projected density of states (DOS) of $SrVO_3$ as calculated by GGA (LAPW).

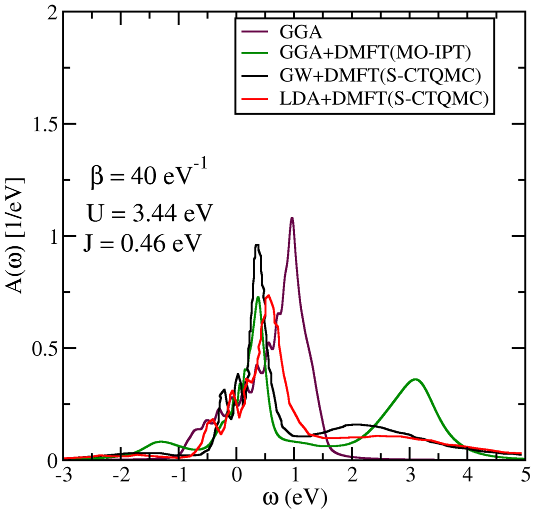

Figure 2.19: (color online) Comparison of spectral function of $SrVO_3$ obtained from different methods for U = 3.44 eV and J = 0.46 eV (see text for details).

given by

$$\hat{\mathcal{H}} = \hat{H}_{DFT}(\mathbf{k}) + \hat{H}_{int} \,, \tag{2.21}$$

where $\hat{H}_{int}$ is the interaction term is given by

$$\hat{H}_{int} = U \sum_{i,\alpha} n_{i\alpha\uparrow} n_{i\alpha\downarrow} + \sum_{i\alpha\neq\beta,\sigma\sigma'} (U' - \delta_{\sigma\sigma'} J) n_{i\alpha\sigma} n_{i\beta\sigma'} \,. \tag{2.22}$$

In the above expression, i stands for V sites and α is the t_{2g} orbital index with spin σ. U, $U'(= U - 2J)$ and $U' - J(= U - 3J)$ are the local, intra orbital and inter orbital Coulomb repulsion respectively and J is the Hund's exchange. The local, non-interacting lattice Green's function, in the orbital basis, $(\hat{G}_0(\omega))$, can be obtained from the DFT calculated $\hat{H}_{DFT}(\mathbf{k})$ by the following equation as

$$\hat{G}_0(\omega)_{\alpha,\beta} = \sum_{\mathbf{k}} \left(\left[(\omega^+ + \mu)\mathbb{I} - \hat{H}_{DFT}(\mathbf{k}) - \hat{H}_{DC} \right]^{-1} \right)_{\alpha,\beta} \tag{2.23}$$

$$\equiv \left[(\omega^+ + \mu)\mathbb{I} - \hat{\Delta}(\omega) \right]^{-1} \,, \tag{2.24}$$

where μ is the chemical potential and $\hat{\Delta}(\omega)$ is the hybridization. In the DFT approach electronic correlations are partially entered through LDA/GGA exchange-correlation potential. This part of the interaction($\hat{H}_{DC}$) has to be subtracted in LDA+DMFT approach to avoid double-counting. This is not an important issue when the low enery effective Hamiltonian contains only d-manifold because we can absorb it into chemical potential. However it is an important issue when the low energy effective Hamiltonain contains O-2p orbitals also. Various schemes for finding the double-counting correction $\hat{H}_{DC}$ exist, each with a different physical motivation. Details about such schemes may be found in the work by Lechermann et al.[72] and Nicolaus Parragh[73]. In general we can construct the modified host Green's function for the α^{th} orbital as

$$\tilde{\mathcal{G}}_\alpha = \left(\left[\hat{G}_0^{-1} + \hat{\epsilon} + \hat{H}_{DC} - (\mu - \mu_0)\,\mathbb{I} \right]^{-1} \right)_{\alpha\alpha} \,, \tag{2.25}$$

We find the pseudo-chemical potential using the same procedure as in the model calculations. The self-energy could be found, e.g. through the MO-IPT method outlined in the section 2.2. The second-order self-energy $\Sigma^{(2)}_{\alpha\beta}$ in equation 2.9 is a functional of the modified host Green's functions, $\left\{\tilde{\mathcal{G}}_\alpha\right\}$. The full local Green's function for the lattice Hamiltonian (equation 2.21) is given by

$$\hat{G}_{\alpha,\beta} = \sum_{\mathbf{k}} \left(\left[(\omega^+ + \mu)\mathbb{I} - \hat{H}_{DFT}(\mathbf{k}) - \hat{H}_{DC} - \hat{\Sigma}(\omega) \right]^{-1} \right)_{\alpha,\beta} . \tag{2.26}$$

The above Green's function may be used to obtain a new host Green's function through the Dyson's equation:

$$\tilde{\mathcal{G}}_\alpha(\omega) = \left(\left[\hat{G}^{-1} + \hat{\Sigma} + \hat{H}_{DC} + \hat{\epsilon} - (\mu - \mu_0)\,\mathbb{I} \right]^{-1} \right)_{\alpha\alpha} . \tag{2.27}$$

In general, the chemical potential, μ is found by fixing the total occupancy from the full Green's function, $\hat{G}$ to be equal to the value found from DFT.

$$-\frac{1}{\pi}\mathrm{Im} \int_{-\infty}^{0} \mathrm{Tr}\hat{G} = n^{DFT}_{tot} , \tag{2.28}$$

where the trace is over spin and orbital indices.

Thus the full solution of the problem proceeds as follows: Given the $\hat{H}_{DFT}(\mathbf{k})$, we guess an initial self-energy, as well as the μ and μ_0; and use these to find the local and the host Green's functions through equations 2.26 and 2.27. The host Green's functions are then used to find the self-energy, $\hat{\Sigma}$. Equations 2.26 and 2.28 are used to find the chemical potential. For a fixed μ_0, these equations are then iterated, until the self-energy converges. With the chosen pseudo-chemical potential, the Luttinger's integral, equation 2.12 is computed using the converged self-energy and local Green's functions. If the Luttinger's theorem is satisfied within a numerical tolerance, the solution is considered to be obtained, else the μ_0 is tuned, and the DMFT equations are iterated, until the Luttinger's theorem is satisfied.

The DFT predicted occupancy per spin on the three correlated V-t_{2g} orbitals in

$SrVO_3$ is 0.166, which implies $SrVO_3$ is a d^1 system. For the DMFT calculations, we employ interaction parameters $U = 3.44$ eV and $J = 0.46$ eV, that were obtained by Taranto et al. [74] through the random phase approximation (RPA). For $SrVO_3$, we haven't introduced explicit double counting correction because we choose the correlated subspace that is identical with the set of Wannier bands. We absorb the double counting correction and orbital energies in the lattice chemical potential, which we find by using equation 2.28.

Our computed GGA+DMFT spectrum for $SrVO_3$ is shown in Fig. 2.19 and compared with results obtained from other impurity solvers. The GGA result (shown in blue) has no signatures of correlation, while each of the DMFT calculations exhibit a three peak structure. The CTQMC results from GW+DMFT (black) agree qualitatively with those from LDA+DMFT. However, the details do differ. Namely, the positions and weights of the resonance at the Fermi level and of the Hubbard bands differ to a significant extent. This difference, naturally, can be attributed to the different starting points, namely GW vs LDA, of the CTQMC calculations. Results from the MO-IPT solver agree with those from CTQMC in the neighborhood of the chemical potential as well as in the proximity of the lower Hubbard band. The upper Hubbard band is clearly in disagreement with the CTQMC results.

As a final benchmark of the GGA+DMFT(MO-IPT) calculation, we compare our result with the experimentally measured photo emission spectrum (PES) which is shown in Fig. 2.20. A Hubbard satellite at ~ -1.5 eV is seen in the experimental PES spectrum. Our GGA+DMFT(MO-IPT) calculation predicts the Hubbard satellite at -1.25 eV. Results from other approaches, namely LDA, LDA+DMFT(CTQMC) and GW+DMFT(CTQMC) are also reproduced. Surprisingly, the closest match with the experiment is achieved by the GGA+DMFT(MO-IPT) in terms of the position and width of the resonance at the Fermi level and of the lower Hubbard band. Thus, we infer that the MO-IPT method outlined in this work may be used as an efficient tool to study the electronic structure of real material systems.

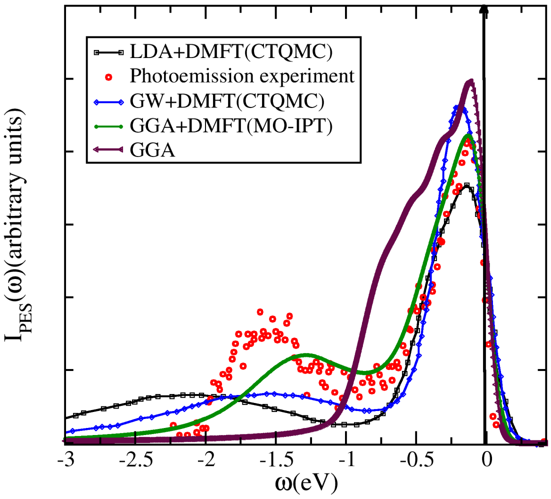

Figure 2.20: (color online) Comparison of photo emission spectra obtained from different methods GW+DMFT [74], GGA+DMFT (MO-IPT), LDA+DMFT (CTQMC)[74] and experiment [75].

2.4 Conclusions

The development of iterated perturbation theory as an impurity solver for single band models and for multi-band models dates back to almost two decades. Although a few comparisons with numerically exact methods have been made, being a perturbative approach, the method has suffered from reliability issues, especially for multi-orbital systems. Nevertheless, several multi-orbital extensions of IPT have been proposed and used to investigate model Hamiltonians and even real material systems. In this work, we have outlined a multi-orbital extension of IPT, and benchmarked it extensively against continuous time quantum Monte Carlo results. One of the main bottlenecks in methods based on spectral moment expansions is the evaluation of high-order correlation functions. We find that including such correlations that are beyond two-particle type through approximate methods such as CPA or lower order decomposition, can lead to spurious features at the chemical potential. We find the best benchmarks simply by neglecting correlations beyond two-particle. We conjecture that evaluation of the higher-order correlations through exact methods such as ligand field theory might be able to circumvent the issues mentioned above[76, 77]. We are presently implementing such a procedure. Such a procedure will also enable us to treat the Hund's coupling term in the rotationally invariant form rather than the simpler and approximate density-density type treated in the present work. Apart from the benchmarks for model Hamiltonians in various parameter regimes, we have also carried out a GGA+DMFT(MO-IPT) study of the perovskite $SrVO_3$, and compared the photoemission with experiments and results from other methods. The agreement with experiment was found to be excellent. A full scale implementation of the method outlined here, with detailed instructions for installation and use may be found at http://www.institute.loni.org/lasigma/package/mo-ipt/.

Bibliography

[1] A. Georges, G. Kotliar, W. Krauth, and M. J. Rozenberg, Rev. Mod. Phys. **68**, 13 (1996), URL `http://link.aps.org/doi/10.1103/RevModPhys.68.13`.

[2] E. Gull, Ph.D. thesis, ETH Zürich (2008).

[3] M. Jarrell and J. E. Gubernatis, Physics Reports **269**, 133 (1996).

[4] R. Bulla, T. A. Costi, and T. Pruschke, Rev. Mod. Phys. **80**, 395 (2008), URL `http://link.aps.org/doi/10.1103/RevModPhys.80.395`.

[5] T. Pruschke and R. Bulla, Eur. Phys. J. B **44**, 217 (2005), URL `http://dx.doi.org/10.1140/epjb/e2005-00117-4`.

[6] M. Caffarel and W. Krauth, Phys. Rev. Lett. **72**, 1545 (1994), URL `http://link.aps.org/doi/10.1103/PhysRevLett.72.1545`.

[7] D. J. Garc´ia, K. Hallberg, and M. J. Rozenberg, Phys. Rev. Lett. **93**, 246403 (2004), URL `http://link.aps.org/doi/10.1103/PhysRevLett.93.246403`.

[8] A. Rüegg, E. Gull, G. A. Fiete, and A. J. Millis, Phys. Rev. B **87**, 075124 (2013), URL `http://link.aps.org/doi/10.1103/PhysRevB.87.075124`.

[9] T. A. Costi, J. Kroha, and P. Wölfle, Phys. Rev. B **53**, 1850 (1996), URL `http://link.aps.org/doi/10.1103/PhysRevB.53.1850`.

[10] K. Haule, S. Kirchner, J. Kroha, and P. Wölfle, Phys. Rev. B **64**, 155111 (2001), URL `http://link.aps.org/doi/10.1103/PhysRevB.64.155111`.

[11] K. Morita, H. Maebashi, and K. Miyake, Physica B: Condensed Matter **312313**, 547 (2002), ISSN 0921-4526, the International Conference on Strongly Correlated Electron Systems, URL `http://www.sciencedirect.com/science/article/pii/S0921452601015320`.

[12] G. Kotliar, S. Y. Savrasov, K. Haule, V. S. Oudovenko, O. Parcollet, and C. A. Marianetti, Rev. Mod. Phys. **78**, 865 (2006), URL `http://link.aps.org/doi/10.1103/RevModPhys.78.865`.

[13] V. Drchal, V. Janiš, J. Kudrnovský, V. S. Oudovenko, X. Dai, K. Haule, and G. Kotliar, Journal of Physics: Condensed Matter **17**, 61 (2005), URL `http://stacks.iop.org/0953-8984/17/i=1/a=007`.

[14] D. E. Logan, M. P. Eastwood, and M. A. Tusch, Journal of Physics: Condensed Matter **10**, 2673 (1998), URL `http://stacks.iop.org/0953-8984/10/i=12/a=009`.

[15] M. T. Glossop and D. E. Logan, Journal of Physics: Condensed Matter **14**, 6737 (2002), URL `http://stacks.iop.org/0953-8984/14/i=26/a=313`.

[16] M. R. Galpin, A. B. Gilbert, and D. E. Logan, Journal of Physics: Condensed Matter **21**, 375602 (2009), URL `http://stacks.iop.org/0953-8984/21/i=37/a=375602`.

[17] P. Kumar, Ph.D. thesis, Jawaharlal Nehru Centre for Advanced Scientific Research (2013).

[18] A. Mart´in-Rodero, E. Louis, F. Flores, and C. Tejedor, Phys. Rev. B **33**, 1814 (1986), URL `http://link.aps.org/doi/10.1103/PhysRevB.33.1814`.

[19] K. Yosida and K. Yamada, Progress of Theoretical Physics Supplement **46**, 244 (1970), URL `http://ptps.oxfordjournals.org/content/46/244.abstract`.

[20] A. Georges and G. Kotliar, Phys. Rev. B **45**, 6479 (1992), URL `http://link.aps.org/doi/10.1103/PhysRevB.45.6479`.

[21] H. Kajueter, Ph.D. thesis, Rutgers University, New Brunswick (1996).

[22] A. Mart´in-Rodero, F. Flores, M. Baldo, and R. Pucci, Solid State Communications **44**, 911 (1982), URL `http://www.sciencedirect.com/science/article/pii/0038109882903039`.

[23] K. Yamada, Progress of Theoretical Physics **53**, 970 (1975), URL `http://ptp.oxfordjournals.org/content/53/4/970.abstract`.

[24] X. Y. Zhang, M. J. Rozenberg, and G. Kotliar, Phys. Rev. Lett. **70**, 1666 (1993), URL `http://link.aps.org/doi/10.1103/PhysRevLett.70.1666`.

[25] H. Kajueter and G. Kotliar, Phys. Rev. Lett. **77**, 131 (1996), URL `http://link.aps.org/doi/10.1103/PhysRevLett.77.131`.

[26] H. Kajueter, G. Kotliar, and G. Moeller, Phys. Rev. B **53**, 16214 (1996), URL `http://link.aps.org/doi/10.1103/PhysRevB.53.16214`.

[27] M. Potthoff, T. Wegner, and W. Nolting, Phys. Rev. B **55**, 16132 (1997), URL `http://link.aps.org/doi/10.1103/PhysRevB.55.16132`.

[28] T. Wegner, M. Potthoff, and W. Nolting, Phys. Rev. B **57**, 6211 (1998), URL `http://link.aps.org/doi/10.1103/PhysRevB.57.6211`.

[29] L.-F. Arsenault, P. Sémon, and A.-M. S. Tremblay, Phys. Rev. B **86**, 085133 (2012), URL `http://link.aps.org/doi/10.1103/PhysRevB.86.085133`.

[30] A. L. Yeyati, F. Flores, and A. Mart´in-Rodero, Phys. Rev. Lett. **83**, 600 (1999), URL `http://link.aps.org/doi/10.1103/PhysRevLett.83.600`.

[31] A. Liebsch, Phys. Rev. B **70**, 165103 (2004), URL `http://link.aps.org/doi/10.1103/PhysRevB.70.165103`.

[32] M. S. Laad, L. Craco, and E. Müller-Hartmann, Phys. Rev. Lett. **91**, 156402 (2003), URL `http://link.aps.org/doi/10.1103/PhysRevLett.91.156402`.

[33] T. Fujiwara, S. Yamamoto, and Y. Ishii, Journal of the Physical Society of Japan **72**, 777 (2003), URL `http://journals.jps.jp/doi/abs/10.1143/JPSJ.72.777`.

[34] S. Y. Savrasov, V. Oudovenko, K. Haule, D. Villani, and G. Kotliar, Phys. Rev. B **71**, 115117 (2005), URL `http://link.aps.org/doi/10.1103/PhysRevB.71.115117`.

[35] V. Oudovenko, K. Haule, S. Y. Savrasov, D. Villani, and G. Kotliar, unpublished.

[36] E. Gull, A. J. Millis, A. I. Lichtenstein, A. N. Rubtsov, M. Troyer, and P. Werner, Rev. Mod. Phys. **83**, 349 (2011), URL `http://link.aps.org/doi/10.1103/RevModPhys.83.349`.

[37] B. Bauer, L. D. Carr, H. G. Evertz, A. Feiguin, J. Freire, S. Fuchs, L. Gamper, J. Gukelberger, E. Gull, S. Guertler, et al., Journal of Statistical Mechanics: Theory and Experiment **2011**, P05001 (2011), URL `http://stacks.iop.org/1742-5468/2011/i=05/a=P05001`.

[38] H. Barman, Ph.D. thesis, Jawaharlal Nehru Centre for Advanced Scientific Research (2011).

[39] A. L. Fetter and J. D. Walecka, *Quantum Theory Of Many-Particle Systems* (Dover Publications, 2003).

[40] H. Terletska, J. Vučičević, D. Tanaskovi, and V. Dobrosavljević, Phys. Rev. Lett. **107**, 026401 (2011), URL `http://link.aps.org/doi/10.1103/PhysRevLett.107.026401`.

[41] R. Bulla, Phys. Rev. Lett. **83**, 136 (1999), URL `http://link.aps.org/doi/10.1103/PhysRevLett.83.136`.

[42] R. Bulla, T. A. Costi, and D. Vollhardt, Phys. Rev. B **64**, 045103 (2001), URL `http://link.aps.org/doi/10.1103/PhysRevB.64.045103`.

[43] K. Inaba, A. Koga, S.-i. Suga, and N. Kawakami, Phys. Rev. B **72**, 085112 (2005), URL `http://link.aps.org/doi/10.1103/PhysRevB.72.085112`.

[44] P. Zhang, P. Reis, K.-M. Tam, M. Jarrell, J. Moreno, F. Assaad, and A. K. McMahan, Phys. Rev. B **87**, 121102 (2013), URL `http://link.aps.org/doi/10.1103/PhysRevB.87.121102`.

[45] P. A. Lee, N. Nagaosa, and X.-G. Wen, Rev. Mod. Phys. **78**, 17 (2006), URL `http://link.aps.org/doi/10.1103/RevModPhys.78.17`.

[46] M. Z. Hasan and C. L. Kane, Rev. Mod. Phys. **82**, 3045 (2010), URL `http://link.aps.org/doi/10.1103/RevModPhys.82.3045`.

[47] J. Kuneš and V. I. Anisimov, Phys. Rev. B **78**, 033109 (2008), URL `http://link.aps.org/doi/10.1103/PhysRevB.78.033109`.

[48] V. Jaccarino, G. K. Wertheim, J. H. Wernick, L. R. Walker, and S. Arajs, Phys. Rev. **160**, 476 (1967), URL `http://link.aps.org/doi/10.1103/PhysRev.160.476`.

[49] C. Petrovic, Y. Lee, T. Vogt, N. D. Lazarov, S. L. Bud'ko, and P. C. Canfield, Phys. Rev. B **72**, 045103 (2005), URL `http://link.aps.org/doi/10.1103/PhysRevB.72.045103`.

[50] M. Sentef, J. Kuneš, P. Werner, and A. P. Kampf, Phys. Rev. B **80**, 155116 (2009), URL `http://link.aps.org/doi/10.1103/PhysRevB.80.155116`.

[51] A. J. Kim, M. Y. Choi, and G. S. Jeon, Phys. Rev. B **89**, 165117 (2014), URL `http://link.aps.org/doi/10.1103/PhysRevB.89.165117`.

[52] A. E. Antipov, I. S. Krivenko, V. I. Anisimov, A. I. Lichtenstein, and A. N. Rubtsov, Phys. Rev. B **86**, 155107 (2012), URL `http://link.aps.org/doi/10.1103/PhysRevB.86.155107`.

[53] S. Biermann, L. de' Medici, and A. Georges, Phys. Rev. Lett. **95**, 206401 (2005), URL `http://link.aps.org/doi/10.1103/PhysRevLett.95.206401`.

[54] L. de' Medici, Phys. Rev. B **83**, 205112 (2011), URL `http://link.aps.org/doi/10.1103/PhysRevB.83.205112`.

[55] L. de' Medici, J. Mravlje, and A. Georges, Phys. Rev. Lett. **107**, 256401 (2011), URL `http://link.aps.org/doi/10.1103/PhysRevLett.107.256401`.

[56] G. Kotliar, S. Y. Savrasov, K. Haule, V. S. Oudovenko, O. Parcollet, and C. A. Marianetti, Rev. Mod. Phys. **78**, 865 (2006), URL `http://link.aps.org/doi/10.1103/RevModPhys.78.865`.

[57] P. Werner and A. J. Millis, Phys. Rev. Lett. **99**, 126405 (2007), URL `http://link.aps.org/doi/10.1103/PhysRevLett.99.126405`.

[58] E. Pavarini, S. Biermann, A. Poteryaev, A. I. Lichtenstein, A. Georges, and O. K. Andersen, Phys. Rev. Lett. **92**, 176403 (2004), URL `http://link.aps.org/doi/10.1103/PhysRevLett.92.176403`.

[59] E. Pavarini, A. Yamasaki, J. Nuss, and O. K. Andersen, New Journal of Physics **7**, 188 (2005), URL `http://stacks.iop.org/1367-2630/7/i=1/a=188`.

[60] K. Held, Advances in Physics **56**, 829 (2007).

[61] O. Andersen, A. Liechtenstein, O. Jepsen, and F. Paulsen, Journal of Physics and Chemistry of Solids **56**, 1573 (1995), ISSN 0022-3697, proceedings of the Conference on Spectroscopies in Novel Superconductors, URL `http://www.sciencedirect.com/science/article/pii/0022369795002693`.

[62] N. Marzari and D. Vanderbilt, Phys. Rev. B **56**, 12847 (1997), URL `http://link.aps.org/doi/10.1103/PhysRevB.56.12847`.

[63] H. T. Dang, X. Ai, A. J. Millis, and C. A. Marianetti, Phys. Rev. B **90**, 125114 (2014), URL `http://link.aps.org/doi/10.1103/PhysRevB.90.125114`.

[64] P. Blaha, K. Schwarz, G. Madsen, D. Kvasnicka, and J. Luitz, *Computer Code WIEN2k: An Augmented Plane Wave plus Local Orbitals Program for Calculating Crystal Properties (Vienna University of Technology, Vienna, 2001)* (2001).

[65] M. Rey, P. Dehaudt, J. Joubert, B. Lambert-Andron, M. Cyrot, and F. Cyrot-Lackmann, Journal of Solid State Chemistry **86**, 101 (1990), ISSN 0022-4596, URL `http://www.sciencedirect.com/science/article/pii/002245969090119I`.

[66] G. Trimarchi, I. Leonov, N. Binggeli, D. Korotin, and V. I. Anisimov, Journal of Physics: Condensed Matter **20**, 135227 (2008), URL `http://stacks.iop.org/0953-8984/20/i=13/a=135227`.

[67] J. P. Perdew, K. Burke, and M. Ernzerhof, Phys. Rev. Lett. **77**, 3865 (1996), URL `http://link.aps.org/doi/10.1103/PhysRevLett.77.3865`.

[68] K. Jan, R. Arita, P. Wissgott, A. Toschi, H. Ikedaa, and K. Held, Comp. Phys. Commun. **181**, 1888 (2010).

[69] A. A. Mostofi, J. R. Yates, Y.-S. Lee, I. Souza, D. Vanderbilt, and N. Marzari, *Wannier90: A Tool for Obtaining Maximally-Localised Wannier Functions*, Comp. Phys. Commun. **178**, 685 (2008).

[70] H. Ishida, D. Wortmann, and A. Liebsch, Phys. Rev. B **73**, 245421 (2006), URL `http://link.aps.org/doi/10.1103/PhysRevB.73.245421`.

[71] I. A. Nekrasov, G. Keller, D. E. Kondakov, A. V. Kozhevnikov, T. Pruschke, K. Held, D. Vollhardt, and V. I. Anisimov, Phys. Rev. B **72**, 155106 (2005), URL `http://link.aps.org/doi/10.1103/PhysRevB.72.155106`.

[72] F. Lechermann, A. Georges, A. Poteryaev, S. Biermann, M. Posternak, A. Yamasaki, and O. K. Andersen, Phys. Rev. B **74**, 125120 (2006), URL `http://link.aps.org/doi/10.1103/PhysRevB.74.125120`.

[73] N. Parragh, Ph.D. thesis, Universitt Wrzburg (2013).

[74] C. Taranto, M. Kaltak, N. Parragh, G. Sangiovanni, G. Kresse, A. Toschi, and K. Held, Phys. Rev. B **88**, 165119 (2013), URL `http://link.aps.org/doi/10.1103/PhysRevB.88.165119`.

[75] A. Sekiyama, H. Fujiwara, S. Imada, S. Suga, H. Eisaki, S. Uchida, K. Takegahara, H. Harima, Y. Saitoh, I. Nekrasov, et al., Phys. Rev. Lett. **93**, 156402 (2004), URL `http://link.aps.org/doi/10.1103/PhysRevLett.93.156402`.

[76] O. Miura and T. Fujiwara, Phys. Rev. B **77**, 195124 (2008), URL `http://link.aps.org/doi/10.1103/PhysRevB.77.195124`.

[77] A. I. Lichtenstein and M. I. Katsnelson, Phys. Rev. B **57**, 6884 (1998), URL `http://link.aps.org/doi/10.1103/PhysRevB.57.6884`.

Chapter 3

Analytic continuation of hybridization expansion continuous-time quantum Monte-Carlo data using maximum entropy method [*]

3.1 Introduction

Computational methods based on quantum Monte-Carlo (QMC) algorithms are powerful tools to study the properties of interacting quantum many-particle systems. These methods are numerically exact, and they provide data for single and two-particle correlation functions on the Matsubara (imaginary) time or frequency axes. However, experiments measure either single or two particle dynamical quantities like photoemission spectra, transport and nuclear magnetic resonance on the real frequency axis. To get real frequency data from QMC methods, we need to carry out analytic continuation of QMC data from the imaginary to the real frequency axis. The relation between fermionic single particle Green's function and real frequency spectrum ($A(\omega)$) in Matsubara time and frequency[1, 2] is given by

---

[*] Nagamalleswararao Dasari, Juana Moreno, N. S. Vidhyadhiraja and Mark Jarrell, Draft under revision.

$$G(\tau) = \int d\omega A(\omega) K_\tau(\tau, \omega) \tag{3.1}$$

$$G(i\omega_n) = \int d\omega A(\omega) K_n(i\omega_n, \omega)\,, \tag{3.2}$$

where the kernels are given by $K_\tau(\tau, \omega) = e^{-\tau\omega}/(1+e^{-\beta\omega})$ and $K_n(i\omega_n, \omega) = 1/(i\omega_n - \omega)$[2–4]. Obtaining $A(\omega)$ from $G(\tau)$ or $G(i\omega_n)$ amounts to inverting the integrals in equations 3.1 and 3.2. Such an inversion is, however, an ill-posed problem as seen from the following argument. At finite τ and for large frequency ω, the kernel $K_\tau(\tau, \omega)$ in equation 3.1 is exponentially small. This would imply that the high-frequency features of $A(\omega)$ are insensitive to $G(\tau)$. In other words, there exist an infinite number of $A(\omega)$ functions for a given $G(\tau)$ within numerical accuracy and hence the problem of analytic continuation is ill-posed. If we approximate the $G(\tau)$ and $A(\omega)$ in the above equations by equal length vectors and the kernel by a square matrix, we would find that the determinant of K is exponentially small implying that K^{-1} is ill-defined.

Previously, methods such as least square fit, Pade approximation, and regularization have addressed the analytic continuation problem. In case of the least square method, the spectrum is approximated with a set of box functions [3, 4]. By minimizing the least-square misfit between the spectrum and QMC data, we can determine the location and weight of the box functions. For a better resolution of features in the spectrum, if the number of box functions are increased, then the misfit becomes unstable and noisy. In the Pade approximation[5] technique, we fit $G(\tau)$ or $G(i\omega_n)$ to the ratio of two polynomials, which is then analytically continued by replacing $i\omega_n \rightarrow \omega + i0^+$. It works only when the QMC data (i.e. $G(\tau)$ or $G(i\omega_n)$) is very precise or when the fitting function is known *a priori.* In general the Pade approximation method is unreliable. The regularization approach works by regularizing the kernel so that K^{-1} exists[6]. But this method produces a spectrum $A(\omega)$ with features that are overly smeared out by regularization.

In this work, the maximum entropy method (MEM) has been employed for analytic continuation of QMC data. By taking advantage of Bayesian methods, MEM recasts this problem of inversion into that of optimization. In general, a posterior probability [2, 7, 8] of the spectra $P(A \mid G)$ for a given data G is defined. The final analytically continued spectrum is the one that maximizes $P(A \mid G)(\propto P(A)P(G \mid A))$ for a given prior probability $P(A)$. Care must be taken while defining the prior probability function $P(A)$, such that A has only the correlations that are required to reproduce the data G. The likelihood function $P(G \mid A)$ is defined by taking advantage of statistical sampling nature of the QMC process.

Recently developed continuous time Monte-Carlo (CTQMC) algorithms [9–11] have greatly improved our understanding of strongly correlated systems. These algorithms have been used extensively as impurity solvers to study correlated lattice models within the dynamical mean field theory (DMFT)[12] framework. Previously used QMC algorithms like Hirsch-Fye quantum Monte-Carlo (HF-QMC)[13, 14] suffered from sign problems as well as Trotter-decomposition error[15]. Most of the CTQMC algorithms are free from the latter problem although some of them do have the sign problems, but proper tools[9] to handle them do exist. At least in the case of single site DMFT, the CTQMC methods have been performing far better than previous QMC algorithms. In these methods, the Matsubara time action integral is not discretized, so they are free from Trotter-decomposition error. The single and two particle Green's functions are accumulated by using fine equidistant grid called bins[16] for the interval [0,β]. The advantage of such kind of accumulation is, we can measure the Green's functions very efficiently and as we increase the number of grid points(bins) to get smooth data then the performance of algorithm will not be reduced. But the data obtained as such is highly correlated, and is hence useless for MEM. The binning procedure is the standard way of removing correlations, however binning the data during Monte-Carlo simulation time is numerically expensive and it also slow downs the performance of the algorithm. Here, we propose an alternative way to create bins by mapping each bin to a different random seed used in the Markovian chain of the CTQMC algorithm. The bins obtained by each random seed, if used to generate a covariance matrix, is amenable to analytic continuation by MEM. The data for single and two particle quantities thus obtained is used for analytic continuation through the maximum entropy method.

The chapter is organized in the following way: In Section 3.2, we review the technical aspect of maximum entropy method. In sections 3.3 and 3.4 we apply the MEM to analytically continue the single and two particle quantities of single-impurity Anderson model computed through hybridization expansion continuous time quantum MonteCalo (HY-CTQMC). In Section 3.5, we calculate the experimentally observable thermodynamic quantities like the nuclear magnetic relaxation rate(NMR), Knight shift and Korringa ratio. In section 3.6, we discuss the procedure for analytic continuation of data obtained from correlated lattice models. Finally, we conclude the chapter with the summary of our results.

3.2 A brief review of the maximum entropy method (MEM)

3.2.1 Prior probability

As explained in the introduction (below equations 3.1 and 3.2), the exponential nature of the kernel makes the determination of a unique $A(\omega)$ that reproduces the data $G(\tau)$ within numerical error an ill-posed problem. Thus, we can not answer the question – " For a given $G(\tau)$ what is A?". Instead, we can ask –"Given $G(\tau)$, what is the most probable A?". The maximum entropy method can be used to answer this question. This is done by using Bayesian statistics. If we have two events a and

b, then according to Bayes theorem,[17] the joint probability of these two events is,

$$P(a,b) = P(a \mid b)P(b) = P(b \mid a)P(a), \tag{3.3}$$

where $P(a \mid b)$ is the conditional probability for a given b. These probabilities are normalized so that $P(a) = \int dbP(a,b)$ and $1 = \int daP(a)$. As explained before, the MEM transforms the inversion problem to one of optimization. The way this is done is to find the spectrum A, which maximizes the conditional probability $P(A \mid G)$ which is given by,

$$P(A \mid G) = \frac{P(G \mid A)P(A)}{P(G)}. \tag{3.4}$$

In the above equation $P(\bar{G} \mid A)$ is the likelihood function and $P(A)$ is the prior probability of A. $P(G)$ is a constant because we work with one set of QMC data.

For bosonic and fermionic Green's functions, we can define a positive definite unnormalized spectrum, so we can think of it as an unnormalized probability density

$$\int_{-\infty}^{\infty} d\omega A(\omega) < \infty. \tag{3.5}$$

Skilling *et al*[18, 19] argue that the prior probability for such an unnormalized probability density is proportional to $\exp(\alpha S)$ where S is the entropy defined relative to some positive definite function $m(\omega)$, called the default model.

$$S = \int d\omega \left[A(\omega) - m(\omega) - A(\omega)\ln\left(\frac{A(\omega)}{m(\omega)}\right)\right]. \tag{3.6}$$

Now the prior probability is conditional on two unknown quantities m(ω) and α. We can write prior probability as,

$$P(A \mid m\alpha) = \exp(\alpha S). \tag{3.7}$$

We can show very easily that $P(A \mid G, m, \alpha) \propto P(A \mid m, \alpha)$ in the absence of the data G. i.e the optimal A is equal to m.

3.2.2 Likelihood function

We utilize the central limit theorem (CLT) to define a likelihood function. According to the CLT, in the limit of large measurements (N_d), the distribution of G_l^i (where "l" is an integer from 1 to L, and "i" an integer from 1 to N_d) will approach a Gaussian form if each of these measurements are completely uncorrelated. Then the probability of a particular value of G_l is given by,

$$P(G_l) = \frac{1}{\sqrt{2\pi\sigma}} e^{-\frac{\chi^2}{2}}, \tag{3.8}$$

where

$$\chi^2 = \frac{1}{\sigma^2}\left(\frac{1}{N_d}\sum\nolimits_{i=1}^{N_d} G^i{}_l - G_l\right)^2 = \frac{1}{\sigma^2}(\langle G_l\rangle - G_l)^2, \tag{3.9}$$

and

$$\sigma^2 = \frac{1}{N_d(N_d-1)}\sum_i \left(\langle G_l\rangle - G_l^i\right)^2. \tag{3.10}$$

Here the angular bracket indicates an average over the bins of data. Data obtained from QMC simulations are not free from correlations. Correlations exist not only between adjacent measurements G_l^i and G_l^{i+1} but also between errors of data at adjacent time slices G_l^i and G_{l+1}^i. The removal of these correlations is one of the most critical steps in the MEM procedure.

3.2.3 Preparing uncorrelated data

Here, we describe the procedure to quantify and remove the correlations between 'ideally independent' sets of data in general terms. The procedure specific to data obtained from continuous time quantum Monte-Carlo data will be described later in Section 3.4. To know whether the data has correlations between adjacent measurements or not, we plot the histogram of QMC data for all measurements at a given

Matsubara time G_l or frequency $G(i\omega_n)$. Then, we compare the histogram of data with a Gaussian fit. To quantify the deviation of the histogram from Gaussian fit, we measure the moments of the distribution. We calculate the third moment(skewness) and fourth moment (kurtosis) because these are the relevant ones in the present case. Skewness measures the degree of asymmetry around the mean and kurtosis measures the flatness of the distribution about the Gaussian fit. Correlated data has a significant skew and kurtosis. We measure these values about what is expect from a Gaussian distribution, and we will use such relative values. To remove these correlations, we re-bin the data for example by setting G_l^1 equal to the average of 20 measurements, G_l^2 equal to the average of 20 measurements, etc. A priori, we don't know the bin size (average number of measurements). We should take a bin size large enough that we can remove the correlation between bin-averages and at the same time it should be small enough so that we have sufficient number of bins that justify our assumption about probability density of likelihood function. Jarrell et. al.,[2] has described a procedure to find the smallest bin size that yields uncorrelated data. We refer the reader to the above reference.

Once we remove the correlations between adjacent measurements, then only the correlations between errors of the Green's function at adjacent time slices remain. These correlations in Matsubara time are characterized by using covariance matrix,

$$C_{lk} = \frac{1}{N_{bins}(N_{bins}-1)} \sum_{j=1}^{N_{bins}} \left(\langle G_l\rangle - G_l^j\right)\left(\langle G_l\rangle - G_l^k\right). \tag{3.11}$$

According to the central limit theorem, the likelihood function is $P(G \mid A) = \exp(\frac{-\chi^2}{2})$. Here

$$\chi^2 = \sum_{l=1}^{L} \left(\frac{G_l - \sum_j K_{l,j} A_j}{\sigma_l} \right)^2 . \tag{3.12}$$

σ_l^2 represent the diagonal elements of C. In general, the covariance matrix C_{lk} is not diagonal since the errors at different values of τ are correlated. To remove these correlations, we must find the transformation U, which diagonalizes the covariance matrix,

$$U^{-1}CU = \sigma_i^{'2}\delta_{ij}. \tag{3.13}$$

Now we rotate the data and kernel into this diagonal representation $K' = U^{-1}K$, $G' = U^{-1}G$. Then each measurement of G_l' becomes statistically independent in the diagonal representation. In such a diagonal representation, we will define χ^2 as

$$\chi^2 = \sum_l \left(\frac{G_l' - \sum_j K_{l,j}' A_j}{\sigma_l'} \right)^2 . \tag{3.14}$$

To remove correlations between adjacent measurements we re-bin the data with large bin size and many bins are required to calculate the covariance matrix accurately. If we do not have enough bins of data, then the eigenvalue spectrum of the covariance matrix can become pathological, i.e., produce a sharp break. Empirically we find that the number of bins must be chosen such that $N_{bins} \geq 2L$, where L is the number of required independent eigenvectors, to remove the kink in the eigenvalue spectrum.

If we use a small time step in QMC simulations to reduce systematic errors, the QMC data between adjacent times can become highly correlated. In such a case, the covariance matrix becomes ill-conditioned and can not be diagonalized. We resolve this problem by eliminating a fraction of the data from every other time step.

3.2.4 Selection of α

The prior probability $P(A) \propto \exp(\alpha S)$ has a constant α which strongly affects the choice of most probable spectrum because it controls the competition between S and χ^2 in $P(A \mid G, m, \alpha) \propto P(G \mid A, m, \alpha)P(A \mid m, \alpha) = \frac{\exp(\alpha S - \chi^2)}{Z_s Z_L}$. Where Z_s and Z_L are the normalization factors. If α is large, then the entropy term in $P(A \mid G, m, \alpha)$ dominates. In this case, we obtain the spectrum A to be almost similar to the default model m. If α is smaller in $P(A \mid G, m, \alpha)$, then the numerical error in the QMC data starts to dominate, so that the spectra display random oscillations and noise. So care should be taken while selecting α. There are three flavors of MEM based on the selection of α, which will not be discussed here and more details can be found elsewhere[8]. In our calculations, we used Bryan's MEM, which calculates the optimal spectrum $\hat{A}(\alpha)$ for each α. The final solution is,

$$\bar{A} = \int d\alpha \hat{A}(\alpha) P(\alpha \mid Gm). \tag{3.15}$$

where $P(\alpha \mid Gm)$ is the posterior probability of α for given data and model. Even when the data is less precise but still uncorrelated, Bryans method produces more acceptable results and converges to the good results faster than other methods such as classic MEM and historic MEM[8]. Care has to be taken while using Bryan's method, because we calculate $P(\alpha \mid Gm)$ using a Gaussian approximation. If this approximation fails, calculations tend towards a smaller value of α. We can easily identify this situation during the simulations and can resolve this by increasing the quality of data or by choosing a better default model.

3.2.5 Default model selection

Here again we take advantage of Bayesian statistics to select the default model. One can prepare different default models based on set of parameters used to define the model. But we select a model based on its posterior probability which is given by,

$$P(m \mid G) = \int d\alpha P(\alpha \mid G) P(m). \tag{3.16}$$

Since the prior probability of the model $P(m)$ is unknown, $P(m \mid G)$ determines only the relative probability of one default model over the other. The best default model is the one that has largest posterior probability by assuming that $P(m)$ is flat. One can try very informative models such as spectrum with sharp distinct features. Such default models often have large posterior probabilities $P(m \mid G)$. However such informative models should be avoided unless the sharp features in the spectrum are certain and real.

3.2.6 Annealing method

A default model may be obtained from perturbation theory at high temperature. The spectrum obtained at that temperature through analytic continuation serves as a default model for a lower temperature. Such a procedure has a strong physical motivation. At high temperatures, the perturbation theory becomes exact so we initiate the annealing procedure with exact results. As we cool the system we expect that the high-frequency features of the spectrum to freeze out. Thus, we required QMC to provide low-frequency information or features of the spectrum. QMC is a statistical sampling procedure, according to Nyquist theorem, QMC data has information only below the Nyquists frequency $\omega_N = \frac{\pi}{\Delta\tau}$. Thus, perturbation theory provides high-frequency information and QMC provides the low frequency information enabling MEM to be a natural choice to treat both low and high frequency information in the spectra. Till now, we have discussed the standard procedure of binning, quantifying QMC data and selection of the default model. Now we are going to present relation between different dynamical correlation functions with their spectral functions in the context of single-impurity Anderson model. Later we will show our results of MEM obtained from CTQMC data along with our new binning procedure.

3.3 Model and formalism

The effective action for a single impurity Anderson model (SIAM) is given by[11],

$$S_{eff} = -\int\int_0^\beta d\tau d\tau' \sum_\sigma c^\dagger_{0\sigma}(\tau)\mathcal{G}^0(\tau-\tau')^{-1} c_{0\sigma}(\tau') + \int_0^\beta d\tau U n_{0\uparrow}(\tau) n_{0\downarrow}(\tau)\,, \quad (3.17)$$

where $\mathcal{G}^0(\tau-\tau')$ is the time dependent bare Green's function, which in Matsubara frequency is given by

$$\mathcal{G}^0(i\omega_n) = \frac{1}{i\omega_n + \mu - \Delta(i\omega_n)}\,, \quad (3.18)$$

where $\Delta(i\omega_n)$ is the hybridization function given by,

$$\Delta(i\omega_n) = \sum_k \frac{{V_k}^2}{i\omega_n - \epsilon_k} = \int d\epsilon \frac{V^2 D^0(\epsilon)}{i\omega_n - \epsilon}\,, \tag{3.19}$$

and $V_k = V\ \forall k$ is the hybridization matrix element and $D^0(\epsilon) = \sum_k \delta(\epsilon - \epsilon_k)$ is the host/bath density of states[1, 20]. In this work, we consider a flat band host of half-band width, D=2t and V = t = 1 define the units. The SIAM can be solved by using the CTQMC solver and subsequently be used to measure observables like the Green's functions[11],

$$G(\tau - \tau^{'}) = -\langle T_\tau c(\tau) c^\dagger(\tau')\rangle_{S_{eff}} \tag{3.20}$$

by using the effective action defined in equation 3.17. We used hybridization expansion continuous-time quantum Monte-Carlo(CTQMC) solver for these calculations. We analytically continue the single and two particle Greens' functions on to the real frequency axis by using maximum entropy method. Here we used annealing method to ensure robustness with respect to an ambiguity in the choice of default models and to capture low energy scales properly. Throughout the chapter, we have done MEM calculations in Matsubara frequency space.

3.3.1 Single particle quantities

We describe the procedure of analytic continuation for the self-energy below. In QMC methods, we calculate the self-energy $\Sigma(i\omega_n)$ from the Dyson equation which is given by $\Sigma(i\omega_n) = \mathcal{G}^{-1}(i\omega_n)$ - $G^{-1}(i\omega_n)$. The bare and interacting Green's function ($\mathcal{G}$, G) obtained from QMC methods always has statistical and systematic errors and the coefficient of $1/i\omega_n$ of Green's functions are not equal to -1. Then the linear coefficient of the imaginary part of self-energy in the Dyson equation diverges when $i\omega_n \to \infty$. Thus, the imaginary part of self-energy obtained from QMC methods do not have correct high-frequency behavior. In the MEM procedure we ensure the high-frequency behavior of self-energy on real frequency axis from high-frequency moments of $\Sigma(i\omega_n)$. The high-frequency expansion of self-energy in Matsubara frequency[21, 22] is given by,

$$\Sigma(i\omega_n) = \Sigma_H + \frac{\Sigma_1}{i\omega_n} + O((i\omega_n)^{-2}). \tag{3.21}$$

where the expansion coefficients in case of single orbital are given by,

$$\Sigma_H = U\langle n\rangle\,, \tag{3.22}$$

$$\Sigma_1 = U^2\langle n\rangle(1 - \langle n\rangle)\,. \tag{3.23}$$

The expansion coefficients for models with multiple orbitals are discussed in other works[11]. Now we define a new quantity to ensure correct high-frequency behavior of self energy on real frequency axis and for normalized spectrum, which is given by,

$$\Sigma^{''}(i\omega_n) = \frac{\Sigma(i\omega_n) - \Sigma_H}{\Sigma_1}\,. \tag{3.24}$$

The relation between $\Sigma^{''}(i\omega_n)$ and the real frequency spectrum is given by,

$$\Sigma^{''}(i\omega_n) = \int \frac{D^{''}(\omega)d\omega}{i\omega_n - \omega}\,, \tag{3.25}$$

where D$^{''}(\omega)$= $-\frac{1}{\pi}\text{Im}\Sigma^{''}(\omega)$ is non-negative and normalized to one.

$$\int -\frac{1}{\pi}\text{Im}\Sigma^{''}(\omega)d\omega = 1 \tag{3.26}$$

Instead of dealing with the self-energy directly, we analytically continue the ‘Hartree corrected’ and high-frequency treated quantity in equation 3.24. Subsequent to obtaining $D^{''}(\omega)$ using MEM, it is straight forward to get the real part of self energy using the Kramers-Krönig relation,

$$\mathrm{Re}\,\Sigma(\omega) = \Sigma_1 \int \frac{D''(\omega')d\omega'}{\omega - \omega'} + \Sigma_H \,. \tag{3.27}$$

Finally, the spectral function of the impurity may be computed using,

$$A(\omega) = \frac{-1}{\pi}\mathrm{Im}\left[\frac{1}{\omega^+ + \mu - \Delta(\omega) - \Sigma(\omega)}\right]. \tag{3.28}$$

3.3.2 Two particle quantities

Within linear response theory the spectral functions of two particle Green's functions[23, 24] can be related to the experimentally measured quantities. Calculation of two particle quantities is one of the most challenging tasks because these measurements take a lot of computational time and lack of perturbative theory calculations makes analytical continuation more difficult. Nevertheless, these quantities give more detailed information about the system. For example, materials like FeSi, FeSb_2 exhibit a charge gap, but they do not have a spin gap[25]. So, by computing spin and charge susceptibilities, one can find spin and charge gaps. In our calculations, we have implemented analytic continuation for two particle quantities related to impurity.

CTQMC impurity solver measures impurity two-particle correlation function $\chi(\tau) = \langle S_z(\tau)S_z(0)\rangle$. By using MEM, we have calculated the dynamical spin susceptibility $\chi(\omega) = \chi'(\omega) + i\chi''(\omega)$. The relation between the $\chi(\tau)$ and $\chi(\omega)$ is given by Hilbert transform[8, 26],

$$\chi(i\nu_n) = \int_0^\beta d\tau e^{i\nu_n\tau}\chi(\tau) = \int_{-\infty}^{\infty} \frac{\chi''(\omega)}{i\nu_n - \omega}d\omega \,. \tag{3.29}$$

The above bosonic spectral function is anti-symmetric, so we will make it symmetric by redefining it in the following way,

$$\chi(i\nu_n) = \int_{-\infty}^{\infty} \frac{\omega^2 A(\omega)}{\nu_n^2 + \omega^2}d\omega \,. \tag{3.30}$$

Because $A(\omega) = \frac{\chi^{''}(\omega)}{\omega}$ is a symmetric function, only the real part of $\chi(i\nu_n)$ survives. Although the above spectral function is a positive definite quantity, it is not normalized. This can be done using spectral moments. As mentioned earlier, an absence of perturbative theories for use as default models leads us to use an alternative procedure developed by Jarrell et.al.[8], which is again based on moment expansion. The moments used for generating the default model are,

$$\frac{1}{2}\chi(\omega = 0) = \int_0^\infty d\omega \frac{\chi^{''}(\omega)}{\omega}\,, \tag{3.31}$$

$$\chi(\tau = 0) = \int_0^\infty d\omega \frac{\chi^{''}(\omega)}{\omega}\omega \coth(\frac{\beta\omega}{2})\,. \tag{3.32}$$

These moments used as constraints to the principle of maximum entropy. By maximizing the entropy in addition to the above mentioned two conditions in equation 3.32 with Lagrangian multipliers λ_0 and λ_1 we obtain default model, given by

$$m(\omega) = e^{\left[\lambda_0 + \lambda_1 \omega \coth(\frac{\beta\omega}{2})\right]}\,. \tag{3.33}$$

The model generated above is normalized by scaling the dynamical susceptibility by $\chi(\omega = 0)$, given by (using equation 3.29)

$$\chi(i\nu_n = 0) = \int_{-\infty}^{\infty} \frac{\chi^{''}(\omega)}{\omega} d\omega = \chi(\omega = 0)\,. \tag{3.34}$$

Thus, the normalized spectrum dynamical spin susceptibility spectrum $\tilde{A}(\omega)$ is given by inverting the following equation:

$$\frac{\chi(i\nu_n)}{\chi(\omega = 0)} = \int_{-\infty}^{\infty} \frac{\omega^2 \tilde{A}(\omega)}{\nu_n^2 + \omega^2} d\omega\,. \tag{3.35}$$

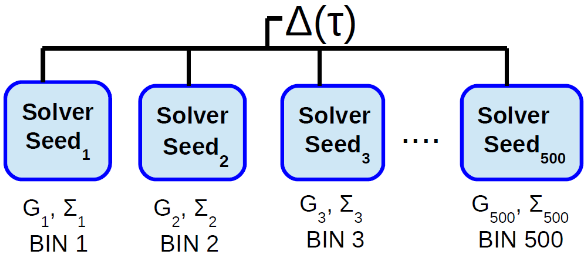

Figure 3.1: (color online) Schematic of the binning procedure for impurity problem.

3.4 Results and discussion

3.4.1 Binning in CTQMC

As we mentioned before, the proper preparation of uncorrelated QMC data is the most critical step in MEM procedure. Because of the way we are accumulating the Green's function to get efficient measurements and for good performance of algorithm we observe that CTQMC data on Matsubara time is highly correlated. We will come back to this point at a later stage. The procedure we use to get binned data is the following, we prepare say N (in practice, about $500 - 1000$) input files for the SIAM, each with a distinct random seed. Then a CTQMC solver is initiated for each input file as a single process. The data set obtained from each input file (for each random seed) is treated as a single bin of data. The number of measurements we have done for each bin is about 1000. The number of measurements has to be chosen carefully and they should be neither too large nor too small. The reason for the latter is obvious, namely, the data would be so noisy that making any sense of it would be impossible. The former is however a subtle point. Normally, one would assume that a larger number of measurements would yield a lower noise to signal ratio. However, the downfall of making a very large number of measurements, especially for MEM, is that the stochastic errors become very small, even smaller than systematic errors. This naturally leads to a breakdown of the Gaussian assumptions in the MEM procedure. Namely, that in MEM, we need to normalize likelihood function P(G|A) and P(A|α m) to locate most likely spectrum $\hat{A}$ and the value of α. It will be done by Gaussian approximate to the integrals so we require that the errors should also have a Gaussian distribution. But the systematic errors do not have such distribution, which results in spurious features appearing in the spectrum. Once we obtain the binned data in this procedure (as shown in figure 3.1), we test the quality of data by using different techniques as mentioned Section 3.2. In our procedure we always ensure that the binned data has a Gaussian distribution. We have confirmed it by measuring the skew and kurtosis, which are very small ($\sim 10^{-1}$ to 10^{-2}). We then calculate the covariance matrix from equation 3.11 and the number of data points we used to calculate covariance matrix should satisfy empirical relation $N_{bins} \geq 2L$, where L is the number of data points otherwise the eigenvalue spectrum of the covariance matrix can become pathological, i.e., produce a sharp break[8]. We observe that the off-diagonal elements of the covariance matrix are, in general, non zero implying that data at different times are correlated. To remove these correlations, we diagonalize the covariance matrix followed by rotating the kernel and data into this diagonal space. In the literature, we observe that the diagonalization and rotation steps have been avoided in many works by assuming that the off-diagonal elements are very small, but this is really a crucial step, without which the features in the spectra may not be reliable.

With the aforementioned considerations, we compute the covariance matrix for the Green's function in Matsubara time as well as the self-energy in Matsubara frequency, which are then diagonalized. Figures 3.2(a) and 3.2(b) show the square root of eigenvalues(σ_L) of the covariance matrices of $G(\tau)$ and $\Sigma(i\omega_n)$ respectively, as a function of matrix index L independent eigen vectors for $\beta = 4$ and $\frac{U}{W} = 1.0$. In our calculations we used 1000 bins of data and at $\beta = 4$ the number of data points (L) we have considered for $G(\tau)$ is 28 and for $\Sigma(i\omega_n)$ is 10, which are satisfying the empirical relation $N_{bins} \geq 2L$ to avoid pathology in the eigenvalue spectrum of the covariance matrix. In case of $G(\tau)$ (see figure 8.1(a)) still we encountered a sharp break in the eigenvalue spectrum of covariance matrix while it is absent in case

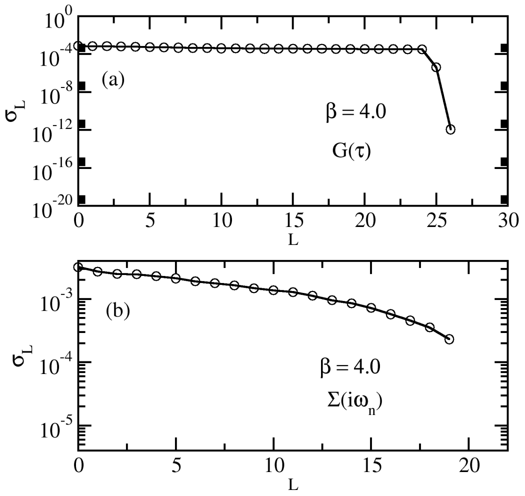

Figure 3.2: Square root of eigen values of the covariance matrix obtained from (a) Matsubara time Green's function and (b) Matsubara frequency self-energy for $U/W = 1$ and $\beta = 4$.

of $\Sigma(i\omega_n)$ and shown in figure 8.1(b). As we mentioned in Section 3.2, to remove pathology in the eigenvalue spectrum of the covariance matrix, we need to increase the number of bins. We increased the number of bins for $G(\tau)$ then calculated the covariance matrix and even with an increase of bins we could not able to remove sharp break in the eigenvalue spectrum of covariance matrix. It seems to us this is an inherent problem of continuous-time QMC data on Matsubara time because these algorithms do not require discretization of action on Matsubara time. To confirm it further, we diagonalize the covariance matrix obtained from Matsubara frequency Green's function. The eigenvalue spectrum not shown here, but interestingly, the sharp break observed in Matsubara time, was not found in this case. Such a sharp break is indicative of correlations within data. Hence, we believe that the presence of a sharp break in the imaginary time data is because the Green's functions are being accumulated in Matsubara time, which makes the corresponding data at adjacent times highly correlated.

To get binned data and covariance matrix for two particle quantities, we use the same procedure as that for single particle quantities. Figures 3.3(a) and (b) show

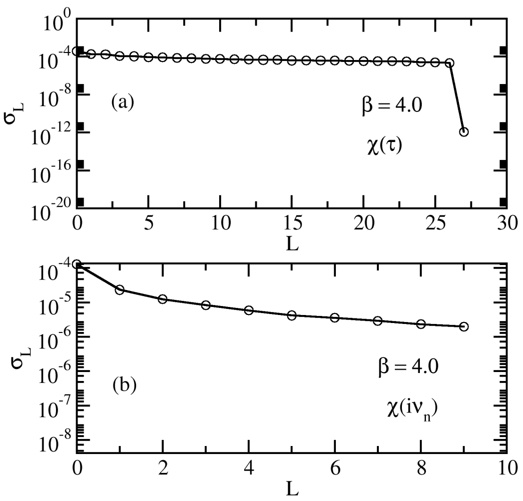

Figure 3.3: Square root of eigen values of the covariance matrix obtained from (a) Matsubara time two particle correlation function and (b) Matsubara frequency two particle correlation function.

the square root of eigenvalues of the covariance matrix obtained from two-particle correlation function in Matsubara time and frequency respectively at β=4.0 and $\frac{U}{W}$ = 1.0. As observed in the case of single particle quantities, a kink is found in the eigenvalue spectrum of the Matsubara time data, which could not be removed by rebinning or increasing the number of bins. Hence, we have carried out MEM in Matsubara frequency for two particle quantities as well.

In the next two subsections, we consider the half-filled and doped cases of the single-impurity Anderson model (equation 3.17). We have implemented the maximum entropy method as detailed above for single and two-particle quantities.

3.4.2 Half-filling case

In the particle-hole symmetric case of the single impurity Anderson model(SIAM), the annealing procedure (section 3.2.6) in MEM is initiated with a Gaussian default model. In figure 3.4(a) we show the impurity self-energy for various temperatures.

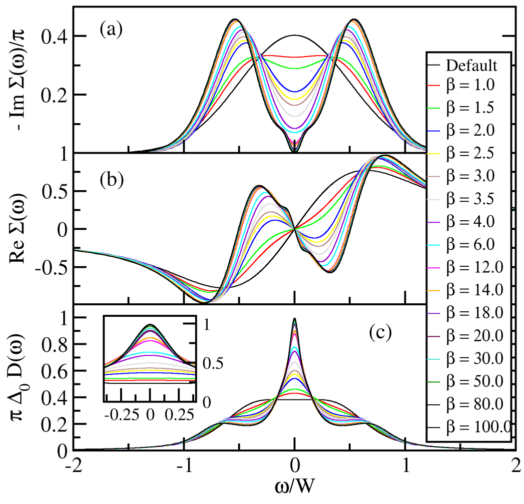

Figure 3.4: (color online) (a) Imaginary part of the analytically continued self energy on real frequency axis for different β and $U/W = 1$ (b) Real part of self energy on real frequency axis and (c) the impurity spectral function for same parameters as (a). ($\Delta_0 = \frac{\pi V^2}{W}$= 0.7853)

As we cool the system, we can see that the high energy features remain unaffected, and spectral weight transfers occur at progressively lower energy scales. Figure 3.4(b) shows the real part of self-energy obtained by a Kramers-Kr$\ddot{o}$nig transformation of the imaginary part of self-energy. The bottom panel of figure 3.4 is the corresponding temperature dependent single-particle spectral function. In figure 3.4(a) & 3.4(b), the evolution of low energy features is not clear but it is clearly visible in the single-particle spectral function. At high-temperatures the single-particle spectral function is broad and featureless as must be expected. As we cool the system, a three peak structure emerges; two symmetrical Hubbard bands at $\omega \sim \pm U/2$ and a central Abrikosov-Suhl(AS) resonance at the Fermi level ($\omega = 0$). The two Hubbard bands corresponds to local quasi-particles with lifetime $\sim \frac{\hbar}{2\Delta_0}$ ($\Delta_0 = \frac{\pi V^2}{W}$), which describes the behaviour of additional electron in the localized state. In strong coupling, the width of the central peak is proportional to Kondo temperature (T_K) which corresponds to the low energy spin-flip excitations in the system. If we do not eliminate the correlations in the CTQMC data, there will be glitches in the low energy part of the spectrum, which are clearly absent here (see inset of figure 3.4(c) for better visibility) for the properly prepared data.

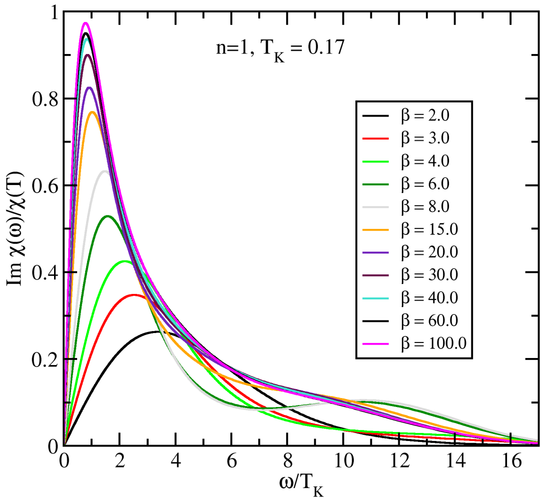

Figure 3.5: (color online) Imaginary part of dynamical spin susceptibility on real frequency axis for different β and $U/W = 1$.

The dynamical susceptibility has been obtained using the annealing method described in section 3.2.6. As a consistency check, a default model given by Salomaa (for the resonant level model) was also employed for the MEM. We observe that both methods yield similar spectral features. We present results obtained from the annealing method in figure 3.5, where the imaginary part of dynamical spin susceptibility for various temperatures at $U/W = 1$ and $n = 1$ is shown. At high temperature, the spectral function Im$\chi(\omega)$ has a broad peak whose maximum is $\sim \omega/T_K \sim 3-4$ and there is almost no spectral weight at high frequencies. With decreasing temperature, the single broad maximum observed at high temperature splits into two: a low and high frequency peak. The latter acquires greater spectral weight with decreasing T and remains broad, while the former becomes sharper. As $T \to 0$, the low frequency peak position is at $\omega \sim 0.67T_K$, and its width is also proportional to the Kondo scale. Such behaviour can be used to extract the low energy scale from a computed or measured dynamical susceptibility.

3.4.3 Doped case

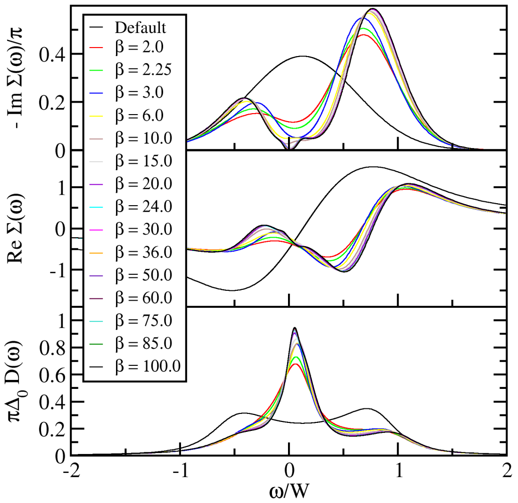

Figure 3.6: (color online) (a) Imaginary part of self energy on real frequency axis for different β and $U/W = 1.0$ (b) Real part of self energy and (c) impurity spectral functions for same parameters as (a). ($\Delta_0 = \frac{\pi V^2}{W}$= 0.7853)

Now, we consider the SIAM away from particle-hole symmetry at a filling of $n = 0.83$. Again, the annealing procedure in MEM is initiated with an asymmetric Gaussian default model which is given by $\mathrm{m}(\omega) = \frac{1}{\pi\sqrt{\gamma}}\exp[-(\frac{\omega-\epsilon_d}{\gamma})^2]$. In figure 3.6, we show the self-energy and single-particle spectral function at $\frac{U}{W} = 1.0$ for different temperatures. As observed in the symmetric case, the high temperature spectrum is broad and featureless, while at low T, a three peak structure emerges. The Hubbard band below the Fermi level is quite close to the central AS resonance, while the upper Hubbard band is asymmetrically placed and distinct.

In figure 3.7, shows the imaginary part of dynamic spin susceptibility for different temperatures at $U/W = 1$ and $n = 0.83$. Although the value of the Kondo scale is much higher as compared to the symmetric case, the frequency and temperature dependence of the $\mathrm{Im}\chi(\omega)$ is very similar, hence the low frequency peak, may be

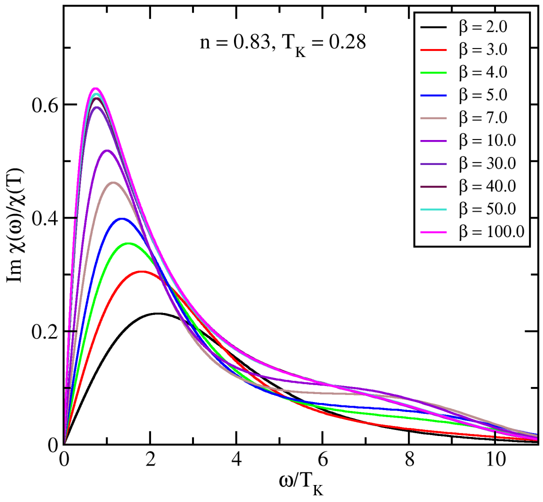

Figure 3.7: (color online) Imaginary part of dynamical spin susceptibility on real frequency axis for different β and $U/W = 1$.

used, in general to obtain information about the coherence scale in the system. In the next section, we use the dynamical susceptibilities calculated in this and the previous sub-sections to compute experimental observables such as the nuclear magnetic relaxation rate, Knight shift and the Korringa ratio.

3.5 Thermodynamic observables: NMR, Knight shift and Korringa ratio

The computation of dynamical susceptibility, $\chi(\omega) = \chi^{'}(\omega) + i\chi^{''}(\omega)$, allows us to predict experimentally observable quantities such as the nuclear magnetic relaxation rate (NNMR)($\frac{1}{T_1T}$), Knight shift(K_s) and Korringa ration(κ) through the following expressions[27, 28]:

$$\frac{1}{T_1T} = \frac{2K_B|\tilde{A}|^2}{\gamma_e^2\hbar^4}\lim_{\omega\to 0}\frac{\chi^{''}(\omega)}{\omega}\,, \tag{3.36}$$

$$K_s = \frac{|\tilde{A}|\chi^{'}(0)}{\gamma_e\gamma_N\hbar^2}\,, \tag{3.37}$$

$$\kappa = \frac{\hbar}{4\pi K_B}\left(\frac{\gamma_e}{\gamma_N}\right)^2\frac{1}{T_1TK_s^2}\,. \tag{3.38}$$

In the above equations, γ_N (γ_e) is the nuclear (electronic) magnetic moment and $\tilde{A}$ is hyperfine coupling constant, which is assumed to be momentum independent. $\chi^{'}(0)$ is the real part of local dynamical spin susceptibility obtained from Kramers-Kr$\ddot{o}$nig transformation of imaginary part of local dynamical spin susceptibility. We can show very easily that it is nothing but the local static susceptibility($\chi_{loc}(T)$).

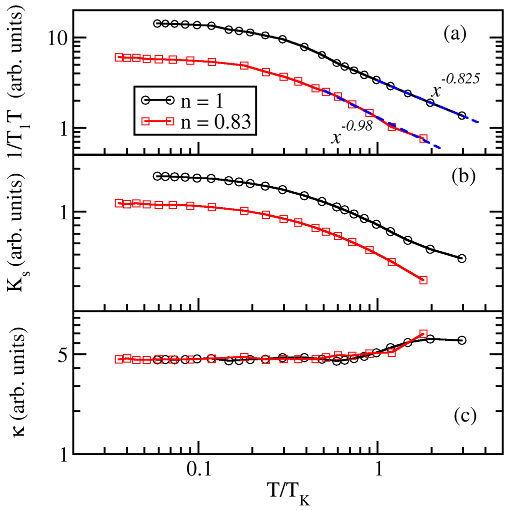

Figure 3.8: (color online) (a) Nuclear magnetic relaxation rate (b) Knight shift and (c) Korringa ratio at $U/W = 1$ and for $n = 1, 0.83$.

In figure 3.8(a), we show the NMR rate as a function of $\frac{T}{T_K}$, at $\frac{U}{W} = 1.0$ for particle-hole symmetric and asymmetric cases. We observe that NMR is proportional to $\frac{1}{T^\alpha}$ at high-temperatures in the local moment region where $\alpha \sim 1$ (see power law fit in figure 3.8(a)) and with decreasing temperature becomes independent of temperature in the Kondo singlet region. The fluctuating field due to impurity spin couples to the probe nuclear spin represents a relaxation mechanism and hence T_1 is finite in the local moment region. With decreasing T, the local moment is screened and hence the probe spin does not relax, and hence T_1 diverges. The Knight shift measures the response of such a fluctuating local moment to the external field is simply proportional to the local impurity susceptibility. Indeed, the behavior of the Knight shift presented in figure 3.8(b) is very similar to that of the NMR. The Korringa ratio shown in figure 3.8(c) should be independent of temperature in the Kondo region as expected from the exact result derived by Shiba for the single impurity Anderson model[29].

3.6 MEM for real materials: $SrVO_3$

Until now, we have done MEM calculations for a simple model, namely the SIAM. The procedure we have implemented to get binned data for the impurity problem can also be used for lattice problems using the framework of DMFT. Here we demonstrate the implementation of MEM for analytic continuation of CTQMC data obtained through a first principles calculation using density functional theory (DFT)+DMFT. Details about DFT+DMFT procedure can be found elsewhere in the literature[30–33]. Here, we follow the method described in our recent work on the multi-orbital iterative perturbation theory[33].

The method has been described briefly below. First we have done DFT calculations for $SrVO_3$ within the generalized gradient approximation using the plane wave pseudo-potential code QUANTUM ESPRESSO[34]. A low energy window near the Fermi-level in the band structure is chosen using which maximally localized Wannier orbitals[35] are constructed within the energy window by using projection technique[32]. The low-energy effective Hamiltonian H(k) in the Wannier basis is computed using Wannier 90. Local electronic correlation are treated within DMFT using CTQMC. To get binned data from DFT+DMFT, we have taken the bath

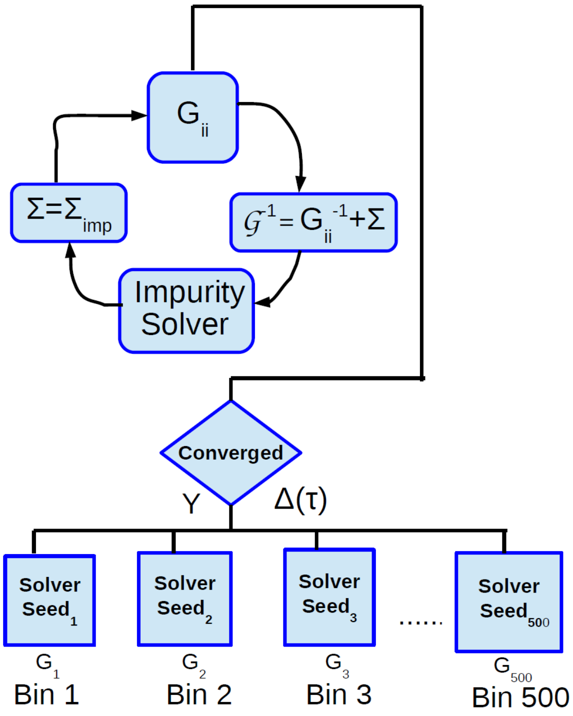
G_ii
𝒢^-1 = G_ii^-1 + Σ
Impurity Solver
Σ=Σ_imp
Converged
Y
Δ(τ)
Solver Seed_1
Solver Seed_2
Solver Seed_3
......
Solver Seed_500
G_1
Bin 1
G_2
Bin 2
G_3
Bin 3
G_500
Bin 500

Figure 3.9: (color online) Schematic of the binning procedure for lattice problem.

Green's function from the last iteration of the DFT+DMFT converged loop. Then a single DMFT iteration is executed on 1000 single processors with distinct random seeds. Once the binned data as shown in figure 3.9 is obtained, we proceed further to check the quality of data. We have used a spectrum obtained from MO-IPT as the default model, instead of finding it from the annealing procedure. In figure 3.10, we show the MEM spectrum obtained from DFT+DMFT(HY-CTQMC) at $\beta = 40$ eV^{-1} by using default model obtain from MO-IPT. Our MEM calculations successfully reproduce the features in the spectra at all energy scales.

3.7 Conclusions

Continuous time quantum Monte-Carlo methods are powerful tools for studying quantum impurity problems. For efficient measurements, CTQMC algorithms accumulate the Green's functions on a fine grid of Matsubara time for the interval of [0,β]. Such an accumulation procedure yields highly correlated data in Matsubara

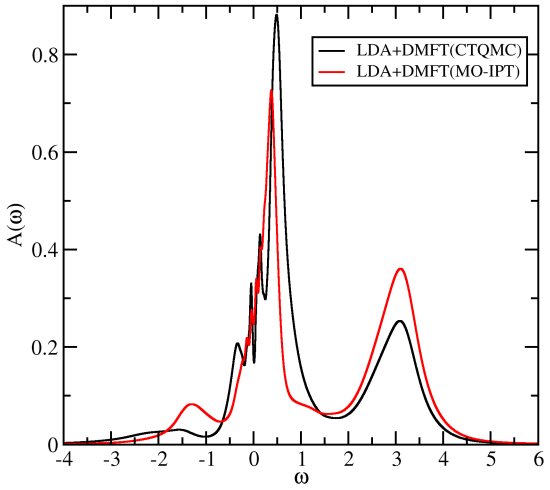

Figure 3.10: (color online) MEM spectrum obtained from DFT+DMFT(HY-CTQMC) data (using MO-IPT as a default model) for $\mathrm{SrVO_3}$ at $U = 3.4$ eV, $J = 0.44$ eV and $\beta = 40\ \mathrm{eV}^{-1}$.

time. We show that uncorrelated data may be obtained by mapping the random seeds used for initiating the Markov process to a bin and using imaginary frequency data rather than imaginary time. A somewhat subtle issue is the choice of number of measurements, which should neither be too low which will result in incorrect data, nor too high, because the systematic error will then dominate over the stochastic error, and hence the maximum entropy method cannot be applied. The implemented MEM for single and two particle quantities of SIAM and real material $\mathrm{SrVO_3}$ exhibit well known features and for the latter, compare well with other theories.

Bibliography

[1] J. E. Gubernatis, M. Jarrell, R. N. Silver, and D. S. Sivia, Phys. Rev. B **44**, 6011 (1991), URL `http://link.aps.org/doi/10.1103/PhysRevB.44.6011`.

[2] M. Jarrell and J. E. Gubernatis, Physics Reports **269**, 133 (1996).

[3] H. B. Schüttler and D. J. Scalapino, Phys. Rev. Lett. **55**, 1204 (1985), URL `http://link.aps.org/doi/10.1103/PhysRevLett.55.1204`.

[4] H. B. Schüttler and D. J. Scalapino, Phys. Rev. B **34**, 4744 (1986), URL `http://link.aps.org/doi/10.1103/PhysRevB.34.4744`.

[5] H. Vidberg and J. Serene, Journal of Low Temperature Physics **29**, 179 (1977), ISSN 0022-2291, URL `http://dx.doi.org/10.1007/BF00655090`.

[6] G. Wahba, SIAM Journal on Numerical Analysis **14**, 651 (1977), `http://dx.doi.org/10.1137/0714044`, URL `http://dx.doi.org/10.1137/0714044`.

[7] C. Huscroft, R. Gass, and M. Jarrell, Phys. Rev. B **61**, 9300 (2000), URL `http://link.aps.org/doi/10.1103/PhysRevB.61.9300`.

[8] E. Pavarini, E. Koch, F. Andres, and M. Jarrell, *Correlated Electrons: From Models to Materials* (Forschungszentrum Julich Gmbh, Institute of Advanced Simulation, 2012), vol. 2, chap. The Maximum Entropy method: Analytic Continuation of QMC Data, pp. 13.0–13.29.

[9] A. N. Rubtsov, V. V. Savkin, and A. I. Lichtenstein, Phys. Rev. B **72**, 035122 (2005), URL `http://link.aps.org/doi/10.1103/PhysRevB.72.035122`.

[10] E. Gull, A. J. Millis, A. I. Lichtenstein, A. N. Rubtsov, M. Troyer, and P. Werner, Rev. Mod. Phys. **83**, 349 (2011), URL `http://link.aps.org/doi/10.1103/RevModPhys.83.349`.

[11] E. Gull, Ph.D. thesis, ETH ZURICH (2008).

[12] A. Georges, G. Kotliar, W. Krauth, and M. J. Rozenberg, Rev. Mod. Phys. **68**, 13 (1996), URL `http://link.aps.org/doi/10.1103/RevModPhys.68.13`.

[13] J. E. Hirsch and R. M. Fye, Phys. Rev. Lett. **56**, 2521 (1986), URL `http://link.aps.org/doi/10.1103/PhysRevLett.56.2521`.

[14] R. M. Fye and J. E. Hirsch, Phys. Rev. B **38**, 433 (1988), URL `http://link.aps.org/doi/10.1103/PhysRevB.38.433`.

[15] K. Mikelsons, A. Macridin, and M. Jarrell, Phys. Rev. E **79**, 057701 (2009), URL `http://link.aps.org/doi/10.1103/PhysRevE.79.057701`.

[16] E. Gull, H. Hafermann, and P. werner, *Documentation - Hybridization Expansion CT-QMC solver version 3.0b1* (2009).

[17] A. Papoulis, *Probability and statistics* (Prentice Hall, 1989), 1st ed.

[18] J. Skilling, *Maximum Entropy and Bayesian Methods* (Kluwer Academic, 1989).

[19] S. F. Gull and J. Skilling, IEE proceedings pp. 646–659 (1984).

[20] M. Jarrell, J. E. Gubernatis, and R. N. Silver, Phys. Rev. B **44**, 5347 (1991), URL `http://link.aps.org/doi/10.1103/PhysRevB.44.5347`.

[21] S. Fuchs, E. Gull, M. Troyer, M. Jarrell, and T. Pruschke, Phys. Rev. B **83**, 235113 (2011), URL `http://link.aps.org/doi/10.1103/PhysRevB.83.235113`.

[22] *The maximum entropy method*, URL `http://www.institute.loni.org/lasigma/document_files/int_seminarseries2011/MEMPrimer.pdf`.

[23] E. Pavarini, *DMFT at 25: Infinite Dimensions* (Forschungszentrum Julich Gmbh, Institute of Advanced Simulation, 2014), vol. 2, chap. Linear Response Functions, pp. 13.0–13.29.

[24] *Linear response functions*, URL `http://www.cond-mat.de/events/correl14/manuscripts/pavarini.pdf`.

[25] M. Sentef, J. Kuneš, P. Werner, and A. P. Kampf, Phys. Rev. B **80**, 155116 (2009), URL `http://link.aps.org/doi/10.1103/PhysRevB.80.155116`.

[26] O. Gunnarsson, M. W. Haverkort, and G. Sangiovanni, Phys. Rev. B **82**, 165125 (2010), URL `http://link.aps.org/doi/10.1103/PhysRevB.82.165125`.

[27] E. Yusuf, B. J. Powell, and R. H. McKenzie, Phys. Rev. B **75**, 214515 (2007), URL `http://link.aps.org/doi/10.1103/PhysRevB.75.214515`.

[28] A. C. Hewson, *The Kondo Problem to Heavy Fermions* (Cambridge University Press, 1993), chap. Theory and Experiment, pp. 233–312.

[29] H. Shiba, Progress of Theoretical Physics **54**, 967 (1975), `http://ptp.oxfordjournals.org/content/54/4/967.full.pdf+html`, URL `http://ptp.oxfordjournals.org/content/54/4/967.abstract`.

[30] G. Kotliar, S. Y. Savrasov, K. Haule, V. S. Oudovenko, O. Parcollet, and C. A. Marianetti, Rev. Mod. Phys. **78**, 865 (2006), URL `http://link.aps.org/doi/10.1103/RevModPhys.78.865`.

[31] N. Parragh, Ph.D. thesis (2013).

[32] F. Lechermann, A. Georges, A. Poteryaev, S. Biermann, M. Posternak, A. Yamasaki, and O. K. Andersen, Phys. Rev. B **74**, 125120 (2006), URL `http://link.aps.org/doi/10.1103/PhysRevB.74.125120`.

[33] N. Dasari, W. R. Mondal, P. Zhang, J. Moreno, M. Jarrell, and N. Vidhyadhiraja, arXiv preprint arXiv:1504.04097 (2015).

[34] P. Giannozzi, S. Baroni, N. Bonini, M. Calandra, R. Car, C. Cavazzoni, D. Ceresoli, G. L. Chiarotti, M. Cococcioni, I. Dabo, et al., Journal of Physics: Condensed Matter **21**, 395502 (19pp) (2009), URL `http://www.quantum-espresso.org`.

[35] N. Marzari, A. A. Mostofi, J. R. Yates, I. Souza, and D. Vanderbilt, Rev. Mod. Phys. **84**, 1419 (2012), URL `http://link.aps.org/doi/10.1103/RevModPhys.84.1419`.

Chapter 4

Quantum critical dynamics of a magnetic impurity in a semiconducting host [⋆]

4.1 Introduction

The screening of a magnetic impurity by conduction electrons is a quantum many body phenomenon that generates an exponentially small Kondo scale, T_K, in strong coupling. The emergence of a Kondo scale has been confirmed in dilute metallic alloys[1] and mesoscopic quantum dot[2] systems. The Kondo effect, arising in Anderson impurity model and the effect of magnetic impurities on thermodynamic properties in the Kondo limit are well understood and studied theoretically as well as experimentally. The issue that remains to be fully understood is the fate of dilute magnetic impurities in a semiconducting bath. This problem is of relevance to valence fluctuating insulators and dilute magnetic semiconductors[3]. Theoretical investigations of this issue have focused on the gapped Anderson impurity model (GAIM), which describes a correlated impurity coupled to a bath of conduction

---

[⋆] Nagamalleswararao Dasari, Swagata Acharya, A. Taraphder, Juana Moreno, Mark Jarrell and N. S. Vidhyadhiraja, to be submitted, arXiv:1509.09163.

electrons whose density of states has a hard gap at Fermi-level.

The GAIM has been studied by various analytical and numerically exact methods. Ogura and Saso[4, 5] investigated GAIM using poor man's scaling, $1/N$ expansion, self consistent perturbation method within non-crossing approximation [4, 5] (NCA) and Hirsch-Fye QMC (HF-QMC). In case of the particle-hole symmetric model, they concluded that as we increase the gap (δ) the ground state of the magnetic impurity changes from a generalized Fermi-liquid (GFL), singlet state to a local moment (LM) doublet state. The $\frac{1}{N}$ expansion and NCA yield a finite critical gap, δ_c=T$_K$ for the transition from the GFL to the LM state, while HF-QMC gives $\delta_c \approx \frac{T_K}{2}$. An improved version of NRG later used by Chen and Jayaprakash [6] to calculate thermodynamics of the GAIM showed that, δ_c is identically zero i.e the ground state is a doublet for any finite gap. A recent study by Galpin et. al. [7] using a non-perturbative method called the local moment approach(LMA) arrived at the same conclusions as the NRG. A closed scaling form for the single particle spectral function was also obtained. A Kondo resonance like feature survives only for $\frac{\delta}{T_K} \approx 1$. Although non-Fermi liquid LM behavior is observed at low frequency scales, the 'high' frequency ($\frac{|\omega|}{T_K} \gg \frac{\delta}{T_K}$) form was found to be identical to that of the gapless case. These studies have focused on the $T = 0$ dynamics. At finite but 'low' temperatures, we expect the local moment ground state to manifest in non-Fermi liquid behaviour which should crossover to a generalized Fermi liquid behaviour at 'higher' temperatures, $\frac{T}{T_K} \gg \frac{\delta}{T_K}$. Such a thermally induced crossover, albeit not studied hitherto, should have very interesting consequences in the single-particle and two-particle quantities.

In this chapter, we have studied the finite temperature dynamics of the particle-hole symmetric case of the GAIM using the hybridization expansion version of the continuous time quantum Monte-Carlo(CTQMC)[8]. The main advantages with CTQMC are that the method is numerically exact and very low temperatures ($T \ll T_K$) may be accessed without a sign problem. Our results have confirmed that the critical gap of particle-hole symmetric case of GAIM, δ_c is indeed zero. Using the temperature dependent Matsubara self-energy, we construct a 'phase' diagram in the $U-T$ plane, which not only shows the aforementioned crossover from LM to GFL 'phases', but also provides insight into the specific NFL behaviour of the LM phase. We have computed the static and dynamical susceptibility. The former shows the gradual reduction of screening and hence the uncovering of the local moment as the gap is increased. The latter was computed on the imaginary frequency axis and then transformed to the real axis through analytic continuation (using maximum entropy method[9]). Further, the dynamical susceptibility is used to predict the magnetic relaxation rate, the Knight shift and the Korringa ratio. Each of these quantities exhibit highly anomalous behaviour when there is a gap in the conduction band as compared to the gapless case. We begin with a brief review of the model and formalism in section 4.2. Subsequently, in section 4.3, we discuss single-particle dynamics and construct the phase diagram. The results for two-particle quantities are discussed and this section ends with predictions for experimentally measurable quantities. We conclude the chapter in section 4.4.

4.2 Model and Formalism

The generic Anderson model that describes the quantum impurity coupled to a bath of conduction electrons is given by

$$\mathcal{H} = \sum_{k\sigma} \epsilon_k c^{\dagger}_{k\sigma} c_{k\sigma} + V \sum_{k\sigma} (c^{\dagger}_{k\sigma} d_{\sigma} + h.c) + \epsilon_d n_d + U n_{d\uparrow} n_{d\downarrow} \,.$$

where ϵ_k is the host dispersion and V is hybridization matrix which couples the impurity to the bath. ϵ_d is the energy for the non-dispersive impurity and U is the energy cost for double occupancy on the impurity. The bath Green's function in the

Matsubara frequency space can be written as

$$\mathcal{G}^0(i\omega_n) = \frac{1}{i\omega_n - \epsilon_d - \Delta(i\omega_n)} \,. \tag{4.1}$$

Here $\Delta(i\omega_n)$ is the hybridization function and is given by

$$\Delta(i\omega_n) = -\frac{iV^2}{D-\delta}\left[\tan^{-1}\left(\frac{D}{\omega_n}\right) - \tan^{-1}\left(\frac{\delta}{\omega_n}\right)\right] \,, \tag{4.2}$$

which corresponds to a flat band density of states with band width W and a gap of 2δ at the Fermi level. We have employed hybridization expansion CTQMC[8] to measure dynamical quantities such as single and two particle Green's functions. Hybridization expansion CTQMC method yields the data on Matsubara axis then we have calculated the dynamical spin susceptibility by using maximum entropy method[9].

4.3 Results and Discussion

The critical gap for the level crossing transition, from a singlet ground state (of a Fermi liquid) to a doublet, is zero in the symmetric case. Hence at $T = 0$, we expect a local moment ground state for any non-zero δ. However, it is known from $T = 0$ LMA studies that, although the low frequency single-particle spectrum of the gapped case is very different from that of the $\delta = 0$ case, the high frequency ($\omega/T_K \gg \delta/T_K$) dynamics of the gapped system is identical to the scaling spectrum of the gapless case. Such a crossover in the zero temperature ω-dependence must manifest in the temperature dependence. Hence, for any finite gap, the system is expected to cross over from a generalized Fermi liquid (GFL) to a local moment (LM) state with decreasing temperature. We now show the GFL to LM crossover in single particle and two-particle quantities.

The imaginary part of the self-energy is shown in figure 4.1 for various gap values

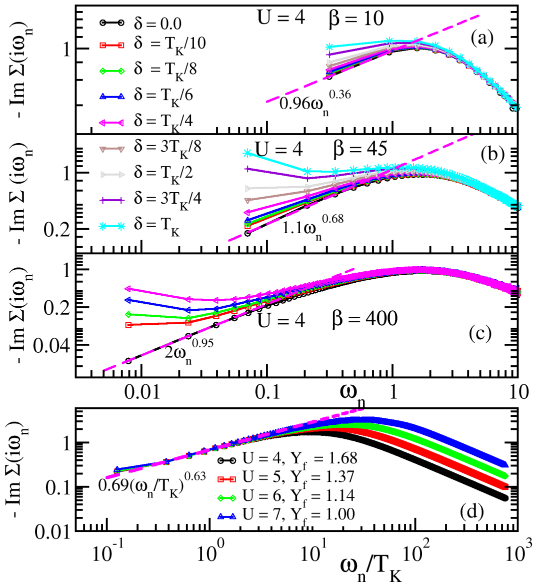

Figure 4.1: (color online)Imaginary part of Matsubara frequency self energy for a range of values of gap in the conduction bath density of states at (a) $\beta = 10$, (b)$\beta = 45$ and (c) $\beta = 400$ with $U = 4.0$ and $V = 1.0$. The dashed line is a power law fit to the low frequency part of the gapless case.(d) For a fixed δ/T_K=0.1 and $\beta = 500$, the low frequency imaginary part of the self-energy for various U-values collapses onto a universal scaling power law when plotted *vs* ω_n/T_K and scaled by a multiplicative factor, $Y_f \sim \mathcal{O}(1)$.

and decreasing temperature (from top to bottom) for a fixed interaction strength. A low frequency power law is observed in the gapless case at all temperatures, the exponent of which approaches unity as $T \to 0$. This is characteristic of Fermi liquid formation in the $\delta = 0$ case. For the $\delta > 0$ cases however, the $-\text{Im}\Sigma(i\omega_n)$ decreases with increasing ω_n initially and subsequently merges into a power law. The bottom panel of figure 4.1 shows $-\text{Im}\Sigma(i\omega_n)$ for various U-values, but a fixed δ/T_K *vs* ω_n/T_K. The collapse onto a single power law with $\mathcal{O}(1)$ multiplicative factors indicates that, in strong coupling, the exponent has a universal value, dependent only on T/T_K and δ/T_K. Furthermore, the lower the gap value, the upturn occurs at a lower temperature. The scale at which this change in the ω_n dependence (from a power law form to an upturn followed by a power law) occurs marks the crossover from a GFL to LM state and is denoted by $T_{co}(\delta, U)$. The locus of such crossover temperatures as a function of gap values for fixed U may be used to construct a ‘phase diagram’ in the $\tilde{\delta} - \tilde{T}$ plane which is shown in figure 4.2.

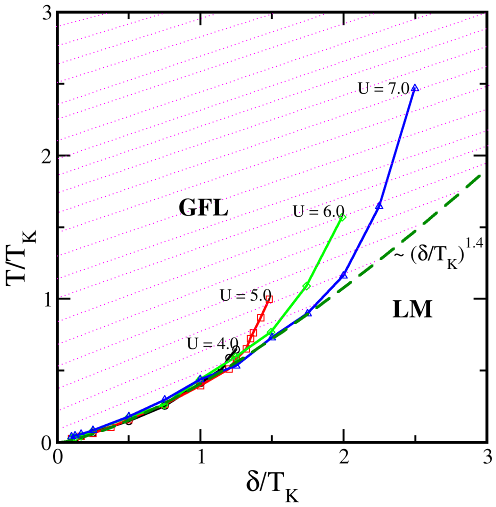

Figure 4.2: (color online) A phase diagram in the $\frac{T}{T_K}$-$\frac{\delta}{T_K}$ plane for varying U values. The shaded region is the generalized Fermi liquid while the unshaded is the local moment regime. The dashed line is the extrapolated, asymptotic strong coupling separatrix between the GFL and LM phases.

The region above the loci (for each U) represents the GFL, while the region below is the LM state. The universal, strong coupling asymptotic locus of the crossover points will be the dashed line (in figure 4.2), which has a form $T_{co} = a(\delta/T_K)^b$ with $a \sim \mathcal{O}(1)$ and $b \sim 1.4$. In the limit of vanishing gap, the crossover temperature, $T_{co} \to 0$. This corroborates the result from earlier investigations[6, 7] that the critical gap for a local moment ground state is zero in the symmetric case.

For the gapless case (δ=0), the local static spin susceptibility, namely; $\chi_{loc}(T) = \int_0^\beta d\tau \langle S_z(\tau) S_z(0) \rangle$ is known[10] to be temperature-independent for $T \ll T_K$, which represents Pauli-paramagnetic behaviour. Such behaviour indicates a complete screening of the local moment. Nozieres had proposed[11] an exhaustion argument for heavy fermion systems, wherein one of the assumptions was that only those conduction electrons within an interval of $k_B T_K$ of the chemical potential are involved in the screening. However, it is now established[12] that such an assumption is unjustified. The screening process involves electrons from infrared scales all the way

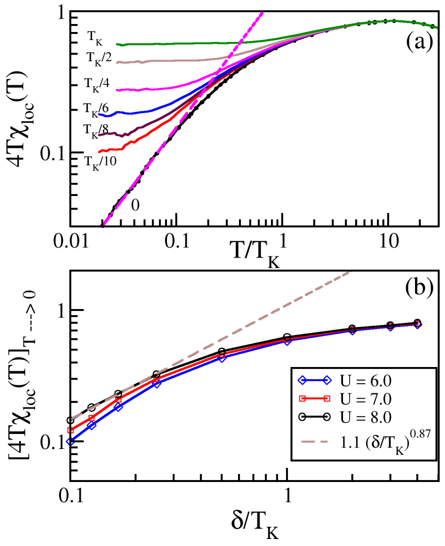

Figure 4.3: (color online) (a) The product of temperature and the local static spin susceptibility (4T$\chi_{loc}(T)$) as a function of T/T_K for a range of gap values (indicated in legends) for a $U = 6.0$. The dashed line is a linear fit in the gapless case. (b)The $T \to 0$ residual moment on the impurity for different U values as a function of gap. The brown dashed line is a power law fit to the low gap part of the $U = 8.0$ data.

to logarithmically high energy scales. Thus, with a gap in the vicinity of the chemical potential, we should expect that while the screening process *will* occur, the moment will not be completely screened. Indeed, this is seen in the upper panel of figure 4.3 where we show $4T\chi_{loc}(T)$ for various gap fractions ($0.1 \leq \delta/T_K \leq 1$) as a function of temperature for a fixed $U = 6.0$. The gapless case (black symbols) shows a linear dependence (dashed line is a linear fit) as expected. However it must be noted that the linearity extends only upto about $T/T_K \sim 0.1$. For any finite gap, it is seen that the low temperature $T\chi_{loc}(T)$ becomes flat indicating an unscreened moment, m given by $\lim_{T\to 0}(4T\chi_{loc}(T)) = m^2$. A higher gap would lead to a lesser number of conduction states available for screening, hence the limiting zero temperature value of m must increase with increasing δ. This is shown in the lower panel of figure 4.3, where the square of the moment *vs* δ/T_K is shown for three different U values. A fit to the lower gap values indicates a power law dependence of m on δ/T_K with the exponent ~ 0.9. We also note that, even with a large gap of $4T_K$, only about three-fourths of the moment is unscreened, hence states from non-universal scales are involved in the Kondo screening of the magnetic moment.

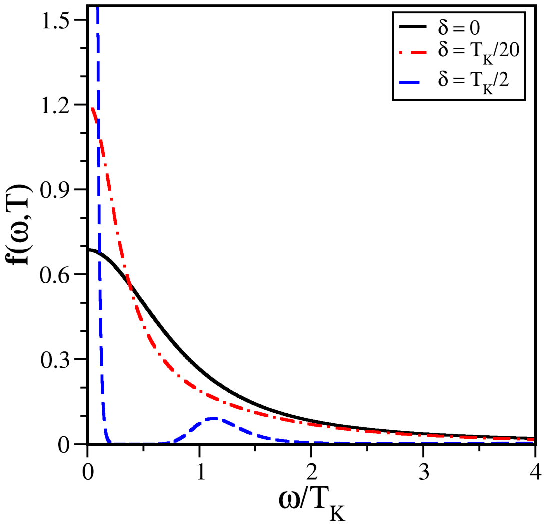

Figure 4.4: (color online) Spectral function f(ω,T)= $\frac{\pi\chi''(\omega)T_K}{2\omega\chi_{loc}(T)}$ for different gap values and $\beta = 100$, which corresponds to a $T/T_K = 0.06$ for $U = 4.0$.

The dynamics of collective excitations of GAIM is much less understood than the single particle excitations. Hence, we compute the dynamical spin susceptibility $\chi''(\omega)$ through an analytical continuation of the two particle correlation function $\chi_{loc}(i\omega_n)$ using the maximum entropy method[9]. The closed form results of Salomaa[13] for the resonant level model were employed as the default model for the analytic continuation. In the Salomaa model the parameter Γ was chosen such that it maximizes the, posterior probability of the model. We have also calculated $\chi''(\omega)$ by using a model which has obtained from annealing procedure[14]. We have found that our results are robust against the choice of the model. In figure 4.4, we show $f(\omega, T) = \frac{\pi T_K \chi''(\omega)}{2\omega\chi_{loc}(T)}$ for three gap values at $\beta = 100$ and $U = 4.0$. The three gap values correspond to three different regimes, namely the low temperature gapless case ($\delta = 0$ and $T \ll T_K$), the small gap case ($\delta = T_K/20 < T \ll T_K$) and the finite gap case ($T \ll \delta = T_K/2$). For the gapless case, we observe a Kondo like peak centered at $\omega = 0$ with a width $\sim \mathcal{O}(T_K)$[9]. With further decrease in temperature, this width does not change. In the small gap case, a peak like structure resembling that of the gapless case is observed. This implies a partial screening of the local moment since the temperature is higher than the gap. With decreasing temperature, the local moment emerges in the form of a narrow peak at $\omega = 0$, as seen in the third case. The width of this peak vanishes as $T \to 0$, signifying a free local moment with a zero energy cost for a spin-flip. The weight of this Dirac delta peak is proportional to $\langle S_z^2 \rangle$ of the impurity[15]. Apart from this peak at $\omega = 0$, a continuous spectrum, albeit of low weight, corresponding to excitations of particle-hole pairs[15] is observed for $\omega \gtrsim \delta$.

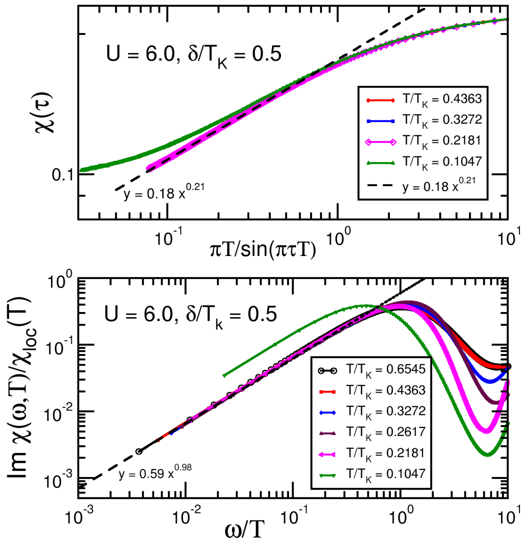

Figure 4.5: (color online) Dynamical susceptibility scaling collapse: (a) $\chi(\tau)$ *vs* $\pi T/\sin(\pi\tau T)$, (b) $\frac{\mathrm{Im}\chi(\omega)}{\chi_{loc}(T)}$ *vs.* ω/T for various temperature fractions with $U = 6.0$ and $\delta/T_K = 0.5$. The dashed lines in both the panels are power law fits.

Since the critical gap for the quantum phase transition from a singlet to a doublet ground state is $\delta_c = 0$, and the transition is continuous, we must expect a finite temperature critical scaling region of this quantum critical point. This critical scaling region is characterised by an ω/T scaling for real frequency quantities. It has been shown through conformal boundary field theoretic arguments that such a scaling manifests as a $\pi T/\sin(\pi\tau T)$ scaling for imaginary time quantities [16, 17]. In top panel of figure 4.5, we show the susceptibility $\chi(\tau)$ computed for $U = 6$ and $\delta/T_K = 0.5$ as a function of $\pi T/\sin(\pi\tau T)$ for various temperature fractions. A scaling collapse is evident for temperatures $T/T_K \gtrsim 0.218$, while for lower T/T_K, a deviation

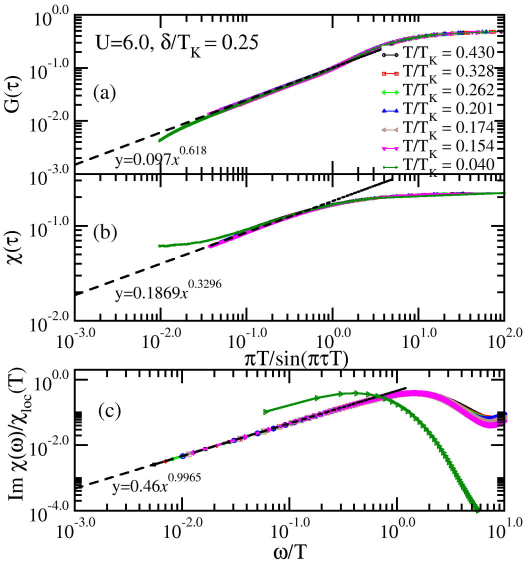

Figure 4.6: (color online) Single particle, two particle Green's functions and Dynamical susceptibility scaling collapse: (a) $G(\tau)$ *vs* $\pi T/\sin(\pi\tau T)$, (b) $\chi(\tau)$ *vs* $\pi T/\sin(\pi\tau T)$, (c) $\frac{\mathrm{Im}\chi(\omega)}{\chi_{loc}(T)}$ *vs.* ω/T for various temperature fractions with $U = 6.0$ and $\delta/T_K = 0.25$. The dashed lines in all panels are power law fits.

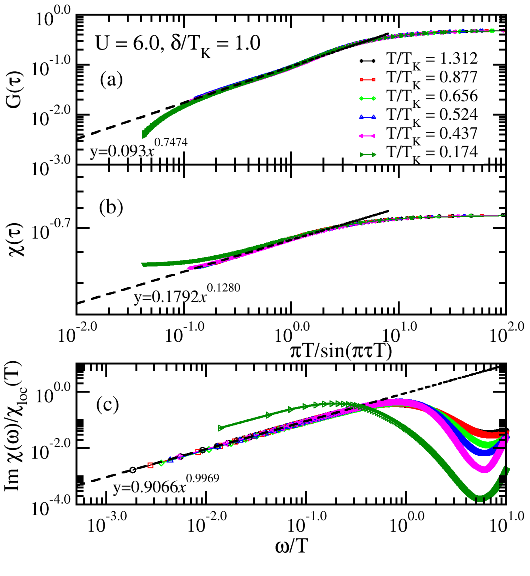

Figure 4.7: (color online) Single particle, two particle Green's functions and Dynamical susceptibility scaling collapse: (a) $G(\tau)$ *vs* $\pi T/\sin(\pi\tau T)$, (b) $\chi(\tau)$ *vs* $\pi T/\sin(\pi\tau T)$, (c) $\frac{\mathrm{Im}\chi(\omega)}{\chi_{loc}(T)}$ *vs.* ω/T for various temperature fractions with $U = 6.0$ and $\delta/T_K = 1.0$. The dashed lines in all panels are power law fits.

from the power law scaling is observed. In the lower panel, a similar universal scaling collapse of the real frequency susceptibility (obtained through MEM; see chapter on

MEM for details) is observed when plotted as a function of ω/T and this kind of scaling collapse has been observed in Bose-Fermi Kondo models[18]. We note that the self-energy and static susceptibility showed a crossover from local moment like behaviour to generalized Fermi liquid behaviour at precisely the temperature above which the scaling collapse is observed (see figures 4.1 and 4.2). We have verified that the same holds for other gaps as well (e.g. $\delta/T_K = 0.25$ and 1 in figures 4.6 and 4.7 respectively). Thus the shaded region of the finite temperature 'phase diagram' shown in figure 4.2 is in fact the critical scaling region (or the 'fan') of the $\delta_c = 0$ QCP.

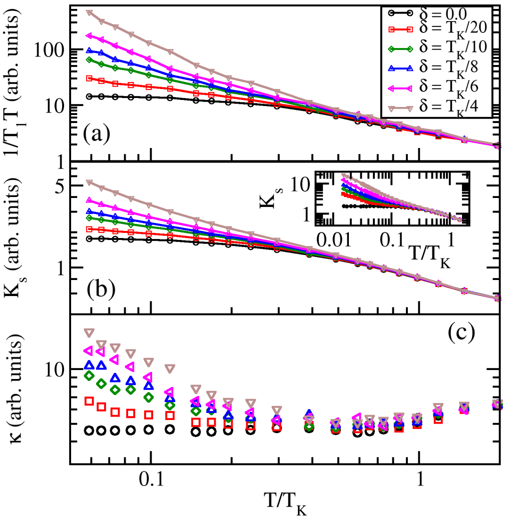

Figure 4.8: (color online) (a) Nuclear spin-lattice relaxation rate, (b) Knight shift and (c) Korringa ratio as a function of temperature for various gap values and $U = 4.0$. Inset: Knight shift at low temperature.

The dynamical susceptibility ($\chi(\omega, T) = \chi'(\omega, T) + i\chi''(\omega, T)$) may be used directly to calculate experimentally measurable observables such as the nuclear spin-lattice relaxation rate ($1/(T_1 T)$), Knight shift(K_s) and Korringa ratio ($\mathcal{K}$) as follows [9, 19]:

$$\frac{1}{T_1 T} = A \lim_{\omega\to 0} \frac{\chi''(\omega, T)}{\omega} \tag{4.3}$$

$$\mathrm{K}_s(T) = B\chi'(0, T) = B\left[P\int \frac{d\epsilon\,\chi''(\epsilon, T)}{\pi\epsilon}\right] = B\chi_{loc}(T) \tag{4.4}$$

$$\mathcal{K} = \frac{C}{T_1 T [K_s(T)]^2}\,. \tag{4.5}$$

Where A $= \frac{2k_B}{\gamma_e^2 \hbar^4}|\tilde{A}|^2$, B $= \frac{|\tilde{A}|}{\gamma_e \gamma_n \hbar^2}$ and C $= \frac{\hbar}{4\pi k_B}(\frac{\gamma_e}{\gamma_n})^2$. $\tilde{A}$ is the hyperfine coupling between the nuclear and electron spins, and γ_n (γ_e) is the nuclear (electronic) gyromagnetic ratio. The main assumption in the above expressions is that the hyperfine coupling is momentum independent. These three observables have been computed for various gap values and a fixed interaction strength ($U = 4$) and are shown in fig. 4.8 as a function of T/T_K. The singlet ground state in the gapless case implies that the relaxation mechanisms for the probe nuclear spin (e.g ^{63}Cu) due to the impurity spin (e.g. Fe) fluctuations would be suppressed sharply as the temperature drops below the Kondo scale. Thus the relaxation time scale should diverge with decreasing temperature. This is observed precisely in the top panel of figure 4.8 for the gapless case where the $1/T_1T$ saturates as $T \to 0$ implying that $T_1 \to \infty$. As seen from the figure 4.3, the residual moment is finite for any non-zero gap, and moreover the magnitude of the moment increases with increasing gap as $\sim (\delta/T_K)^{0.87}$. This would then imply that the coupling between the probe nuclear spin and the impurity moment would remain finite even as $T \to 0$. For all $\delta \gtrsim T_K/10$, we find that the $1/(T_1T) \sim T^{-\alpha}$ with $\alpha > 1$ implying that $T_1 \sim T^{\alpha-1}$ and hence vanishes as $T \to 0$. However for $\delta = T_K/20$, we find that $\alpha \sim 0.67$, implying that T_1 diverges even though a residual moment exists. A diverging T_1 for a finite gap is surprising, and the origin of such a result is not clear. Nevertheless, the relaxation *rate* $1/(T_1T)$ does diverge for any finite gap, and is hence consistent with the critical gap being zero in the symmetric case.

The Knight shift is proportional to the static susceptibility, $\chi_{loc}(T)$. Hence, at temperatures below the Kondo scale in the gapless case, the K_s should saturate, which is indeed seen in the middle panel of figure 4.8. For any non-zero gap, the ground state being a doublet should yield a $1/T$ behaviour. For the higher gaps, the $1/T$ is clearly seen while for the lower gaps, much lower temperatures ($T \ll \delta$)

need to be accessed to see such behaviour (see inset of the middle panel). Shiba has considered the gapless Anderson impurity model[20] and has proved to all orders in perturbation theory that the Korringa ratio (κ) must be a constant as $T \to 0$. The bottom panel of figure 4.8 confirms this, while showing that the κ diverges with decreasing temperature for any finite gap in the host.

4.4 Conclusions

In the present work, the manifestation of the zero gap quantum critical point in a precisely determined finite temperature region has been demonstrated through a striking scaling collapse of the dynamical susceptibility. We have also shown that this critical scaling region is characterised by anomalous behaviour of various single-particle and two-particle static and dynamical quantities. Based on dynamical spin susceptibility scaling as a function of ω/T , we classified the zero gap quantum critical point as an interacting type. The gapped Anderson impurity model is believed to be the appropriate model for many material systems, such as dilute magnetic semiconductors. It could also be of potential relevance for lattice systems, where within the dynamical mean field theory framework, a gap could arise in the hybridization of the self-consistently determined host. Our study yields an insight into the region and extent of the influence of the zero gap quantum critical point on the finite temperature properties and hence could prove to be important for the understanding of such systems.

Bibliography

[1] J. Kondo, Progress of Theoretical Physics **32**, 37 (1964), `http://ptp.oxfordjournals.org/content/32/1/37.full.pdf+html`.

[2] S. M. Cronenwett, T. H. Oosterkamp, and L. P. Kouwenhoven, Science **281**, 540 (1998), `http://www.sciencemag.org/content/281/5376/540.full.pdf`.

[3] J. Schmid, J. Weis, K. Eberl, and K. v. Klitzing, Physica B: Condensed Matter **256258**, 182 (1998), ISSN 0921-4526, URL `http://www.sciencedirect.com/science/article/pii/S092145269800533X`.

[4] T. Saso, Journal of the Physical Society of Japan **61**, 3439 (1992), URL `http://journals.jps.jp/doi/abs/10.1143/JPSJ.61.3439`.

[5] J. Ogura and T. Saso, Journal of the Physical Society of Japan **62**, 4364 (1993), `http://dx.doi.org/10.1143/JPSJ.62.4364`, URL `http://dx.doi.org/10.1143/JPSJ.62.4364`.

[6] K. Chen and C. Jayaprakash, Phys. Rev. B **57**, 5225 (1998), URL `http://link.aps.org/doi/10.1103/PhysRevB.57.5225`.

[7] Galpin, M. R. and Logan, D. E., Eur. Phys. J. B **62**, 129 (2008), URL `http://dx.doi.org/10.1140/epjb/e2008-00138-5`.

[8] P. Werner, A. Comanac, L. de' Medici, M. Troyer, and A. J. Millis, Phys. Rev. Lett. **97**, 076405 (2006), URL `http://link.aps.org/doi/10.1103/PhysRevLett.97.076405`.

[9] M. Jarrell, J. E. Gubernatis, and R. N. Silver, Phys. Rev. B **44**, 5347 (1991), URL `http://link.aps.org/doi/10.1103/PhysRevB.44.5347`.

[10] H. R. Krishna-murthy, J. W. Wilkins, and K. G. Wilson, Phys. Rev. B **21**, 1003 (1980), URL `http://link.aps.org/doi/10.1103/PhysRevB.21.1003`.

[11] P. Nozires, The European Physical Journal B - Condensed Matter and Complex Systems **6**, 447 (1998), ISSN 1434-6028, URL `http://dx.doi.org/10.1007/s100510050571`.

[12] S. Burdin, A. Georges, and D. R. Grempel, Phys. Rev. Lett. **85**, 1048 (2000), URL `http://link.aps.org/doi/10.1103/PhysRevLett.85.1048`.

[13] M. Salomaa, Zeitschrift fr Physik B Condensed Matter **25**, 49 (1976), ISSN 0722-3277, URL `http://dx.doi.org/10.1007/BF01343309`.

[14] N. Dasari, J. Moreno, N. S. Vidhyadhiraja, and M. Jarrell, *Analytic continuation of hybridization expansion continuous-time quantum monte-carlo data using maximum entropy method*, unpublished.

[15] C. Raas and G. S. Uhrig, Phys. Rev. B **79**, 115136 (2009), URL `http://link.aps.org/doi/10.1103/PhysRevB.79.115136`.

[16] S. Kirchner and Q. Si, Phys. Rev. Lett. **100**, 026403 (2008), URL `http://link.aps.org/doi/10.1103/PhysRevLett.100.026403`.

[17] A. Tsvelik, *Quantum Field Theory in Condensed Matter Physics* (Cambridge University Press, Cambridge, England, 1996).

[18] L. Zhu, S. Kirchner, Q. Si, and A. Georges, Phys. Rev. Lett. **93**, 267201 (2004), URL `http://link.aps.org/doi/10.1103/PhysRevLett.93.267201`.

[19] E. Yusuf, B. J. Powell, and R. H. McKenzie, Phys. Rev. B **75**, 214515 (2007), URL `http://link.aps.org/doi/10.1103/PhysRevB.75.214515`.

[20] H. Shiba, Progress of Theoretical Physics **54**, 967 (1975), `http://ptp.oxfordjournals.org/content/54/4/967.full.pdf+html`, URL `http://ptp.oxfordjournals.org/content/54/4/967.abstract`.

Chapter 5

A continuous time quantum Monte-Carlo study of local quantum critical dynamics in the asymmetric gapped Anderson impurity model [⋆]

5.1 Introduction

One of the main challenges in condensed matter physics is to address the universal behavior of correlated quantum systems. The quantum critical region, that fans out from the quantum critical point (QCP) determines the physical properties of a system in a large range of temperature and control parameters such as magnetic field, pressure and chemical substitution. The existence of a novel class of quantum critical points(QCP) in heavy fermion metals manifesting in highly anomalous physical properties has been experimentally established[1–6]. It has been observed that in

---

[⋆] Nagamalleswararao Dasari, Juana Moreno, Mark Jarrell and N. S. Vidhyadhiraja, Manuscript in preparation.

the quantum critical region, the dynamical spin susceptibility and single particle relaxation rates are linear in T and dynamical spin susceptibility satisfies the $\frac{\omega}{T}$ scaling [3, 4]. To describe these novel QCPs require the introduction of additional critical modes beyond standard Landau's order parameter fluctuations[7]. It has been proposed that these additional critical modes are those arising from the critical destruction of Kondo effect[7]. Experiments such as quantum oscillation and Hall effect observed [1, 8] the critical Kondo destruction through a sudden change of Fermi surface at the quantum critical point. If such an effect is local in space, we should expect to find it in a quantum impurity model by varying some athermal parameter[9]. Indeed, the quantum impurity models which shows critical Kondo destruction are the pseudo-gap Anderson model[9–11] and gapped Anderson impurity model(GAIM)[12–15].

The symmetric and asymmetric GAIM have been studied extensively by various methods. An early Hirsch-Fye QMC study[16] identified the critical gap, δ_c, as zero in the symmetric case ($\eta = 0$), and also argued that the $\delta_c \neq 0$ in the asymmetric case ($\eta \neq 0$). Another early study[17, 18] employed an impressive range of methods including poor man's scaling, $1/N$ expansion, non-crossing approximation and Hirsch-Fye QMC (HF-QMC). The conclusion reached by the latter by the analytical methods was that $\delta_c = 2T_K$, where T_K is the Kondo scale of the gapless case; while the HF-QMC yielded $\delta_c \sim T_K$. Later studies using numerical renormalization group (NRG)[12, 15] and local moment approach (LMA)[13, 14] showed that $\delta_c = 0$ for $\eta = 0$, while δ_c is non-zero and depends quite non-trivially on η in the asymmetric case. A recent NRG study[15] confirmed the results of the previous $T = 0$ NRG and LMA works. Thus, at $T = 0$, a line of quantum critical points exist in the gap-asymmetry plane that separate a singlet Fermi liquid state from a local moment doublet state.

In case of the pseudogap Anderson model, the dynamical scaling and relaxation behavior in the quantum critical regime is very well understood [9–11, 13]. However, a similar study for the GAIM model has not yet been carried out. Such a study would be extremely useful in classifying the nature of quantum critical points (QCP) in the gap-asymmetry plane. Especially from the experimental point of view because calculations of such kind would yield characteristic signatures in the transport properties of dilute magnetic impurities in semiconductors and superconductors.

Recently, by using hybridization expansion continuous-time quantum Monte-Carlo (HY-CTQMC) approach[19], we identified[20] the critical scaling region of the zero gap QCP in the particle-hole symmetric case as the region above the separatrix of the low temperature local moment phase from the high temperature generalized Fermi liquid. In this work, we have carried out a finite temperature study of the particle-hole asymmetric GAIM in the strong coupling limit by using the same method, namely HY-CTQMC[19]. We find, in agreement with the previous works[12–16], that critical Kondo destruction occurs in the quantum relaxation regime and manifests as a line of QCPs in the gap-asymmetry plane, which separates a Kondo screened generalized Fermi liquid phase from a local moment phase.

5.2 Model and Formalism

The generic Anderson model that describes the quantum impurity coupled to a bath of conduction electrons is given by

$$\mathcal{H} = \sum_{k\sigma} \epsilon_k c^{\dagger}_{k\sigma} c_{k\sigma} + V \sum_{k\sigma} (c^{\dagger}_{k\sigma} d_\sigma + h.c) + \epsilon_d n_d + U n_{d\uparrow} n_{d\downarrow} \tag{5.1}$$

where ϵ_k is the host dispersion and V represents the strength of hybridization, that couples the impurity to the bath. ϵ_d is the energy of the non-dispersive impurity and U is the Coulomb repulsion for two electrons on the impurity. The bath Green's function can be written in the Matsubara frequency space as

$$\mathcal{G}^0(i\omega_n) = \frac{1}{i\omega_n - \epsilon_d - \Delta(i\omega_n)}\,,$$

where $\Delta(i\omega_n)$ is the hybridization function and is given by

$$\Delta(i\omega_n) = -\frac{iV^2}{D-\delta}\left[\tan^{-1}\left(\frac{D}{\omega_n}\right) - \tan^{-1}\left(\frac{\delta}{\omega_n}\right)\right] .$$

Such a $\Delta(i\omega_n)$ corresponds to a flat, conduction band density of states having a band width of $W = 2D$ and gap of 2δ at the Fermi level. The particle-hole asymmetry parameter is defined by $\eta = 1 + \frac{2\epsilon_d}{U}$. We note here that it is only the impurity level that is away from particle-hole symmetry while the conduction band is symmetric.

As mentioned in the introduction, the hybridization expansion version of CTQMC as implemented in the ALPS[21] library has been employed to solved the model in equation 5.1. The advantages of this method as compared to earlier versions of QMC are manifold $-$ A much reduced sign problem, access to far lower temperatures and larger interaction strengths are a few. Nevertheless, since the data obtained is on the imaginary time/frequency axis, analytic continuation is required for viewing real frequency single-particle or two-particle quantities. In the following section, we begin by reviewing the key results of the previous works and subsequently describe the results obtained in this work.

5.3 Results and Discussion

As mentioned before in the introduction, previous NRG[12, 15] and LMA[13, 14] studies of the GAIM in the particle-hole symmetric case demonstrated critical Kondo destruction for $\delta_c = 0$. Thus, even an infinitesimal gap in the conduction electron density of states results in complete absence of screening at $T = 0$ and the ground state is doubly degenerate local moment (LM) state. Surprisingly, the single particle dynamics such as the spectral function of the GAIM was found to be similar to that of the gapless case on an energy scale $\omega > \delta$[13]. For small gaps, $\delta/T_K \ll 1$ (where T_K is the Kondo temperature in the gapless case), the spectral function shows a hallmark of Kondo effect, namely a Kondo resonance at frequencies $\omega \sim T_K$, while true non-Fermi liquid LM behaviour can be seen only at $\omega \ll \delta$. Furthermore, the single particle spectral function exhibits universal scaling as a function of ω/T_K for fixed gap values, δ/T_K. In the particle-hole asymmetric case the ground state of the system evolves from a generalized Fermi-Liquid (GFL) state to LM state with increasing δ and a finite δ_c is found for any non-zero asymmetry. As in the symmetric case, the single-particle spectral function across the transition for small gap values ($\delta/T_K \ll 1$) shows a Kondo resonance for $\omega > \delta$ and a collapse of high energy tails onto the gapless case for $\omega \gg \delta$. The ground state of the symmetric case cannot be perturbatively connected to the non-interacting ground state while the asymmetric case does.

Recently we have studied the particle-hole symmetric case of GAIM at finite temperature by using HY-CTQMC[20]. Our key findings are as follows; The imaginary part of Matsubara self-energy (-Im $\Sigma(\omega_n)$) exhibits universal scaling in terms of ω_n/T_K for a fixed gap of δ/T_K, which is in parallel to the single-particle spectral function on real frequency axis. The zero gap quantum critical point at T=0 manifests in a finite temperature quantum critical region, which has been demonstrated through a scaling collapse of single particle, two particle static and dynamical quantities. Based on dynamical spin susceptibility scaling as a function of ω/T, we classified the zero gap quantum critical point as an interacting type. Now we present our results of single and two-particle quantities for the asymmetric GAIM.

We begin with the results of single particle irreducible impurity self energy. We have measured the gap in terms of the Kondo temperature of the gapless case (δ = 0) which is given by $T_K = \sqrt{(\frac{U\pi V^2}{4D})}\exp(\frac{-\epsilon_d(\epsilon_d+U)D}{UV^2})$ [18]. For $U = 6.0, V = 1.0$ and η of 0.4 we find $T_K \sim 0.12$; while the $\frac{U}{\pi\Delta}$ is 2.43 which corresponds to the strong coupling limit or Kondo limit. As in our previous work[20] on the symmetric limit of the GAIM, we identify the ground state phase based on the low frequency behavior of self energy defined on the imaginary frequency axis. In the generalized Fermi liquid region, we should expect $-\text{Im}\Sigma(i\omega_n \to 0) \propto A|\omega_n|^\alpha$, where the exponent

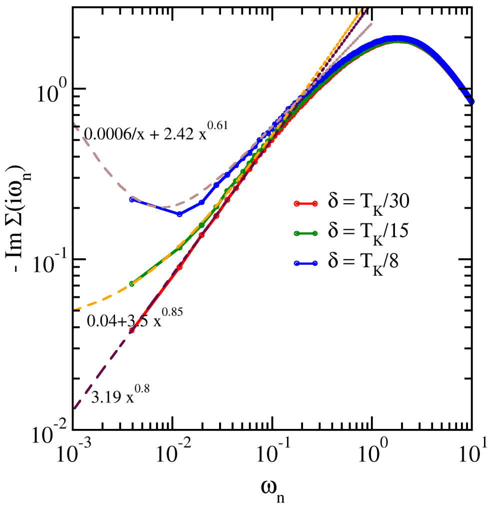

Figure 5.1: (color online) Imaginary part of Matsubara self energy for different gap values in the bath density of states for a $U = 6.0$ corresponding to which a gapless Kondo scale is obtained as $T_K = 0.12$. The temperature is $\beta = 1/T = 800$ and the particle-hole asymmetry, $\eta = 0.4$.

$\alpha \to 1$ as $T \to 0$. The local moment (LM) phase is characterized by a partially screened impurity moment, the fluctuations of which cost no energy at $T = 0$. In this phase, the imaginary part of self energy would diverge at low Matsubara frequencies i.e, $-\text{Im}\Sigma(i\omega_n) \sim B/\omega_n$. In the crossover region or quantum critical region, the imaginary part of self energy may be described by $-\text{Im}\Sigma(i\omega_n) \sim C + D|\omega_n|^\alpha$ where $0 < \alpha \leq 1$ and $C \neq 0$. In figure 5.1 we show the imaginary part of Matsubara self energy for three gap values and T_K of 0.12 at $\beta = 800$. For a gap of $\delta = T_K/30$, the imaginary part of self energy has GFL behavior. As we increase the gap value to $\delta = T_K/15$, the (extrapolated) intercept becomes finite and the above mentioned crossover form is seen. At higher gap values such as $T_K/8$ shown in figure 5.1, the local moment form is seen which crosses over to a power law at higher ω_n. Thus, for a given asymmetry η, by varying the gap δ in the conduction band density of states, we observe a crossover from a GFL phase to LM phase.

The manifestation of such a crossover is also seen in the local static spin susceptibility, given by $\chi(T) = \int_0^\beta d\tau \langle S_z(\tau) S_z(0) \rangle$. In figure 5.2 we have plotted the

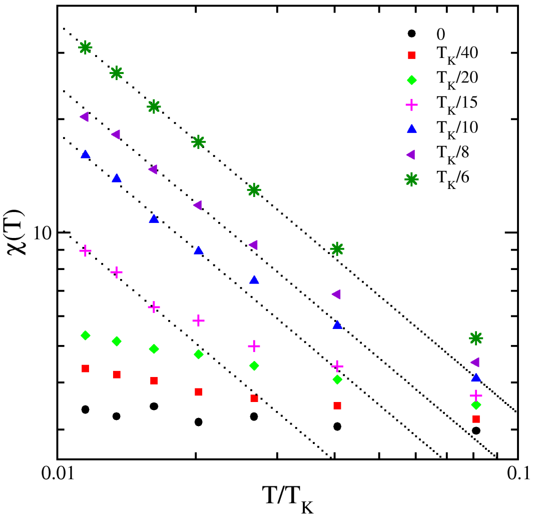

Figure 5.2: (color online) Local static spin susceptibility as a function of temperature for different gap values at $U = 6$ and and $\eta = 0.4$, for which $T_K = 0.12$.

$\chi(T)$ as a function of temperature for various gap values (shown in legends), with a $U = 6$ and $\eta = 0.4$ (hence $T_K = 0.12$). The dotted line is a $1/T$ or a local moment fit to the low temperature part. In the gapless case, the susceptibility is almost flat (within numerical tolerance), which is natural for a Fermi liquid, since we expect it to be of the Pauli paramagnetic type. As the gap is increased, a slight upturn is seen, and beyond $T_K/20$, a qualitative change is seen in the form of a $1/T$ form at low temperature for all $\delta > T_K/15$. In fact, the region over which the local moment form fits the $\chi(T)$ increases with increasing δ. From this finite temperature crossover of Pauli paramagnetic behaviour to local moment behaviour, we may conclude that a zero temperature quantum phase transition occurs in the interval $\delta \in (T_K/20, T_K/15)$. That the transition is continuous cannot be stated without carrying out a zero temperature calculation, which is impossible with quantum Monte Carlo methods. Nevertheless, previous LMA and NRG calculations have conclusively established a line of quantum critical points in the $\eta - \delta$ plane. Our calculations show the finite temperature manifestation of these QCPs.

In order to further confirm the range (in δ) of the quantum phase transition

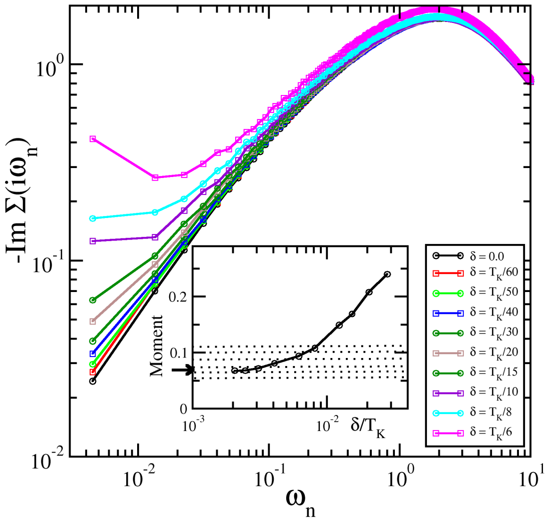

Figure 5.3: (color online) Self energy in the main panel and moment in the inset.U=6, $\eta = 0.4, \beta = 700$.

underlying this finite temperature crossover, we refer to figure 5.3. In the main panel, we show the same data as in the figure 5.1, but for a larger number of gap values, while the inset shows the square of the unscreened moment as a function of gap. From the main panel, we see that the low frequency part of $-\text{Im}\Sigma(i\omega_n)$ is a power law for all $\delta \leq T_K/20$, while for $\delta \geq T_K/15$, a deviation from the power law is seen in the form of an upturn at the lowest ω_n. Since the power law with a zero intercept is characteristic of a GFL, we identify the ground state for all $\delta \leq T_K/20$ as a GFL, and for gaps higher than $T_K/15$ as a local moment state. This analysis restricts the range of a possible co-existence region due to a first order transition to between $T_K/20$ and $T_K/15$, which matches with the inference from the susceptibility data. The inset shows the unscreened moment as a function of gap. The shaded region denotes gaps in the range of $\delta < T_K/20$. For the gapless case, the screened moment should be zero at $T = 0$. However, since our calculations are at a finite temperature of $\beta = 700$ (in figure 5.3) a small T^2 contribution is expected. With increasing gap, although a clear rise of the moment cannot be identified, a crude estimation yields a result that concurs with that of the main panel. The shaded region represents

$\delta \leq T_K/20$, for which the moments are close to that of $\delta = 0$. The first point above this region is $\delta = T_K/15$, which, is quite above the shaded region, and hence can be crudely identified as a lower bound for the LM phase.

A similar analysis for other asymmetries yields the critical gap (in practice, a range is obtained) as a function of η, and hence a phase diagram in the $\eta - \delta$ plane as shown in figure 5.4 for $U = 5.0$ and $U = 6.0$. With a rescaling of gap with respect to the Kondo scale, the two data sets collapse onto a single universal phase boundary. The plateaus seen are, naturally, an artifact of the finite resolution in identifying the critical gap. In agreement with previous works[12–16], the critical gap for the transition from the GFL phase (at low δ) to a LM phase (at higher δ) increases with increasing asymmetry. The symmetric case ($\eta = 0$) data point is from our previous work[20].

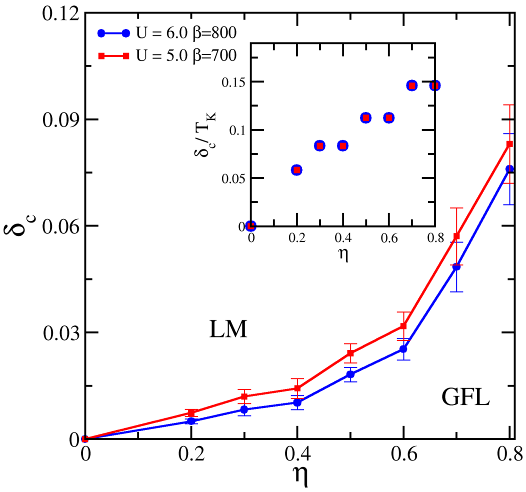

Figure 5.4: (color online) Critical δ *vs.* η phase diagram (a) for $T_K = 0.172$ and $\beta = 700$. (b) for $T_K = 0.12$ and $\beta = 800$.

Now, that we have derived a ground state phase diagram from finite temperature crossovers in single and two particle quantities, we examine the manifestation of the quantum critical points in other finite temperature properties. A quantity which determines the low energy behavior of single particle excitations on the impurity is

$Z(T) = [1 - \mathrm{Im}\Sigma(i\omega_0)/\omega_0]^{-1}$, which reduces to the quasiparticle weight[22] in the limit $T \to 0$. In figure 5.5 we have plotted the $Z(T)$ as a function of temperature for different gap values and $T_K \sim 0.172$. As has been argued before, at a sufficiently high temperature ($T \gtrsim \delta$), the physics of a gapped impurity is identical to that of a gapless impurity, and this underlies the collapse of all curves at high temperature. As we decrease the temperature, three distinct kinds of behaviour are observed. For low gaps ($\delta \lesssim T_K/20$), the $Z(T)$ saturates implying FL behaviour, while for the largest gaps shown, a power law with exponent one (dotted line fit) implies that $Z(T) \to 0$ as $T \to 0$ implying LM behaviour. The intermediate gaps display a crossover behaviour, where the the $T \to 0$ behaviour cannot be determined with certainty unless calculations at much lower T are carried out. Although the hybridization expansion version of CTQMC allows us to access far lower temperatures than e.g. the Hirsch-Fye version, $\beta > 700 - 800$ calculations were impossible with the currently available resources. Thus, we are forced to conclude that the 'quasiparticle weight' could not be used to clearly support the phase diagram shown in figure 5.4.

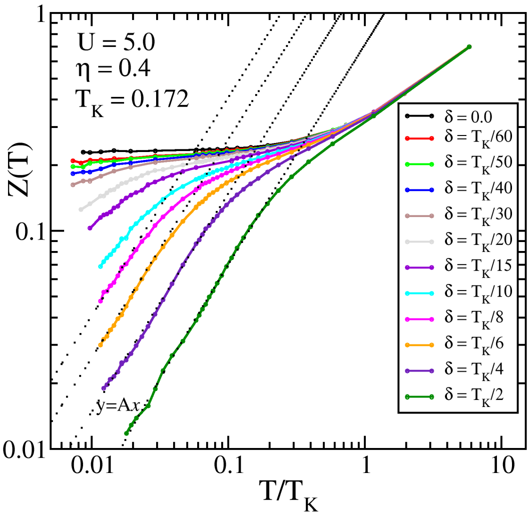

Figure 5.5: (color online) Quasi particle weight (Z(T)) as a function of temperature for different gap values at $T_K = 0.172$. The interaction strength, $U = 5.0$ and asymmetry, η is 0.4.

Finally, we examine the dynamical spin-spin correlation functions as a function

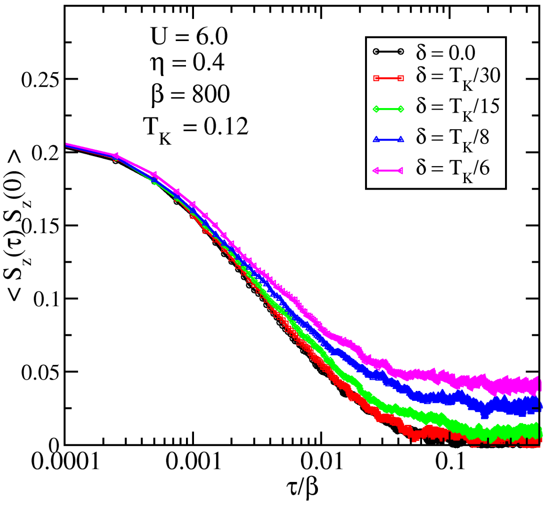

Figure 5.6: (color online) Matsubara time spin-spin correlation function for different gap values at $T_K = 0.12$, $\beta = 800$ and for $\eta = 0.4$.

of Matsubara time to understand the behavior of spin dynamics. In figure 5.6 we plot the spin-spin correlation function $\chi_{zz}(\tau)= \langle S_z(\tau) S_z(0)\rangle$ for various gap values and T_K of 0.12. The value of $\chi_{zz}(\tau)$ at $\tau = 0$ represents the bare local moment[23] of spin $\frac{1}{2}$ electron which is given by $m_{loc} = g \times \sqrt{\chi(\tau = 0)} \approx 0.93$. The bare local moment which is formed at $\tau = 0$ is dynamically screened by conduction electrons at larger $\tau \sim \beta/2$. In the figure 5.6 we observe that the bare local moment does not change as we change the gap value but the dynamically screened moment depends on the gap value significantly. For a generalized Fermi-liquid at low temperature, $\chi_{zz}(\tau)$ at $\tau = \frac{\beta}{2}$ should be proportional to T^2; while in case of LM phase it has a finite constant value. Our results are consistent with the GFL behavior of $\chi_{zz}(\beta)$ for the gap of $\delta = 0.0$, $\frac{T_K}{30}$ and for larger gap values we have LM behavior in $\chi_{zz}(\beta)$. We note that from the behaviour of dynamical spin-spin correlation function, it is very hard to distinguish the critical gap which separates GFL from LM behavior, since the noise at high τ makes it impossible to make a precise identification of the dynamically screened moment value at $\tau = \beta/2$.

5.4 Conclusions

Our study of the particle-hole asymmetric gapped Anderson model at finite temperature in the quantum relaxation regime reveals the existence of a line of Kondo destruction quantum critical points in the gap-asymmetry plane, in agreement with previous works[12–16]. The critical gap increases monotonically as we increase the asymmetry. We found that, although the frequency dependence of the self-energy and the local susceptibility as a function of temperature may be used to construct the phase diagram, the quasiparticle weight or the dynamical susceptibility require much higher precision calculations at much lower temperatures than possible with the current resources for identifying critical gaps. A classification of the quantum critical points using critical scaling analysis and transport calculations are under progress.

Bibliography

[1] H. v. Löhneysen, A. Rosch, M. Vojta, and P. Wölfle, Rev. Mod. Phys. **79**, 1015 (2007), URL `http://link.aps.org/doi/10.1103/RevModPhys.79.1015`.

[2] Q. Si and F. Steglich, Science **329**, 1161 (2010), `http://www.sciencemag.org/content/329/5996/1161.full.pdf`, URL `http://www.sciencemag.org/content/329/5996/1161.abstract`.

[3] M. C. Aronson, R. Osborn, R. A. Robinson, J. W. Lynn, R. Chau, C. L. Seaman, and M. B. Maple, Phys. Rev. Lett. **75**, 725 (1995), URL `http://link.aps.org/doi/10.1103/PhysRevLett.75.725`.

[4] S. Friedemann, N. Oeschler, S. Wirth, C. Krellner, C. Geibel, F. Steglich, S. Paschen, S. Kirchner, and Q. Si, Proceedings of the National Academy of Sciences **107**, 14547 (2010), `http://www.pnas.org/content/107/33/`

14547.full.pdf+html, URL http://www.pnas.org/content/107/33/14547.abstract.

[5] M. Okawa, M. Matsunami, K. Ishizaka, R. Eguchi, M. Taguchi, A. Chainani, Y. Takata, M. Yabashi, K. Tamasaku, Y. Nishino, et al., Phys. Rev. Lett. **104**, 247201 (2010), URL http://link.aps.org/doi/10.1103/PhysRevLett.104.247201.

[6] S. Sachdev, *Quantum Phase Transitions* (Cambridge University Press,Cambridge,England, 1999).

[7] P. Coleman, C. Ppin, Q. Si, and R. Ramazashvili, Journal of Physics: Condensed Matter **13**, R723 (2001), URL http://stacks.iop.org/0953-8984/13/i=35/a=202.

[8] H. Shishido, R. Settai, H. Harima, and Y. nuki, Journal of the Physical Society of Japan **74**, 1103 (2005), http://dx.doi.org/10.1143/JPSJ.74.1103, URL http://dx.doi.org/10.1143/JPSJ.74.1103.

[9] C. Gonzalez-Buxton and K. Ingersent, Phys. Rev. B **57**, 14254 (1998), URL http://link.aps.org/doi/10.1103/PhysRevB.57.14254.

[10] M. T. Glossop, S. Kirchner, J. H. Pixley, and Q. Si, Phys. Rev. Lett. **107**, 076404 (2011), URL http://link.aps.org/doi/10.1103/PhysRevLett.107.076404.

[11] J. H. Pixley, S. Kirchner, K. Ingersent, and Q. Si, Phys. Rev. Lett. **109**, 086403 (2012), URL http://link.aps.org/doi/10.1103/PhysRevLett.109.086403.

[12] K. Chen and C. Jayaprakash, Phys. Rev. B **57**, 5225 (1998), URL http://link.aps.org/doi/10.1103/PhysRevB.57.5225.

[13] M. R. Galpin and D. E. Logan, The European Physical Journal B **62**, 129 (2008), ISSN 1434-6028, URL http://dx.doi.org/10.1140/epjb/e2008-00138-5.

[14] M. R. Galpin and D. E. Logan, Phys. Rev. B **77**, 195108 (2008), URL `http://link.aps.org/doi/10.1103/PhysRevB.77.195108`.

[15] C. P. Moca and A. Roman, Phys. Rev. B **81**, 235106 (2010), URL `http://link.aps.org/doi/10.1103/PhysRevB.81.235106`.

[16] K. Takegahara, Y. Shimizu, and O. Sakai, Journal of the Physical Society of Japan **61**, 3443 (1992), `http://dx.doi.org/10.1143/JPSJ.61.3443`, URL `http://dx.doi.org/10.1143/JPSJ.61.3443`.

[17] T. Saso, Journal of the Physical Society of Japan **61**, 3439 (1992), URL `http://journals.jps.jp/doi/abs/10.1143/JPSJ.61.3439`.

[18] J. Ogura and T. Saso, Journal of the Physical Society of Japan **62**, 4364 (1993), `http://dx.doi.org/10.1143/JPSJ.62.4364`, URL `http://dx.doi.org/10.1143/JPSJ.62.4364`.

[19] E. Gull, A. Millis, A. Lichtenstein, A. Rubtsov, M. Troyer, and P. Werner, Rev. Mod. Phys. **83**, 349 (2011), URL `http://link.aps.org/doi/10.1103/RevModPhys.83.349`.

[20] N. Dasari, S. Acharya, A. Taraphder, J. Moreno, M. Jarrell, and N. S. Vidhyadhiraja, *Quantum critical dynamics of a magnetic impurity in a semiconducting host*, unpublished.

[21] B. Bauer, L. D. Carr, H. G. Evertz, A. Feiguin, J. Freire, S. Fuchs, L. Gamper, J. Gukelberger, E. Gull, S. Guertler, et al., Journal of Statistical Mechanics: Theory and Experiment **2011**, P05001 (2011), URL `http://stacks.iop.org/1742-5468/2011/i=05/a=P05001`.

[22] N. S. Vidhyadhiraja, A. Macridin, C. Şen, M. Jarrell, and M. Ma, Phys. Rev. Lett. **102**, 206407 (2009), URL `http://link.aps.org/doi/10.1103/PhysRevLett.102.206407`.

[23] A. Toschi, R. Arita, P. Hansmann, G. Sangiovanni, and K. Held, Phys. Rev. B **86**, 064411 (2012), URL `http://link.aps.org/doi/10.1103/PhysRevB.86.064411`.

Chapter 6

Interplay of strong correlations and covalency in ionic band insulators[*]

6.1 Introduction

The recent discovery of interaction-driven topological phases[1, 2], such as, fractional quantum-Hall states, spin-liquids, Kondo-insulators and bosonic topological phases has created a huge interest in, otherwise considered to be mundane, band insulators. Some questions of fundamental interest in band insulators are: how do correlations drive a band insulator into a metal and a Mott insulator(MI) and are correlated band insulators fundamentally different from simple band insulators which have identical charge and spin excitation gaps? Theoretically these issues have been addressed in all dimensions, from one to infinity, by various studies of model Hamiltonians such as the ionic Hubbard model[3–12], a two-sublattice model with inter-orbital hybridization[13, 14], a two-band Hubbard model with crystal field splitting[15] and a bilayer model with two identical Hubbard planes[16–20].

---

[*] Nagamalleswararao Dasari, Juana Moreno, Mark Jarrell and N. S. Vidhyadhiraja, Draft under revision.

The ionic Hubbard model, which comprises a two-sublattice system having orbital energies, V and $-V$ with a local Coulomb repulsion, drew a lot of attention after the pioneering work by Arti Garg et. al.,[6], which showed that correlations can turn a band insulator into a metal and for higher interaction strengths, U, into a Mott insulator. The $U - V$ phase diagram, found through a iterated perturbation theory (IPT) solution of the self-consistent impurity problem within dynamical mean field theory (DMFT), exhibited a finite metallic region, which transformed into a line at large U and V, as should be the case in the exactly known atomic limit. Later studies using a modified form of IPT, and numerical renormalization group at zero temperature ($T = 0$), and a continuous time quantum Monte-Carlo (CTQMC) study, while confirming the existence of an intervening metallic phase, were not in agreement about the extent of the metallic region. Furthermore, one could ask if there exist parameters other then interaction strength, that could induce metallicity in band insulators, and what would be the interplay of interactions with such an athermal parameter. In this work, we have answered this question within a two orbital Hubbard model with on-site repulsion, U, between electrons of opposite spin. The novelty of the model is embodied by a parameter "$x \in [0, 1]$" which may be interpreted as the degree of ionicity, while $1 - x$ is comcomitantly interpreted as the degree of covalency. Such a parametrization permits us to explore the interplay of ionicity and covalency in interacting band insulators. So for $x = 1$, we obtain purely ionic band insulators[6] while for $x = 0$, the model reduces to purely covalent band insulators[13]. One of the main findings is that, while the two extremes of $x = 0$ and $x = 1$ are, indeed, band insulators, albeit of different kinds, the $x = 0.5$ turns out to be a metal even in the non-interacting case. The interaction driven metallic region found in Ref[6] is shown analytically to be just a line of measure zero in the $U - V$ plane for the ionic Hubbard model. We find that the phase diagram in the $U - T$ plane is strongly dependent on the degree of covalency (or ionicity).

This chapter is organized as follows: In Sec. 6.2, we define the model and methods chosen to study correlation effects in different kinds of band insulators. In Sec. 6.3, first we discuss the analytical results at zero and finite temperatures and then we present and discuss our numerical results. Finally, in Sec. 6.4, we present our conclusions.

6.2 Models and Methods

We have considered a two orbital Hubbard model with a local Coulomb interaction between two electrons of opposite spin on same orbital. In the second quantized notation, the Hamiltonian reads,

$$\mathcal{H} = -\mu \sum_{i\alpha\sigma} \hat{n}_{i\alpha\sigma} + \sum_{ij\alpha\beta\sigma} t_{ij}^{\alpha\beta} (c_{i\alpha\sigma}^{\dagger} c_{j\beta\sigma} + h.c) + \sum_{i\alpha\sigma} \frac{U}{2} \hat{n}_{i\alpha\sigma} \hat{n}_{i\alpha\bar{\sigma}} \,, \tag{6.1}$$

where $c_{i\alpha\sigma}^{\dagger}(c_{i\alpha\sigma})$ creates (annihilates) an electron at lattice site i, in orbital α with spin σ. We set the chemical potential $\mu = \frac{U}{2}$ so that each site has a total average occupancy of 2 (i.e. half filling). We are mainly interested in local single particle electron dynamics, which is given by the momentum sum of the lattice Green's function,

$$\mathbf{G}_{\sigma}(\omega^{+}) = \sum_{\mathbf{k}} \left[(\omega^{+} + \mu)\mathbb{I} - \mathbf{H}_{\sigma}(\mathbf{k}) - \mathbf{\Sigma}_{\sigma}(\mathbf{k}, \omega^{+}) \right]^{-1} \,, \tag{6.2}$$

where $\omega^{+} = \omega + i\eta$ and $\eta \to 0^{+}$. Here, $\mathbf{H}_{\sigma}(\mathbf{k})$ comprises intra-unit-cell hybridization and nearest neighbour inter-unit-cell hopping, namely

$$\mathbf{H}_{\sigma}(\mathbf{k}) = \mathbf{H}^{\sigma}{}_{intra} + \mathbf{H}^{\sigma}(\mathbf{k})_{inter} \,. \tag{6.3}$$

We have calculated the local single particle propagators within the DMFT framework, wherein the single particle irreducible self-energy $\mathbf{\Sigma}_{\sigma}(\omega^{+})$ is local, and will be determined by solving the auxiliary Anderson impurity model. The local, interacting Green's function (equation 6.2) may be related to the non-interacting Green's function

$\mathbf{G}_{0\sigma}(\omega^+)$ through the Dyson equation:

$$\mathbf{G}_{0,\sigma}^{-1}(\omega^+) = \mathbf{G}_{\sigma}^{-1}(\omega^+) - \mathbf{\Sigma}_{\sigma}(\omega^+)\,, \tag{6.4}$$

where $\mathbb{I}$ is the identity matrix. We construct a non-interacting Hamiltonian $\mathbf{H}_\sigma(\mathbf{k})$ as an interpolation between an ionic band insulator (IBI) and a covalent insulator (CI) as follows:

$$\begin{aligned}\mathbf{H}_\sigma(\mathbf{k},x) &= \mathbf{H}_{IBI} + \mathbf{H}_{CI} \\ &= x\begin{pmatrix}\Delta & \epsilon_{k\sigma} \\ \epsilon_{k\sigma} & -\Delta\end{pmatrix} + (1-x)\begin{pmatrix}\tilde{\epsilon}_{k\sigma} & V \\ V & -\tilde{\epsilon}_{k\sigma}\end{pmatrix}.\end{aligned} \tag{6.5}$$

In the IBI, a two sublattice system has staggered ionic potentials Δ and -Δ and and a k-dependent hybridization ($\epsilon_{k\sigma}$) between sites on sublattice 1 and 2. The CI is characterized by two semicircular bands having opposite sign of the hopping parameter and a k-independent hybridization V. The diagonal dispersion in the CI corresponds to intra-band electron hopping, while the off-diagonal dispersion in the IBI corresponds to inter-band electron hopping. By varying the parameter x from 1 to 0, we can interpolate smoothly between a purely ionic limit (for $x = 1$) and a purely covalent limit($x = 0$). The percentage of covalency in the ionic band insulator increases as we decrease x from 1 to 0.

The motivation to build and study the above Hamiltonian is twofold: (a) There are three primary chemical bonds namely ionic, covalent and metallic bonds and in general, there is no perfect ionic bond i.e., it always has partial covalency. Quantifying the covalency or the ionicity of a given bond is not without ambiguities[21, 22]. Depending upon the percentage of covalency in the ionic bond, properties of the system changes drastically[21, 22]. Equation 6.5 is one the simplest and of course, non-unique, ways of parametrizing a system wherein the bonding has an ionic as well as covalent character. (b) Another perspective from the view point of real materials is that the non-interacting Hamiltonian $\mathbf{H}_\sigma(\mathbf{k})$ could have both inter-unit cell and intra-unit cell hybridizations, where inter-unit cell hopping is often neglected in model calculations[23].

Throughout the chapter we have considered the case where V = Δ and $\epsilon_k = \tilde{\epsilon}_k$. The structure of $\mathbf{H}_\sigma(\mathbf{k}, x)$ strongly affects the structure of the impurity Greens functions and for orbital (or sublattice) 1, it is given by,

$$G_{1\sigma}(\omega^+) = \int d\epsilon \frac{\zeta_{2\sigma}(\omega^+,\epsilon)\rho_0(\epsilon)}{\zeta_{1\sigma}(\omega^+,\epsilon)\zeta_{2\sigma}(\omega^+,\epsilon) - [V(1-x)+\epsilon x]^2}\,, \tag{6.6}$$

where

$$\zeta_{1\sigma}(\omega^+,\epsilon) = \omega + i\eta + \mu - [Vx + \epsilon(1-x)] - \Sigma_{1\sigma}(\omega^+)\,,$$
$$\zeta_{2\sigma}(\omega^+,\epsilon) = \omega + i\eta + \mu + [Vx + \epsilon(1-x)] - \Sigma_{2\sigma}(\omega^+)\,,$$

and $\rho_0(\epsilon) = \frac{2}{\pi D}\sqrt{1-(\epsilon/D)^2}$. $D = 1$ is our energy unit and η is the convergence factor. In the half-filling case, the Hamiltonian has mirror type symmetry between orbitals, which reflects in the impurity Green's function and self-energy in the following way,

$$G_{1\sigma}(\omega^+) = -\left[G_{2\sigma}(-\omega^+)\right]^*\,, \tag{6.7}$$
$$\Sigma_{1\sigma}(\omega^+) = U - \left[\Sigma_{2\sigma}(-\omega^+)\right]^*\,. \tag{6.8}$$

By using above self-energy symmetry relation, we can readily show,

$$\zeta_{1\sigma}(\omega^+,\epsilon) = -[\zeta_{2\sigma}(-\omega^+,\epsilon)]^*\,, \tag{6.9}$$

then equation 6.6 can be written as,

$$G_{1\sigma}(\omega^+) = \int d\epsilon \frac{\zeta^*_{1\sigma}(-\omega^+,\epsilon)\rho_0(\epsilon)}{\zeta_{1\sigma}(\omega^+,\epsilon)\zeta^*_{1\sigma}(-\omega^+,\epsilon) + [V(1-x)+\epsilon x]^2}\,. \tag{6.10}$$

Now we are going to present a few analytical results for the density of states at the Fermi level ($\omega = 0$) and subsequently, we will discuss our numerical results.

6.3 Results and Discussion:

6.3.1 Analytical results: T=0

We assume that in the band insulator and metallic phases, a Fermi-liquid expansion of self-energy holds, namely that $\Sigma(\omega) \overset{\omega\to 0}{\to} \Sigma(0) + \omega(1 - 1/Z) + \mathcal{O}(\omega^2)$. Then, the value of imaginary part of self-energy at zero frequency is $\text{Im}\Sigma_{1\sigma}(0) = 0$, and the corresponding density of states (DOS) $D_{1\sigma}(0) = -\frac{1}{\pi}\text{Im}G_{1\sigma}(0)$ is given by,

$$D_{1\sigma}(0) = \int \frac{d\epsilon\rho_0(\epsilon)\frac{\eta}{\pi}}{\eta^2 + [\text{Re}(\zeta_{1\sigma}(0,\epsilon))]^2 + [V(1-x) + \epsilon x]^2} . \tag{6.11}$$

Where $\text{Re}(\zeta_{1\sigma}(0,\epsilon))$=$[\mu - (Vx + \epsilon(1-x)) - \text{Re}\Sigma_{1\sigma}(0)]$. For a metallic system there should be a finite DOS at the Fermi level, while in the case of insulators, it should be zero. In the following sub-sections for different values of x, we are going to find the conditions for existence of metallicity.

(a) x=1 (Ionic band insulator)

By substituting $x = 1$ in equation 6.5 the non-interacting $\mathbf{H}_\sigma(\mathbf{k}, x))$ reduces to:

$$\mathbf{H}_\sigma(\mathbf{K}) = \begin{pmatrix} V & \epsilon_k \\ \epsilon_k & -V \end{pmatrix} . \tag{6.12}$$

In literature it is called an "ionic Hubbard model (IHM)", where there are two semi-circular electronic bands with staggered ionic potential V and -V and $\epsilon_{k\sigma}$ is the dispersion of the bands. The name ionic band insulator suggests the non-interacting excitation spectrum ($\text{E}_k = \sqrt{\epsilon_k^2 + V^2}$) has a gap due to ionic potential (V). The

DOS at the Fermi level is given by,

$$D_{1\sigma}(0) = \int \frac{d\epsilon \rho_0(\epsilon)\frac{\eta}{\pi}}{[\eta^2 + \epsilon^2 + (\mu - \mathrm{Re}\Sigma_{1\sigma}(0) - V)^2]} \,. \tag{6.13}$$

By taking the limit $\eta \to 0$, we get

$$D_{1\sigma}(0) = \int d\epsilon \rho_0(\epsilon) \delta\left(\sqrt{\epsilon^2 + (\mu - \mathrm{Re}\Sigma_{1\sigma}(0) - V)^2}\right) \,. \tag{6.14}$$

This expression states that if $\mu - \mathrm{Re}\Sigma_{1\sigma}(0) - V = 0$ then $\mathrm{D}_{1\sigma}(0) = \rho_0(0)$, else $\mathrm{D}_{1\sigma}(0)$ = 0. For a given V, in the non-interacting case the condition is never satisfied while in the interacting case it can only be satisfied for a single value of U. Thus, the metallic phase (because this state is adiabatically connected to U=0 and V=0 state) for x=1 exists only on a single line ratherthan a region of U values in the U-V phase diagram. In the limit of $V \to \infty$ and U $\to \infty$, $\mathrm{Re}\Sigma_{1\alpha}(0) \to 0$, this implies the asymptote of the metallic phase is $\frac{U}{2}$=V, which agrees exactly with the atomic limit.

(b) x=0 (covalent band insulator)

In this limit, $\mathbf{H}_\sigma(\mathbf{k}, x)$ can be written as,

$$\mathbf{H}_\sigma(\mathbf{K}) = \begin{pmatrix} \epsilon_k & V \\ V & -\epsilon_k \end{pmatrix} \,. \tag{6.15}$$

In the the literature the systems defined by this type of Hamiltonian are called as "Covalent band insulators (CBI)", where there are two semi-circular electronic bands of dispersion $\epsilon_{k\sigma}$, -$\epsilon_{k\sigma}$ and k independent hybridization(V) between the orbitals. The name covalent band insulator suggests that the gap in the non-interacting excitation spectrum ($\mathrm{E}_k = \sqrt{\epsilon_k^2 + V^2}$) is due to the inter-orbital hybridization V (i.e., covalency). The two bands have dispersion with opposite in sign ensuring the finite gap in non-interacting excitation spectrum, E_k, for any value of V. The DOS at the Fermi level, for x=0, reduces to the following form,

$$D_{1\sigma}(0) = \int \frac{d\epsilon \rho_0(\epsilon)\frac{\eta}{\pi}}{[\eta^2 + V^2 + (\mu - \mathrm{Re}\Sigma_{1\sigma}(0) - \epsilon)^2]} \,. \tag{6.16}$$

By taking the limit $\eta \rightarrow 0$, we get

$$\begin{aligned} D_{1\sigma}(0) &= \int d\epsilon \rho_0(\epsilon)\delta\left(\sqrt{V^2 + (\mu - \mathrm{Re}\Sigma_{1\sigma}(0) - \epsilon)^2}\right) \\ &= 0 \,\mathrm{for\,any\,non-zero\,V}\,. \end{aligned} \tag{6.17}$$

Thus for the covalent band insulators, interactions do not close the gap, no matter how strong they are. That means there is no existence of metallicity in the covalent band insulators.

(c) x=0.5

It corresponds to the case where the ionicity and covalency are in equal ratio and the structure of $\mathbf{H}_\sigma(\mathbf{k}, x)$ is given by,

$$\mathbf{H}_\sigma(\mathbf{K}) = 0.5 * \begin{pmatrix} V + \epsilon_{k\sigma} & V + \epsilon_{k\sigma} \\ V + \epsilon_{k\sigma} & -(V + \epsilon_{k\sigma}) \end{pmatrix} \,. \tag{6.18}$$

The DOS at the Fermi level is given by,

$$D_{1\sigma}(0) = \int \frac{d\epsilon \rho_0(\epsilon)\frac{\eta}{\pi}}{\eta^2 + \frac{(\epsilon+V)^2}{4} + [\mu - \mathrm{Re}\Sigma_{1\sigma}(0) - (\frac{\epsilon+V}{2})]^2} \,. \tag{6.19}$$

In the non-interacting case i.e., U=0 ($\Rightarrow \mu$=0 & $\mathrm{Re}\Sigma_{1\sigma}(0)$=0),

$$D_{1\sigma}(0) = \int \frac{d\epsilon \rho_0(\epsilon)\frac{\eta}{\pi}}{\eta^2 + \frac{(\epsilon+V)^2}{2}} \,, \tag{6.20}$$

$$D_{1\sigma}(0) = \int d\epsilon \rho_0(\epsilon)\delta\left(\frac{\epsilon+V}{\sqrt{2}}\right) = \rho_0(-V)\sqrt{2}\,,$$
$$= \frac{2\sqrt{2}}{\pi D}\sqrt{1-\left(\frac{-V}{D}\right)^2}\,. \quad (6.21)$$

Thus, there is finite DOS at the Femi-level in the non-interacting case, i.e., the ground state is a metal. This can also be proven from the non-interacting excitation spectrum (E$_k = \sqrt{2}(\epsilon_k+V)$), which has zero gap. For finite U the DOS at Fermi-level is given by,

$$D_{1\sigma}(0) = \int d\epsilon\rho_0(\epsilon)\delta\left(\sqrt{\frac{(\epsilon+V)^2}{4}+\left(\mu-\mathrm{Re}\Sigma_{1\sigma}(0)-\frac{(\epsilon+V)}{2}\right)^2}\right)\,, \quad (6.22)$$

and it is finite only when $\frac{U}{2} - \mathrm{Re}\Sigma_{1\sigma}(0) = 0$. When U $\rightarrow 0^+$, $\frac{U}{2} - \mathrm{Re}\Sigma_{1\sigma}(0) \neq 0$ since, $\mathrm{Re}\Sigma_{1,\sigma}(0) \approx Un_{1\sigma} \neq \frac{U}{2}$. Thus, the metallic phase exists only at U = 0, beyond which we get a band insulator for a range of U values. As we increase the U value, $\frac{U}{2} - \mathrm{Re}\Sigma_{1\sigma}(0)$ decreases, since n$_{1,\sigma} \rightarrow 0.5$. Thus a second interaction induced metallic phase arises at a finite U value when $\mu - \mathrm{Re}\Sigma_{1\sigma}(0) = 0$, beyond which the system becomes a Mott insulator. An interaction induced band insulator sandwitch between two metallic phases emerge due to the local electronic correlations.

(d) 0.5> x <1.0 and 0> x <0.5

In the general case, the DOS at Fermi level is given by,

$$D_{1\sigma}(0) = \int d\epsilon\rho_0(\epsilon)\delta\left(g(\epsilon)\right)\,. \quad (6.23)$$

Where g(ϵ) is given by,

$$g(\epsilon) = \sqrt{(V(1-x)+\epsilon x)^2 + (\mathrm{Re}(\zeta_{1\sigma}(0,\epsilon)))^2}$$
$$= \sqrt{(V(1-x)+\epsilon x)^2 + [\mu - \mathrm{Re}\Sigma_{1\sigma}(0) - (Vx+\epsilon(1-x))]^2}\,. \quad (6.24)$$

When g(ϵ) = 0 then there are finite DOS at the Fermi level. It is possible only when,

$$\epsilon = \frac{-V(1-x)}{x} \quad \& \quad \mu - \mathrm{Re}\Sigma_{1\sigma}(0) - (Vx - V\frac{(1-x)^2}{x}) = 0.$$

If $\mu - \mathrm{Re}\Sigma_{1\sigma}(0) = -V\frac{(1-2x)}{x}$, then

$$\begin{aligned} \mu - \mathrm{Re}\Sigma_{1\sigma}(0) - (Vx + \epsilon(1-x)) &= -V\frac{(1-2x)}{x} - Vx - \epsilon(1-x) \\ &= -\frac{(1-x)}{x}[V(1-x) + \epsilon x] \end{aligned} \tag{6.25}$$

After substituting the above equation in equation 6.24, we can write g(ϵ) as,

$$\begin{aligned} g(\epsilon) &= \sqrt{1 + \frac{(1-x)^2}{x^2}(V(1-x) + \epsilon x)^2} \\ &= \sqrt{x^2 + (1-x)^2}\left(\epsilon + V\frac{(1-x)}{x}\right) \end{aligned} \tag{6.26}$$

If $\mu - \mathrm{Re}\Sigma_{1\sigma}(0) + V(\frac{1-2x}{x})$= 0 satisfied for some U-value, then

$$D_{1\sigma}(0) = \frac{1}{\sqrt{x^2 + (1-x)^2}}\rho_0\left(-\frac{V(1-x)}{x}\right) \tag{6.27}$$

$$= \frac{1}{\sqrt{x^2 + (1-x)^2}}\frac{2}{\pi D}\sqrt{1 - \left(\frac{-V(1-x)}{x}\right)^2}. \tag{6.28}$$

For a given x, whether the condition $\mu - \mathrm{Re}\Sigma_{1\sigma}(0) + V(\frac{1-2x}{x}) = 0$ is satisfied or not is completely decided by $n_{1\sigma}$. For $x > \frac{1}{2}$ (i.e., 1-2x < 0), if $n_{1\sigma}$<0.5, then $\mathrm{Re}\Sigma(0) \approx$ U$n_{1\sigma} < \frac{U}{2}$, and hence, $\frac{U}{2}$-$\mathrm{Re}\Sigma_{1\sigma}(0)$>0 i.e., a specific U might exists which satisfies the condition. If $n_{1\sigma}$>0.5 then for any U value the condition is never satisfied. For x < $\frac{1}{2}$(i.e., 1-2x > 0), the condition $\mu - \mathrm{Re}\Sigma(0) = -\frac{1-2x}{x}$ is never satisfied unless $n_{1\sigma}$ > 0.5.

6.3.2 Analytical results: T>0

At low enough temperatures the expression for Fermi-liquid form of self energy is, Im $\Sigma_{1\sigma}(\omega) \sim \max(\omega^2 + T^2)$. It has a finite value at zero frequency (i.e., Im $\Sigma_{1\sigma}(0) \neq 0$) then we can write equation 6.10 for zero frequency as,

$$G_{1\sigma}(0) = \int \frac{d\epsilon\rho_0(\epsilon)[-i\mathrm{Im}\Sigma_{1\sigma}(0) + \mathrm{Re}(\zeta^*_{1\sigma}(0,\epsilon))]}{[\mathrm{Im}\Sigma_{1\sigma}(0)]^2 + [V(1-x) + \epsilon x]^2 + [\mathrm{Re}(\zeta^*_{1\sigma}(0,\epsilon))]^2}, \tag{6.29}$$

and the corresponding DOS as,

$$D_{1\sigma}(0) = \int \frac{d\epsilon\rho_0(\epsilon)[\mathrm{Im}\Sigma_{1\sigma}(0)]}{[\mathrm{Im}\Sigma_{1\sigma}(0)]^2 + [V(1-x) + \epsilon x]^2 + [\mathrm{Re}(\zeta^*_{1\sigma}(0,\epsilon)]^2}. \tag{6.30}$$

The above integral is finite when $[V(1-x)+\epsilon x]^2 + [\mathrm{Re}(\zeta^*_{1\sigma}(0,\epsilon)]^2 \leq [\mathrm{Im}\Sigma_{1\sigma}(0)]^2$ and it will be satisfied for a range of U values. The integral has a maximum value only when $[V(1-x) + \epsilon x]^2 + [\mathrm{Re}(\zeta^*_{1\sigma}(0,\epsilon)]^2$=0. Thus, at finite temperature, we have a metallic region rather than a metallic point (which is observed at T=0).

6.3.3 Numerical results

Now we are going to describe the numerical results, which are obtained by solving the auxiliary Anderson impurity model of equation 6.1 with in DMFT. For zero temperature calculations we have used iterated perturbation theory (IPT) which is developed[24] by the authors of this thesis, and for finite temperature calculations, we have used numerically exact method called hybridization expansion continuous-time quantum Monte-Carlo (HY-CTQMC)[25, 26]. In the numerical calculations we have fixed the value of V=0.5.

(a) x=1 (ionic band insulator)

In the Hartree-Fock (HF) theory the excitation spectrum $\left[E_k = \sqrt{\epsilon_k^2 + (V - U\frac{\delta n}{2})^2}\right]$ has a gap of $(V - U\frac{\delta n}{2})$ for any non-zero value of V and it becomes gapless only when V =0 ($\Rightarrow \delta n$ = ($n_{1\sigma}$-$n_{2\sigma}$)=0). So for a given δn, the value of Re$\zeta_{1\sigma}(0)$(i.e.,

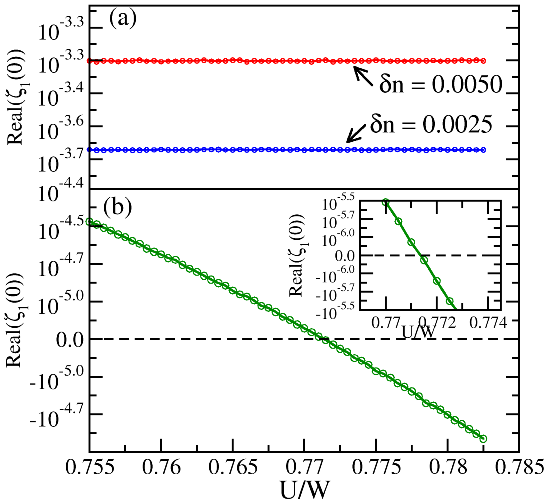

Figure 6.1: (color online) (a) Re$\zeta_{1\sigma}(0)$ as a function of U for δn = 0.0025,0.0050 obtained from HF-theory (b) Re$\zeta_{1\sigma}(0)$ as a function of U for δn = 0.0025 obtained from DMFT (IPT). In the inset we have zoomed on the zero crossing to show that we have a single zero crossing as a function of U (We have used η=10^{-9} and energy unit D = $\frac{W}{2}$ = 2).

$\mu - \mathrm{Re}\Sigma_{1\sigma}(0) - V)$ is constant with respect to U and it goes to zero only when δn=0. Thus, the metallic phase exists in HF-theory only when V = 0 ($\Rightarrow \delta n = 0$) and indeed we observed the same as shown in figure 6.1(a). Once we turn on local electronic fluctuations beyond static (HF) theory a completely different picture emerges. In figure 6.1(b), we have plotted Re$\zeta_{1\sigma}(0)$ as a function of U for δn = 0.0025 which is obtained by using IPT. When we increase the U value, Re$\zeta_{1\sigma}(0)$ starts decreasing and it reaches zero at a critical value, U$_c$. Above critical value, U$_c$, Re$\zeta_{1\sigma}(0)$ changes its sign. The local electronic correlations in the ionic Hubbard model initially renormalizes the gap in the non-interacting spectrum(charge gap) and at critical value, U$_c$, charge gap closes. Above U$_c$ gap opens in the spectral function. Hence in the U-V phase diagram of IHM, metallic phase exists only on a single line, rather than a finite range of U values.

We have calculated the Fermi-level spectral weight $\tilde{A}_{1\sigma} = -G_{1\sigma}(\tau = \frac{\beta}{2})/T\pi$ as a function of $\frac{U}{W}$ for different temperatures by using HY-CTQMC and plotted in

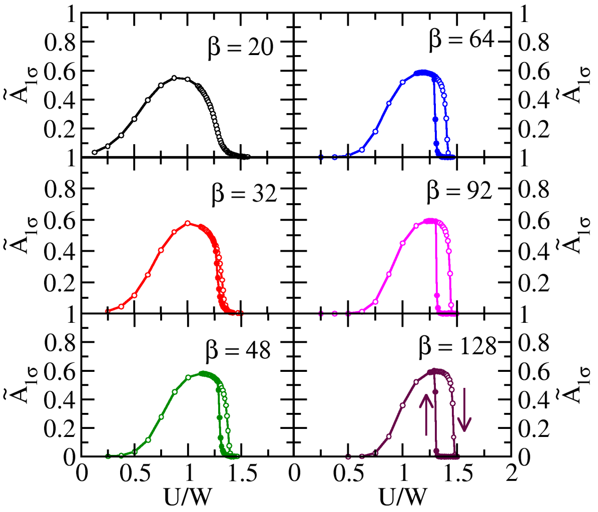

Figure 6.2: (color online) Fermi-level spectral weight $\tilde{A}_{1\sigma}$ as a function of U for different β values obtained from HY-CTQMC for x=1.(Downarrow corresponds to increase in U, Uparrow corresponds to decrease in U, Energy unit D = $\frac{W}{2}$ = 1)

figure 6.2. We will first focus on the results obtained for the lowest temperature ($\frac{1}{T} = \beta = 128$) that we have reached through our calculations. At low U value, the Fermi-level spectral weight $\tilde{A}_{1\sigma}$ is zero up to $\frac{U}{W} = 0.75$. Beyond that, it starts increasing with U and it reaches a maximum value(~ 0.6) around $\frac{U}{W} = 1.25$. Then it becomes constant for a range of U value. As we increase the U-value further, there is a discrete jump (first order transition) in $\tilde{A}_{1\sigma}$, where the DOS at the Fermi-level is zero. This means, for small U-values we have a band insulator (BI) and for intermediate U-values BI crosses-over (U_{co}) to a metal (M) then finally it becomes Mott-insulator (MI) for large U-values ($> U_{c1}$). At the same temperature ($\beta = 128$), starting with MI state, we reduce the U-value, system went to a metallic state at U_{c2} which is smaller than U_{c1}. The region between critical values(U_{c2}, U_{c1}) corresponds to the coexistence region, where M and MI solutions simultaneously exist. As we increase the temperature, beyond β=32 the transition from M to MI turns into a crossover. At finite temperature, we observed a metallic region in the ionic Hubbard model rather than a metallic point.

We find the crossover value (U_{co}) from BI to M by a linear fit of $\tilde{A}_{1\sigma}$ to the

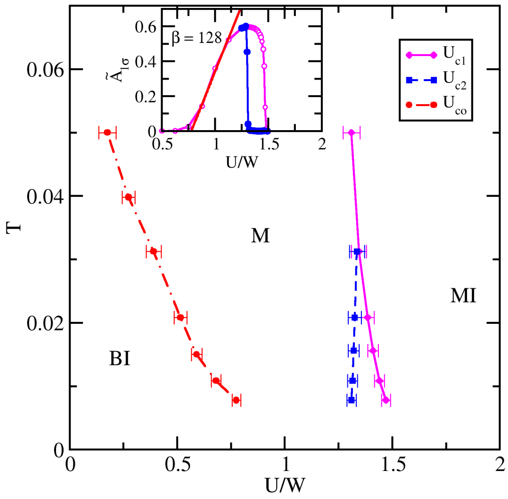

Figure 6.3: (color online) Finite temperature phase diagram of Ionic band Insulator (x=1.0) obtained from HY-CTQMC (BI: Band Insulator, M: Metal and MI: Mott Insulator), Inset: Linear fit to $\tilde{A}_{1\sigma}$ in the metallic region at β=128.

region where it grows linearly with U, which has shown in the inset of figure 6.3. We identified the critical values (U_{c2},U_{c1}) based on low frequency behaviour of imaginary part of self energy (MI state: -Im $\Sigma_{1\sigma}(i\omega_n) \propto \frac{1}{\omega_n}$ and M state: -Im $\Sigma_{1\sigma}(i\omega_n) \propto \omega_n$). We have used the same procedure throughout the chapter to find critical values at each temperature and x. We have determined the critical values at each temperature, for $x = 0$ as shown in figure 6.3. As we increase the temperature, the metallic region which is bounded between two insulators increases (i.e., BI region decreases) and the coexistence region between M and MI decreases and finally disappears at β=32. By extrapolating the critical values in figure 6.3 to zero temperature, we cannot conclude the existence of metallic phase. But as we increase the U value, CTQMC yields the impurity occupancy which is always less than 0.5 (i.e., $n_{1\sigma} < 0.5$). That means there will be a single U value, where the metallic condition $\mu - \text{Re}\Sigma_{1\sigma}(0) = V$ satisfies, since $\text{Re}\Sigma_{1\sigma}(0) < \frac{U}{2}$. The existence of metallic region at finite temperature in IHM for a broad range of U values is mainly due to the proximity of existence of metallic point at zero temperature which is confirmed by analytics, IPT and HY-CTQMC.

(b) x=0 (covalent band insulator)

We have calculated the low energy quasi-particle weight (Z) and gap in the spectral function (charge gap: Δ_c) which are obtained from MO-IPT and plotted in figure 6.4 as a function of U. As we increase the U-value, Z smoothly decreases, because of correlations. On the other hand, charge gap is also goes to zero with U. But we didn't observe the closing of gap in the spectral function for any U-value before the system goes to MI state (Z $\sim$ 0). This means as we increase the U value, system evolves from BI to MI without a metallic point, which is consistent with our analytical results. Local electronic correlations in the CBI renormalizes the charge gap, but they can't close the gap. The critical U where the system is goes from BI to MI is almost at twice the bandwidth because of strong bonding nature of a covalent character.

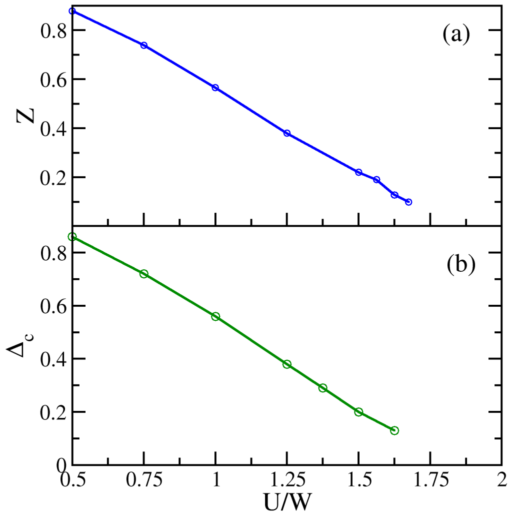

Figure 6.4: (color online) (a) Quasi particle weight(Z) as a function of $\frac{U}{W}$ obtained from IPT. (b) Charge gap as a function of $\frac{U}{W}$ obtained from IPT.(We have used η= 10^{-2} and energy unit is D=$\frac{W}{2}$=2)

We have calculated the $\tilde{A}_{1\sigma}$ as a function $\frac{U}{W}$ from HY-CTQMC and plotted in figure 6.5 for different temperatures. The behavior of $\tilde{A}_{1\sigma}$ for x = 0(CBI) is completely different from x = 1(IHM) case. For example, $\tilde{A}_{1\sigma}$ is zero up to large value of $\frac{U}{W}$(=2.0) even though both insulators have same band-widths, i.e., BI phase in CBI persists up to large U values. The increment of $\tilde{A}_{1\sigma}$ with respect to U increases rather sharp and it is finite for a narrow range of U values in compare with IHM.

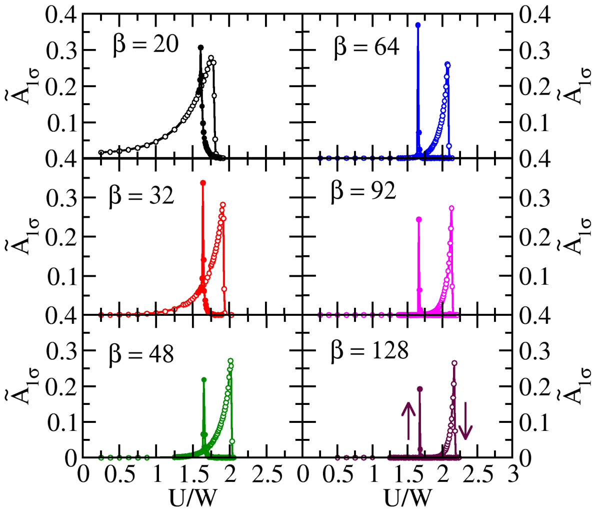

Figure 6.5: (color online) Fermi-level spectral weight as a function of $\frac{U}{W}$ for different β values obtained from HY-CTQMC for x=0.0 (Energy unit D=W/2=1.0)

As we increase U, system first evolves from BI to M (U$_{co}$) then finally went to a MI state at critical U$_{c1}$. The transition from M to MI is a first-order type and it persists even for higher temperatures. For fixed β, we have also calculated the $\tilde{A}_{1\sigma}$ value by decreasing U value from MI then system evolves into a BI state at critical U$_{c2}$ without an intermediate metallic state. The region between critical U$_{c2}$ and U$_{c1}$ corresponds to the coexistence region, where BI, M, and MI solutions coexist.

We extracted the critical values at each temperature from the procedure mentioned it earlier and plotted in figure 6.6. We observed BI phase for a wide range of U values. At low-temperature metallic region exists for a narrow range of U values and it broadens as we increase the temperature. Previous calculations on CBI by using HY-CTQMC have not found such a narrow metallic region. The coexistence region(U$_{c2}$, U$_{c1}$) between BI, M, and MI decreases as we increase temperature. The critical values obtained from HY-CTQMC at low temperature confirms that there is no metallic point in CBI at zero temperature, and it is consistent with the analytical arguments and IPT results.

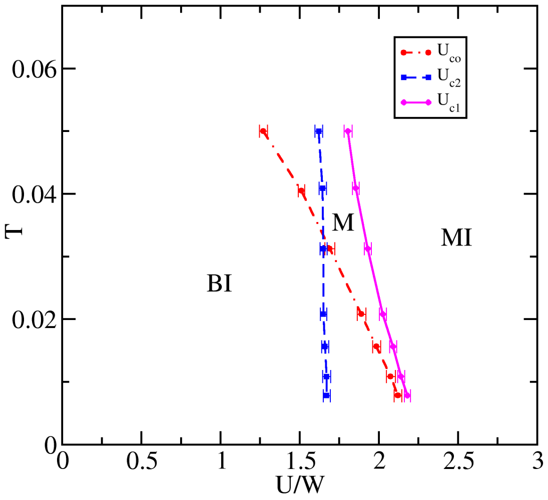

Figure 6.6: (color online) Finite temperature phase diagram of Covalent band Insulator (x=0.0) on T Vs U plane (Energy unit D=W/2=1.0).

(c) x=0.5 (Equal ratio of ionicity and covalency)

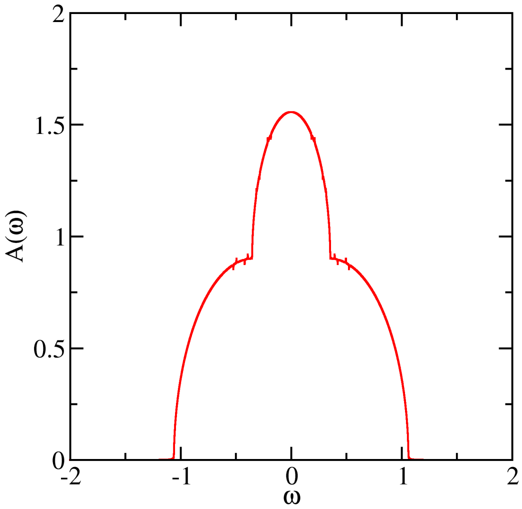

Figure 6.7: (color online) Non-interacting spectral function for x=0.5 (We have used η=10^{-2} and energy unit = D = $\frac{W}{2}$ = 1)

The non-interacting spectral function A(ω)=$\rho_{1\sigma}(\omega) + \rho_{2\sigma}(\omega)$ plotted in figure 6.7 for x = 0.5 has finite DOS at Fermi level and the value is 0.7797, which is good agreement with the analytical expression of $\sqrt{2}\rho(-V)$ i.e., non-interactng ground state is a metal.

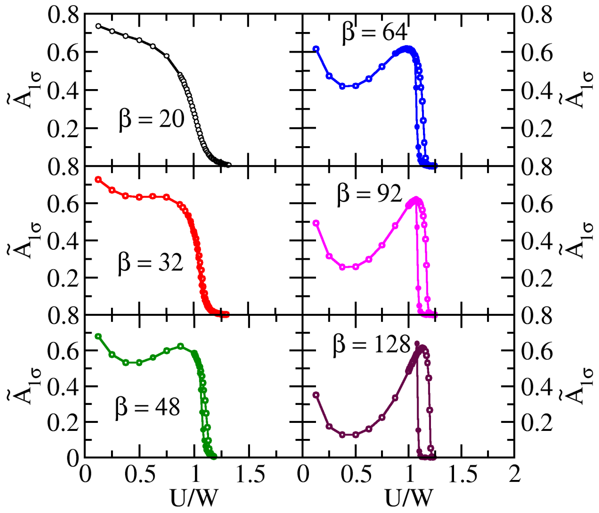

Figure 6.8: (color online) Fermi-level spectral weight as a function of $\frac{U}{W}$ obtained from HY-CTQMC for different β values and x=0.5 (Energy unit D = $\frac{W}{2}$ = 1).

We have calculated the Fermi-level spectral weight $\tilde{A}_{1\sigma}$ as a function of U from HY-CTQMC for different temperatures and plotted in figure 6.8. At low temperature (β=128) as we increase U, there is a minimum in $\tilde{A}_{1\sigma}$ before the system went to a MI state and the highest value of 0.6 in $\tilde{A}_{1\sigma}$ reached at $\frac{U}{W}$=1.1. The extrapolation of $\tilde{A}_{1\sigma}$ to U = 0 axis confirms there is a finite weight at Fermi-level. There are two metallic regions one is at small $\frac{U}{W}$(<0.5) another one is at large $\frac{U}{W}$(=1.1). An interaction induced band insulator has been emerged in between these two metallic regions, and MI state is at large U values. As a function of temperature, the minimum of $\tilde{A}_{1\sigma}$ which has observed at low-temperature starts filling up.

Next, we need to address whether the metallic behaviour observed at low U values, is it due to thermal broadening or not? To know this we did low temperature (β=300) calculations using HY-CTQMC then we plotted $\tilde{A}_{1\sigma}$ in figure 6.9(a). The extrapolation of $\tilde{A}_{1\sigma}$ to $\frac{U}{W}$=0 axis confirms that there is a metal at U=0, i.e., the emergence of metal is not due to thermal broadening. Once we turn on U, then the non-interacting metal turn into a band insulator that means correlations created a band insulator. It is well known that correlations in the metal create MI (charge

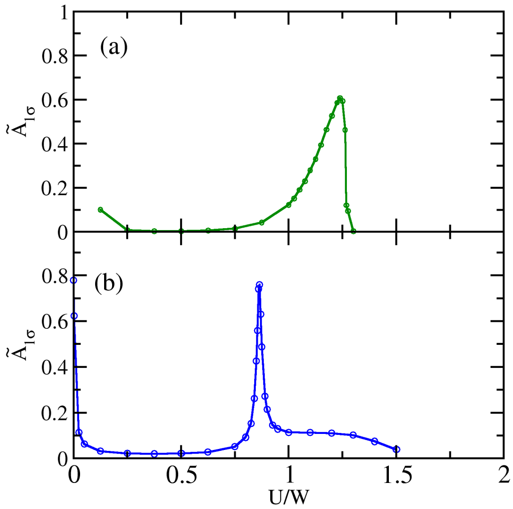

Figure 6.9: (color online)(a) Fermi-level spectral weight as a function of $\frac{U}{W}$ obtained from HY-CTQMC for x=0.5 and $\beta = 300$ (c) Fermi-level spectral weight as a function $\frac{U}{W}$ obtained from IPT for x=0.5 and $\beta = 300$ (Energy unit D=$\frac{W}{2} = 1$).

gap is an order of U). The local electronic correlations turn band insulator into a metal seems counter-intuitive, but the creation of band insulator due to electronic correlations seems even more counter-intuitive. It is very difficult to reach low U-values using HY-CTQMC to find the $\tilde{A}_{1\sigma}$ value and to compare it with our analytical value. So we have done IPT calculations at β=300 and we plotted $\tilde{A}_{1\sigma}$ as a function of $\frac{U}{W}$ in the figure 6.9(b). We can clearly see at U=0, there is a metal $\tilde{A}_{1\sigma} = 0.76$, which is in close agreement with the exact value derived from the analytical expression. IPT also predicted two metallic regions, a BI region in between them and MI region at large U. The critical U-values predicted from IPT are somewhat different from HY-CTQMC, due to the lack of correct strong coupling behavior in the interpolative methods.

In figure 6.10, we have plotted the critical values as a function of $\frac{U}{W}$ obtained from HY-CTQMC at different temperatures. According to analytical predictions, metallic behavior which exists at U=0 turns into a BI with increase of U and there is a possibility of existence of second metallic phase at larger U-value if the condition $\mu - Re\Sigma_{1\sigma}(0)$=0 satisfied, before the BI turns into a MI. The extrapolation of critical lines to zero temperature axis gives a metallic point at zero U-value and it turns

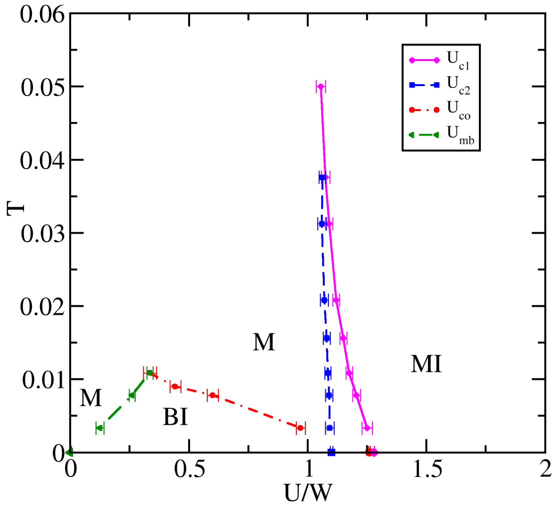

Figure 6.10: (color online) Finite temperature phase diagram (T Vs U) for x=0.5 covalency (Energy unit D=W/2=1).

into a BI with increase of U at critical U$_{mb}$. Finally the BI went to MI state without second metallic phase. The reason for the absence of second metallic phase is because of the metallic condition ($\mu - Re\Sigma_{1\sigma}(0)$=0) never satisfied, since n$_{1\sigma}$ <0.5 for any value of U. At finite temperature, we observed two metallic phases followed by BI and MI insulators up to β of 100 and beyond this, the BI region disappears and only M and MI regions survives. The metallic behaviour observed at finite temperature for large U values is due to the thermal broadening and the region between critical values (U$_{c2}$,U$_{c1}$) corresponds to the coexistence of M and MI solutions.

(d) 0>x<0.5 and 0.5>x<1.0

Before going to analyze the interacting case results for general x value, let's focus on the results from the non-interacting case. In figure 6.11, we have plotted the occupancy of each orbital i.e., n$_{1\sigma}$, n$_{2\sigma}$ and the gap in the spectral function as a function of x, at V=0.5. When $x = 1$, due to staggered ionic potential, the occupancy of orbital 2 is almost filled while the orbital 1 is almost empty and the gap in the spectral function is in the order of V=0.5. As we decrease x from 1 up to x=0.5,

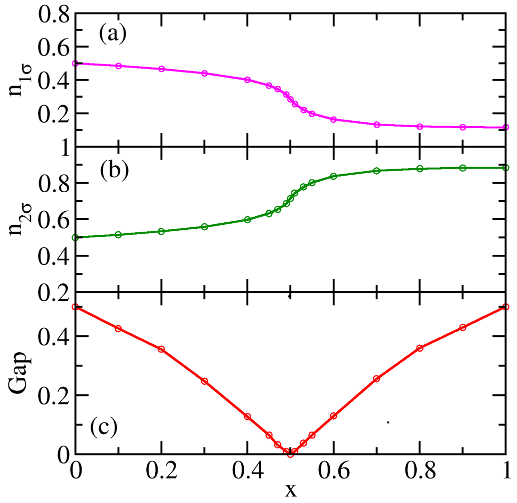

Figure 6.11: (color online) Non-interacting occupancy (a) for orbital 1 (b) for orbital 2 and (c) gap in the spectral function as function of x (V = 0.5 and Energy unit=D=$\frac{W}{2}$=1)

there is no much change in the orbital occupancies. On the other hand, the gap in the non-interacting spectrum smoothly decreases, and reaches zero at x=0.5. As we decrease x, below 0.5, then the occupancy of the orbital 2 decreases while it increases for orbital 1 and the gap in the spectral function increases. For x=0, the gap reaches a value of 0.5 and the corresponding occupancy of each orbital is 0.5.

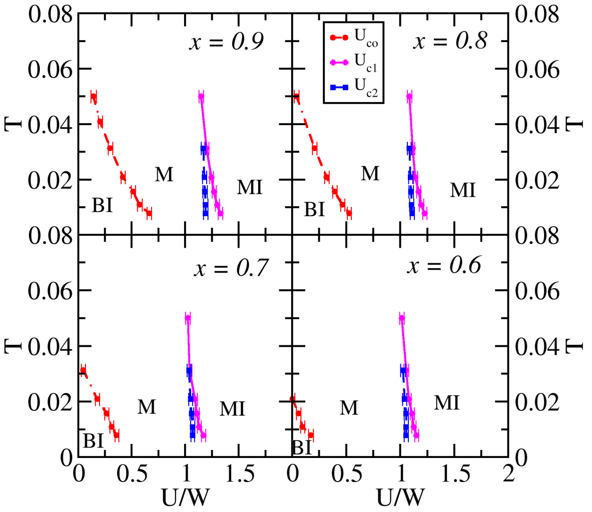

Figure 6.12: (color online) T Vs U phase diagram for 0.5> x <1.0 (Energy unit = D = $\frac{W}{2}$=1).

At each temperature, we have calculated the critical values as a function of $\frac{U}{W}$ for 0.5> x <1.0 and plotted in figure 6.12. As we decrease x from 1, then the metallic region that exists between BI and MI increases (i.e., a small amount of covalency favors metallicity) and the coexistence region between metal and MI decreases. From analytical results we know the condition that needs to be satisfied to get a metallic phase at zero temperature is $\mu - \mathrm{Re}\Sigma(0) = -\frac{1-2x}{x}$. It will be satisfied with a single U-value for 0.5> x <1 and only when $n_{1\sigma}$ <0.5. From finite temperature data by extrapolation of critical curves to T=0 axis we cannot confirm the existence of metallic phase, but we can confirm it from the value of $n_{1\sigma}$. For any value of U, and for 0.5> x <1, we find that $n_{1\sigma}$ <0.5, that means there is a possibility for the existence of metallic point at single U-value at T=0. The metallic region observed at finite temperature is not only due to thermal broadening but also from the existence of metallic point at T=0. As we decrease x from 1, the critical value U_{co} decreases. From this, at least we can speculate, the existence of metallic point at T=0 shifts towards low U-values and it reaches U=0 for some value of x.Indeed, we determined it for x=0.5, where non-interacting ground state itself is a metal.

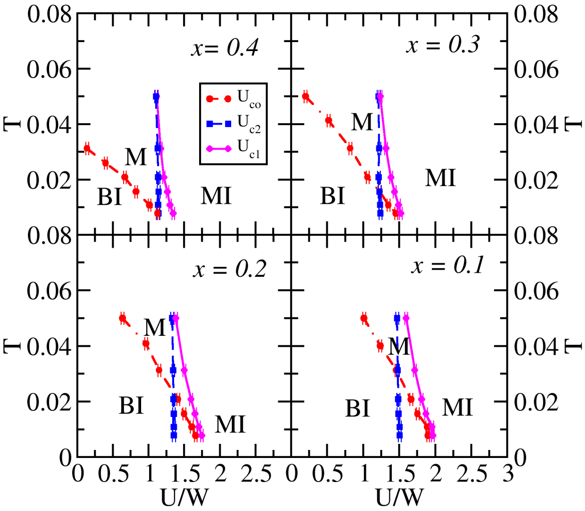

Figure 6.13: (color online) T Vs U phase diagram for 0.0> x <0.5 (Energy unit = D = $\frac{W}{2}$=1)

In figure 6.13, we have plotted the critical values for 0.0> x <0.5. As we decrease x from 0.5, the metallic region sandwiched between BI and MI decreases (i.e., critical value of crossover from BI to M increases) while the coexistence region between BI, M and MI increases. At zero temperature, for 0.0> x <0.5, the metallic condition $\mu - \mathrm{Re}\Sigma(0) = -\frac{1-2x}{x}$, will be satisfied at a single U-value only when $\mathrm{n}_{1\sigma} > 0.5$. For 0.0> x <0.5, and for any value of U, we find that $\mathrm{n}_{1\sigma}$ <0.5 means that there is no chance of satisfying the metallic condition. Thus there is no metallic point at zero temperature. This can also be confirmed from the behavior of critical critical at low enough temperature. The metallic region observed at finite temperature for 0.0> x <0.5 is due to the thermal broadening and this is because of disappearance of metallic point at zero temperature.

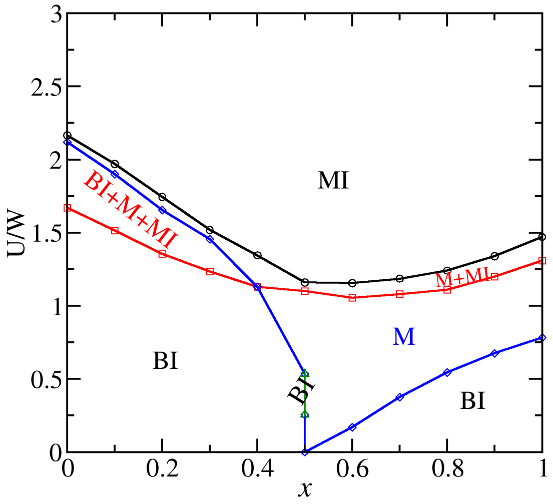

Figure 6.14: (color online) Critical U values Vs x Phase diagram for V = 0.5 and β=128 (Energy unit D=W/2=1)

6.4 Conclusions

We have studied the role of local electronic correlations in different kinds of band insulators by changing the parameter x. Our analytical results predict that there is a metallic point in the IHM model where it is absent for the case of CBI. For x=0.5 non-interacting ground state is a metal but the correlations turns non-interacting metal into a BI. We derived an expression for the value of the density of states at the Fermi level for the general case. We also derived the conditions for the existence of metallic phase in the general value of x. The summary of numerical results are plotted in figure 6.14. Our numerical results confirmed the analytical predictions of the existence of metallic point in IHM while the absence of it in CBI at zero temperature. For x=0.5, non-interacting ground state (GS) is a metal, but with correlations GS changes from metal to a Band Insulator. We observed an interaction induced BI for x=0.5 and this phase was counter-intuitive in the sense of our fundamental understanding of correlation effects. The value of $\mathrm{n}_{1\sigma}$ obtained from HY-CTQMC confirms the existence of metallic point at zero temperature for 0.5< x <1.0 and while there is no such point for 0.0> x <0.5. The metallic point observed for 0.5> x <1.0 moves towards lower U values as we decrease x from 1 then finally it reached U=0 for x=0.5. At finite temperature we observed a broad metallic region for x=1 then it becomes widen as we decrease it from 1. This is because of the existence of metallic point at zero temperature. For x=0.5 at finite temperature we observed a two metallic regions followed by BI and MI. For 0.0> x <0.5, we observed a metal in a narrow range of U values and the range decrease as we decrease x from 0.5. The metal we observed for 0.0> x <0.5 is due to thermal broadening. The electronic correlations favor the metallicity when the covalency is smaller than ionicity, and it has opposite effect when covalency greater than ionicity. Our results will open new directions in the study of electronic correlations of band insulators.

Bibliography

[1] A. M. Turner, A. Vishwanath, and Head, Topological Insulators **6**, 293 (2013).

[2] X. Chen, Z.-C. Gu, Z.-X. Liu, and X.-G. Wen, Phys. Rev. B **87**, 155114 (2013),

URL `http://link.aps.org/doi/10.1103/PhysRevB.87.155114`.

[3] A. P. Kampf, M. Sekania, G. I. Japaridze, and P. Brune, Journal of Physics: Condensed Matter **15**, 5895 (2003), URL `http://stacks.iop.org/0953-8984/15/i=34/a=319`.

[4] S. R. Manmana, V. Meden, R. M. Noack, and K. Schönhammer, Phys. Rev. B **70**, 155115 (2004), URL `http://link.aps.org/doi/10.1103/PhysRevB.70.155115`.

[5] C. D. Batista and A. A. Aligia, Phys. Rev. Lett. **92**, 246405 (2004), URL `http://link.aps.org/doi/10.1103/PhysRevLett.92.246405`.

[6] A. Garg, H. R. Krishnamurthy, and M. Randeria, Phys. Rev. Lett. **97**, 046403 (2006), URL `http://link.aps.org/doi/10.1103/PhysRevLett.97.046403`.

[7] S. S. Kancharla and E. Dagotto, Phys. Rev. Lett. **98**, 016402 (2007), URL `http://link.aps.org/doi/10.1103/PhysRevLett.98.016402`.

[8] L. Craco, P. Lombardo, R. Hayn, G. I. Japaridze, and E. Müller-Hartmann, Phys. Rev. B **78**, 075121 (2008), URL `http://link.aps.org/doi/10.1103/PhysRevB.78.075121`.

[9] N. Paris, K. Bouadim, F. Hebert, G. G. Batrouni, and R. T. Scalettar, Phys. Rev. Lett. **98**, 046403 (2007), URL `http://link.aps.org/doi/10.1103/PhysRevLett.98.046403`.

[10] K. Byczuk, M. Sekania, W. Hofstetter, and A. P. Kampf, Phys. Rev. B **79**, 121103 (2009), URL `http://link.aps.org/doi/10.1103/PhysRevB.79.121103`.

[11] A. Hoang, Journal of Physics: Condensed Matter **22**, 095602 (2010).

[12] A. J. Kim, M. Y. Choi, and G. S. Jeon, Phys. Rev. B **89**, 165117 (2014), URL `http://link.aps.org/doi/10.1103/PhysRevB.89.165117`.

[13] M. Sentef, J. Kuneš, P. Werner, and A. P. Kampf, Phys. Rev. B **80**, 155116 (2009), URL `http://link.aps.org/doi/10.1103/PhysRevB.80.155116`.

[14] A. Euverte, S. Chiesa, R. T. Scalettar, and G. G. Batrouni, Phys. Rev. B **87**, 125141 (2013), URL `http://link.aps.org/doi/10.1103/PhysRevB.87.125141`.

[15] P. Werner and A. J. Millis, Phys. Rev. Lett. **99**, 126405 (2007), URL `http://link.aps.org/doi/10.1103/PhysRevLett.99.126405`.

[16] G. Moeller, V. Dobrosavljević, and A. E. Ruckenstein, Phys. Rev. B **59**, 6846 (1999), URL `http://link.aps.org/doi/10.1103/PhysRevB.59.6846`.

[17] A. Fuhrmann, D. Heilmann, and H. Monien, Phys. Rev. B **73**, 245118 (2006), URL `http://link.aps.org/doi/10.1103/PhysRevB.73.245118`.

[18] S. S. Kancharla and S. Okamoto, Phys. Rev. B **75**, 193103 (2007), URL `http://link.aps.org/doi/10.1103/PhysRevB.75.193103`.

[19] M. Fabrizio, Phys. Rev. B **76**, 165110 (2007), URL `http://link.aps.org/doi/10.1103/PhysRevB.76.165110`.

[20] H. Hafermann, M. I. Katsnelson, and A. I. Lichtenstein, EPL (Europhysics Letters) **85**, 37006 (2009), URL `http://stacks.iop.org/0295-5075/85/i=3/a=37006`.

[21] C. Kittel, *Introduction to Solid State Physics, 8th Edition* (Wiley, 2004), chap. CRYSTAL BINDING AND ELASTIC CONSTANTS, pp. 47–85.

[22] Ashcroft/Mermin, *Solid State Physics* (THOMSON BROOKS/COLE, 2007), chap. Classification of Solids, pp. 373–393.

[23] J. E. Han, M. Jarrell, and D. L. Cox, Phys. Rev. B **58**, R4199 (1998), URL `http://link.aps.org/doi/10.1103/PhysRevB.58.R4199`.

[24] N. Dasari, W. R. Mondal, P. Zhang, J. Moreno, M. Jarrell, and N. Vidhyadhiraja, arXiv preprint arXiv:1504.04097 (2015).

[25] P. Werner, A. Comanac, L. de' Medici, M. Troyer, and A. J. Millis, Phys. Rev. Lett. **97**, 076405 (2006), URL `http://link.aps.org/doi/10.1103/PhysRevLett.97.076405`.

[26] B. Bauer, L. D. Carr, H. G. Evertz, A. Feiguin, J. Freire, S. Fuchs, L. Gamper, J. Gukelberger, E. Gull, S. Guertler, et al., Journal of Statistical Mechanics: Theory and Experiment **2011**, P05001 (2011), URL `http://stacks.iop.org/1742-5468/2011/i=05/a=P05001`.

Chapter 7

A first principles investigation of cubic $BaRuO_3$: A Hund's metal [⋆]

7.1 Introduction

Transition metal oxides (TMOs) have occupied a unique and very significant position in the investigations of correlated electron systems. The interplay of spin, charge and orbital degrees of freedom in the partially filled and localized 3d and 4d orbitals leads to a rich set of phenomena including high temperature superconductivity, colossal magneto-resistance and the Mott metal-insulator transition. Due to the extended nature of 4d orbitals, the corresponding TMOs exhibit strong hybridization with oxygen. This leads to a large crystal field splitting that could be of the order of the local screened Coulomb interaction(U) and a broad 4d band of width W. As a consequence, these materials prefer a low spin state rather than the high spin state.

Furthermore, the wide d-band in 4d-orbital based TMOs such as Ruthenates leads to a moderate screened Coulomb interaction $U \simeq W$ as compared to the much narrower d-band in 3d-orbital based TMOs[1]. Surprisingly however, most of the Ru-based TMOs show strong correlation effects that are reflected in the enhanced

---

[⋆] Nagamalleswararao Dasari, S. R. K. C. Sharma Yamijala, Swapan K. Pati, Manish Jain, T. Saha Dasgupta, Juana Moreno, Mark Jarrell and N. S. Vidhyadhiraja, to be submitted.

linear coefficient of specific heat γ. A few of such Ruthenates are mentioned in Table 7.1, where we have also indicated the magnetic order of the ground state as well as the effective mass computed as the ratio of experimentally[1–4] measured γ to γ_{LDA}, computed[2] within a local density approximation(LDA). The origin of such enhanced effective mass could be a local Coulomb repulsion induced proximity to a insulating state. An alternative origin could be Hund's[1, 5, 6] coupling J(intra-atomic exchange), which, as has been shown recently for several materials, especially Ruthenates[3, 4], leads to their characterization as 'Hund's metals'. A prominent member of this class is $BaRuO_3$ which, depending on synthesis conditions, can exist in four polytypes[7]. These are nine-layered rhombohedral (9R), four-layered hexagonal(4H), six-layered hexagonal(6H) and cubic(3C). The 9R has a paramagnetic insulating (PI) ground state while 4H and 6H are paramagnetic metals(PM). The 3C-$BaRuO_3$ polytype is a ferromagnetic metal with Curie temperature, $T_c = 60$ K, which is much smaller than the value of $T_c(= 160$ K) in $SrRuO_3$[8]. The experimental value of the saturated magnetic moment of 3C-$BaRuO_3$[7] is 0.8 μ_B/Ru, which is far less than 2.8 μ_B/Ru, expected for a low spin state of 4d Ru. It is also smaller than measured value of 1.4 μ_B/Ru in $SrRuO_3$[8]. The observed effective magnetic

Table 7.1: Magnetic ground state and the ratio of γ to γ_{LDA} for 4d Ru-based compounds

Compound	Magnetic order	$\frac{\gamma}{\gamma_{LDA}}$
Sr_2RuO_4	PM	4
$Sr_3Ru_2O_7$	PM	10
$CaRuO_3$	PM	7
$SrRuO_3$	FM < 160 K	4
3C-$BaRuO_3$	FM < 60 K	–
4H-$BaRuO_3$	PM	3.37
6H-$BaRuO_3$	PM	3.37
9R-$BaRuO_3$	PI	1.54

moment (μ_{eff}) in the paramagnetic phase of $BaRuO_3$ and $SrRuO_3$, is however, very close to the S=1 moment. From Table 7.1, we can readily understand that electron correlations in 4H-$BaRuO_3$ and 6H-$BaRuO_3$ are comparable with $SrRuO_3$ and in case of 9R-$BaRuO_3$ they are weak. Although the strength of electron correlations in 3C-$BaRuO_3$ is still unknown, a non-Fermi liquid behavior in the experimental measured resistivity[7, 9]($\rho(T) \propto T^{1.85}$) hint towards a strongly correlated system.

In the present work, the following questions have been addressed: Is 3C-$BaRuO_3$ a correlated metal or not? If yes, then what is the origin and strength of correlations? What is the probable origin of non-Fermi liquid NFL signature[7, 9] in the resistivity? We have employed the dynamical mean field theory(DMFT) framework in combination with an *ab initio* method[10], namely density functional theory(DFT) within the generalized gradient approximation (GGA)[11]. In the DMFT[12] framework, a lattice problem may be mapped on to a single impurity Anderson model with a self-consistently determined bath. The resulting quantum impurity problem has been solved by using hybridization expansion[13, 14] continuous-time quantum Monte-Carlo algorithm (HY-CTQMC). The main finding is that 3C-$BaRuO_3$ is a Hund's correlated metal. Furthermore we find that 3C-$BaRuO_3$ is in a spin-frozen state at temperatures in the neighbourhood of the experimental ferromagnetic transition temperature. This state, we speculate, is the precursor of the ferromagnetic ground state and also a possible origin of the experimentally observed NFL behavior in resistivity.

The rest of the chapter is organised as follows. In Section 7.2, we describe the DFT details and Wannier projection briefly. In Section 7.3, we describe our results from GGA+DMFT(HY-CTQMC) for 3C-$BaRuO_3$. We present our conclusions in the final section.

7.2 Details of the density functional theory calculations and results

Density functional theory (DFT) calculations have been performed within the generalized gradient approximation using the plane wave pseudo-potential code QUANTUM ESPRESSO[15]. We have used ultra-soft pseudo-potentials with Perdew-Burke-Ernzerhof exchange-correlation functional. An 8×8×8 Monkhorst-Pack k-grid is used for optimization together with an 80 Ry energy cutoff and a 640 Ry charge cutoff. The system is considered to be optimized if the forces acting on all the atoms are less than 10^{-4} Ry/Bohr. After optimization, we find the lattice parameter to be 4.0745 $\AA$. Throughout the calculations, Marzari-Vanderbilt cold smearing is used with a degauss value of 0.01 Ry. A 20×20×20 k-grid without any symmetries is used for all the nonself-consistent calculations (including Wannier90 calculations). To extract the information of the low-energy subspace, which will be used by the DMFT code, we have projected the Bloch wave-functions obtained from our DFT calculations on to the Ru-t_{2g} orbitals using the maximally localized Wannier functions[16] (MLWF) technique as implemented in the Wannier90 code[17]. The electronic bandstructure, density of states (DOS) and projected DOS (pDOS) of $BaRuO_3$ in its non-magnetic (NM) phase are given in figure 7.1 and 7.2. Clearly, $BaRuO_3$ is a metal in its NM-phase with major contributions from the Ru-4d and O-2p orbitals across the Fermi-level. Hybridization between Ru-4d orbitals and O-2p orbitals spans from $\sim$ -8 eV below the Fermi level to $\sim$ 5 eV above the Fermi level. Bands above 5 eV are mainly composed of Ba-d orbitals and Ru-p orbitals. We find that, due to the octahedral environment of the oxygen atoms surrounding the Ruthenium atoms, the Ru-4d orbitals split into two sets, namely, t_{2g} and e_g, where t_{2g} (e_g) orbitals contribution to the DOS is mainly below (above) Fermi-level, supporting the low-spin t_{2g} configuration of the nominal valence Ru^{4+} (d^4). From figure 7.2, we infer that the low energy subspace (-2.5 to 1 eV) which is relevant for the DMFT

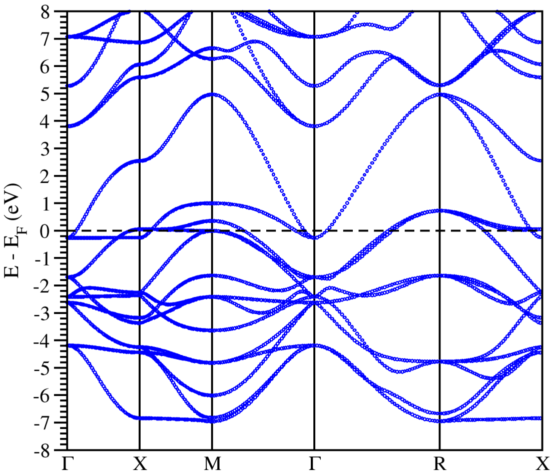

Figure 7.1: (color online) Band-structure of cubic $BaRuO_3$ in its nonmagnetic phase. Energies are scaled to the Fermi-level (dotted line).

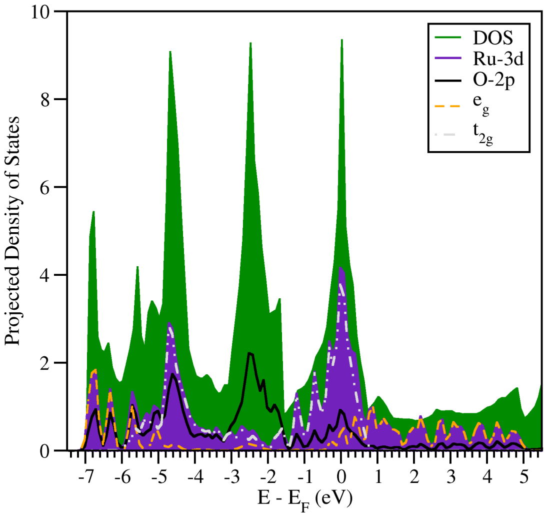

Figure 7.2: (color online) Projected density of states (PDOS) of $BaRuO_3$. Green (shaded light gray), violet (shaded dark gray), black (thick line), gray (dotted and dashed line) and orange (dashed line) colors represents the density of states (DOS) of whole system, Ru-atom, O-atom, Ru-t_{2g} and Ru-e_g, respectively.

calculations is mainly composed of the Ru-t_{2g} orbitals (with minor contributions of O-2p orbitals and Ru-e_g orbitals) have occupancy of $\sim$ 4 electrons. Hence, to extract this low energy subspace Hamiltonian in an effective Wannier function basis, we

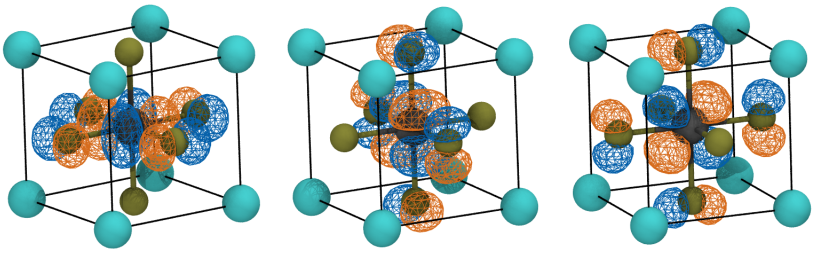

Figure 7.3: (color online) Orbital plots of maximally localized Wannier functions used to reproduce the low energy subspace Hamiltonian.

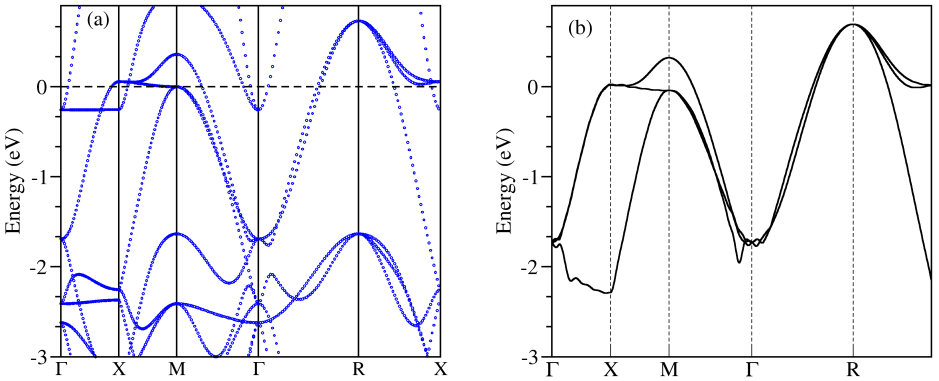

Figure 7.4: (color online) Low energy subspace band-structure obtained from (a) Plane-wave basis and (b) Wannier basis.

have projected the Bloch-wave-functions obtained from our DFT calculations onto the d$_{xz}$, d$_{yz}$, and d$_{xy}$ orbitals. The optimized Wannier functions calculated using the MLWF method as implemented in Wannier90[17] code are given in figure 7.3 and the corresponding low energy subspace band-structure calculated using these Wannier functions are given in figure 7.4. Clearly, band-structures obtained from both the basis sets (Wannier, plane-wave) compare fairly well in the low energy subspace, validating the proper choice of our projections. Also, as shown in figure 7.3, the Wannier functions show the d$_{xz}$, d$_{yz}$, and d$_{xy}$ orbital character and in addition have a substantial O-2p character due to their contributions near the Fermi-level. The H($\mathbf{k}$) obtained in this Wannier basis is used for all the DMFT calculations, as the unperturbed or the 'non-interacting' Hamiltonian.

7.3 GGA+DMFT: Results and Discussion

In DMFT calculations we have introduced a local Coulomb interaction of density-density type between orbitals. The interaction part of the Hamiltonian is given in the second quantization notation by,

$$H_{ii}^{int} = \sum_{i\alpha=1}^{3} U n_{i\alpha\uparrow} n_{i\alpha\downarrow} + \sum_{i\alpha\neq\beta} \sum_{\sigma\sigma'} (V - J\delta_{\sigma\sigma'}) n_{i\alpha\sigma} n_{i\alpha\sigma'} \, ,$$

where i represents lattice site and α, β represent orbital indices. U is the Coulomb repulsion between two electrons with opposite spin on the same orbital. We impose orbital rotational symmetry on the above Hamiltonian by setting $V = U - 2J$, where J is the Hund's coupling, which lowers the energy of a configuration with different orbitals ($\alpha \neq \beta$), and parallel spins $\sigma = \sigma'$. We have solved the effective impurity problem within DMFT by using HY-CTQMC. In the literature, a range of U and J values have been used for 4d-Ru based TMOs. Indeed, determining these without ambiguity is not possible at present. In a recent work[3], using the constrained random phase approximation(cRPA) method, the U value for Ruthenates was found to be 2.3 eV. Thus, we choose U_{Ru}=2.3 eV. We fix the J_{Ru} such that the theoretically calculated paramagnetic magnetic moment matches the corresponding experimentally measured value. Apart from this specific set of model parameters, we have investigated a range of (U, J) values in the neighbourhood of (U_{Ru},J_{Ru}) to ascertain the position of 3C-BaRuO$_3$ in the phase diagram. In the DMFT calculations, we find the chemical potential by fixing the occupancy should be equal to 4 electrons per Ru, which is obtained from threefold degenerate t$_{2g}$ bands in the Wannier basis or 'non-interacting' Hamiltonian. Now, we are going to discuss our results for single and two particle dynamics obtained from GGA+DMFT by using HY-CTQMC as an impurity solver.

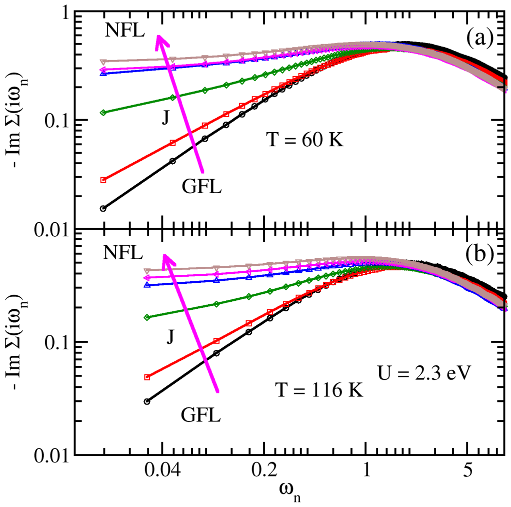

Figure 7.5: (color online) Imaginary part of Matsubara self energy ($-\text{Im}\Sigma(i\omega_n)$) for $U = 2.3$ eV and different J values for (a) T=60 K, and (b) T=116 K.

7.3.1 Single Particle Dynamics

To begin with, we focus on single particle dynamics that is mainly determined by the self-energy $\Sigma(i\omega_n)$. Figure 7.5(a) shows the imaginary part of Matsubara self-energy for $U = 2.3$ eV and $T = 60$ K for a range of J values. For $J \lesssim 0.1$, the low-frequency behavior of self-energy has a generalized Fermi liquid (GFL) form i.e., $-\text{Im}\Sigma(i\omega_n) \sim a\omega_n^\alpha$ where $0 < \alpha \leq 1$. As we increase J, a deviation from the power law is seen at low ω_n as the $-\text{Im}\Sigma(i\omega_n)$ acquires a non-zero intercept. The latter is characteristic of non-Fermi liquid behaviour, where the imaginary part of self-energy has a finite value as $\omega_n \to 0$ i.e, $-\text{Im}\Sigma(i\omega_n \to 0)) \sim \Gamma\text{sgn}(\omega_\text{n})$. Thus as a function of J, we observe a finite T crossover in the single particle dynamics driven by Hund's exchange[18]. Moreover, the crossover persists even for a higher temperature T= 116 K and is shown in figure 7.5(b).

A natural question arises about the choice of the $U = 2.3$eV for 3C-BaRuO$_3$. Does this crossover from GFL to NFL survive with respect to variations in U? The imaginary part of self-energy for $U = 3$ and 4eV computed at a temperature, T=60 K is shown in figure 7.6. Clearly, for $U = 2.3$ and 3 eV, the intercept of the

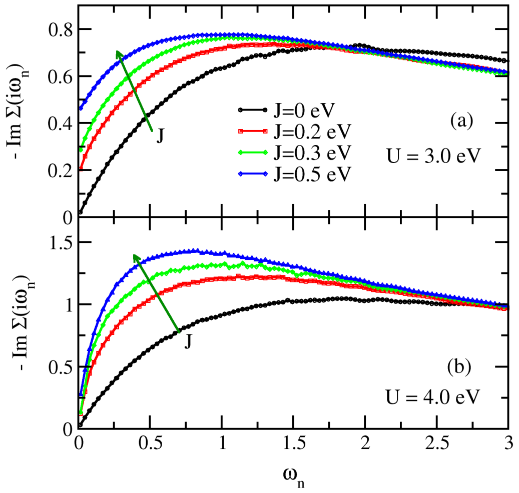

Figure 7.6: (color online) Imaginary part of Matsubara Self energy for T=60 K and different J values (mentioned in legends) with (a) U = 3 eV, and (b) U = 4 eV.

.

imaginary part of the self-energy is finite for $J \gtrsim 0.2$ (from figure 7.5 and the top panel of figure 7.6), while for $U = 4$ eV, a GFL form of $-\text{Im}\Sigma(i\omega_n)$ is obtained for $0 \leq J \leq 0.5$ eV. This implies that the NFL behaviour for higher values of $U(\gtrsim 4)$ eV, if at all occurs, must be for $J > 0.5$eV. Hence, we conclude that the $U_{Ru} = 2.3$eV, corresponding to 3C-BaRuO$_3$ is somewhat special, since it places this material in a crossover region for *physically reasonable* values of the Hund's exchange.

It is known from recent works on Ruthenates that the NFL behaviour seen in the single-particle dynamics is characteristic of a finite temperature spin-frozen phase which crosses over to a Fermi liquid ground state at lower temperatures. This incoherent spin-frozen state[4] is characterised by finite intercepts in the imaginary part of self-energy and fluctuating local moments (through susceptibility). In order to understand the crossover phase in a better way, we carry out a quantitative analysis of the imaginary part of the self-energy for many more J values in the same range as considered in figure 7.5. The imaginary part of self-energy at low Matsubara

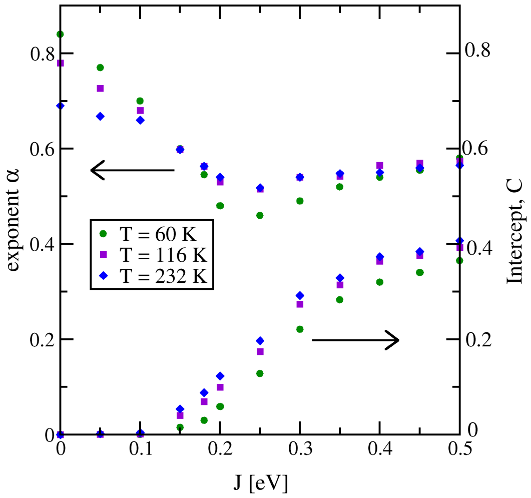

Figure 7.7: (color online) Exponent α (left) and intercept C (right) obtained by fitting the data to -Im $\Sigma(i\omega_n) = C + A\ |\omega_n|^\alpha$ at different J values, U = 2.3 eV and T = 60 K, 116K and 232K.

frequencies is fit to the form[18]

$$-\mathrm{Im}\Sigma(i\omega_n) \overset{\omega_n \to 0}{\to} C + A|\omega_n|^\alpha \tag{7.1}$$

, and figure 7.7 shows the exponent α (circles) and intercept C (squares) as a function of J at various temperatures from 60K to 230K, for U =2.30 eV. The exponent α initially decreases with increasing J, goes through a minimum value of 0.5 at a $J \sim$ 0.25eV and increases gradually for higher J. Such behaviour has been found previously by Werner[18] et. al., in the model calculations of three orbital Hubbard model with fully rotationally invariant interactions for fixed filling n=2.0, Hund's coupling J and varying the U value. The $\sqrt{\omega}$ behavior of self-energy at the minimum attributed[18] to the experimentally observed mysterious optical conductivity $\sigma(\omega) \sim \omega^{-1/2}$ of SrRuO$_3$[19–21] and CaRuO$_3$[22, 23]. In the recent study of CaRuO$_3$ within DFT+DMFT showed that rotation and tilting distortion of ideal cubic perovskite structure[24] mimicking the non-Fermi liquid signatures in the optical conductivity down to frequencies of terahertz, even systems have proper Fermi-liquid form of self-energy. The intercept C remains zero for $J \lesssim 0.15$ eV and above that it has a finite value which increases with J. Thus we identify a crossover Hund's exchange $J_0 = 0.15$ eV such that for $J < J_0$ the GFL phase exists, while for $J > J_0$ the crossover NFL phase exists at $\sim 60 - 80$K, where frozen moments are expected to scatter the conduction electrons. It is interesting to note that the exponent α in the GFL or in the NFL region is not equal to 1. In the GFL phase, the exponent must approach 1 with decreasing temperature, and indeed, it does, as seen in figure 7.7 for $J < J_0$. Curiously, the exponent hardly changes with either temperature or J in the spin-frozen phase even until 60K. For 3C-BaRuO3, a ferromagnetic transition occurs at $T_c = 60K$. Thus, it is likely that the spin-frozen phase is a precursor of the FM phase, and the local moments condense into a magnetically ordered state for $T < 60K$. We have repeated the above analysis for $U = 3$eV and find that the crossover $J_0 \sim 0.15$eV is the same as that for $U = 2.3$ eV within numerical tolerance. Even the intercept depends very weakly on temperature, thus, the spin-frozen phase appears to be almost temperature independent. This implies that the NFL behaviour should manifest in transport and thermodynamic quantities over a wide range from about 60K to at least 230K.

The crossover function, given in equation 7.1 does not have a microscopic basis, and has been used purely as a fitting function. Since the latter is not unique, the identification of J_0 must be verified through an alternative fit. Hence, we have used a fourth order polynomial also to fit $-\mathrm{Im}\Sigma(i\omega_n)$ and confirm the robustness of J_0. The intercept C_0 shown in the top panel of figure 7.8 does become non-zero only for $J \gtrsim J_0$. Thus, the identification of J_0 remains robust. For a Fermi liquid, the linear coefficient of the self-energy, C_1 is related to the quasiparticle weight, Z by $C_1 = -(1 - 1/Z)$ at $T = 0$. Although C_1 does not have the same interpretation at finite temperature, a qualitative picture may be obtained by examining the dependence of $Z = 1/(1 + C_1)$. The lower panel of figure 7.8 shows that the Z decreases throughout the GFL phase. Although the Z lacks any interpretation in

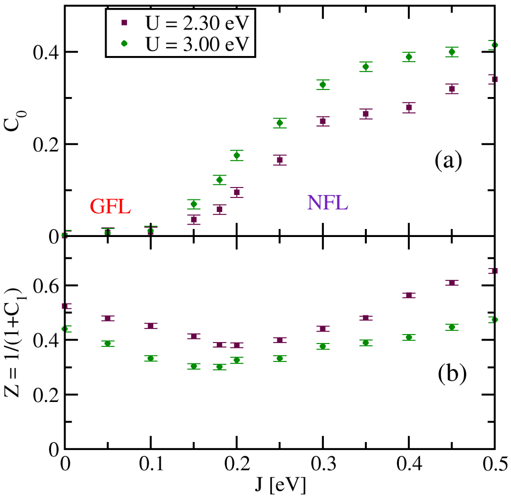

Figure 7.8: (color online) Imaginary part of self energy (-Im $\Sigma(\mathrm{i}\omega_n)$) fitted to 4th order polynomial: (a) zeroth order coefficient, C_0 (b) $Z = 1/(1 + C_1)$, where C_1 is the linear coefficient, for different J values, U=2.3 and 3.0 eV and T = 60 K.

the NFL phase ($J > J_0$), a finite Z is, nevertheless, obtained which behaves in a similar way as the exponent of the power law fit (figure 7.7).

7.3.2 Two Particle Dynamics

The collective excitations of a system are described by two particle dynamical correlation functions. The observed non-Fermi liquid behavior of single particle quantities for $J > J_0$ should manifest through collective excitations also. To see such effects, the two particle dynamical spin-spin correlation function $\chi_{zz}(\tau) = \langle \hat{S}_z(\tau)\hat{S}_z(0)\rangle$ is computed for different J values at U = 2.30 eV and T = 60 K and shown in figure 7.9. The instantaneous value of $\chi_{zz}(\tau)$ at $\tau = 0$ represents the bare local moment[25], which is increasing with increasing J. This can be understood from the fact that time spent by the impurity in the low lying atomic multiplet [26] states (S=1) is larger when compared to the other multiplet states of higher energy. Due to the presence of conduction electrons, the bare local moment formed at $\tau = 0$ is dynamically screened at large τ. The difference between value of $\chi_{zz}(\tau)$ at $\tau = 0$

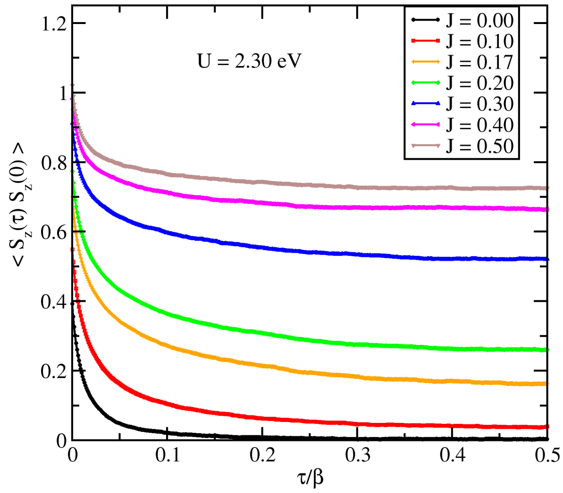

Figure 7.9: (color online) Matsubara time spin-spin correlation function for different J values and $U = 2.3$ eV, $T = 60$ K.

and $\tau \approx \frac{\beta}{2}$ signifies the dynamical screening time i.e., larger the difference smaller the screening time and vice-versa. As we increase the J, the difference between value of $\chi_{zz}(\tau)$ at $\tau = 0$ and $\tau \approx \frac{\beta}{2}$ reduces, implying reduced screening. It has been shown[18], at low temperature, for GFL $\chi_{zz}(\tau)$ around $\tau = \frac{\beta}{2}$ is proportional to T^2 while in NFL phase it has finite value. Our results are consistent with the GFL behavior of $\chi_{zz}(\tau)$ for a small value of J, and we observed a finite value for $\chi_{zz}(\tau)$ as we increased the J corresponding to a NFL phase. As a function of J the two particle dynamical spin-spin correlation function signals an electronic crossover.

The effect of temperature on spin correlations may be gauged through the local static spin susceptibility, given by $\chi_{loc}(T) = \int_0^\beta d\tau \chi_{zz}(\tau)$. Figure 7.10, shows $\chi_{loc}(T)$ as a function of temperature for a range of J values. For $J \lesssim 0.1$, $\chi_{loc}(T)$ is very weakly dependent of temperature over the entire range shown, which is characteristic of Pauli-paramagnetic behavior and hence corresponds to a GFL behaviour. For larger J values, we observe local moment behavior ($\chi_{loc}(T) \sim \frac{1}{T}$) behaviour at lower temperatures as well (see dashed line fit in the main panel). Thus with increasing J, χ_{loc} also crosses over to local moment region from GFL regime. We will see later

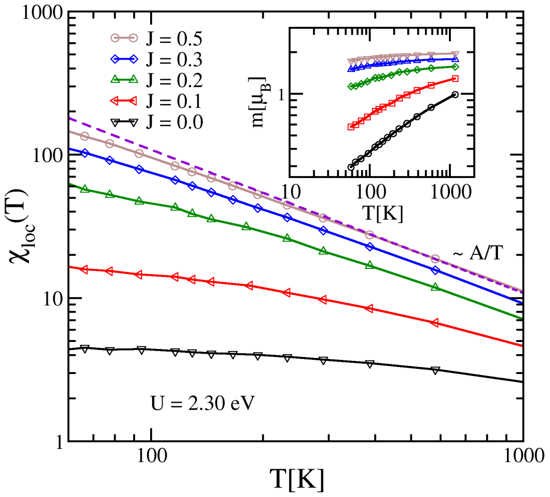

Figure 7.10: (online) Local static spin susceptibility; Dashed curves represent a power law fit at low temperatures. Inset: screened magnetic moment as a function of temperature for different J values and $U = 2.30$ eV.

that the temperature dependence of susceptibility allows to identify the value of Hund's exchange coupling appropriate for 3C-BaRuO$_3$.

In most of the 4d Ru-based TM oxides, most theoretical studies are restricted to single-particle spectral functions and static susceptibilities[4, 5]. There are only a few studies on two particle spectral functions including vertex corrections[25], and even those are limited to fixed U and J values. However there are no studies available for the behavior of two particle spectral functions (including vertex corrections) across the GFL to NFL crossover. We have calculated the dynamical spin susceptibility $\chi(\omega, T)$ on the real frequency axis by using maximum entropy method[27]. In figure 7.11, we show the imaginary part of $\chi(\omega, T)$ for various J values at $U = 2.30$ eV and T=60 K. A large scale spectral weight transfer to the infrared occurs upon increasing J of $\chi(\omega, T)$. Concomitantly, the half-width at half maximum also decreases. The peak in $\chi(\omega, T)$ represents the characteristic energy scale of the system, below which a Fermi liquid should emerge. The dramatic red shift of the peak with increasing J implies a strong suppression of the coherent scale[28–30]. Thus with increasing J,

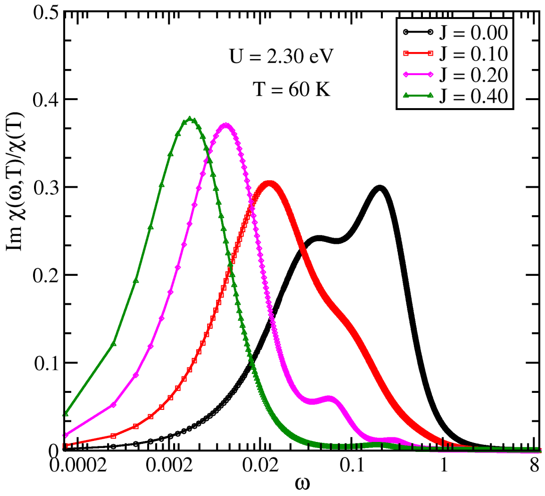

Figure 7.11: (color online) Imaginary part of dynamical spin susceptibility on real frequency axis obtained from maximum entropy method for various J values, U = 2.3 eV and T = 60 K.

the Fermi liquid ground state should crossover to an incoherent phase at increasingly lower temperatures (with increasing J). Since the only other scale (apart from the coherence scale) are the non-universal scales such as J or the bandwidth or U, the incoherent crossover phase should exist from very low temperatures to quite high temperatures. This explains the wide temperature range over which an incoherent spin-frozen phase, and the corresponding non-Fermi liquid behaviour is found, e.g in the resistivity[1, 7, 31].

7.3.3 Cubic(3C)-BaRuO$_3$

Now we turn to an identification of model parameters appropriate for 3C-BaRuO$_3$ in the (U, J) plane. CaRuO$_3$ and SrRuO$_3$ crystallizes in orthorhomic distorted perovskite of space group $Pnma$ while BaRuO$_3$ belongs to the space group of Pm-$3m$ which corresponds to a structure of ideal cubic perovskite. The significant structural changes from CaRuO$_3$ to SrRuO$_3$ and to BaRuO$_3$ is decrease in bending angle[7] (180°-ϕ) of Ru-O-Ru bonds and it becomes zero for BaRuO$_3$. Apart from slight distortions of RuO_6 octahedra of $CaRuO_3$, $SrRuO_3$ in compare with $BaRuO_3$, all of these materials have threefold degenerate t_{2g} bands near the Fermi-level with a formal valance of 4 electrons i.e., $t^4_{2g}e^0_g$. The strong ionic character of Ba^{2+} broadens the 4d bandwidth so we can expect weak electronic correlations in $BaRuO_3$ compare with $CaRuO_3$ and $SrRuO_3$. Recently different materials are placed together[1] on a map of interaction strength and the filling of electronic shell. Based on strength of electronic correlations we can expect $BaRuO_3$ to be placed in that map[1] just below $SrRuO_3$. As mentioned earlier, we have chosen U_{Ru}=2.3 eV for 3C-$BaRuO_3$ which has been obtained through cRPA for its closely related cousins in the Ruthenate family[3, 4, 32]. The J_{Ru} is obtained by comparing the theoretically computed, temperature dependent, static susceptibility (from figure 7.10) with that of the experiment[7]. From experiments, it is know that the saturated magnetic moment at 5K (in the ferromagnetic state) is $0.8\mu_B$/Ru, while the high temperature paramagnetic moment is $2.6\mu_B$/Ru. Since our theory is valid only in the paramagnetic phase, we choose the latter for theoretical comparison. One more issue in the theory is the use of Ising-type or density-density type Hund's coupling, which results in a $S = 1$ state corresponding to an ideal magnetic moment of $2\mu_B$/Ru rather than $2.8\mu_B$ as would be expected for a true $S = 1$ state with a rotationally invariant J term. Thus, the high temperature moment that we would be comparing to is $(2.6/2.8) \times 2 = 1.86\mu_B$/Ru. We see from the inset of figure 7.10 that such a moment is obtained for $J \sim 0.5$ eV. Hence we identify $J_{Ru} \sim 0.5eV$. We observe that the experimentally measured $\chi^{-1}_{loc}(T)$ is linear at high temperature, and deviates from linearity at $T \lesssim 150K$. Again, such deviation from the high temperature $1/T$ form is seen for $J \sim 0.5$ at $T \lesssim 150K$ (in the main panel of figure 7.10), thus lending support to the identification of $J_{Ru} \sim 0.5$ eV from the magnetic moment. We have checked that the deviations from linearity occur at much higher temperatures ($\gtrsim 300K$) for $J = 0.3$ and 0.4eV, hence the error bar on J_{Ru} should be less than 0.1eV.

The value of Hund's coupling $J_{Ru} \sim 0.5$ eV places 3C-$BaRuO_3$ deep in the incoherent spin-frozen phase for $T \gtrsim 60K$, and thus could explain the transition into a magnetically ordered state at $T \lesssim 60K$. This could very well also be the main reason for the experimentally observed non-Fermi liquid behavior in $\rho(T)$. For the values of U=2.3 eV and $J \sim 0.5$ eV, we obtain a relatively modest effective mass $\frac{m^*}{m_{GGA}}$ of 1.562 at $T = 60K$. A definitive comment about the effective mass in the ground state cannot be made with the preceding estimate at finite temperature, since the quasiparticle weight has a proper meaning only below the Fermi liquid coherence scale, which is strongly suppressed for $J = 0.5$ as seen from the dynamical susceptibility results (from figure 7.11). Thus, unless extremely low temperature calculations are carried out, a proper estimate of m^* is not possible. Nevertheless, the strong suppression of the Fermi liquid scale suggests that 3C-BaRuO3 could be very strongly correlated. Here, we would like to comment on the value of $U(=$ 4.0 eV) and J(=0.6 eV) chosen in a previous work [33] on 3C-BaRuO$_3$ within the dpp model. They obtained the interaction parameters from a “local spin density approximation constraint” technique. For those parameters, a recent study of one of the 4d Ruthenium compounds[3] within a five d-band model finds that correlations are induced due to the proximity of a Mott insulating state, which concurs with our results for a three d-band model (from the lower panel of figure 7.6). However, the proximity of a Mott insulating state does not violate adiabatic continuity and hence as shown above, the choice of $(U, J) = (4.0, 0.6)$ eV would not explain several anomalous features of 3C-BaRuO$_3$ including the wide $1/T$ behaviour of $\chi_{loc}(T)$, or the NFL behaviour of resistivity. These and the transition to a ferromagnetically ordered state at low temperature are naturally explained by the presence of a spin-frozen phase as found for $U_{Ru} = 2.3$eV and $J_{Ru} \sim 0.5$ eV.

7.4 Conclusions

We have studied the 3C-BaRuO$_3$ in the paramagnetic phase by using GGA+DMFT (HY-CTQMC). In the dynamical correlation functions and static spin susceptibility, we observed a crossover from GFL to NFL region with respect to J and by fitting the self-energy to simple cross-over function (linear in ω_n^α) determined the cross-over boundary i.e., $J_0 = 0.15$ eV. The local, on-site Coulomb repulsion, $U_{Ru} = 2.3$ eV, was chosen to be the same as that found through constrained random phase approximation calculations for the closely related $SrRuO_3$. We determine the Hunds exchange, J, appropriate for 3C-BaRuO3 such that the computed high temperature paramagnetic moment matches the experimentally found value i.e., $J_{Ru} \sim 0.5$ eV. Non-magnetic calculations with these parameters (U_{Ru}, J_{Ru}) for single-particle dynamics and static spin susceptibility show that cubic-BaRuO3 is in a spin-frozen state at temperatures above the ferromagnetic transition point. A strong red shift with increasing J of the peak in the dynamical susceptibility indicates a dramatic suppression of the Fermi liquid coherence scale in cubic-BaRuO3 . This state, we speculate, is the precursor of the ferromagnetic ground state and also a possible origin of the experimentally observed NFL behavior in resistivity. For the values of $U_{Ru} = 2.3$ eV and $J_{Ru} \sim 0.5$ eV, we obtain a relatively modest effective mass $\frac{m^*}{m_{GGA}}$ of 1.562 at T = 60K. However the quasiparticle weight has a proper meaning only below the Fermi liquid coherence scale, which is strongly suppressed for $J_{Ru} \sim 0.5$ eV.

Bibliography

[1] A. Georges, L. d. Medici, and J. Mravlje, Annu. Rev. Condens. Matter Phys **4**, 137 (2013), URL `http://www.annualreviews.org/doi/pdf/10.1146/annurev-conmatphys-020911-125045`.

[2] J. Zhao, L. Yang, Y. Yu, F. Li, R. Yu, Z. Fang, L. Chen, and C. Jin, Journal of Solid State Chemistry **180**, 2816 (2007), ISSN 0022-4596, URL `http://www.sciencedirect.com/science/article/pii/S0022459607003027`.

[3] H. T. Dang, J. Mravlje, A. Georges, and A. J. Millis, Phys. Rev. B **91**, 195149 (2015), URL `http://link.aps.org/doi/10.1103/PhysRevB.91.195149`.

[4] J. Mravlje, M. Aichhorn, T. Miyake, K. Haule, G. Kotliar, and A. Georges, Phys. Rev. Lett. **106**, 096401 (2011), URL `http://link.aps.org/doi/10.1103/PhysRevLett.106.096401`.

[5] K. Haule and G. Kotliar, New Journal of Physics **11**, 025021 (2009), URL `http://stacks.iop.org/1367-2630/11/i=2/a=025021`.

[6] L. de' Medici, J. Mravlje, and A. Georges, Phys. Rev. Lett. **107**, 256401 (2011), URL `http://link.aps.org/doi/10.1103/PhysRevLett.107.256401`.

[7] C.-Q. Jin, J.-S. Zhou, J. B. Goodenough, Q. Q. Liu, J. G. Zhao, L. X. Yang, Y. Yu, R. C. Yu, T. Katsura, A. Shatskiy, et al., Proceedings of the National Academy of Sciences **105**, 7115 (2008), `http://www.pnas.org/content/105/20/7115.full.pdf`, URL `http://www.pnas.org/content/105/20/7115.abstract`.

[8] G. Cao, S. McCall, M. Shepard, J. E. Crow, and R. P. Guertin, Phys. Rev. B **56**, 321 (1997), URL `http://link.aps.org/doi/10.1103/PhysRevB.56.321`.

[9] J.-S. Zhou, K. Matsubayashi, Y. Uwatoko, C.-Q. Jin, J.-G. Cheng, J. B. Goodenough, Q. Q. Liu, T. Katsura, A. Shatskiy, and E. Ito, Phys. Rev. Lett. **101**, 077206 (2008), URL `http://link.aps.org/doi/10.1103/PhysRevLett.101.077206`.

[10] G. Kotliar, S. Y. Savrasov, K. Haule, V. S. Oudovenko, O. Parcollet, and C. A. Marianetti, Rev. Mod. Phys. **78**, 865 (2006), URL `http://link.aps.org/doi/10.1103/RevModPhys.78.865`.

[11] J. P. Perdew, K. Burke, and M. Ernzerhof, Phys. Rev. Lett. **77**, 3865 (1996), URL `http://link.aps.org/doi/10.1103/PhysRevLett.77.3865`.

[12] A. Georges, G. Kotliar, W. Krauth, and M. J. Rozenberg, Rev. Mod. Phys. **68**, 13 (1996), URL `http://link.aps.org/doi/10.1103/RevModPhys.68.13`.

[13] P. Werner, A. Comanac, L. de' Medici, M. Troyer, and A. J. Millis, Phys. Rev. Lett. **97**, 076405 (2006), URL `http://link.aps.org/doi/10.1103/PhysRevLett.97.076405`.

[14] E. Gull, A. J. Millis, A. I. Lichtenstein, A. N. Rubtsov, M. Troyer, and P. Werner, Rev. Mod. Phys. **83**, 349 (2011), URL `http://link.aps.org/doi/10.1103/RevModPhys.83.349`.

[15] P. Giannozzi, S. Baroni, N. Bonini, M. Calandra, R. Car, C. Cavazzoni, D. Ceresoli, G. L. Chiarotti, M. Cococcioni, I. Dabo, et al., Journal of Physics: Condensed Matter **21**, 395502 (19pp) (2009), URL `http://www.quantum-espresso.org`.

[16] N. Marzari and D. Vanderbilt, Phys. Rev. B **56**, 12847 (1997), URL `http://link.aps.org/doi/10.1103/PhysRevB.56.12847`.

[17] A. A. Mostofi, J. R. Yates, Y.-S. Lee, I. Souza, D. Vanderbilt, and N. Marzari, Computer Physics Communications **178**, 685 (2008), ISSN 0010-4655, URL `http://www.sciencedirect.com/science/article/pii/S0010465507004936`.

[18] P. Werner, E. Gull, M. Troyer, and A. J. Millis, Phys. Rev. Lett. **101**, 166405 (2008), URL `http://link.aps.org/doi/10.1103/PhysRevLett.101.166405`.

[19] G. Koster, L. Klein, W. Siemons, G. Rijnders, J. S. Dodge, C.-B. Eom, D. H. A. Blank, and M. R. Beasley, Rev. Mod. Phys. **84**, 253 (2012), URL `http://link.aps.org/doi/10.1103/RevModPhys.84.253`.

[20] P. Kostic, Y. Okada, N. C. Collins, Z. Schlesinger, J. W. Reiner, L. Klein, A. Kapitulnik, T. H. Geballe, and M. R. Beasley, Phys. Rev. Lett. **81**, 2498 (1998), URL `http://link.aps.org/doi/10.1103/PhysRevLett.81.2498`.

[21] J. S. Dodge, C. P. Weber, J. Corson, J. Orenstein, Z. Schlesinger, J. W. Reiner,

and M. R. Beasley, Phys. Rev. Lett. **85**, 4932 (2000), URL `http://link.aps.org/doi/10.1103/PhysRevLett.85.4932`.

[22] Y. S. Lee, J. Yu, J. S. Lee, T. W. Noh, T.-H. Gimm, H.-Y. Choi, and C. B. Eom, Phys. Rev. B **66**, 041104 (2002), URL `http://link.aps.org/doi/10.1103/PhysRevB.66.041104`.

[23] S. Kamal, D. M. Kim, C. B. Eom, and J. S. Dodge, Phys. Rev. B **74**, 165115 (2006), URL `http://link.aps.org/doi/10.1103/PhysRevB.74.165115`.

[24] H. T. Dang, J. Mravlje, A. Georges, and A. J. Millis, Phys. Rev. Lett. **115**, 107003 (2015), URL `http://link.aps.org/doi/10.1103/PhysRevLett.115.107003`.

[25] A. Toschi, R. Arita, P. Hansmann, G. Sangiovanni, and K. Held, Phys. Rev. B **86**, 064411 (2012), URL `http://link.aps.org/doi/10.1103/PhysRevB.86.064411`.

[26] J. Kuneš, V. Křápek, N. Parragh, G. Sangiovanni, A. Toschi, and A. V. Kozhevnikov, Phys. Rev. Lett. **109**, 117206 (2012), URL `http://link.aps.org/doi/10.1103/PhysRevLett.109.117206`.

[27] M. Jarrell and J. E. Gubernatis, Physics Reports **269**, 133 (1996).

[28] M. Jarrell, J. E. Gubernatis, and R. N. Silver, Phys. Rev. B **44**, 5347 (1991), URL `http://link.aps.org/doi/10.1103/PhysRevB.44.5347`.

[29] C. Raas and G. S. Uhrig, Phys. Rev. B **79**, 115136 (2009), URL `http://link.aps.org/doi/10.1103/PhysRevB.79.115136`.

[30] N. Dasari, S. Acharya, A. Taraphder, J. Moreno, M. Jarrell, and N. S. Vidhyadhiraja, *Quantum critical dynamics of a magnetic impurity in a semiconducting host*, unpublished.

[31] P. B. Allen, H. Berger, O. Chauvet, L. Forro, T. Jarlborg, A. Junod, B. Revaz, and G. Santi, Phys. Rev. B **53**, 4393 (1996), URL `http://link.aps.org/doi/10.1103/PhysRevB.53.4393`.

[32] Z. V. Pchelkina, I. A. Nekrasov, T. Pruschke, A. Sekiyama, S. Suga, V. I. Anisimov, and D. Vollhardt, Phys. Rev. B **75**, 035122 (2007), URL `http://link.aps.org/doi/10.1103/PhysRevB.75.035122`.

[33] L. Huang and B. Ao, Phys. Rev. B **87**, 165139 (2013), URL `http://link.aps.org/doi/10.1103/PhysRevB.87.165139`.

Chapter 8

Weak ferromagnetism and magnetization reversal in $YFe_{1-x}Cr_xO_3$ [⋆]

8.1 Introduction

Rare-earth orthoferrites and orthochromites with the general formula RMO_3, where R = Rare earth or Yttrium and M = Fe and Cr, have perovskite structure with orthorhombic distortion (space group: Pnma) and an antiferromagnetic ground state. Below the Néel temperature T_N, all these compounds exhibit a weak ferromagnetic behavior, arising from a slight canting of the antiferromagnetic backbone, similar to that observed in compounds such as α-Fe_2O_3 and few transition metal carbonates. Such weak ferromagnetism (WFM) could result from either an antisymmetric superexchange, also known as Dzyaloshinskii-Moriya (DM) interaction or single-ion magnetic anisotropy or both[1, 2]. In orthoferrites and orthochromites, although both of these mechanisms operate, it has been argued that the antisymmetric exchange interaction is the dominant cause of the observed WFM[2]. Neutron diffraction

---

[⋆] Nagamalleswararao Dasari, P. Mandal, A. Sundaresan and N. S. Vidhyadhiraja, published in Europhysics Letters, 99, 17008 (2012).

studies have shown that the magnetic structure is G-type with the magnetic easy axis lying along the z-direction[3, 4]. In these weakly ferromagnetic orthoferrites, the spontaneous moment orients along the y-direction whereas the Dzyaloshinskii vector **D** points along the x-direction[2, 5]. When R is a magnetic ion, most of these compounds undergo a spin re-orientation transition below which the direction of easy axis is changed to y. At low temperatures, some compounds exhibit magnetization reversal (MR) due to antiferromagnetic coupling of R-moments with the canted Cr-moments[6–8].

In a similar orthorhombic compound with nonmagnetic R-ion, namely YVO_3, weak ferromagnetism and MR have been reported[9]. The origin of MR has been explained based on a competition between DM interaction and single-ion magnetic anisotropy[10](SIMA). MR is also well known in several ferrimagnetic systems such as spinels[11, 12], garnets[13] and Prussian blue analogs[14, 15]. In these materials, MR has been explained by different temperature dependence of sublattice magnetization arising from different crystallographic sites, as predicted by Néel for spinel systems. In antiferromagnetic perovskite systems, like YVO_3, the magnetic ions occupy a single crystallographic site and therefore Néel's mechanism cannot explain the MR[16, 17]. In previous studies we demonstrated temperature induced MR in several canted antiferromagnetic oxides with nonmagnetic R-ion and mixed transition metal ions such as $La_{1-x/2}Bi_{x/2}(Fe_{0.5}Cr_{0.5})O_3$, $BiFe_{0.5}Mn_{0.5}O_3$ and $YFe_{1-x}Mn_xO_3$ $(0.1 \leq x \leq 0.45)$[16–18]. In these systems, magnetic ions (Fe, Cr and Mn) in trivalent state are disordered at the B-site of the perovskite.

Here, we report a systematic and combined, experimental and theoretical study of a solid solution of two weakly ferromagnetic materials namely $YFeO_3$ and $YCrO_3$, that have $T_N \simeq 640K$ and $140K$ respectively. We find, predictably, that at low and high values of x in $YFe_{1-x}Cr_xO_3$, the compounds show WFM behaviour. However, for intermediate compositions $x = 0.4$ and 0.5, a surprising temperature-dependent MR is observed. The possibility of finding MR in this system was indeed conjectured more than three decades ago[19], but was not demonstrated until recently [20] (for $x = 0.5$). The previously mentioned mechanisms for MR do not explain our findings. Thus, based on the experimental results and previous theoretical insights, we propose a simple mechanism based on an interplay of competing DM interactions that is able to explain the data quantitatively.

Polycrystalline samples of $YFe_{1-x}Cr_xO_3$ (0≤x≤1) have been synthesized by solid state reaction route by mixing stoichiometric amount of Y_2O_3 (preheated at 1223 K), Fe_2O_3 and Cr_2O_3 and sintered at 1743 K for 24 hours with several intermittent grindings. Rietveld refinement was carried out on the room temperature x-ray powder diffraction (XRPD) data collected with Bruker D8-Advance diffractometer. Magnetic measurements were carried out with a vibrating sample magnetometer in a Physical Property Measurement System (PPMS), Quantum Design, USA.

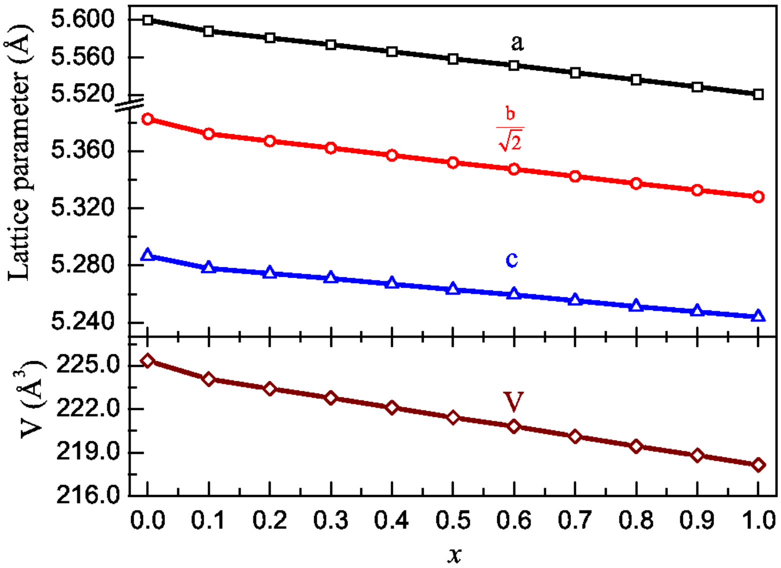

Figure 8.1: (color online) Variation of lattice parameters and volume as a function of x in $YFe_{1-x}Cr_xO_3$.

A complete solid solution exists in $YFe_{1-x}Cr_xO_3$ as the two end members $YFeO_3$ and $YCrO_3$ have the orthorhombic structure (Pnma). In this structure, the Fe and Cr ions are randomly distributed at the 4b site. Unit cell parameters a, b, c and cell volume V, as extracted from Rietveld refinement, are shown in figure 8.1. All these parameters decrease with x and follow Vegard's law as expected from the difference in ionic radii between Fe^{3+} and Cr^{3+} (0.645 and 0.615 Å), respectively. Field-cooled magnetization measurements of $YFe_{1-x}Cr_xO_3$ at an applied magnetic field of 100 Oe for various x in the temperature interval 10 - 650 K were carried out. Our magnetization measurements reveal that the Néel temperature varies non-linearly with x. Further, all samples exhibit weak ferromagnetism below T_N and the samples with $x = 0.4$, and 0.5 exhibit magnetization reversal. These results are explained based on the model described below.

Neutron scattering results show that the $Y(Fe,Cr)O_3$ system is a G-type Néel antiferromagnet for all doping. As the Fe and Cr ions are disordered at the B-site, the Hamiltonian must have antiferromagnetic superexchange interaction term, of the form $J_{ij}\hat{\mathbf{S}}_i \cdot \hat{\mathbf{S}}_j$ with $J_{ij} > 0$ for three possible pairs[20], namely Fe-O-Fe, Cr-O-Cr and Fe-O-Cr. The Fe^{3+} ions have a spin $S = 5/2$ while the Cr^{3+} have $S = 3/2$. In a solid solution, the two ions would occupy sites randomly with probability $P_{Fe} = (1 - x)$ and $P_{Cr} = x$. The superexchange term will only be able to explain the antiferromagnetic order, while the explanation of weak ferromagnetism requires invoking other mechanisms such as Dzyaloshinskii-Moriya interactions (DM) or the single-ion magnetic anisotropy (SIMA). In the parent compounds, $YFeO_3$ and $YCrO_3$, the WFM has been understood as arising purely from DM interactions of the Fe-Fe and Cr-Cr pairs respectively. For compositions not equal to 0 or 1, we continue to keep only DM interactions, neglecting SIMA completely. Furthermore, for $x \neq 0, 1$, we must consider D_{FeCr} along with the usual D_{FeFe} and D_{CrCr} interactions. In previous work on this system, the authors have suggested [20]the choice of DM interactions to have the form $\vec{D}_{FeFe} \parallel \vec{D}_{CrCr} \parallel -\vec{D}_{FeCr}$. We arrive at the same conclusion by eliminating other possibilities, and indeed find excellent explication of the experimental results with this approach (described below).

8.2 Model and Results

The Heisenberg hamiltonian[21] without the DM or SIMA can be written in a general form as

$$\mathcal{H}_s = \sum_{ij\alpha\beta} J^{ij}_{\alpha\beta} \hat{\mathbf{S}}_{i\alpha} \cdot \hat{\mathbf{S}}_{j\beta} \,. \tag{8.1}$$

Here i, j denote lattice site indices and α, β indicate the type of magnetic ion, which in our case could be either Fe or Cr. Employing the molecular field approximation (MFA) for the antiferromagnetic case and ignoring the spin-flip terms, the above Hamiltonian reduces to

$$\mathcal{H}_{MFA} = -\sum_{\alpha=Fe,Cr} (H^{eff}_{B\alpha} \sum_{i\in A} \hat{S}^z_{i\alpha} + H^{eff}_{A\alpha} \sum_{i\in B} \hat{S}^z_{i\alpha}) \tag{8.2}$$

with z being the number of nearest neighbours and $H^{eff}_{B\alpha}$ is the mean field due to the B-sublattice atoms on the A-sublattice which is explicitly given by

$$H^{eff}_{B\alpha} = 2zP_{Fe}J_{\alpha Fe}\langle \hat{S}^z_{Fe}\rangle_B + 2zP_{Cr}J_{\alpha Cr}\langle \hat{S}^z_{Cr}\rangle_B \,. \tag{8.3}$$

Correspondingly, $H^{eff}_{A\alpha}$ is the mean field due to the A-sublattice atoms on the α-atoms in the B-sublattice. Note that the mean fields are different for the Fe and the Cr atoms and depend on doping levels as well. Using the above MFA Hamiltonian, the partition function may be obtained in a straightforward way by tracing over the $\hat{S}^z_{Fe}$ and $\hat{S}^z_{Cr}$ eigenvalues, which yields the self-consistent equations that describe the temperature dependence of the Fe and Cr spins as $\langle \hat{S}^z_\alpha \rangle = S_\alpha B_J(X_\alpha) \quad \alpha = Fe, Cr\,$, where the sublattice index has been suppressed (for clarity) and $B_J(x)$ is the Brillouin function; The X_α's are given by

$$X_{Fe} = \frac{2zS_{Fe}}{kT}\left[J_{Fe,Fe}P^2_{Fe}\langle \hat{S}^z_{Fe}\rangle + J_{Fe,Cr}\, P_{Fe}P_{Cr}\langle \hat{S}^z_{Cr}\rangle\right]$$

and

$$X_{Cr} = \frac{2zS_{Cr}}{kT}\left[zJ_{Cr,Fe}\,P_{Cr}P_{Fe}\langle\hat{S}^z_{Fe}\rangle + J_{Cr,Cr}\,P^2_{Cr}\langle\hat{S}^z_{Cr}\rangle\right] .$$

Solving the above coupled nonlinear equations, we can obtain the A-sublattice magnetization as $M_A(T) = \frac{n}{2}g\mu_B(P_{Fe}\langle\hat{S}^z_{Fe}\rangle_A + P_{Cr}\langle\hat{S}^z_{Cr}\rangle_A)$. For a perfect antiferromagnet considered until now, the total magnetization ($M_{tot} = M_A + M_B$) is naturally zero. To find the Néel temperature of the doped system, we can follow the usual procedure of linearizing the above equations in the limit $T \to T_N^-$, where we expect $\langle S^z_\alpha\rangle \to 0$. It is easy to see that the requirement of getting non-zero values of $\langle S^z_\alpha\rangle$ yields a 4×4 determinant which when further simplified yields the equation $1 - 2LM - 2KMLN - N^2 - K^2 + L^2M^2 + K^2N^2 = 0$ where

$$\begin{aligned} K &= \frac{2zP^2_{Fe}S_{Fe}(S_{Fe}+1)}{3KT}J_{FeFe}\,, \quad L = \frac{P_{Cr}}{P_{Fe}}\frac{J_{FeCr}}{J_{FeFe}}K \\ N &= \frac{2zP^2_{Cr}S_{Cr}(S_{Cr}+1)}{3KT}J_{CrCr}\,, \quad M = \frac{P_{Fe}}{P_{Cr}}\frac{J_{FeCr}}{J_{CrCr}}N\,. \end{aligned}$$

For $J/kT \ll 1$, we retain terms of $\mathcal{O}((J/kT)^2)$ and neglect the higher order terms, thus getting

$$T_N(x) = \frac{2z}{3k}\left(\sum_{\alpha\beta} S_\alpha(S_\alpha+1)S_\beta(S_\beta+1)P^2_\alpha P^2_\beta J^2_{\alpha\beta}\right)^{\frac{1}{2}} \tag{8.4}$$

where $\alpha, \beta = Fe, Cr$, $P_\alpha = (1-x)\delta_{Fe,\alpha} + x\delta_{Cr,\alpha}$ is the probability of site occupancy, and the spins are given by $S_{Fe} = 5/2$ and $S_{Cr} = 3/2$. The nearest neighbour coordination number z is 6 for the present case. In a previous molecular field theoretical study of the doped system, the T_N *vs* x expression was obtained[22], which was different than the one obtained above. However, their result seems inconsistent with undoped system Néel temperature expression, i.e., if $x = 0$ or $x = 1$, we should recover the pure compound Néel temperature expressions, which their expression does not while the above equation does. This inconsistency could be because they neglected to consider the probabilistic aspect of the occupancy of the site on which the mean-field is acting. Using the above equation for $x = 0$ and $x = 1$ with T_N from experimental measurement [4, 23] being 640 K and 140 K respectively, we can extract the values of J_{FeFe} and J_{CrCr} as 18.4 K and 9.3 K respectively. These small $J/kT(\sim 0.03 - 0.07)$ values self-consistently justify the neglect of cubic and higher order terms in (J/kT). To find J_{FeCr}, we carry out a best fit of the above equation to the experimentally measured $T_N(x)$, as shown in figure 8.2 (circles: theory and experiment: diamonds). This yields a $J_{FeCr} = 24.0$ K, which is surprisingly higher than the superexchange in the parent compounds. The agreement of experimental data with the theoretical expression given above is remarkable. The

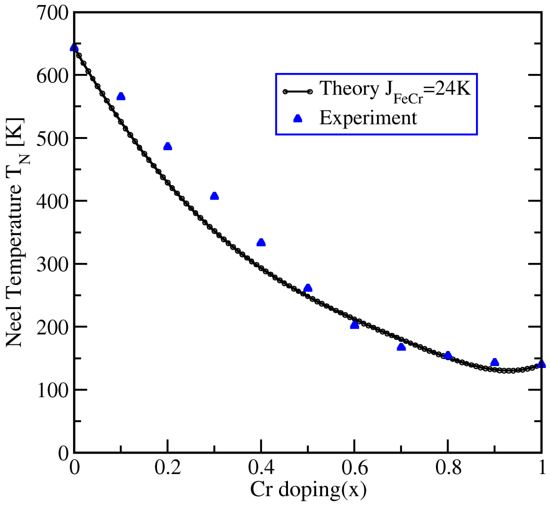

Figure 8.2: (color online) Variation of Néel temperature (experiment:triangles and theory:circles) with increasing Cr content. The theoretical curve has been computed with $J_{FeCr} = 24$ K.

dominant x dependence near low Cr concentration is $T_N(x \to 0) = T_{N,Fe}(1 - 2x)$ and at high concentration, close to $YCrO_3$ is $T_N(x \to 1) = T_{N,Cr}(1 - 2(1 - x))$. The Néel temperatures at intermediate concentrations are, as usual, somewhere between those of the two parent compounds, but at the two ends, as is seen in experiment as well, the doped compound has a lower T_N than the parent compound.

Now we build upon the underlying antiferromagnetism and outline our approach for understanding the weak ferromagnetism and magnetization reversal in the $YFe_{1-x}Cr_xO_3$ system. To begin with, consider the parent compounds, $YFeO_3$ and $YCrO_3$. As the experimental results(see later) show, the parent compounds are weak ferromagnets [4, 23]. Such weak ferromagnetism (WFM) is caused by a small canting of the underlying antiferromagnetic lattice. In general, the canting could be strongly temperature dependent and could arise due to a variety of reasons most important of which are the DM and the SIMA interactions. For YVO_3, it was argued [10] that a strongly temperature dependent DM interaction energy along with a staggered easy axis leads to a magnetization sign reversal with decreasing temperature. The authors did include SIMA in their semi-classical approach, albeit without temperature dependence. Although a good agreement with experimental data was achieved, the anisotropy term was found (by fitting to experiments) to be about 1.7 times the Heisenberg exchange. Such a result violates the initial assumption that the DM/SIMA interactions are much weaker compared to the Heisenberg exchange and may thus be treated perturbatively. Furthermore, such a large anisotropy is physically unjustified.

We present a alternative approach to the present problem that is minimalist but physically and internally consistent. It has been argued in the literature (see for instance [1]) that for relatively high Neel temperatures ($T_N \gtrsim 100$ K), the canting is caused primarily by DM interactions, while for lower T_N materials, the single-ion anisotropy dominates. Since the parent compounds have high T_N, our minimalist approach neglects the effects of SIMA completely and aims to understand all of the magnetization behaviour in the doped system purely through DM interactions.

The Hamiltonian including only the superexchange and the DM interactions in the absence of an external field is given by

$$\mathcal{H}_{\mathcal{S}} = \sum_{\langle ij \rangle} (J_{ij} \hat{\mathbf{S}}_i \cdot \hat{\mathbf{S}}_j - \vec{D}_{ij} \cdot (\hat{\mathbf{S}}_i \times \hat{\mathbf{S}}_j)) \,. \tag{8.5}$$

The classic DM interaction has been derived by Dzyaloshinskii and Moriya [1] for the non-centrosymmetric anion mediated antisymmetric exchange interaction between two *same* magnetic ions. Yamaguchi extended this result to different kinds of magnetic ions, [24] namely R^{3+} and Fe^{3+} in $RFeO_3$. Extending this idea to the doped system here, we consider DM interactions between neighbouring Fe and Cr ions. We employ the molecular field approximation again, and with the model shown in figure 8.3, the average energy reduces to a function of the canting angles θ and ϕ. To find the canting angles, we minimize the energy above with respect to θ and ϕ. In the small angle limit, we end up with two linear equations, which are in terms of $J_{FeFe}, J_{CrCr}, J_{FeCr}, D_{FeFe}, D_{CrCr}$ and D_{FeCr}.

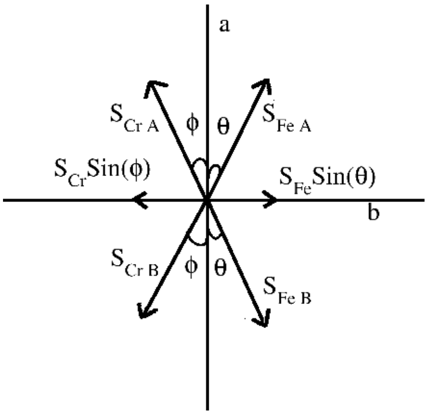

Figure 8.3: Schematic spin structure for the $YFe_{1-x}Cr_xO_3$ system.

The superexchange parameters $J_{\alpha\beta}$ are obtained from the experimental Néel temperatures and the $D_{\alpha\beta}$ are obtained by comparing theory to the experimentally measured weak ferromagnetic magnetization in the parent and the doped compounds. For the parent compounds ($x = 0$ and $x = 1$), we find temperature independent canting angles (as in [25]) $\theta = D_{FeFe}/2J_{FeFe}$ and $\phi = D_{CrCr}/2J_{CrCr}$. The net magnetization is given in the general case (for a powder sample[26]) as

$$M_{net} = \frac{ng\mu_B}{2}\left(P_{Fe}\langle\hat{S}^z_{Fe}\rangle\theta + P_{Cr}\langle\hat{S}^z_{Cr}\rangle\phi\right) \tag{8.6}$$

where the average z-component of each of the spins is given by the earlier found mean field expressions. By comparing the temperature dependence of the theoretically obtained magnetization to the experimentally measured one for the parent compounds, we can extract the magnitudes of the Dzyaloshinskii vectors, D_{FeFe} and D_{CrCr}.

Taking the physically reasonable [4] DM values of D_{FeFe} and D_{CrCr} as 0.4K and 0.32K respectively, we compute the magnetization *vs.* temperature. As shown in figure 8.4, the description of weak ferromagnetism purely using DM interactions agrees remarkably with experiment. The inset shows that a common mechanism underlies the WFM of both the parent compounds, since the $M/M_{\max}$ *vs.* T/T_N is almost identical for both. The slight deviation of theory from experiment for $YCrO_3$ suggests that single-ion magnetic anisotropy might need to be invoked to get a better fit. The canting angles θ and ϕ do not depend on temperature in the parent compounds. We will see below that this will not be the case for the doped case.

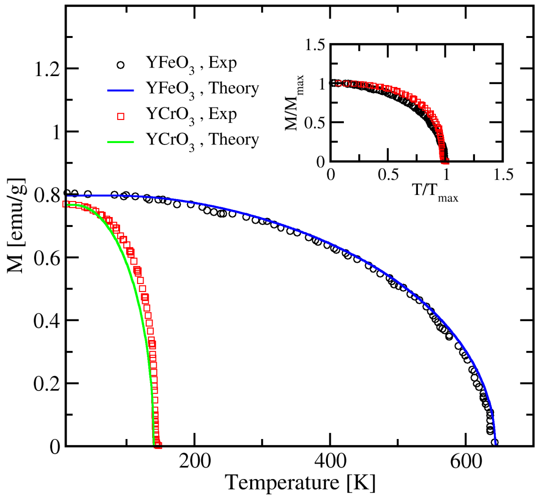

Figure 8.4: (color online) Magnetization (experiment and theory, see legends) as a function of temperature for the parent compounds $YFeO_3$ and $YCrO_3$. The inset shows that a common mechanism underlies the WFM of both the parent compounds, since the $M/M_{\max}$ *vs.* T/T_N is almost identical for both.

The DM interaction between the Fe and Cr atoms must be expected to depend on the concentration x. So, to obtain the values of D_{FeCr} as a function of x, we follow the same route as for the parent compounds. The parameter D_{FeCr} is obtained for each concentration x using a best fit to the experimental data. The g factor has been varied slightly for obtaining a quantitative fit, which amounts to a simple multiplicative scaling of the y-axis. We first consider the doping range $x = 0.1, 0.2$

and 0.3. The experimental data is shown in figure 8.5 (black circles). The Néel temperature decreases with increasing x, and the overall magnetization value also comes down. A broad maximum appears and this is a characteristic signature of spin reorientation. The limiting zero temperature ($T \to 0$) magnetization is seen to decrease sharply. Thus it can be expected that at higher doping, a magnetization reversal will occur, and indeed this is seen as we show below. Before that, let us discuss the comparison to theory. In the top panels of figure 8.5, the theoretically computed magnetization (in red) with the same exchange couplings as before and best fit values of D_{FeCr}=-1.3 K, -0.84 K and -0.35 K for x=0.1,0.2,0.3 respectively are superimposed on the experimental data. The agreement is seen to be excellent over the entire temperature range. The canting angles, as inferred from the above comparison (not shown) depend on temperature and in fact increase monotonically in magnitude. Thus the different dependences of θ and ϕ on T seems to be responsible for the continuous spin reorientation.

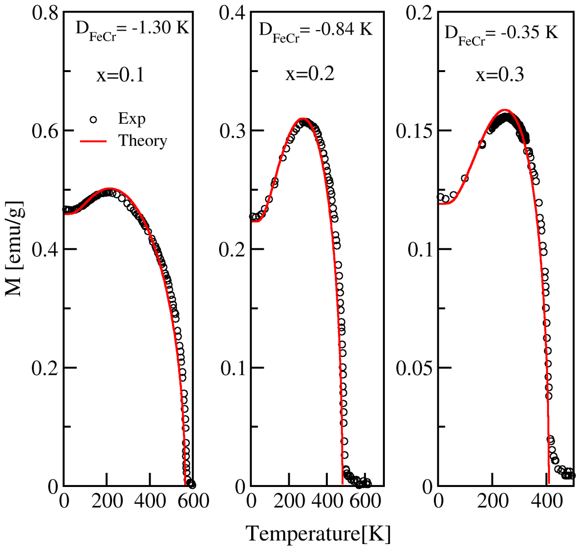

Figure 8.5: (color online) Magnetization (experiment:black and theory:red) as a function of temperature for three compositions, $x = 0.1$ (left), 0.2(middle) and 0.3 (right).

The experimental data for $x = 0.4$ and 0.5 is shown (in black circles) in figure 8.6. For $x = 0.4$, a smooth magnetization reversal with a compensation point at $T_{\text{comp}} \sim$

170 K is seen. In fact, for temperatures below the compensation point, the magnetic behaviour must be described as weak diamagnetism, since these are field cooled experiments, albeit with a small applied field (100 Oe). For $x = 0.5$, the onset of antiferromagnetism also signals WFM, but with a slight decrease in temperature, magnetization reversal occurs. The theory curves are again superimposed (in red) onto the experiment, with D_{FeCr}=-0.39 K and -0.31 K and again the whole temperature dependence is captured faithfully. Thus, in this approach, the magnetization reversal may be argued to arise from the competition between the magnetization of the Fe-Fe and Cr-Cr pairs *vs.* that of the Fe-Cr pairs, induced by the interatom DM interaction. In other words, if D_{FeCr} were zero, then the magnetization of Fe atoms and the Cr atoms would just add up, and there would be no temperature dependent reversal or even spin reorientation. But in the presence of D_{FeCr}, which is antiparallel to D_{FeFe} and D_{CrCr}, the Fe-Cr nearest neighbour pairs would exhibit WFM in a direction opposite to the Fe-Fe and Cr-Cr neighbour pairs, and thus at values of composition where heterogenous pairs are expected to be large in number as compared to homogenous pairs, one can expect a reversal of magnetization with decreasing temperature. The composition at which the reversal should occur should be determined by the relative magnitudes of the isotropic exchange strength. This is larger for Fe-Fe ($\sim$ 18 K) than for Cr-Cr ($\sim$ 9K), and hence the Cr atoms, which would normally order antiferromagnetically at much lower temperatures, begin ordering much above the Néel temperature of the parent compound $YCrO_3$, because of the J_{FeCr} exchange. Thus the reversal must happen closer to $YFeO_3$ and indeed it is seen at x=0.4.

The compositions $x = 0.6, 0.7$ and 0.9, which are closer to the parent Cr compound $YCrO_3$ are discussed in figure 8.7. It is seen that WFM is recovered for these compositions, since the number of homogenous pairs (Cr-Cr) would be expected to be larger than the heterogenous pairs. The theory agrees reasonably well with experiment. For $x = 0.7$, the middle panel of figure 8.7 shows that the agreement

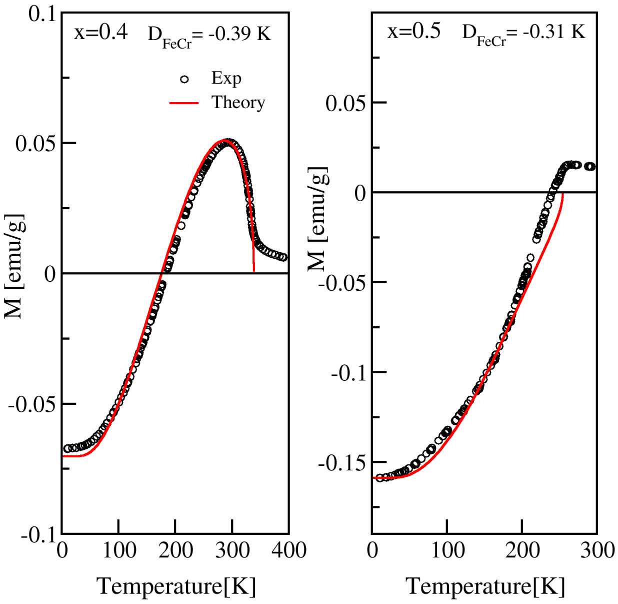

Figure 8.6: (color online) Magnetization (experiment:black and theory:red) as a function of temperature for $x = 0.4$ (left) and 0.5 (right). Magnetization reversal is seen in this composition range.

between theory and experiment is excellent for temperatures $\gtrsim$ 100 K, while at low temperatures, the theory predicts lower magnetization than what is observed in the experiment. We conjecture that at higher concentrations of Cr, the theory might need to be modified and other interactions like the single-ion-anisotropy that have been neglected in the present approach might have to be included to get better agreement. In fact, for $x = 0.8$, the experiments (not shown here) show two magnetization reversals, but the absolute value of magnetization is very small and almost comparable to the field induced magnetization values. Such a double reversal simply cannot be captured by the present theoretical approach.

8.3 Conclusions

In conclusion, we have investigated the magnetization behaviour as a function of temperature and doping for the solid solution $YFe_{1-x}Cr_xO_3$. An interplay of different DM interactions leads to interesting spin-reorientation and magnetization

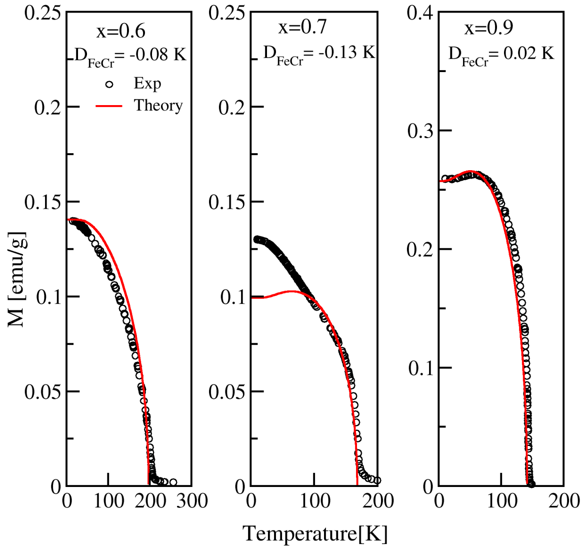

Figure 8.7: (color online) Temperature dependent magnetization (experiment: black and theory:red) for $x = 0.6$ (left), 0.7 (middle) and 0.9(right).

reversal. It is interesting to note that even though the parent compounds are weak ferromagnets with monotonic temperature dependence of magnetization $M(T)$, the mixed compounds display magnetization reversal and a non-monotonic $M(T)$. In our approach, this behaviour finds a natural explanation in terms of the doping dependence of D_{FeCr} (shown in figure 8.8) and the negative sign of the parameter, which suggests that the DM vector $\mathbf{D}_{FeCr}$ is opposite in direction to the $\mathbf{D}_{FeFe}$ and $\mathbf{D}_{CrCr}$ vectors in the parent compounds. This opposite direction introduces a competition between the canting driven by the DM interactions of the heterogenous pairs (Fe-Cr) versus the homogenous pairs (Fe-Fe and Cr-Cr). Thus we are able to obtain quantitative agreement between theory and agreement for the whole range of doping and temperature with a very simple, consistent and transparent approach. This also suggests that doping could be used very effectively to tune the antisymmetric exchange parameter. Furthermore, we opine that the interplay of various interactions considered here must exist in other similar B-site disordered perovskite materials.

The canting angles were found to depend appreciably on temperature and doping. The DM interaction too seems to be dependent strongly on the composition. These

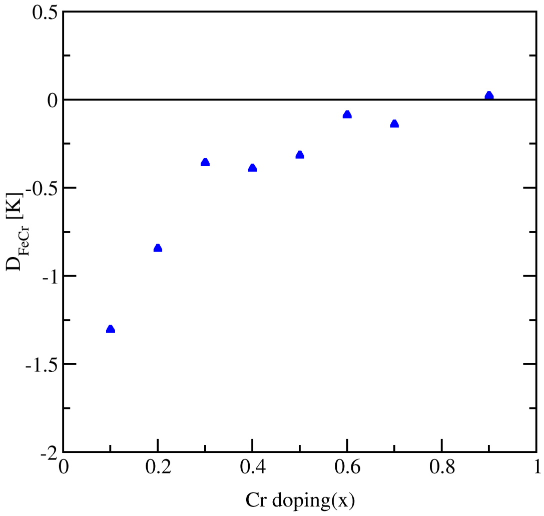

Figure 8.8: (color online) The DM interaction D_{FeCr} between the Fe and Cr atoms, as obtained from the comparison of theory and experiment is shown as a function of composition x. It is intriguing to note that it is maximum in magnitude close to $YFeO_3$ and decreases almost monotonically with increasing x.

two together suggest that changes in spin structure induce changes in the lattice structure, which implies the existence of significant spin-phonon coupling. Indeed, recent experiments [20] have indicated a multiferroic nature of the $YFe_{0.5}Cr_{0.5}O_3$ material. The microscopic justification for the x dependence of the parameters obtained here would require a detailed analysis of the structural changes in the orthorhombic lattice due to the size differences in the Fe/Cr ions. Additionally, we would also require to find out the changes in the spin interactions due to the lattice distortions. These investigations will be the subject of future studies.

Bibliography

[1] T. Moriya, Phys. Rev. **120**, 91 (1960), URL `http://link.aps.org/doi/10.1103/PhysRev.120.91`.

[2] D. Treves, Phys. Rev. **125**, 1843 (1962), URL `http://link.aps.org/doi/10.1103/PhysRev.125.1843`.

[3] W. Koehler and E. Wollan, Journal of Physics and Chemistry of Solids **2**, 100 (1957), ISSN 0022-3697, URL `http://www.sciencedirect.com/science/article/pii/0022369757900951`.

[4] V. Judin, A. Sherman, and I. Myl'nikova, Physics Letters **22**, 554 (1966), ISSN 0031-9163, URL `http://www.sciencedirect.com/science/article/pii/0031916366906494`.

[5] R. C. Sherwood, J. P. Remeika, and H. J. Williams, Journal of Applied Physics **30**, 217 (1959), URL `http://scitation.aip.org/content/aip/journal/jap/30/2/10.1063/1.1735136`.

[6] K. Yoshii, Journal of Solid State Chemistry **159**, 204 (2001), ISSN 0022-4596, URL `http://www.sciencedirect.com/science/article/pii/S0022459600991527`.

[7] K. Yoshii, A. Nakamura, Y. Ishii, and Y. Morii, Journal of Solid State Chemistry **162**, 84 (2001), ISSN 0022-4596, URL `http://www.sciencedirect.com/science/article/pii/S002245960199351X`.

[8] V. Khomchenko, I. Troyanchuk, R. Szymczak, and H. Szymczak, Journal of Materials Science **43**, 5662 (2008), ISSN 0022-2461, URL `http://dx.doi.org/10.1007/s10853-008-2799-3`.

[9] Y. Ren, T. T. M. Palstra, D. I. Khomskii1, E. Pellegrin, A. A. Nugroho, A. A. Menovsky3, and G. A. Sawatzky, Nature **396**, 441 (1998), URL `http://dx.doi.org/10.1038/24802`.

[10] Y. Ren, T. T. M. Palstra, D. I. Khomskii, A. A. Nugroho, A. A. Menovsky, and G. A. Sawatzky, Phys. Rev. B **62**, 6577 (2000), URL `http://link.aps.org/doi/10.1103/PhysRevB.62.6577`.

[11] E. W. Gorter and J. A. Schulkes, Phys. Rev. **90**, 487 (1953), URL `http://link.aps.org/doi/10.1103/PhysRev.90.487.2`.

[12] N. Menyuk, K. Dwight, and D. G. Wickham, Phys. Rev. Lett. **4**, 119 (1960), URL `http://link.aps.org/doi/10.1103/PhysRevLett.4.119`.

[13] R. Pauthenet, Journal of Applied Physics **29**, 253 (1958), URL `http://scitation.aip.org/content/aip/journal/jap/29/3/10.1063/1.1723094`.

[14] S.-i. Ohkoshi, T. Iyoda, A. Fujishima, and K. Hashimoto, Phys. Rev. B **56**, 11642 (1997), URL `http://link.aps.org/doi/10.1103/PhysRevB.56.11642`.

[15] S.-i. Ohkoshi, Y. Abe, A. Fujishima, and K. Hashimoto, Phys. Rev. Lett. **82**, 1285 (1999), URL `http://link.aps.org/doi/10.1103/PhysRevLett.82.1285`.

[16] P. Mandal, A. Sundaresan, C. N. R. Rao, A. Iyo, P. M. Shirage, Y. Tanaka, C. Simon, V. Pralong, O. I. Lebedev, V. Caignaert, et al., Phys. Rev. B **82**, 100416 (2010), URL `http://link.aps.org/doi/10.1103/PhysRevB.82.100416`.

[17] P. Mandal, C. Serrao, E. Suard, V. Caignaert, B. Raveau, A. Sundaresan, and C. Rao, Journal of Solid State Chemistry **197**, 408 (2013), ISSN 0022-4596, URL `http://www.sciencedirect.com/science/article/pii/S0022459612006007`.

[18] K. Vijayanandhini, C. Simon, V. Pralong, Y. Brard, V. Caignaert, B. Raveau, P. Mandal, A. Sundaresan, and C. N. R. Rao, Journal of Physics: Condensed Matter **21**, 486002 (2009), URL `http://stacks.iop.org/0953-8984/21/i=48/a=486002`.

[19] A. M. Kadomtseva, A. P. Agafonov, I. A. Zorin, A. S. Moskvin, T. L. Ovchinnikova, and V. A. Timofeeva, Sov. Phys. JETP **57**, 833 (1983).

[20] J. Mao, Y. Sui, X. Zhang, Y. Su, X. Wang, Z. Liu, Y. Wang, R. Zhu, Y. Wang, W. Liu, et al., Applied Physics Letters **98**, 192510 (2011), URL `http://scitation.aip.org/content/aip/journal/apl/98/19/10.1063/1.3590714`.

[21] P. W. Anderson, Phys. Rev. **115**, 2 (1959), URL `http://link.aps.org/doi/10.1103/PhysRev.115.2`.

[22] T. Hashimoto, Journal of the Physical Society of Japan **18**, 1140 (1963), `http://dx.doi.org/10.1143/JPSJ.18.1140`, URL `http://dx.doi.org/10.1143/JPSJ.18.1140`.

[23] C. R. Serrao, A. K. Kundu, S. B. Krupanidhi, U. V. Waghmare, and C. N. R. Rao, Phys. Rev. B **72**, 220101 (2005), URL `http://link.aps.org/doi/10.1103/PhysRevB.72.220101`.

[24] T. Yamaguchi, Journal of Physics and Chemistry of Solids **35**, 479 (1974), ISSN 0022-3697, URL `http://www.sciencedirect.com/science/article/pii/S002236977480003X`.

[25] P. Pincus, Phys. Rev. Lett. **5**, 13 (1960), URL `http://link.aps.org/doi/10.1103/PhysRevLett.5.13`.

[26] E. L. Jr., T. Martins, H. Rechenberg, G. Goya, C. Cavelius, R. Rapalaviciute, S. Hao, and S. Mathur, Journal of Magnetism and Magnetic Materials **320**, 622 (2008), ISSN 0304-8853, URL `http://www.sciencedirect.com/science/article/pii/S030488530700827X`.

Appendix A

Derivations for A$_\alpha$, B$_\alpha$ in the MO-IPT ansatz

In this appendix, we provide the derivations and expression of the unknown parameters appearing in the MO-IPT ansatz for the self energy(equation 2.9).

Derivation for A$_\alpha$:

The spectral representation of the α^{th}-orbital Green's function is given by

$$G^{\alpha\alpha}(z) = \int_{-\infty}^{\infty} \frac{D^{\alpha\alpha}(\epsilon)d\epsilon}{z-\epsilon}\,. \tag{A.1}$$

This can be Taylor expanded to obtain the Green function in terms of spectral moments,

$$G^{\alpha\alpha}(z) = \int_{-\infty}^{\infty} \frac{D^{\alpha\alpha}(\epsilon)d\epsilon}{z}(1+\frac{\epsilon}{z}+\frac{\epsilon^2}{z^2}+\cdots) = \sum_{n=0}^{\infty}\frac{\mu_n}{z^{n+1}}\,, \tag{A.2}$$

where μ_n's are the spectral moments. We can also represent the Green function in terms of a continued fraction expansion and this is given by

$$G^{\alpha\alpha}(z) = \frac{\alpha_1}{z+\frac{\alpha_2}{1+\frac{a_3}{z+a_4+\cdots}}}\,. \tag{A.3}$$

By comparing equation A.3 with the equation A.2, we obtain the continued fraction expansion coefficients in terms of spectral moments. Now we can calculate the spectral moments exactly up to any order by using the following expressions[1]:

$$\mu_n^{\alpha\alpha} = \left\langle \left[\underbrace{[...[[f_\alpha, \mathcal{H}], \mathcal{H}], ...\mathcal{H}]_-}_{\text{(n-p)-fold}}, \underbrace{[\mathcal{H}, ...[\mathcal{H}, [\mathcal{H}, f_\alpha^\dagger]]...]_-}_{\text{p-fold}} \right]_+ \right\rangle$$

$$\text{n = 0,1,2,.... ; } 0 \leq \text{ p } \leq \text{ n}$$

The relation between first few spectral moments and continued fraction expansion coefficients is given by,

$$\alpha_1 = \mu_0^{\alpha\alpha} = \langle \{f_\alpha, f_\alpha^\dagger\} \rangle = 1\,, \tag{A.4}$$

$$\alpha_2 = -\mu_1^{\alpha\alpha} = \langle \{[f_\alpha, \mathcal{H}_{imp}], f_\alpha^\dagger\} \rangle\,,$$

$$\alpha_2 = -[(\epsilon_\alpha - \mu) + \sum_{\beta \neq (\alpha)} U_{\alpha\beta} \langle n_\beta \rangle]\,, \tag{A.5}$$

$$\alpha_3 = -\frac{\mu_2^{\alpha\alpha}\mu_0^{\alpha\alpha} - (\mu_1^{\alpha\alpha})^2}{\mu_1^{\alpha\alpha}\mu_0^{\alpha\alpha}}\,, \tag{A.6}$$

$$\begin{aligned} \mu_2^{\alpha\alpha} = (\epsilon_\alpha - \mu)^2 + \frac{1}{N}\sum_{k\alpha} V_{k\alpha}^2 + 2(\epsilon_\alpha - \mu)\sum_{\beta \neq \alpha} U_{\alpha\beta}\langle n_\beta \rangle \\ + \sum_{\beta \neq \alpha}\sum_{\gamma \neq \alpha} U_{\alpha\beta}U_{\alpha\gamma}\langle n_\beta n_\gamma \rangle\,, \end{aligned} \tag{A.7}$$

$$\alpha_3 = \frac{\frac{-1}{N}\sum_{k\alpha} V^2{}_{k\alpha} - \sum_{\beta,\gamma \neq \alpha} U_{\alpha\beta}U_{\alpha\gamma}\left(\langle n_\beta n_\gamma \rangle - \langle n_\beta \rangle \langle n_\gamma \rangle\right)}{(\epsilon_\alpha - \mu) + \sum_{\beta \neq \alpha} U_{\alpha\beta}\langle n_\beta \rangle}\,. \tag{A.8}$$

For sufficiently large values of z, one can truncate the continued fraction expansion of the Green's function (equation A.3) at the appropriate level and take the limit $z \rightarrow \infty$. Then

$$G^{\alpha\alpha}(z) = \frac{\alpha_1}{z + \alpha_2 - \frac{\alpha_2\alpha_3}{z}} \tag{A.9}$$

After substituting the continued fraction expansion coefficients in equation A.9, we find the self energy contribution for the Green's function in the high frequency limit as

$$\Sigma_\alpha(\omega) \xrightarrow{\omega\to\infty} \sum_{\beta\neq\alpha} U_{\alpha\beta}\langle n_\beta\rangle + \frac{\sum_{\beta,\gamma\neq\alpha} U_{\alpha\beta}U_{\alpha\gamma}\left(\langle n_\beta n_\gamma\rangle - \langle n_\beta\rangle\langle n_\gamma\rangle\right)}{\omega}$$

$$\Sigma_\alpha(\omega) = \sum_{\beta\neq\alpha} U_{\alpha\beta}\langle n_\beta\rangle + \frac{\sum_{\beta\neq\alpha} U^2_{\alpha\beta}\langle n_\beta\rangle\left(1-\langle n_\beta\rangle\right)}{\omega} + \frac{\sum_{\beta\neq\alpha}\sum_{\gamma\neq(\beta\neq\alpha)} U_{\alpha\beta}U_{\alpha\gamma}\left(\langle n_\beta n_\gamma\rangle - \langle n_\beta\rangle\langle n_\gamma\rangle\right)}{\omega} \tag{A.10}$$

It is easy to show that in the limit of high frequencies, $\Sigma^{(2)}_{\alpha\beta}$ has the following form[2],

$$\Sigma^{(2)}_{\alpha\beta} = \frac{U^2_{\alpha\beta}}{\omega}\langle n_{0\beta}\rangle\left(1-\langle n_{0\beta}\rangle\right) \tag{A.11}$$

Here $n_{0\beta}$ is the Hartree-corrected charge on impurity because the propagators used in the second order pair bubble diagram are Hartree-corrected propagators. In the high frequency limit the self energy ansatz reduces to the following form:

$$\Sigma_\alpha(\omega) = \sum_{\beta\neq(\alpha)} U_{\alpha\beta}\langle n_\beta\rangle + A_\alpha \sum_{\beta\neq(\alpha)} \Sigma^{(2)}_{\alpha\beta}\,. \tag{A.12}$$

We obtain the expression for A_α by substituting equation A.11 in the equation A.12 and comparing with equation A.10 as

$$A_\alpha = \frac{\sum_{\beta\neq(\alpha)} U^2_{\alpha\beta}\langle n_\beta\rangle\left(1-\langle n_\beta\rangle\right)}{\sum_{\beta\neq(\alpha)} U^2_{\alpha\beta}\langle n_{0\beta}\rangle\left(1-\langle n_{0\beta}\rangle\right)} + \frac{\sum_{\beta\neq(\alpha)} U_{\alpha\beta}\sum_{\gamma\neq(\beta\neq\alpha)} U_{\alpha\gamma}\left(\langle n_\beta n_\gamma\rangle - \langle n_\beta\rangle\langle n_\gamma\rangle\right)}{\sum_{\beta\neq(\alpha)} U^2_{\alpha\beta}\langle n_{0\beta}\rangle\left(1-\langle n_{0\beta}\rangle\right)}\,.$$

Note that a two-particle correlation function is needed to find A_α.

Derivation for B_α:

The relation between the impurity Green's function and the self energy in the atomic limit is,

$$G_\alpha(\omega) = \frac{1}{\omega^+ + \mu - \epsilon_\alpha - \Sigma_\alpha(\omega)}\,, \tag{A.13}$$

where the self-energy, $\Sigma_\alpha(\omega)$ may be represented as a continued fraction:

$$\Sigma_\alpha(\omega) = \omega^+ + \mu - \epsilon_\alpha - \frac{1}{\frac{\alpha_1}{z+\frac{\alpha_2}{1+\frac{a_3}{z+a_4\cdots}}}} \,. \tag{A.14}$$

As a simple case we consider only two poles in the self energy. In principle we can keep all the poles in the self energy but the difficulty is that pole of order n in the self energy involves the $n + 1^{\text{th}}$ order correlation function. These functions are very hard to calculate without making approximations. With the two pole approximation for self energy, equation A.14 reduces to the following form[3]

$$\Sigma_\alpha(\omega) = \sum_{\beta \neq (\alpha)} U_{\alpha\beta}\langle n_\beta\rangle + \frac{\alpha_2\alpha_3}{\omega^+ + \alpha_3 + \alpha_4} \tag{A.15}$$

$$\text{where } \alpha_2 = -\mu_1^{\alpha\alpha} \,, \tag{A.16}$$

$$\alpha_3 = -\frac{\mu_2^{\alpha\alpha} - (\mu_1^{\alpha\alpha})^2}{\mu_1^{\alpha\alpha}} \,, \tag{A.17}$$

$$\text{and } \alpha_4 = -\frac{\mu_1^{\alpha\alpha}\mu_3^{\alpha\alpha} - (\mu_2^{\alpha\alpha})^2}{\mu_1^{\alpha\alpha}\mu_2^{\alpha\alpha} - (\mu_1^{\alpha\alpha})^2} \,. \tag{A.18}$$

In the atomic limit(V→ 0), the second order pair bubble diagram $\Sigma^{(2)}_{\alpha\beta}(\omega)$ reduces to the following form[4, 5],

$$\Sigma^{(2)}_{\alpha\beta}(\omega) = \frac{U^2_{\alpha\beta}[\langle n_{0\beta}\rangle(1 - \langle n_{0\beta}\rangle)]}{\omega^+ + \mu_0} \,. \tag{A.19}$$

Here μ_0 is the pseudo-chemical potential. As mentioned earlier, we find this quantity by satisfying the Luttinger's theorem or equivalently the Friedel's sum rule. Now, the self energy ansatz becomes

$$\Sigma_\alpha = \sum_{\beta\neq(\alpha)} U_{\alpha\beta}\langle n_\beta\rangle + \frac{A_\alpha \sum_{\beta\neq(\alpha)} U^2_{\alpha\beta}[\langle n_{0\beta}\rangle(1-\langle n_{0\beta}\rangle)]}{\omega^+ + \mu_0 - B_\alpha \sum_{\beta\neq(\alpha)} U^2_{\alpha\beta}[\langle n_{0\beta}\rangle(1-\langle n_{0\beta}\rangle)]}\,. \tag{A.20}$$

By comparing the equation A.20 with equation A.14 we find the expression for B_α in terms of spectral moments as,

$$B_\alpha = \frac{\mu_0 - (\alpha_3 + \alpha_4)}{\sum_{\beta\neq(\alpha)} U^2_{\alpha\beta}[\langle n_{0\beta}\rangle(1-\langle n_{0\beta}\rangle)]} \tag{A.21}$$

After substituting the spectral moments in equation A.21 B_α becomes,

$$\begin{aligned} B_\alpha = & \frac{\mu_0 + \epsilon_\alpha - \mu - \sum_{\beta\neq\alpha} U_{\alpha\beta}\langle n_\beta\rangle}{\tau_\alpha} \\ & - \frac{\sum_{\beta\neq\alpha}\sum_{\gamma\neq\alpha}\sum_{\eta\neq\alpha} U_{\alpha\beta}U_{\alpha\gamma}U_{\alpha\eta}\,[\langle n_\beta\rangle\langle n_\gamma n_\eta\rangle - \langle n_\beta n_\gamma n_\eta\rangle]}{\tau^2_\alpha A_\alpha} \end{aligned} \tag{A.22}$$

where

$$\tau_\alpha = \sum_{\beta\neq\alpha} U^2_{\alpha\beta}\langle n_{0\beta}\rangle(1-\langle n_{0\beta}\rangle) \tag{A.23}$$

Bibliography

[1] M. Potthoff, T. Wegner, and W. Nolting, Phys. Rev. B **55**, 16132 (1997), URL `http://link.aps.org/doi/10.1103/PhysRevB.55.16132`.

[2] A. L. Yeyati, F. Flores, and A. Mart´in-Rodero, Phys. Rev. Lett. **83**, 600 (1999), URL `http://link.aps.org/doi/10.1103/PhysRevLett.83.600`.

[3] V. Oudovenko, K. Haule, S. Y. Savrasov, D. Villani, and G. Kotliar, unpublished.

[4] H. Kajueter and G. Kotliar, Phys. Rev. Lett. **77**, 131 (1996), URL `http://link.aps.org/doi/10.1103/PhysRevLett.77.131`.

[5] A. Mart´in-Rodero, F. Flores, M. Baldo, and R. Pucci, Solid State Communications **44**, 911 (1982), URL `http://www.sciencedirect.com/science/article/pii/0038109882903039`.

Curriculum Vitae

CONTACT INFORMATION

Nagamalleswara Rao Dasari Mobile: (+91)9972763678
Theoretical Sciences Unit, email: nagamalleswararao.d@gmail.com
JNCASR, Bangalore, 560064.
India.

BIOGRAPHICAL DATA

Date and Place of Birth:	September 10, 1983, Andhra Pradesh, India.
Citizenship:	Indian
Language:	Telugu, English

EDUCATION

2009 - Present Ph.D., Jawaharlal Nehru Centre for Advanced Scientific Research, Bangalore, India.

2003 - 2005 Master of Science, Acharya Nagarjuna University, Andhra Pradesh, India.

2001 - 2003 Bachelor of Science, Acharya Nagarjuna University, Andhra Pradesh, India.

TEACHING EXPERIENCE

2007 - 2008 Junior Lecturer, Humanities and Sciences Department, ACE Engineering college, Andhra Pradesh, India.

2005 - 2007 Junior Lecturer, Physics Department, DNR college, Andhra Pradesh, India.

PROFESSIONAL QUALIFICATIONS

- Qualified for the final round Interview of SPM Fellowship in 2009.
- All India Rank **10** in GATE-2009 (99.82 percentile).
- All India Rank **60** in JEST-2009.
- UGC-CSIR (NET) Exam Qualified in Dec 2008 and Dec 2009.

RESEARCH AFFILIATIONS

- Visiting Scholar, TU Wien, Austria, 22nd June 2015 - 5th July 2015.
- Visiting Scholar, University of Würzburg, Germany, 8th June 2015 - 20th June 2015.
- Visiting Scholar, Department of Physics & Astronomy, Louisiana State University, USA, 2012 October - May 2013.
- Visiting Scholar, Department of Condensed Matter Physics and Material Sciences, S. N. Bose National Centre for Basic Sciences, India, 15th November 2011 - 25th December 2011.

AWARDS RECEIVED

- International travel-grant award from JNCASR, India, June 2015.
- International travel award from ICAM-I2CAM, USA, Sept 2012.
- International travel-fellowship award from CICS, India, Jan 2012.
- Senior Research Fellow(SRF) award received from UGC-CSIR, India, Aug 2011.

COMPUTER SKILLS

- Advanced: Fortran, Python, Linux, Latex
- Intermediate: C++

REFERENCES

Prof. N. S. Vidhyadhiraja
Theoretical Sciences Unit,
JNCASR, Bangalore,
Karnataka, India.
Tel: +91-80-22082790
Email: nsvraja@gmail.com

Prof. Mark Jarrell
Department of Physics & Astronomy,
Louisiana State University, Baton Rouge,
LA 70803-4001, USA.
Tel: +1-225(578)-7528
Email: jarrellphysics@gmail.com